Universidade de Aveiro Departamento de Física
2016

Fábio André Barbosa Pereira

Estudo e desenvolvimento de fotodetectores UV com vista ao upgrade do COMPASS RICH-1 e a aplicações

Study and development of UV photodetectors envisaging COMPASS RICH-1 upgrade and applications

Universidade de Aveiro Departamento de Física
2016

Fábio André Barbosa Pereira

Estudo e desenvolvimento de fotodetectores UV com vista ao upgrade do COMPASS RICH-1 e a aplicações

Study and development of UV photodetectors envisaging COMPASS RICH-1 upgrade and applications

Tese apresentada à Universidade de Aveiro para cumprimento dos requisitos necessários à obtenção do grau de Doutor em Engenharia Física, realizada sob a orientação científica do Doutor João Filipe Calapez de Albuquerque Veloso, Professor Auxiliar do Departamento de Física da Universidade de Aveiro e coorientação da Doutora Silvia Dalla Torre, Directora da secção de Trieste do Istituto Nazionale di Fisica Nucleare, Itália

Apoio financeiro da FCT através da bolsa de doutoramento com a referência SFRH/BD/81259/2011 e do FSE/FEDER no âmbito do QREN através dos programas COMPETE e Projetos CERN/FP/123597/2011, CERN/FP/123604/2011, CERN/FP/109283/2009, PTDC/FIS/113005/2009 e PTDC/FIS/110925/2009

o júri / the jury

Presidente / president

Prof. Doutora Ana Isabel Couto Neto da Silva Miranda
Professora Catedrática, Departamento de Ambiente e Ordenamento, Universidade de Aveiro

vogais

Prof. Doutor Joaquim Marques Ferreira dos Santos
Professor Catedrático, Departamento de Física, Faculdade de Ciências e Tecnologia da Universidade de Coimbra.

Prof. Doutor Luís Filipe dos Santos Peralta
Professor Associado com Agregação, Departamento de Física, Faculdade de Ciências da Universidade de Lisboa

Prof. Doutor Luís Manuel Cadillon Martins Costa
Professor Associado com Agregação, Departamento de Física da Universidade de Aveiro

Prof. Doutor Nuno Filipe da Silva Fernandes de Castro
Investigador, LIP — Laboratório de Instrumentação e Física Experimental de Partículas e Professor Auxiliar Convidado, Departamento de Física e Astronomia, Faculdade de Ciências da Universidade do Porto

Prof. Doutor João Filipe Calapez de Albuquerque Veloso
Professor Auxiliar com Agregação, Departamento de Física da Universidade de Aveiro

Agradecimento / Acknowledgement

I would like to express my gratitude, firstly, to all the members of the DRIM team within which I developed a lot of my work, who have been the best of friends and whose help was more than anyone could ever ask.
In particular, I want to thank my advisor, Dr. João Veloso, for the opportunity it was given to me of joining his amazing research group, and to work under his guidance, almost seven years ago. Besides the knowledge that was transmitted to me during that time, I will preserve the memory of his dedication.

To Dr. Silvia Dalla Torre I wish to thank all the guidance I received and that was constant as I joined the Italian group under her direction, in Trieste, an opportunity I deeply valued. I am sure it took patience to give me the tools and knowledge I required in order to contribute meaningfully to the group's work, which I hope I did.
I also thank all the members of INFN – Trieste with whom I shared those periods, who made me feel at home at all times, who never stopped helping me and whose friendship is priceless. Grazie.

I also deeply thank my friends and my family.

palavras-chave

COMPASS, detectores RICH, detectores gasosos, MPGD, THGEM, MICROMEGAS, Câmara Compton

resumo

O COMPASS é uma experiência no SPS do CERN cujo objectivo é estudar a espectroscopia hadrónica e a estrutura dos nucleões. A experiência inclui um detector RICH de larga aceitação, operacional desde 2001 e sujeito a um upgrade de parte dos seus fotodetectores em 2006. Os restantes 75% da área de fotodetecção ainda utilizam as MWPCs do desenho original, que sofrem de limitações de ganho devido ao envelhecimento dos fotocátodos pelo bombardeamento com iões e a instabilidades por eles induzidas. Além destas limitações, o aumento de luminosidade expectável nos próximos anos para a experiência tornam o upgrade dos restantes fotodetectores desejável. Este upgrade deverá acontecer em 2016 e deverá fazer uso de detectores híbridos compostos por ThGEMs e MICROMEGAS.

Este trabalho apresenta o estudo, desenvolvimento e caracterização de fotodetectores gasosos com vista ao upgrade referido, e o progresso na produção e nas técnicas de avaliação necessário para alcançar as maiores áreas de detecção com os desempenhos exigidos. Inclui também a descrição e tratamento de exercícios com irradiação por feixe de partículas dos detectores em causa.

Os MPGDs podem também ser usados em várias outras aplicações, entre as quais se destaca a imagiologia médica nuclear. Este trabalho inclui, adicionalmente, as etapas iniciais de simulação, montagem e caracterização de um protótipo de detector gasoso para aplicação como Câmara Compton.

keywords

COMPASS, RICH detectors, Gaseous detectors, MPGD, THGEM, MICROMEGAS, Compton Camera

abstract

COMPASS is an experiment at CERN's SPS whose goal is to study hadron structure and spectroscopy. The experiment includes a wide acceptance RICH detector, operating since 2001 and subject to a major upgrade of the central region of its photodetectors in 2006. The remaining 75% of the photodetection area are still using MWPCs from the original design, who suffer from limitations in gain due to aging of the photocathodes from ion bombardment and due to ion-induced instabilities.

Besides the mentioned limitations, the increased luminosity conditions expected for the upcoming years of the experiment make an upgrade to the remaining detectors pertinent. This upgrade should be accomplished in 2016, using hybrid detectors composed of ThGEMs and MICROMEGAS.

This work presents the study, development and characterization of gaseous photon detectors envisaging the foreseen upgrade, and the progress in production and evaluation techniques necessary to reach increasingly larger area detectors with the performances required. It includes reports on the studies performed under particle beam environment of such detectors.

MPGD structures can also be used in a variety of other applications, of which nuclear medical imaging is a notorious example. This work includes, additionally, the initial steps in simulating, assembling and characterizing a prototype of a gaseous detector for application as a Compton Camera.

Contents

List of Figures

List of Acronyms

ADC – Analog to Digital Converter
APD – Avalanche Photodiode
COMPASS – COmmon Muon Proton Apparatus for Structure and Spectroscopy
GEM – Gas Electron Multiplier
GPD – Gaseous Photon Detector
GPM – Gaseous Photon Multiplier
HEP – High Energy Physics
HPSC – High Pressure Scintillation Chamber
MAPMT – Multi-Anode PMT
MCA – Multi-Channel Analyzer
MICROMEGAS / Micromegas – MICRO-MEsh GAseous Structure
MIP – Minimum Ionizing Particle
MPV – Most Probable Value of energy deposition by a MIP
MPGD – Micro-Pattern Gaseous Detector
MSGC – Micro-Strip Gas Chamber
MWPC – Multi Wire Proportional Chamber
PCB – Printed Circuit Board
PET – Positron Emission Tomography
PID – Particle Identification
PMT – Photon Multiplier Tube
PS – Power Supply
QE – Quantum Efficiency
RICH – Ring Imaging Cherenkov
SDC – Scintillation Drift Chamber
SiPM – Silicon Photomultipler
SPECT – Single Photon Emission Computed Tomography
THGEM / ThGEM – Thick Gas Electron Multiplier
TPC – Time Projection Chamber
VUV – Vacuum Ultra-Violet

Introduction

In the final decades of the last century, Ring Imaging Cherenkov (RICH) detectors established themselves as the most robust and reliable particle identification (PID) instruments in a wide momentum range [1], evidenced by the high number of High Energy Physics (HEP) experiments that employ such systems [2].

Among those experiments is COMPASS [3] (COmmon Muon Proton Apparatus for Structure and Spectroscopy) at CERN, whose goal is to study hadron structure and spectroscopy using high intensity muon and hadron beams. The experiment counts with a RICH detector operational since 2001 and subject to an upgrade in 2006. The plans to extend the COMPASS physics program foresee an increase in luminosity, raising the requirements for the future performance of COMPASS RICH-1. To cope with the more challenging conditions an upgrade of the photodetection system is schedule for the near future [4]. The new photodetectors to be installed must improve the gain and resolution of the RICH detector while allowing its operation under higher irradiation rates. Taking into account the large active areas that need to be covered (4 m^2) gaseous detectors are the only cost effective solution that fulfill the requirements.

The evolution of microlithographic techniques led in recent years to the establishment of a third generation of Gaseous Photon Detectors (GPDs) based in Micro-Pattern Gaseous Detectors (MPGDs) [5, 6] such as the MSGC, GEM or Micromegas. The new devices present major improvements to the performances of previous generations that made use of MWPCs, especially in terms of stability of operation and in maximum gains achieved. Among the several new structures developed, ThGEMs [7] and MICROMEGAS [8] are particularly promising for applications as RICH counters.

This work is, most of all, the account of R&D studies performed and results achieved with the purpose of developing large area MPGD-based detectors envisaging the upgrade of the COMPASS RICH-1 detector. The research activities took place either at INFN (Trieste section) or at CERN, and under the scope of both the RD51 collaboration and the COMPASS experiment. The efforts culminated on the development of detectors composed of ThGEMs and Micromegas in a Hybrid configuration which have been approved as future RICH-1 photodetectors.

Within the scope of the RD51 collaboration [9] – to which the author is associated as a member of I3N - Department of Physics, University of Aveiro – gaseous detectors, namely MPGDs, are studied and developed for a wide range of applications. One of the most important for the non-

scientific community is the research on nuclear medical imaging, with systems such as PET and SPECT being essential in diagnostic and medical research procedures, but which can be improved or that could be matched by more cost effective solutions. In that context, a Compton Camera is an imaging device whose goal is to compete with Gamma Cameras by achieving increased sensibility and higher flexibility in the choice of radioisotopes.

The author contributed to the proposal and development of a Gaseous Compton Camera [10], a work which is described in the final chapter of this thesis. The studies and simulations regarding this topic were developed in Aveiro.

The present thesis is divided in four chapters, with the scientific contributions of the author confined to the latter two. After this introduction, Chapter 1 will detail some of the theoretical and historical background regarding gaseous detectors and MPGDs, with particular emphasis on the aspects that are relevant for the studies presented later on this work. That is followed by a chapter introducing Cherenkov counters and alternative PID techniques, as well as a small description of the present COMPASS RICH-1 setup.

Chapter 3 encompasses most of the work performed in the development of solutions for the photodetectors of RICH-1. The chapter includes sections of research and development of detectors, done in Trieste, followed by tests of the detectors under beam irradiation, occurring at CERN. In the laboratory, the author contributed to the implementation of detector quality control protocols, and to the assembly and characterization of ThGEMs and Micromegas. Then, the author joined the Test Beam exercises where the detectors were evaluated, and took part in the data analysis of the results.

Chapter 4 includes both the theory and concepts behind Compton Cameras and the development of a gaseous version of this technique for medical imaging. Besides calculations of the expected performance of the detector with different options (such as gas medium), an initial characterization of the proposed chamber is given. A final section presents results obtained from fundamental studies of statistical fluctuations of photoelectron extraction efficiency from CsI photocathodes operating in noble gases.

Finally, closing remarks and future prospects are presented.

Chapter 1

Radiation detection with Gaseous Detectors

Gaseous detectors have been for decades the solution of choice for most large area applications in which radiation detection is required. The widespread implementation of Time Projection chambers (TPCs) in high energy physics experiments is one obvious example attesting that. The reason for this resides mostly in the fact that the alternative solid-state detectors are significantly more expensive, but also because, among other things, they bring a higher material budget within the acceptance of the setup, causing undesired collateral effects.

For photon detection purposes (namely, of Cherenkov light), PMTs (Photomultiplier Tubes) offer the best performances in terms of gains and efficiency, but they are costly solutions for the coverage of large areas and are significantly affected by the possible presence of magnetic fields of few mT. Solid-state detectors such as the ones using SiPMs (Silicon Photomultipliers) or HPDs (Hybrid Photon Detectors) are a recent and promising solution with great spatial, energy and time resolution, but nonetheless suffer from other drawbacks including a trade off between low temperature operation and higher dark count rate, crosstalk between pixels and, with particular interest to RICH applications, feeble UV light detection efficiency at affordable costs.

This chapter is dedicated to a theoretical and historical background of gaseous detectors, and is divided in four sections. The first is an introduction to the interactions of charged particles and electromagnetic radiation with matter, followed by section 1.2 focused on the general principles of operation of gaseous detectors. The third section gives a generic overview of the first two generations of GPDs, using MWPCs with photoconverting vapors (first) and with CsI photocathodes (second). The final section approaches the use of MPGDs as the third generation of GPDs, with emphasis on the two most important detector elements for this work: the Micromegas and the ThGEM.

Each section's goal is to be concise and pertinent, but not exhaustive. As an example, the first section dealing with radiation interactions with matter will focus in charged particles and electromagnetic radiation because these are relevant for the studies analyzed later on, in the

experimental chapters. Conversely, the multitude of gaseous detector architectures that exist, in particular the electron multiplier structures, will pass mostly unmentioned except for a few notable examples.

1.1 Radiation interactions with matter

Even though the focus of this work is in the development of photon detectors, most of the characterization and the preliminary study of detectors presented in the experimental chapters is done using radioactive sources of X-rays, specifically the Fe-55 source. Besides, these detectors are envisaged for operation – and are tested – under charged particle beam irradiation. For these reasons, a generic introduction of the mechanisms that rule the interaction of both types of radiation is hereby presented.

1.1.1 Interaction of charged particles

Charged particles interact with a medium mostly via electromagnetic (Coulomb) effects between the particle and the electrons (with mass m_0) in the atoms. Other effects, involving the nuclei (such as Rutherford scattering), can occur but their probability is considered negligible within this context.

An heavy particle (with mass $m >> m_0$) transversing a medium with kinetic energy E will lose energy to its atoms, promoting them to an excited state or ionizing them. This happens over several interactions with different atoms/electrons, since for each interaction there is a maximum energy E_{max} that is transfered, which for most cases can be approximated by [11]

$$E_{\text{max}} \approx \frac{E^2}{E + m_0^2 c^2/2m} \,. \tag{1.1}$$

The specific differential energy loss of a particle along its path is traditionally described by the Bethe-Bloch formula [12]:

$$-\frac{\mathrm{d}E}{\mathrm{d}x} = \frac{4\pi e^4 z^2}{m_0 v^2} NZ \left[\ln\frac{2m_0 v^2}{I} - \ln\left(1-\frac{v^2}{c^2}\right) - \frac{v^2}{c^2}\right] , \tag{1.2}$$

where V is the particle's velocity, c the speed of light in vacuum, ze is the charge of the particle, N and Z are the number density and atomic number of the absorber medium, and I represents the average excitation and ionization potential of the absorber, usually determined experimentally (for argon it is roughly 190 eV [13]). One should note that x is not a measure of length but a specific path, in $\mathrm{g/cm^2}$, and so $\mathrm{d}E/\mathrm{d}x$ is typically expressed in units such as $\mathrm{MeV/(g/cm^2)}$ or equivalent.

The Bethe-Bloch equation accurately describes the energy loss due to interaction of charged particles in the range of momenta with interest for this work. In a broader range, the behavior of the energy loss function is very different depending, namely, on the energy of the incident particle and in the type of approximations which are considered. Different regions of the energy loss curve are identified in figure 1.1, where the stopping power for muons in copper is plotted.

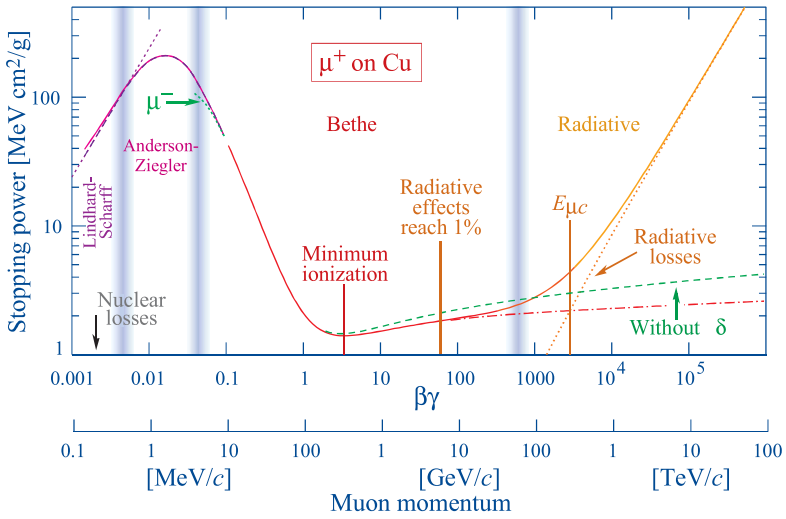

Figure 1.1 Stopping power ($-\mathrm{d}E/\mathrm{d}x$) for positive muons in copper, over a wide range of momenta [13]. Near the minimum ionization region described by the Bethe formula (in red), the particles are called MIPs.

In such example, the Bethe-Bloch function (in red) gives an accurate description for particles with momentum between ~10 $\mathrm{MeV/c}$ and a few tens of $\mathrm{GeV/c}$. For the lower energies/momenta described by it, the dependence of the energy loss scales with $1/v^2$. This means that, in the plot illustrated in figure 1.1, a muon with momentum in the order of tens of $\mathrm{MeV/c}$ will lose increasingly more energy with each collision, eventually stopping. For higher momenta, there is a point of minimum energy loss (at a few hundred $\mathrm{MeV/c}$) and from there a slow increase up to 100 $\mathrm{GeV/c}$ of momentum. This smooth behavior means that a particle with such energy – typically referred to as a MIP (Minimum-ionizing particle) – is weakly affected by each collision and stays in that regime for a very long path, with the resultant energy loss being almost homogeneous along it.

The equation predicts than in the MIP region there is negligible difference between types of particles [14] and the average specific differential energy loss ranges between 1 and 2 $\mathrm{MeV/(g/cm^2)}$ for virtually all materials [15]. As an example, in a gaseous argon atmosphere at standard temperature and pressure, MIPs suffer an average energy loss of ~2.5 $\mathrm{keV/cm}$ [13].

The Bethe-Bloch formula and the other considerations made above were about the average value of energy loss in theoretical conditions. However, in practical applications each single MIP particle crossing a thin region of material will show strong and asymmetric fluctuations of the deposited energy relative to the average value. In fact, for most experimental conditions where the energy deposited is measured, the value predicted by equation 1.2 has little meaning, since it strongly depends of very rare and highly energetic interactions to be actually verified.

For practical applications, the fluctuations of energy loss should be transposed to a spectra where the value with a consistent meaning is the most probable energy loss, i.e. the peak of the probability distribution function (Most Probable Value, MPV). This fluctuations follow a Landau

distribution, whose peak can be estimated from

$$\Delta E_p = \xi \left(\ln \frac{2m_0 c^2 \beta^2 \gamma^2 \xi}{I^2} + j - \beta^2 - \delta \right) , \tag{1.3}$$

where $\beta = v/c$, $\gamma = 1 + E/mc^2$, δ (~10^{-3} $\mathrm{g/cm^3}$) is a correction factor for density effects, j=0.2, and $\xi = (K/2)(Z/A)(x/\beta^2)$ where A is the atomic mass and K = 0.307075 $\mathrm{MeV/(g/cm^2)}$. In this case, for 1 cm of argon, the peak appears at 1.2 keV, which is less than half the average energy loss value predicted.

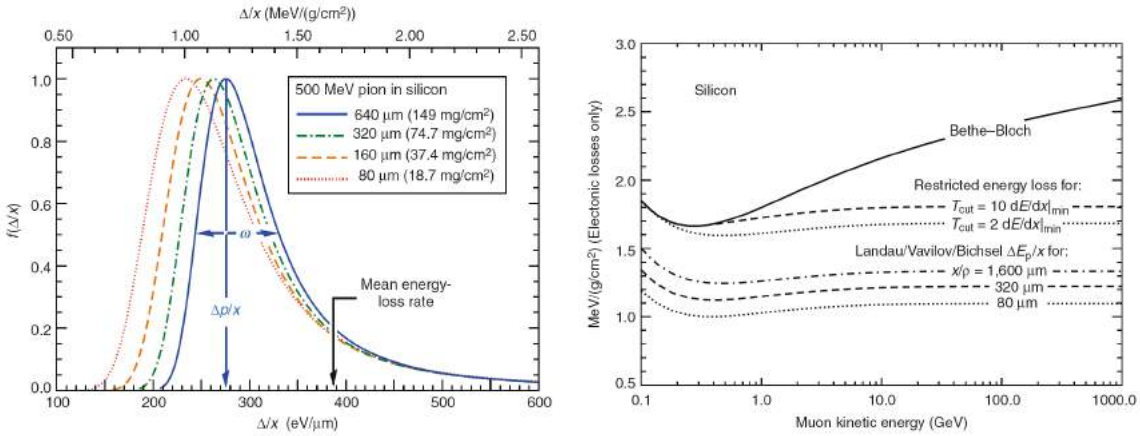

Figure 1.2 Left: Landau distribution of the energy loss for different thicknesses of absorbing medium (silicon) and the corresponding mean energy loss rate. Right: the average stopping power predicted by Bethe-Bloch (solid line) increases after the minimum, while the Landau distribution peak is almost constant for the three silicon absorber thicknesses (lower dashed lines) as a function of the particle's kinetic energy. [15]

Figure 1.2 at the left illustrates typical Landau distributions for different thicknesses of silicon absorbers. While the mean energy loss value remains the same, the Landau peak increases with absorber thickness.

Around the maximum value of the distribution (ΔE_p) the histogram can be approximated by

$$L(\lambda) = \frac{1}{\sqrt{2\pi}} e^{-\frac{1}{2}(\lambda + e^{-\lambda})} , \tag{1.4}$$

where $\lambda = \frac{\Delta E - \Delta E_p}{\xi}$ [11]. The Landau has FWHM ≈ 4ξ [15].

One of the interesting properties of this distribution is that it reinforces the MIP behavior, in the sense that the most probable value of energy loss is virtually constant for any kinetic energy of the particle above the MIP criterion, even more so than the average value given by the Bethe-Bloch equation. The dependence of the mean energy loss (solid line) and of the Landau MPV (three lower dashed lines) as a function of MIP kinetic energy is compared at the right of figure 1.2.

1.1.2 Interaction of high energy electromagnetic radiation

Electromagnetic radiation interacts with matter through several mechanisms. By restricting the focus of this section to the energy ranges of interest the treatment can be simplified. In this section it is dealt solely with electromagnetic radiation whose energy is higher than the UV range.

γ-rays are high energy electromagnetic radiation that originate from nuclear transitions or energetic particle interactions. They differ from X-rays which are emitted as a result of electron interactions with an atom, or during an atom's de-excitation process, but have no different properties except their source, meaning that any statement made regarding γ-rays is valid for X-rays of the same energy.

Unlike charged particles, which interact through the medium in a almost continuous manner with little effect of each event, photons will very likely suffer a single interaction which changes significantly their status. In most practical cases only three interaction processes matter: photoelectric absorption, scattering and pair production. Their preponderance is dependent on the energy of the radiation but also on the atomic number of the material being irradiated.

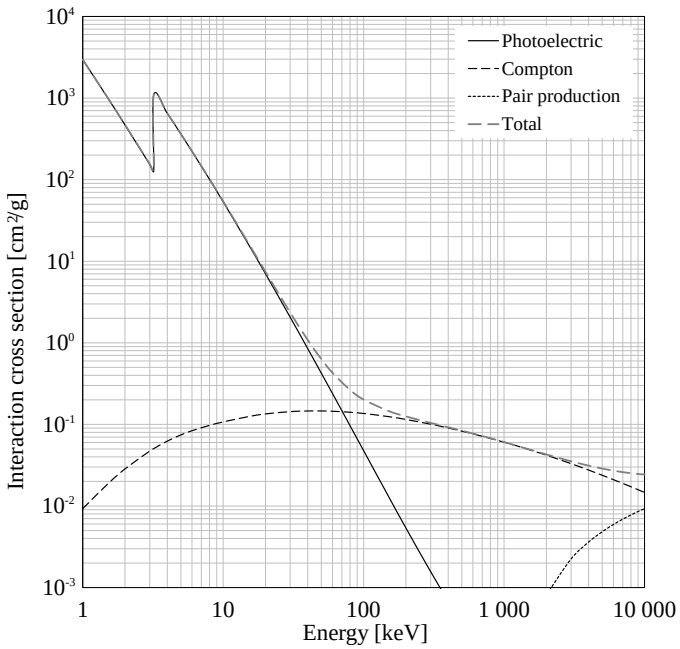

Figure 1.3 Ar:CH_4 - 70:30 mass attenuation coefficients for electromagnetic interactions. The edge at ~3 keV of the photoelectric effect coefficient is caused by the binding energy of argon's K-shell. For lower energy X-rays only the photoelectric effect is relevant. (data from [16])

Pair production, an effect that requires photons to have an energy at least twice that of electrons at rest ($2m_0c^2$, or 1.02 MeV) [12], can be dismissed from this analysis. For the light elements, in particular for the gases that fill the gaseous detectors through most of the studies covered by this work (i.e. argon, neon, methane, carbon dioxide) the Compton scattering cross section is small, even

more so under irradiation with the low energy 5.9 keV X-rays from the Fe-55 source which will be used for most studies (see figure 1.3). Therefore, and because the Compton effect will be subject to a more dedicated analysis in chapter 4 dealing with Compton Cameras, its description is also postponed for now.

Photoelectric effect is, then, the aspect of immediate importance. In this effect, a photon interacts with an atom and is absorbed, leading to the ejection of an electron with kinetic energy $E_{e^-} = E_\gamma - E_b$, where E_b is the binding energy of the electron in its original shell [12]. Because the effect only occurs if $E_\gamma > E_b$, the cross section plot as seen in figure 1.3 shows an absorption edge, i.e. a sharp increase in probability when the photon enters the energy range where a new atom shell can contribute to the effect [11, 12, 15]. The particular case shown in the plot is for Argon's 3.2 keV K-shell.

The cross section of the effect can be roughly approximated as proportional to $Z^n/E_\gamma^{3.5}$, with n varying from 4 to 5, depending on the photon's energy [12]. It is evident the increased probability of the effect for higher Z materials and lower energy radiation.

After the electron is ejected, the now positive ion will have it's vacancy filled either by capturing a free electron from the medium or by rearrangement within the shells of the atom. In any case, either characteristic X-rays of the atom or Auger electrons are emitted as result.

The exact way the process unfurls is strictly dependent on the atom where the photoelectric effect occurs. As a pertinent example, an Ar atom excited by a photoelectric interaction with a 5.9 keV Fe-55 X-ray will, most likely, eject an electron with kinetic energy ~2.7 keV from its K-shell (E_b = 3.2 keV). Then, with 85% probability, the emission of a ~3 keV Auger electron will occur; otherwise, a characteristic X-ray with energy E_{caract}=3 keV is emitted, when an electron from the L-shell fills the K-shell vacancy (fluorescence) [15].

If both the photoelectron and the subsequent Auger electron or fluorescence X-ray are absorbed in a detector volume, the resulting energy deposited and measured will closely match the energy of the original X-ray. However, for argon at normal temperatures and pressures, while the photoelectron and the Auger electron both have practical ranges of <300 $\mu\mathrm{m}$ in the detector, the characteristic X-ray has a mean absorption length of ~4 cm, and therefore a significant probability of not being absorbed, depending on the detector volume [15]. In the latter case, a secondary peak – the escape peak – will be measured by the detector with energy $E_{\text{escape}} = E_\gamma - E_{\text{caract}}$, or 2.9 keV.

1.2 General properties of Gaseous Detectors

Gaseous Detectors work, in a first stage, by converting the energy deposited by the interaction of radiation to a proportional number of electrons and their respective ions, i.e. by creating electron-ion pairs. The primary charge created is usually small, but can be detected without amplification by a ionization chamber, one of the oldest and simplest detector types. In it, the charge created in a gaseous volume is guided, with the help of an electric field, to an electrode where it is collected

and measured.

The production of ion pairs in a gaseous medium is described next. Afterwards, the processes by which the primary charge can be amplified in the gases to produce a larger signal – a method used in most current detectors – are also presented and analyzed.

1.2.1 Ion pair production and collection

Immediately after the interaction of radiation through the mechanisms described in the previous section, the deposited energy results in the creation of ion pairs. In the case of electromagnetic radiation interacting via photoelectric effect only one pair is initially created, while the interaction of heavy charged particles produces a few of them. The first electrons (or the photoelectron) released in the process, however, often have enough energy to further ionize the gas and produce additional pairs. The total number of ion pairs generated in the detector volume, N_t, is much higher than the number produced in the first stage, and can be estimated by the following relation:

$$N_t = \frac{E}{W}\,, \tag{1.5}$$

where E is meant as the energy deposited in the detector volume and the W-value is a parameter that dependents of the gas, type of radiation and its energy, but almost always between 20 to 40 eV [12, 15].

Table 1.1 lists some pertinent parameters for gases of interest, including W-value, average energy deposited by a minimum ionizing particle ($\mathrm{d}E/\mathrm{d}x$) and total number of ion pairs (N_t) produced per cm by such MIP particle. As an example, MIPs crossing 1 cm of the gaseous mixture Ar:CH_4 - 70:30 can be expected to generate, on average, ~84 ion pairs.

Table 1.1 Properties of noble and molecular gases of interest at normal temperature and pressure (20 $^{\circ}\mathrm{C}$, 1 atm); data from [13]

Gas	**W-value** [eV]	$\mathbf{d}\boldsymbol{E}/\mathbf{d}\boldsymbol{x}$ (MIPs) [$\mathrm{keV/cm}$]	$\boldsymbol{N_t}$ [$/\mathrm{cm}$]
Ne	37	1.45	40
Ar	26	2.53	97
Xe	22	6.87	312
CO_2	34	3.35	100
CH_4	30	1.61	54

Like the deposited energy, the number of primaries described is an average value of multiple events. However, unlike the stopping power which follows a Landau distribution, the actual number of primaries for a single crossing MIP should follow a poissonian distribution. In practice, it is experimentally verified that in most gases the statistical uncertainty on the number of ion pairs

produced is well below that of a pure Poisson, the correction being done by introducing the Fano factor, F:

$$F = \frac{\sigma_{N_t}^2}{N_t}\,, \tag{1.6}$$

where $\sigma_{N_t}^2$ is the variance in the number of ion pairs created. F is typically lower than 0.3 in gases [12], so in the detectors that are studied in the present work other factors – namely the charge amplification process – will dominate the statistical uncertainty over the measured charge.

One can take the analysis from the previous section describing the interaction of X-rays and also estimate the total number of ion pairs generated in that case: for a 5.9 keV X-ray originating in the Fe-55 source and being fully absorbed in a Ar:CH_4 - 70:30 filled detector one can expect 5900/2 ~ 220 ion pairs, taking 27 eV as the W-value of the mixture.

It is important to add that, depending on the gas type, the initial interaction generates the excitation of gas molecules and consequent emission of a few photons typically in the UV range, an effect called primary scintillation. If this occurs in a GPD, even though the UV photons can be detected and used for practical purposes – as will be the case in chapter 4 – in many cases they are an unwanted consequence which limits the performance of the detector. In such cases, the introduction of proper gases (mostly polyatomic molecules) can produce a quenching effect that limits such production of photons by channeling the energy of the excited atoms.

Charge migration

Having generated an initial cloud of charges in the detector volume, the natural tendency would be for the free electrons and ions to interact with the medium and the concentration of charges would eventually be neutralized. The processes that rule the behavior of those charges include charge transfer, electron attachment, recombination and diffusion [12]. In order for the charges to be collected in an electrode and measured, an appropriate electric field needs to be established in the detection volume that will drag them and dominate over the random processes mentioned.

The way charges behave under an electric field is different for positive ions and electrons, besides being pushed towards opposite direction. A positive ion, due to its higher mass, will be mostly unaffected by each collision with a gas molecule. Therefore its movement, even though slow, smoothly follows the field lines at a drift velocity V proportional do the electric field E, as

$$v = \frac{\mu E}{p}\,, \tag{1.7}$$

where p is the gas pressure [12]. The mobility coefficient, μ, for ions in most gases is of the order of 10^{-4} $\mathrm{m^2 atm V^{-1} s^{-1}}$, and results in very slow movement of the ion charge compared to electrons.

The electron behavior is quite different due to its lower mass. Firstly, the trajectory is only roughly indicated by the field lines (in the opposite direction of the field vector) since microscopically they have wide deviations from it due to random scattering in collisions with the gas medium. Secondly, their drift velocity as a function of the electric field is no longer well

approximated by a linear behavior and depends strongly on the gaseous mixture. In fact, as the plot in figure 1.4 shows, in some gases the increase in electric field after a certain value actually decreases the drift velocity.

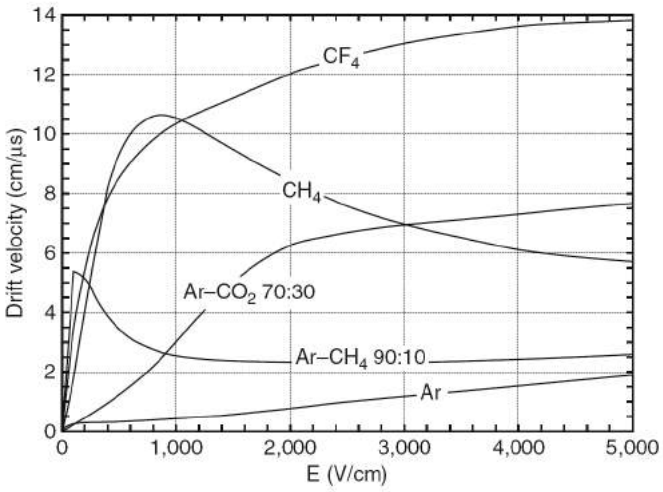

Figure 1.4 Electron drift velocities in different gases, as a function of the electric field. [15]

The understanding of the electron drift dependency of the electric field requires careful analysis of the atomic and molecular structure of the gas medium. In noble gases, with electric fields below excitation and ionization thresholds, the collisions between electrons and atoms are always elastic, favoring the behavior described above. On the other hand, when molecular gases such as CO_2 or CH_4 are used, electrons have a significant probability of transmitting part of the energy gained during their free path to the molecule (which has rotational and vibrational energy levels), colliding inelastically. The latter case results in a large increase in the electron drift velocity in such gases, or in gas mixtures containing them [17].

Electrons, therefore, have a drift velocity which is orders of magnitude higher than ions at the same fields and pressure, and which can be further increased by the addition of a molecular gas to the mixture. Efficient charge collection over long distances can thus be achieved, often at moderate fields even below 1 $\mathrm{kVcm^{-1}}$, given that the choice of gas medium is done so that properties such as its electronegativity don't favor the recombination mechanisms. Because molecules such as O_2 or H_2O are electronegative, the quality control of the gas mixtures to avoid those impurities is important.

1.2.2 Proportional Multiplication

The number of ion pairs created by the interaction of radiation with a gaseous volume depends on the energy deposited, elements that compose the medium and the volume of the chamber. Still, in most cases it's limited to a few hundred, a figure which can rarely be used for practical

purposes of detection and measurement (ionization chambers are an exception). Therefore, most gaseous detectors used today evolved from the simple collection of primary charge, introducing either electron multiplication stages where the charge is amplified or scintillation regions from where photons are emitted.

The process by which the signal is amplified occurs when the electric field is increased beyond the typical values used for drift purposes. At high enough reduced fields, the free electrons acquire in their mean free path between collisions enough kinetic energy to firstly excite and then ionize gas atoms.

Electroluminescence

During charge migration, scintillation light can be produced if the electric field is such that electrons in their paths have the possibility of gaining the energy required to excite gas atoms (the excitation threshold). In the de-excitation process of the atom photons are emitted, mostly in the UV region [18, 19]. The fields required to establish the electroluminescence regime depend on the element and pressure of the medium, but in most cases for pure noble gases occurs at reduced electric fields of at least ~1 $\mathrm{kVcm^{-1}torr^{-1}}$ [18, 19].

In a scintillation region with uniform field, the number of photons produced is proportional to the number of electrons that initiate the process. The ratio between them can be considered as the photon gain, or yield, and is linearly dependent on the field strength and on the region's length. Xenon is probably the noble gas whose electroluminescence has been subject to more study, allowing the deduction of empirical equations for the number of photons N_{ph} produced per electron unit path as a function of the reduced electric field, E/p in $\mathrm{kVcm^{-1}bar^{-1}}$. Several of such empirical equations, with slight differences, can be found in the literature [20], one example being

$$\frac{\mathrm{d}N_{ph}}{\mathrm{d}x} = (140E/p - 116)p\,. \tag{1.8}$$

Using a photon detection system coupled to such a region, it is then possible to estimate the number of charges produced in a given interaction event by the number of photons detected. This is the principle of operation behind the proposed Compton Camera in chapter 4. Detectors based on this principle have typically better energy resolution than the ones operated using charge amplification [18].

In the detectors that use charge amplification to enlarge the measured signal, as the typical GPDs employed in RICH, the light produced by electroluminescence is not desirable. In fact, GPDs using pure noble gases have their greatest limitation in gain due to the photons produced, generating feedback effects in the photocathode which lead to discharges [21]. In those cases, using quenching molecular gases is mandatory to neutralize the scintillation light and allow higher gains to be reached.

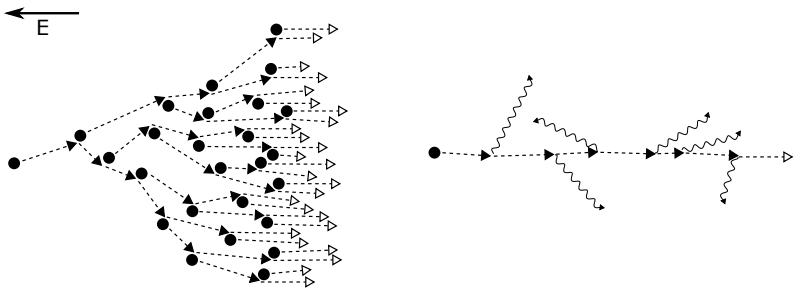

Figure 1.5 Illustration of the amplification processes in gaseous detectors: the Townsend avalanche (left) is an exponential growth of the number of electrons along the cascade, while in the electroluminescence process (right) the number of electrons stays constant, but each electron emits scintillation light continuously along its path.

Townsend avalanche

If the electric fields that guide the charge movement are high enough – above the ionization threshold – an electron can achieve sufficient energy to ionize other gas atoms, freeing one additional electron. Each of the two electrons will then be accelerated by the electric field and possibly ionize other two atoms, after which there will be four free electrons; and so on... Because there is a certain probability of ionization in each collision, the growth of the electron cascade, called Townsend avalanche, is exponential along the path of the avalanche for a uniform electric field E [12]:

$$N_{e^-}(x) = N_{e^-}(0)e^{\alpha x}\,. \tag{1.9}$$

The parameter α is the first Townsend coefficient for the gas, and is the inverse of λ_i, the electron mean free path that enables ionization. α is zero for fields below the ionization threshold, after which it increases exponentially with the field's strength [15]. Since in most detectors the amplification is achieved with nonuniform fields, the actual gain of the amplification stage, $G = N_{e^-}(x)/N_{e^-}(0)$, can't be estimated easily from equation 1.9.

The field at which avalanche multiplication starts to become appreciable depends strongly on the gas. Neon is known to be the noble gas with higher Townsend coefficient at low fields, followed by Argon [13, 17, 22]. However, the latter is a more cost effective solution, especially when large areas of operation are intended.

It should be emphasized that the gain of pure noble gas detectors is restricted as a consequence of electroluminescence effects in the detectors [21]. The addition of polyatomic molecules such as carbon dioxide or methane is mandatory to quench the UV scintillation and allow the detector to reach higher gains [22]. Furthermore, any charge amplification device is intrinsically limited in gain up to the so called Raether limit [23]. This effect is usually noticed at very high gains, when the charge density created by the number of electrons in the avalanche reaches a point (~10^7 - 10^8) where electric breakdown occurs, as a consequence of field distortions [24]. Many proportional detectors, however, reach their gain limits sooner due to other effects and imperfections, namely

sharp electrode edges or the settling of microscopic particles during assembly. Besides, It's experimentally verified in all detectors a strong dependency of discharge probability with the irradiation rate [25].

The gain of each avalanche is affected by strong statistical fluctuations which in most cases dominate over the fluctuation in the number of created ion pairs, N_t, determined by the Fano factor. The statistical uncertainty affecting the average total charge, Q, produced after the conversion and multiplication stages can be expressed as

$$\left(\frac{\sigma_Q}{Q}\right)^2 = \left(\frac{\sigma_{N_t}}{N_t}\right)^2 + \frac{1}{N_t}\left(\frac{\sigma_A}{\bar{A}}\right)^2, \tag{1.10}$$

where the first term relates to ion pair production statistics and the second reflects the statistical uncertainty of a single electron's avalanche process resulting in a charge A [12].

The statistical model that best describes the probability of charge A to be produced by a single avalanche, $P(A)$, is given by the Polya distribution [26]:

$$P(A) = \left(\frac{A(1+\theta)}{\bar{A}}\right)^{\theta} e^{-\left(\frac{A(1+\theta)}{\bar{A}}\right)}, \tag{1.11}$$

where θ is a parameter that can be found experimentally to depend of the Townsend coefficient. From the expression above one can write the relative variance as

$$\left(\frac{\sigma_A}{\bar{A}}\right)^2 = \frac{1}{\bar{A}} + \frac{1}{1+\theta}. \tag{1.12}$$

Experimental studies, in turn, led to the verification that $\theta \approx 0$ for most detectors at usual gains ($\bar{A}$>>1) [27], and so that the variance predicted by equation 1.12 is ~1. With that in mind, equation 1.10 can now be simplified, including also the expression from 1.6:

$$\left(\frac{\sigma_Q}{Q}\right)^2 = \frac{F+1}{N_t}, \tag{1.13}$$

where the Fano factor, F, is typically lower than 0.2 [12]. The avalanche statistics, represented by the right term, dominate the overall process.

The observation that θ ~0 is in fact very useful for practical purposes. Under that condition, the Polya distribution function of equation 1.11 can be simplified as an exponential function [27], in which case it can also be called a Furry distribution. For single photon detectors that use charge amplification, the avalanches are initiated by single photoelectrons, so the distribution of total charge output is a straight consequence of that function. Therefore, when operating the single photon detectors of forthcoming chapters under light irradiation, the histogram of the measured charge, q (often measured in ADC channels), is expected to follow

$$P(q) \propto e^{-q/G}, \tag{1.14}$$

where G is the gain of the detector (in this case, equal to the average avalanche size, $\bar{A}$). Using a logarithmic scale for the histogram, one can then easily estimate the detector gain from the slope of the exponential.

Amplification of charge by Townsend avalanche revolutionized radiation detection and found a wide set of applications. In the scope of this work, the earliest important practical implementation was in the MWPC, a common element of the two first generations of GPDs, which are treated in the next section.

1.3 First and second generations of GPDs

As mentioned in the introduction, GPDs had an evolution closely entangled with the development of RICH systems and it is common to separate this evolution in three generations [28]: the first was characterized by the use of photoconverting vapors to convert photons in electrons, while the second made use of CsI photocathodes, both coupled to MWPC detectors (open geometry); the third generation consisted in CsI photocathodes applied to closed geometry architectures, in particular using MPGDs.

Historically, GPDs have been mostly confined to the detection of light in the VUV region due to the photoconverting substances available. The development of GPDs for the visible range has been pursued [29] and would certainly be quite important for practical purposes, but struggles with some difficulties: the low work function required by their photoconverters (e.g. bialkali) makes them prone to chemical degradation and aging resulting from the ion bombardment; this in turn leads to stricter requirements, in order to control the purity level of the gaseous mixtures at the ppm level, and to ensure that the ion bombardment of the photocathode is limited. Vacuum and solid state photodetectors, on the other hand, are already quite efficient in the visible range.

1.3.1 The MWPC

While the principles mentioned in the previous section where used in many different detectors, the Multi-Wire Proportional Chamber (MWPC) was probably the major breakthrough in radiation detection. Introduced by Charpak in 1968 [30] – a contribution which would earn him the Nobel Prize in Physics (1992) – MWPCs are to this day essential elements in most HEP experiments, particularly in RICH detectors. Because the first two generations of GPDs use MWPCs it's important to introduce some of the characteristics of this detector.

As mentioned before, the key to achieve charge amplification is to guide the electrons to a region of high electric field strength so that a Townsend avalanche can develop. It was soon realized that a practical way to achieve this is by using thin (10 - 30 μm) metallic wires. An electric field can be established by creating a voltage difference between the wire and the surrounding space. Close to the wire, the field is radial, and it's strength is inversely proportional to the distance from the wire surface. A traditional Proportional Counter consists of a single wire and uses a cylindrical cathode enclosing it. The radial electric field guides the electrons generated inside the cylinder – which in the present case defines the detector volume – towards the anode, where electron multiplication occurs [12].

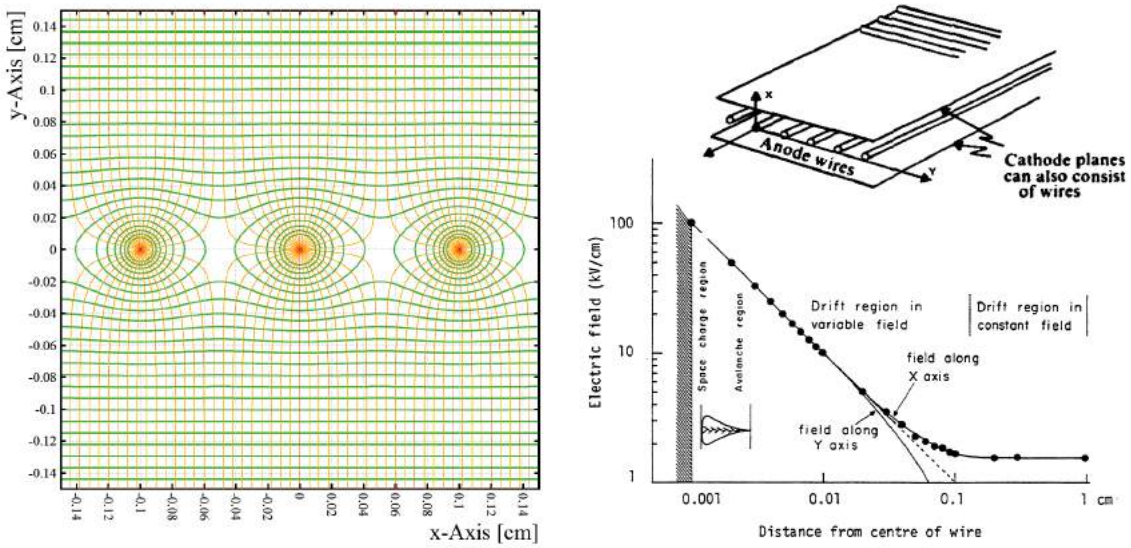

Figure 1.6 Left: MWPC field lines and equipotencials [19]. Right: dependence of the field strength with the distance to the wires along the x-axis illustrated in the inset on top [31] (inset is adapted from [32]).

A MWPC extends that principle using several (multiple) wires in an anode plane, all at the same voltage (often grounded), positioned between two cathode planes, as illustrated at the top right of figure 1.6 [31,32]. The distance between anode wires is usually of 1 - 3 mm, and the cathode-anode distance is typically 5 - 10 mm. The cathode planes can also be made with flat plates or using wire planes, though usually thicker (50 - 100 $\mu\mathrm{m}$) than the ones that compose the anode.

The field lines and equipotentials of a typical MWPC are plotted in figure 1.6 at the left. When an electron originating in the detector volume is guided towards one of the anode wires, it experiences an increasingly stronger field, as depicted in that figure at the right. Because the Townsend coefficient rises sharply with the electric field strength, which in turn is itself increasing rapidly as the electron approaches the wire, the avalanche is quick and localized very near the wire surface [15]. In the wire where the avalanche occurs, a very fast electron signal is immediately followed by a much slower component caused by the receding ions, the latter responsible for most of the measured charge. Induced signals are also frequently created in the neighboring wires. By monitoring the current in the wires one can get 2D position information of the events with accuracy comparable to the wire spacing.

An alternative MWPC design, more important for the purposes of this work, uses a slightly different readout mechanism: the top* cathode consists of a plane of wires, while the bottom cathode consists of a metallic plane segmented into pads over an insulator board; the distance between the bottom cathode and the anode wire plane is similar to the distance between anode wires. In such configuration, the charges induce signals in the cathode pads as well, which can

*Top and bottom are illustrative notions, for explanation purposes.

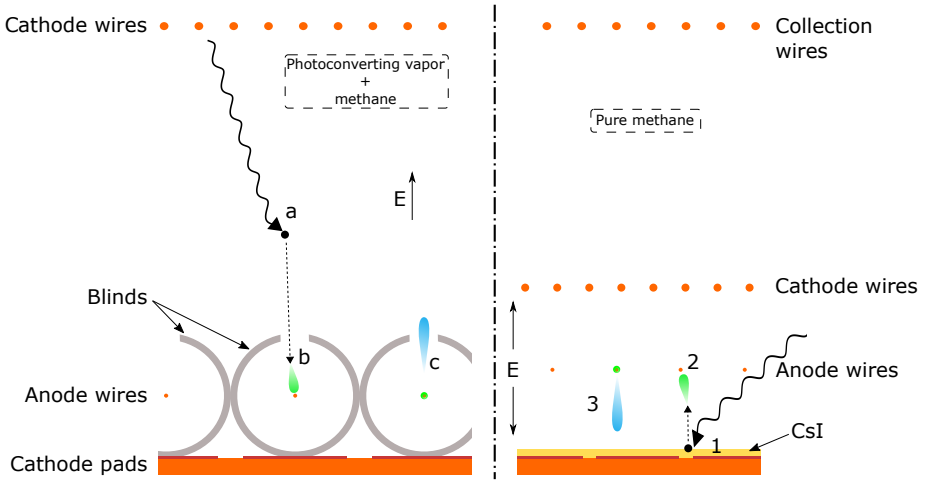

Figure 1.7 Illustration of a typical MWPC design and how the signal is formed. The left architecture is representative of the first generation of GPDs: the photoelectrons originating in the conversion region (a) are guided towards the anode wires and multiplied (b); after the avalanche, the ions drift slowly in the opposite direction (c), generating an induced signal in the pads. Blinds (gray circles) are often used to avoid the occurrence of photon feedback. The right configuration illustrates the MWPC with CsI photocathode, where a photon extracts an electron (1) which generates an avalanche in the wires (2), with the produced ions (3) irradiating the photocathode. The collection wires can be used to establish a reversed field and collect the primary charges generated in the detector by the crossing of MIPs.

therefore work as a readout. One can use the pad coordinates weighted by the signal magnitudes to estimate the position of the interaction.

The architecture described above was often used in the first generation of GPDs, where the photoconversion and amplification media were the same. An illustration of the signal formation process is shown in the left part of figure 1.7: the photoelectrons originating in the conversion region (a) are guided towards the anode wires and multiplied (b); after the avalanche, the ions drift slowly in the opposite direction (c), generating an induced signal in the pads.

In the second generation of GPDs, using CsI photocathodes, the MWPC architecture used was developed by the RD26 (CSI-RICH) collaboration [33, 34] at CERN. In it, as illustrated at the right of figure 1.7, the bottom cathode has a thin photosensitive layer on top, where UV photons are converted to electrons (1). The electron avalanche progresses upwards towards the wires (2), and the ions recede in the opposite direction (3).

1.3.2 Converting Vapors

The first generation of GPDs used conversion gaps where the photons were converted to ion pairs in a organic gas mixture by the photoelectric effect. The resulting charge would then be measured by the MWPC and the position of Cherenkov light interaction reconstructed [35].

The photoconverting vapors with practical importance used in these devices are TMAE (Tetrakis-Dimethylamine-Ethylene) and TEA (Tri-Ethyl-Amine) which are added to methane, argon, or other gaseous atmospheres, required for the MWPC to operate. The conversion efficiency is determined, in part, by the partial vapor pressure of the organic vapor, which is temperature dependent [36].

The quantum efficiency (QE), i.e. the probability that a photon traveling through the conversion region is converted to a photoelectron, is shown in figure 1.8 as a function of photon wavelength for two TEA-based mixtures. The detection efficiency is only significant for photons whose wavelength is below ~165 nm, limiting the choice of transparent windows to fewer options (namely LiF and CaF_2) and creating additional constrains related to purity of the gas mixtures and to chromaticity of the setup when RICH application is envisaged. The fact that TEA's QE extends to the far-UV region (see upper picture of figure 1.8) is also detrimental to the detector performance because it allows photon feedback effects to take place. However, the use of methane in the operating mixture quenches that region of the spectrum (see bottom plot of figure 1.8), and since the conversion gap is quite short, the effect is negligible [37].

Notwithstanding the mentioned negative aspects of using TEA as photoconverting vapor, its high vapor pressure leads to good photon absorption, even for interaction gaps of just a few mm at room temperature [36]. This results in a relatively fast operation.

TMAE benefits from a lower energy threshold, enabling photodetection up to wavelengths of 220 nm (see figure 1.9). This eases the constrains on window selection, so the choice of fused silica (quartz) enables a good absorption range from 160 nm to 220 nm. On the other hand, the carbon

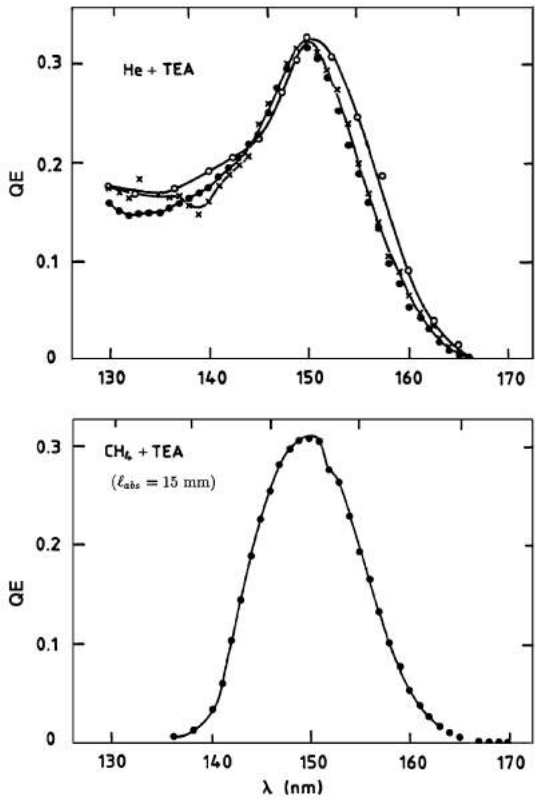

Figure 1.8 Quantum efficiency of the TEA photoconverting vapor in He (top) and CH_4 (bottom) mixtures and a 15 mm conversion region. In the methane mixture the higher energy photons are not emitted, thus reducing the probability of feedback effects. [37]

atoms in the methane molecules typically used as medium for the MWPC multiplication process have two characteristic scintillation lines, at 166 and 193 nm. The electroluminescence light emitted during the electron avalanche is therefore also efficiently detected, which did not happen with TEA, and so the photon feedback effects when using TMAE were found to be much more severe [37]. To overcome the issue of spurious signals and photon feedback effects, modifications to the detector architecture were often implemented: blinds are put around the MWPC anode wires where most of the secondary photons are originated, as illustrated in figure 1.7 at the left. These structures prevent the light from reentering the conversion gap, thus reducing the effect.

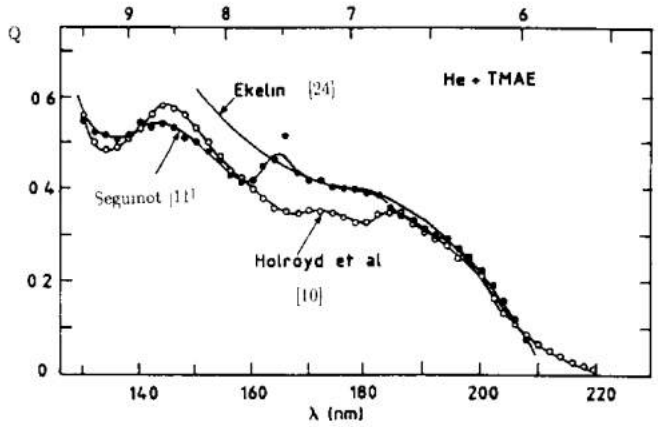

Figure 1.9 Quantum efficiency of the TMAE vapor. The broader range of wavelengths covered compared to TEA allows the use of less expensive windows, but it also favors photon feedback effects. [37]

The vapor pressure of TMAE at room temperature is much lower compared to TEA and so the resulting conversion mixture is less efficient [36]. As a consequence, either the interaction gap has to be made excessively long or the temperature of the detector has to be increased significantly. Most applications opted for applying both measures to a middle ground, with detectors usually operated at temperatures up to 40 $^{\circ}\mathrm{C}$ and still requiring ~5 cm long interaction gaps to allow high detection efficiency [28]. Because of the long drift region, these detectors had typical temporal resolutions of 30 $\mu\mathrm{s}$, a very large value by present standards, but in the late 1980s was enough for their successful implementation in the low rate HEP experiments which required them, namely LEP at CERN [38] and SLC [39]. They were mostly used in a TPC-like approach, where 3D reconstruction of the Cherenkov light is obtained by measuring the drift time of the electrons.

1.3.3 Solid Photocathodes

Overcoming the major difficulties faced with the use of photoconverting vapors was only achieved by the research, within the RD26 collaboration [33, 34] at CERN, on CsI solid state photocathodes [35, 40]. This was a major breakthrough in both GPDs and RICH detectors by adopting a photoconversion process that takes place in a plane, minimizing parallax effects on the

reconstruction and allowing faster operation and much improved time resolution. Besides, the solid photocathode no longer requires that the temperature of operation is increased to ensure efficient conversion: its quantum efficiency depends instead on its thickness, the photon wavelength and the electric fields and gaseous atmosphere used.

As the plots in 1.10 suggest, the QE of reflective CsI photocathodes operated in vacuum is high for photon wavelengths up to 200 nm, reaching ~30% for ~170 nm light. Therefore, it outperforms most of the alternative solid photoconverters, making it the material of choice for virtually all applications [41]. The lower energy threshold enables the use of less expensive window materials such as fused silica. It also compares well to the converting vapors used in the first generation, the only exception being TMAE's higher QE for a small range of lower energy incident photons, which might even be irrelevant if fused silica windows are used.

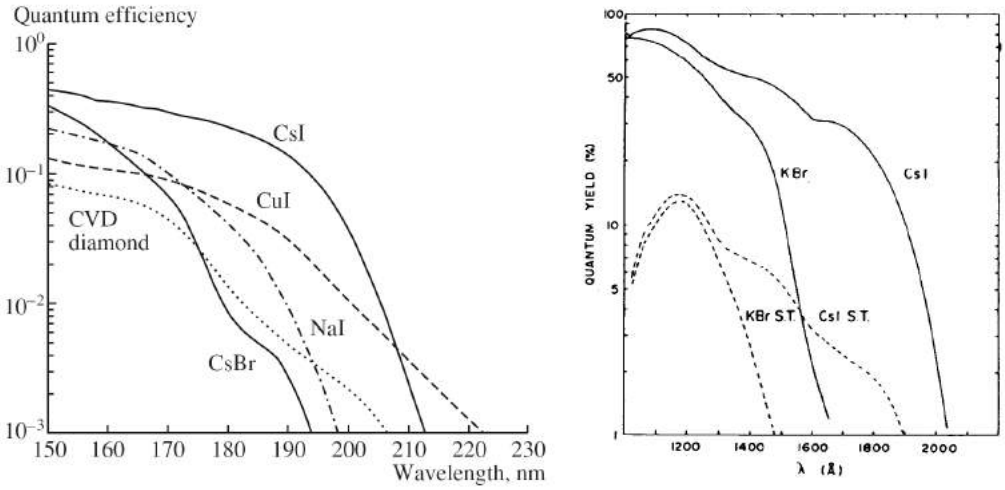

Figure 1.10 Left: quantum efficiency of CsI, CVD diamond, CsBr, CuI and NaI solid photocathodes [42]. Right: quantum efficiency of opaque CsI and KBr photocathodes (continuous lines) compared with semitransparent versions deposited on LiF windows (broken lines) [41].

The CsI photocathode is also advantageous over the alternatives because, even if it has a relatively low energy threshold, it is remarkably non reactive to most gaseous elements, including oxygen, being only affected by the presence of humidity. Under moderate irradiation it does not show evidence of dramatic aging effects on its QE either.

Even though in theory CsI can be deposited in a transparent substrate creating a semitransparent photocathode at the entrance of the detector, this is rarely the chosen implementation. Instead, a reflective CsI layer is preferred for several reasons [28]: it shows higher QE, as evidenced by the plot on figure 1.10 at the right; it does not require the previous coating of the transparent window with a thin metallic film to establish the electric field, which lowers its transparency; and the thickness of the film is not critical, as it is the case with the semitransparent one, which requires particular care and attention for its production over large areas.

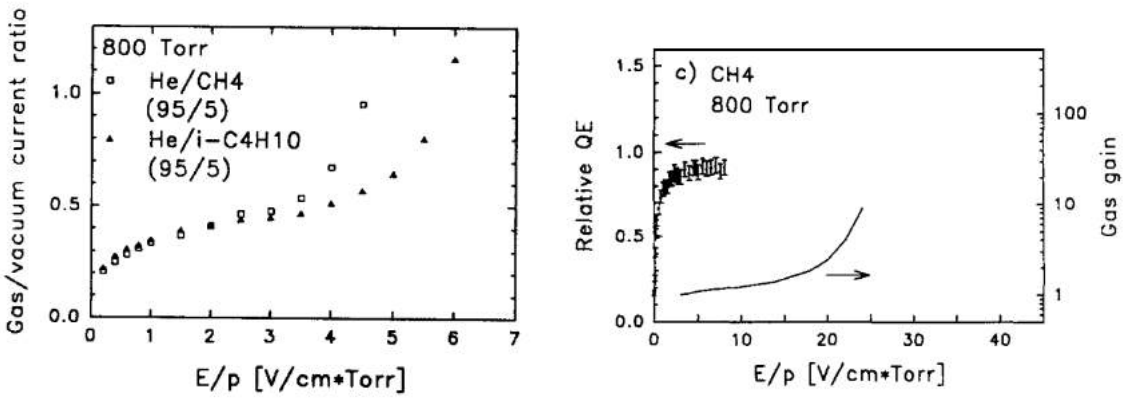

Figure 1.11 Left: QE relative to vacuum values of a CsI photocathode operated in two He-rich gaseous mixtures (left) and pure methane (right.) [43]

When the CsI photocathode is coupled to an MWPC it has to operate against a gaseous atmosphere, introducing some effects not present in vacuum. A very important one is the backscattering of some photoelectrons that collide elastically with a gas molecule and consequently might be reabsorbed by the CsI. This might result in a greatly reduced effective quantum efficiency measured, depending on the field conditions above the photocathode surface and on the gaseous atmosphere present.

Figure 1.11 shows the results of some of the first studies performed to tackle this problem [43]. It shows that, as the electric field present in the photocathode's surface is increased and before electroluminescence effects occur, the measured efficiency of photoelectron extraction reaches a plateau which, for He rich mixtures (left), is less than half of the value achieved in vacuum conditions. The field values required for the maximum collection efficiency are directly proportional to the pressure of the gas medium, i.e. the maximum extraction efficiency for a given gas mixture is only a function of the reduced electric field.

The optimum figures of effective QE, very close to the vacuum levels, are achieved for MWPCs operated with pure methane mixtures (figure 1.11 at the right), assuming proper fields are established. This is the preferred solution when the extraction efficiency is the critical aspect. If, however, the intent is to maximize the gain of the detector, a noble gas (lower Townsend coefficient) has to be used.

The second generation of GPDs, especially the ones targeting RICH applications, virtually all had their design based on the RD26 proposal, with a scheme similar to the one shown in figure 1.12. The CsI photocathode is deposited on the cathode pads of an MWPC, with a thickness of at least 300 nm. Because the CsI reacts with the Cu of the pads, a precursor step is required that deposits a layer of 7 $\mu\mathrm{m}$ of nickel on top of the pads, followed by 0.5 $\mu\mathrm{m}$ of gold – from hereinafter referred to as the Ni-Au treatment – before the CsI is deposited using a simple thermal evaporation procedure. The CsI is then subject to a thermal treatment at 60 $^{\circ}\mathrm{C}$, essential to strongly enhance its QE up to the reference values [35, 44].

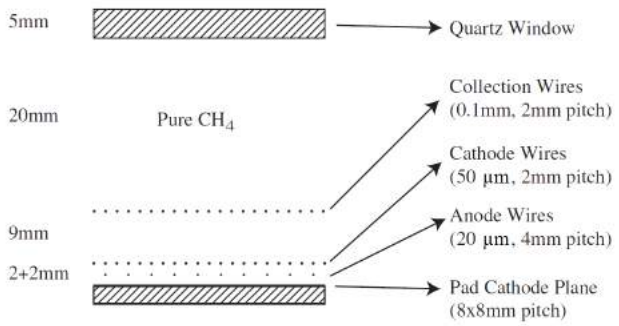

Figure 1.12 Example of a typical MWPC design, developed by the RD26 collaboration and used in many RICH detectors in HEP experiments. This particular configuration is found at COMPASS RICH-1. [28]

As previously illustrated at the right of figure 1.7, when the photon triggers an electron emission from the photocathode (1) which is properly extracted, it will then be directed towards the anode wires where avalanche multiplication will take place (2). The resulting ions will then travel back to the cathode plane (3), producing the measured signal. Intrinsic to this operation mechanism are most of the drawbacks of this solution: since the signal is formed by ion movement, it is relatively slow (even if much faster than the previous generation), and because the ions are collected at the photocathode, the effects of that bombardment cannot be fought against. Aging, with higher than 40% decrease in quantum efficiency, has been reported after collected charges of a few $\mathrm{mC/cm^2}$ [45, 46].

The CsI-based detectors described not only are quite insensitive to magnetic fields, they allowed reaching active areas of detection of up to 60 × 60 $\mathrm{cm^2}$ in a single unit (namely at COMPASS RICH-1). The performance of these detectors is also improved by developments towards faster and lower noise frontend electronics like the ones based in APV25 chips [47]. Nonetheless, their operation is limited in gains up to ~10^4, mainly due to instable operation caused by the photon and ion feedback allowed by their open geometry, followed by very long (~24 hours) recovery time after discharges. Besides, because the signal is mostly dependent on the ion movement, it couples the maximum rate of operation to the ion's drift velocity: the presence of ions creates space charge effects which distort the field, affecting the detection of photons arriving before the charges are evacuated. These were some of the motivations behind the research on closed geometry devices that followed and which led to the establishment of the third generation of GPDs.

1.4 MPGDs: the third generation

The development of micro-lithographic techniques paved the way to a third generation of devices, the Micro-Pattern Gaseous Detectors (MPGDs) [48, 49]. By shaping the electrodes at the micrometer level, the time and spacial resolutions of the detectors increases enormously, while still retaining high gain characteristics.

The Micro-Strip Gas Chamber (MSGC) [50] was the first major success of the new generation of detectors, due to its intrinsic rate capability orders of magnitude higher than MWPCs [51]. However, the structures still showed evidence of substantial aging and, more importantly, exhibited vulnerability to discharges and consequent breakdown, especially in the presence of ionizing radiation in beam environments [21]. In particular, It was experimentally verified that the limits in gain that allowed stable operation seemed to be distant from the Raether limit, while parallel plate architectures achieved values very close to the expected theoretical limit (however, the dependency of maximum stable gains with the irradiation rate is not explained by the conventional electric breakdown theory that explains the Raether limit) [24, 25].

Because the MSGC showed such promising results, a lot of effort went to the research of other MPGD architectures with more robust characteristics. Between 1995 and 1997, two designs were developed and presented which showed the best performances and robustness: the Micromegas [8] and the GEM [52]. To this day, the majority of gaseous detectors under study are either based on them or in structures inspired by them, the ones in this work included.

This section is divided in three subsections dealing with Micromegas, GEMs, and ThGEMs. The focus of the analysis is kept on what are the important aspects regarding the applications envisaged in this thesis.

1.4.1 MICROMEGAS

During the early development of MPGDs, parallel plate architectures were somewhat sidestepped by the research in microstrip structures. Later, renewed interest appeared with the realization that the parallel plate concept applied to sub millimeter gaps could achieve gains very close to the predicted Raether limit. This led to the introduction of the MICRO-MEsh GAseous Structure, or Micromegas [8, 53, 54].

A Micromegas detector, as illustrated in figure 1.13, consists of two regions: a large conversion gap of few mm and an amplification micro-gap of about 100 $\mu\mathrm{m}$. The two regions are separated by a thin (~3 $\mu\mathrm{m}$) metallic micro-grid, or micromesh, which is kept at a uniform distance from the anode pads by evenly spaced small insulating pillars (spacers). One of the most promising aspects of this detector was that its production, by lithography of a photoresistive film, is relatively easy and inexpensive.

The fields in the Micromegas are typically set by applying a negative polarity bias in the mesh while keeping the anode grounded. The drift/collection field is established by a cathode plane above the region, which can be made with wires whose voltage is set even lower than the one on the mesh. Because of this configuration, in the small gap between micromesh and anode, moderate voltage differences can be used to apply very strong fields up to 100 $\mathrm{kV/cm}$, while in the drift region the field is relatively weak (below the excitation threshold) [8].

As can be seen in figure 1.13 at the left, the field lines present a funnel-like distribution near the openings of the mesh, but are very uniform in most of the volume of the detector. The way charge

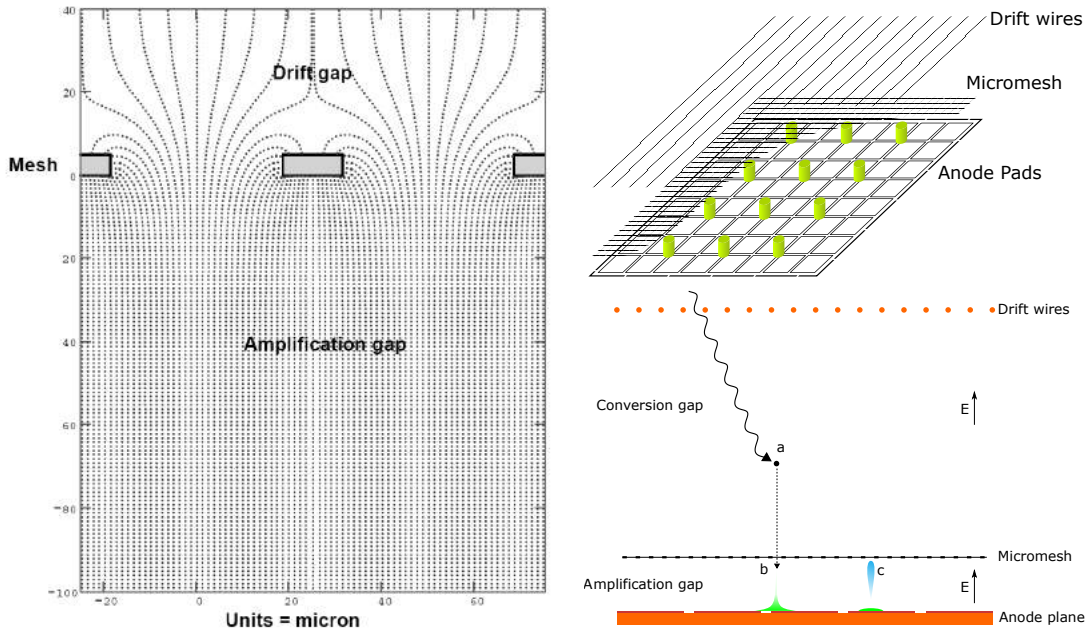

Figure 1.13 Left: illustration of the field lines in a Micromegas [54]. Right: schematic view of the components in a Micromegas detector (top) and of the charge amplification process (bottom): electrons created in the conversion gap (a) drift towards the amplification region and are multiplied (b); the ions produced will then travel the amplification gap in the opposite direction, and are collected in the micromesh.

multiplication is achieved is illustrated at the bottom right of that figure: assuming proper fields are established, photoelectrons released in the conversion gap above the mesh (a) are very efficiently focused into a small zone of the amplification region, where the multiplication avalanche will occur (b). Conversely, the ions there created are directed upwards towards the mesh wires and quickly collected (c).

The ratio between the electric field strength in the amplification and drift regions, ξ, is a defining variable of the detector performance [8], as the plot on figure 1.14 at the right testifies: as ξ is increased to values above 10, the micromesh becomes transparent to electrons and presents full transport efficiency from drift to amplification region; contrarily, the fraction of ions that are not collected in the micromesh and reach the conversion region is inversely proportional to the field ratio. With the use of proper electric fields, the ion transparency has been measured to be in the order of 10^{-3} [55]. The ion entrapment is very useful in reducing charge density effects in the conversion region, allowing high detection rates.

Because of the strong electric fields (E) in the amplification region, the Townsend coefficient (α) of a gas at p pressure reaches a saturation point as predicted by the Rose and Korff formula [53]:

$$\alpha = Ape^{-Bp/E}\,, \tag{1.15}$$

where A and B are gas dependent parameters. If one recalls equation 1.9 and the definition of gain, G, as the number of electrons produced in the avalanche of a single electron, then one can write

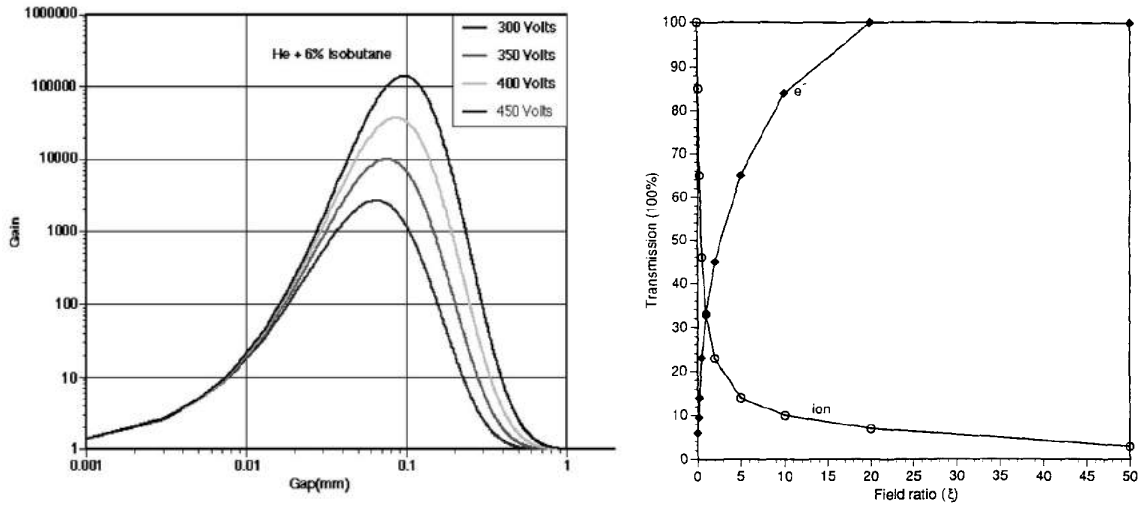

Figure 1.14 Left: gain of a Micromegas detector at 1 atm He:6% C_4H_{10} gas atmosphere as a function of the amplification gap length for several voltages, as calculated from equation 1.16 [54]. Right: electron and ion transmission of a Micromegas detector as a function of the field ratio ξ [8].

for the gain of a Micromegas amplification stage of length d,

$$G = e^{Apde^{-Bp/E}}, \tag{1.16}$$

since the field is mostly uniform in its parallel plate geometry. Figure 1.14 at the left represents the values obtained by the equation above at different applied voltages (V; $E = V/d$) as a function of the gap size d. The result is a broad maximum of the gain for ~100 $\mu\mathrm{m}$ gaps. If the gap is slightly bigger, the expected increase in gain is countered by a decrease in the electric field strength, and vice-versa. This explains why Micromegas detectors show a reduced dependency of the gain with gap variations or gas pressure, ensuring uniformity and stability of response.

The signal generation in Micromegas is, like the MWPC, originated mostly from the ion movement, while the electrons are only responsible for a very fast ($\lesssim$1 ns) initial response. Unlike the MWPC, however, the ions in the Micromegas travel a very short distance – the amplification gap length – before being collected, reducing the response time of such devices to $\lesssim$100 ns. This allowed Micromegas-based detectors to show the same gains reached by the MSGC while operating at rates almost three orders of magnitude higher [53].

A more recent achievement related to this devices is the production of so called *Bulk* Micromegas [56]. These robust and reliable structures are produced in a single process, without requiring additional frame support for the micromesh placement and stretching. As the scheme at the left of figure 1.15 illustrates, one can start from a segmented PCB readout to be used as anode and in it a photosensitive film (Vacrel®[†]) is deposited. On top of it, a woven wire micromesh is properly stretched and then sandwiched by another layer of insulating material on top. In the

[†]Commercialized by DuPont™.

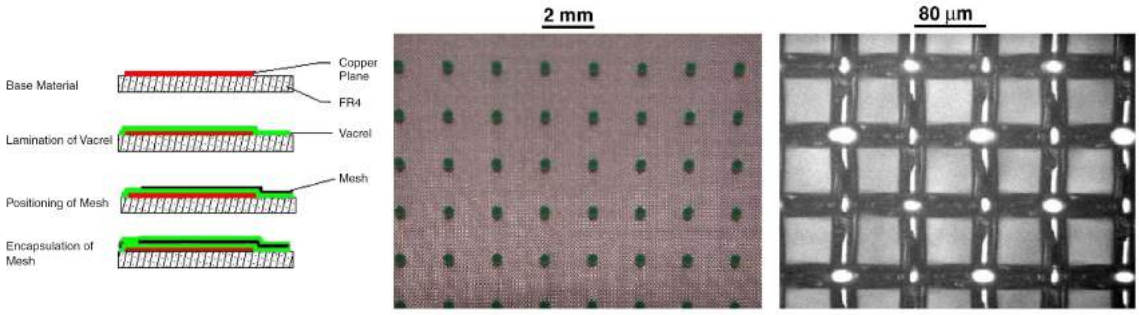

Figure 1.15 Left: generic process of production of a Bulk Micromegas; starting with a standard PCB board (top), a layer of photosensitive polymer with the thickness of the amplification gap intended is applied, followed by the positioning of the micromesh; a second layer of polymer encapsulates the micromesh; finally the etching of the polymer leaves just the supporting pillars. Center and right: photographs of a Bulk Micromegas at the mm scale, showing the pillar structures (center) and at the $\mu\mathrm{m}$ scale, showing the metallic micromesh (right) [56].

end, photolithography with a proper mask is used to erase most of the film while leaving the supporting pillars and a wide border around the detector area, so that proper stretching of the mesh is preserved. The result is Micromegas detectors obtained with inexpensive mass production and showing minimum dead zones and improved gain uniformity.

New methods of production for these structures continue to be sought after, as the recent introduction of the Microbulk production technique [57] shows, and can now be produced with detection areas as high as 1 m^2. Micromegas have been used successfully in several applications, namely in current HEP experiments such as the muon detectors at the COMPASS [58]. They are also planned as detectors for the ATLAS muon spectrometer upgrade [59] and are promising candidates for large area TPCs [60]. Other examples of possible future applications can be found in references [61, 62].

However, the application of Micromegas as photodetectors for the UV is not trivial. Ignoring converting vapors as an outdated solution, reflective photocathodes would need a substrate with high active area, which the micromesh does not usually supply. On the other hand, using a semi-transparent photocathode above the Micromegas has all the inconveniences mentioned previously (in section 1.3.3). The most practical solution, the one exploited in this work, is by using the reflective CsI photocathode on a first multiplication stage using a structure which is able to accommodate it efficiently.

1.4.2 GEMs

The Gas Electron Multiplier (GEM) is an amplification structure introduced by Fabio Sauli [52]. Unlike the parallel plate geometry of the Micromegas, a GEM is composed of micro-sized holes where electric field lines are focused, leading to very high field strengths in localized spots. Figure

1.16 at the left shows an electron microscope view of a GEM foil, and at the right an illustration of the field lines near the holes. The electric field near the GEM surface and holes is often called a dipole field due to the similarity with the shape of a field originated by a pair of opposite charges.

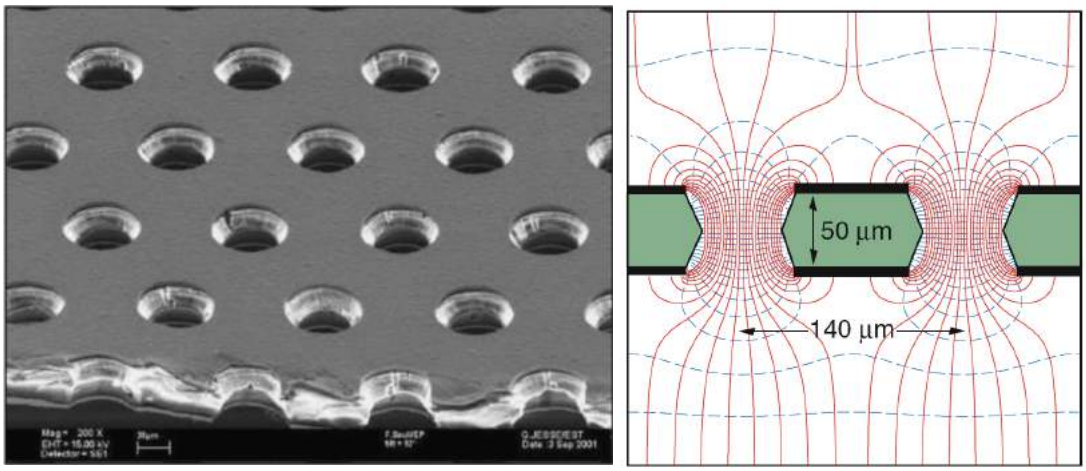

Figure 1.16 Left: electron microscope image of a GEM, 50 μm thick, with 140 μm holes pitch and 70 μm hole diameter [63]. Right: illustration of the field lines when a voltage difference is applied between the electrodes of the GEM [13].

A GEM consists of a thin insulating material – typically 50 μm thick Kapton®[‡] – which is covered in each side by a 5 μm copper layer. The foil is then chemically perforated to produce the characteristic biconical-shape holes, whose diameter is between 25 to 150 μm. The holes are distributed in a hexagonal pattern whose lattice parameter (distance between neighboring holes) is called the pitch, typically 50 - 200 μm. Hole densities of 100 /mm^2 can be obtained.

The device is operated by establishing a voltage difference between the top and the bottom electrodes[§], resulting in electric fields of up to 70 kV/cm. Furthermore, a drift plane – typically made with wires – is placed a few mm above the GEM so a drift/collection field is established to guide electrons generated in that region towards the holes, where the Townsend avalanche takes place. below the bottom electrode of the structure an anode readout is used to collect and measure the amplified charge. The space between the anode readout and the bottom electrode – usually a few mm – is called the induction region, where an induction field is applied to efficiently collect the produced charge. It is common for the anode to be set at the electric ground, and each electrode upwards to be at a lower voltage (i.e. negative). GEMs allow wide freedom in the choice of anode parameters and architecture, because the readout is independent of the structure.

A free electron in the drift region is almost certainly commanded by the drift field towards the holes of the GEM, which act as independent proportional regions, generating an avalanche. The majority of the electrons and ions of the avalanche are generated in the bottom part of the hole and even beyond the bottom electrode plane. The electrons are then guided even further down to

[‡]Commercialized by DuPont™ as well.

[§]Once again, top and bottom are illustrative notions, relative to the schemes used.

the readout, while the ions will follow the inverse direction along the field lines. This leads to two differences in relation to the Micromegas: first, in a GEM the ions have a slightly higher chance of finding their way to the drift region, i.e. the ion transparency is higher; secondly, because the avalanche occurs further away from the anode, the signal that is measured by the readout consists solely in the induced by the electrons in their descent, and so is much faster (at the ns scale).

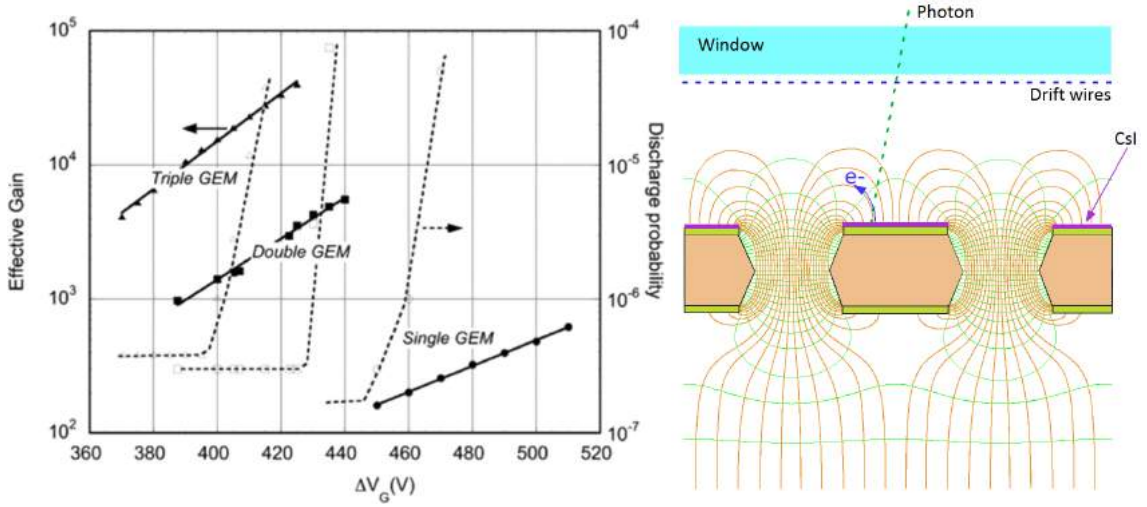

Figure 1.17 Left: comparison between the gain curves measured when using multiple GEM structures in a cascaded configuration (the dashed lines represent the discharge probability) [64]. Right: electric field lines in a GEM detector with CsI photocathode deposited on top [65].

Single GEMs can be operated at gains higher than 10^3 with proper selection of gas medium containing noble elements and polyatomic molecules. A great feature of this device is that the cloud of electrons that emerge from the GEM can be further guided into a second amplification structure, such as an additional GEM. In fact, several GEMs can be cascaded in such way, but the most common configuration is to use three, as illustrated in the scheme at the left of figure 1.18; between GEMs, a transfer field is applied to guide the electrons. Each additional GEM raises the maximum gain that can be obtained from the detector before recurrent discharges are noticed, as the plot at the left of figure 1.17 shows. Multiple-GEM detectors can achieve gains higher than 10^6, with low discharge probability [66].

An advantage of this kind of detectors over the Micromegas is that solid photocathodes can be deposited in the GEM's top surface in order to create a photodetector. For that, the GEM has to undergo the Ni-Au treatment referred in section 1.3.3, since otherwise the copper would react with the CsI film, still the favorite choice of photoconverting material for this application. For effective photoelectron extraction the drift field is usually kept at zero, since the goal is to have the field lines of the first GEM originating in the photocathode's surface to pull out and guide the photoelectrons into the holes, as illustrated at the right of figure 1.17. GEM-based photodetectors can also include multiple cascaded structures, typically three. A remarkable feature of this configuration

is that photons originating in the avalanche, which in open geometry designs give rise to feedback effects, are essentially blocked by the opaque GEM foils from originating additional pulses in the photoconverter. This closed geometry configuration increases the maximum gain at which GEM-based GPDs can be operated.

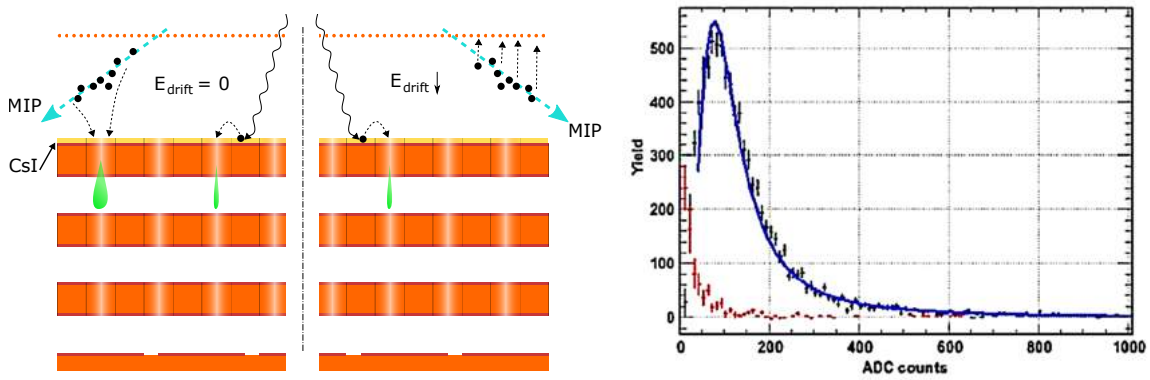

Figure 1.18 Left: scheme illustrating the HBD principle, where a reversed bias in the drift field is applied so that charges produced by crossing MIPs are not collected and amplified in the detector. Right: histograms demonstrating the efficiency of the reverse bias approach, with the MIP-generated signals in the standard configuration (blue) almost completely absent (red) [67].

Triple cascaded GEM detectors allow the implementation of a Hadron Blind Detector (HBD) configuration, as implemented in the threshold Cherenkov detector at the PHENIX experiment [68, 69]. The principle, illustrated at the left of figure 1.18, consists in the application of a weak reverse bias on the drift field which is not enough to disturb the efficient photoelectron extraction from the photocathode's surface [70]. When the detectors are used in beam environments, the presence of ionizing radiation (MIPs) results in the creation of electrons in the drift region. The application of a reverse drift field guides these electrons away from the multiplication region, where otherwise they would be amplified and measured.

, masking the single photoelectron signals and significantly limiting the maximum stable gains that can be reached with the detector.

Overall, current GEM-based GPDs allow the coverage of medium size photosensitive areas (~30 × 30 cm^2 per module) with low material budget and achieve high rate capability with time resolutions at the few ns level. The position resolution, which depends on the anode readout used, is typically lower than 100 $\mu\mathrm{m}$. As examples, GEMs are used in trackers at the COMPASS experiment and in the TOTEM telescope [71,72] and are planed for the upgrade of the ALICE TPC detector [73]. For more examples, the reader is referred to references [61] and [62].

However, they present some inconvenient characteristics, starting with the fact that they are not self sustainable, therefore requiring careful assembly and proper frames so that planarity and parallelism are ensured. This problem is further complicated in the higher photodetection areas envisaged, for which also production techniques are challenging. Related to the thin and delicate

foil used, the handling of the structures is a very sensitive issue. Also, it is possible that electric discharges damage the structure beyond repair, one of the reasons that leads to the segmentation of electrodes in large area structures, to reduce the accumulated charge in the dielectric. Therefore, more robust, sturdier structures with easier handling would be preferred in RICH detectors.

1.4.3 ThGEM

To face the challenges created by the fragile nature of the conventional GEMs, several groups conceived the idea of scaling the dimensions of the GEM by an order of magnitude, introducing the Thick GEM (ThGEM) [74–77]. The production technology of this new structure replaces the copper coated Kapton® foil by a standard Printed Circuit Board (PCB) which can be processed using industrial drilling and etching techniques, making it a good candidate for mass production and enabling cost effective coverage of large areas.

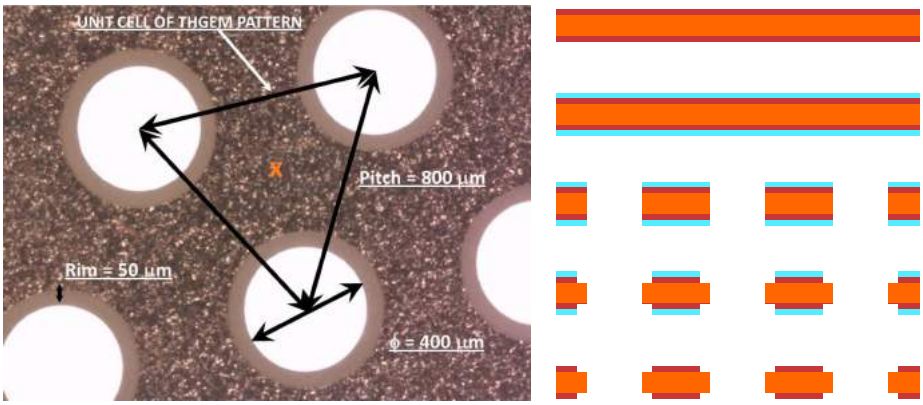

Figure 1.19 Left: photograph of a typical ThGEM surface, with the defining geometrical parameters identified (the cross is the critical point for photoelectron extraction). Right: production scheme of a ThGEM structure, starting with the etching of the PCB (the light blue layer is the photoresist) to form the electrodes, followed by drilling and ending with chemical etching to form the rims.

A ThGEM consists of a PCB board 0.4 - 1 mm thick, where 0.3 - 1 mm diameter holes are mechanically drilled at a hole pitch of 0.7 - 1.2 mm. Then, a chemical etching process removes the copper from a small region ($\lesssim$150 $\mu\mathrm{m}$) around the hole edges, the rim. The rim is introduced because it increases the voltage difference that can be applied to the structure. A picture of a typical ThGEM is shown at the left of figure 1.19; at the center the conventional production process is schematically illustrated.

The ThGEM requires a voltage difference between the two copper surfaces so the electric field – the dipole field – is established. However, when compared to the GEM, the larger dimensions of the thick structure (larger hole diameters and rims) require higher voltage differences to be applied to obtain the same charge multiplication gain. The effect of the increased thickness is particularly crucial when one wants to use solid photocathodes on the top surface: the efficient extraction of

photoelectrons imposes strict requirements on the fields, gas mixtures and other parameters of the detectors, and has been extensively studied both by simulations and experimentally [78–82]. The key aspect to maximize the efficiency of the photocathode is ensuring that at the critical point, in the center of the triangle that links three neighbor holes (see figure 1.19 at the left), the component of the electric field normal to the surface is strong enough. The lower efficiency in the spaces between holes is experimentally verified in measurements with a high resolution scanner [82], and an illustrative example is shown in figure 1.20 at the left.

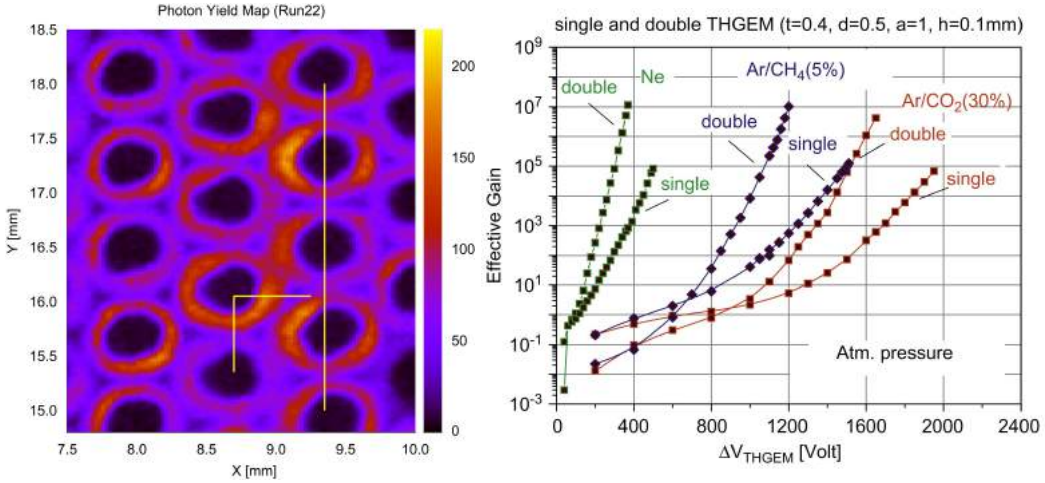

Figure 1.20 Left: the number of extracted photoelectrons from the ThGEM surface by a focused light source, with the application of a typical dipole field. The critical points between holes, as expected, show the lowest efficiency. [82]. Right: comparison between the gain curves achieved when using single or double ThGEM structures in a cascaded configuration, for various gas mixtures [83].

How full efficiency can be achieved depends on limitations imposed on the detector for the envisaged application (see further details in section 3.1). In any case, concerning the choice of gas medium, what has been stated in section 1.3.3 remains valid in ThGEMs: the presence of a polyatomic molecular element is essential to ensure efficient photoelectron extraction. As for the noble gas component, neon's higher Townsend coefficient means a ThGEM operated in it sustains a lower maximum voltage than the same structure in argon, for example. As a consequence, the dipole field strength at the surface of the photocathode when using neon is limited. Argon has the additional advantage of being more affordable to fill large area detectors. Conversely, the highest gains obtained by the charge multiplication process for a given field are maximized in neon-based mixtures, as shown in the plot at the right of figure 1.20.

Due to their higher hole size the electron transparency of this structures is even greater than in GEMs. Therefore, implementation of multiple cascaded ThGEM detectors was immediately achieved, and as before, the maximum gain that can be achieved increases when using more than one structure (see figure 1.20 at the right). As with the GEMs, the triple-cascaded ThGEM configuration seems to be the most commonly adopted in the literature.

The increased collection efficiency of electrons comes at the price of an equally higher transparency of the structure to ion movement in the opposite direction. Even in a triple cascaded detector, ions generated in the last avalanche process are often guided upwards by the field lines and end up being collected at the photocathode. The Ion Backflow Fraction (IBF), which can be approximately described as the ratio between the number of ions collected in the photocathode and the total number of ions produced in the amplification process [84, 85], is the usual figure used to evaluate this effect. While a single Micromegas stage would have an ion transparency of ~10^{-3} [55], and triple cascaded GEM-based detectors can be developed to present IBF values as low as ~10^{-4} [86], ThGEM-based detectors show IBF values consistently above the few %, even when attempting to tackle the issue by using innovative designs such as the ThCOBRA [87].

Despite the mentioned issues, observation of Cherenkov rings with ThGEM-based detectors has been demonstrated [88]. ThGEMs a promising candidate for the COMPASS RICH-1 upgrade, and are expected to integrate the final detector arrangement in a Hybrid configuration, coupled to a Micromegas.

ThGEMs are still in an early process of adoption by large physics experiments. Still, a few dark matter search experiments (e.g. DARWIN [89] and ArDM [90]) have already demonstrated the wish to use them as GPDs in future devices such as the LAr LEM TPC [91]. Some more examples can be found in references [61, 62, 92].

1.4.4 A note on Hybrid MPGD detectors

As will be argued on chapter 3, the years of study within the research program which the author joined point to the conclusion that the ideal architecture for the COMPASS RICH-1 upgrade seems to be a GPD in a hybrid configuration, composed of ThGEMs and a Micromegas.

Hybrid detectors using MPGDs were suggested and tested very early after the development of the GEM, using that structure as preamplification stage to MWPCs or MSGCs [93]. The concept of using a GEM preamplification structure for the Micromegas was suggested a few years later [94,95]. More recently, a ThGEM - Micromegas Hybrid GPD was suggested for nuclear imaging applications [96]. More complex Hybrid architectures based on the latter example have been developed [97,98].

Panda-X, a dark matter search experiment, is studying the possibility to use a Hybrid detector consisting of triple cascaded ThGEMs and a Micromegas as photodetector element [99]. Other similar experiments might follow its lead. Still, as far as the author is aware, the COMPASS RICH-1 upgrade will be the first practical implementation of the concept in applications outside controlled laboratory environments.

Chapter 2

RICH detectors and COMPASS RICH-1

"One of our joys was to go into our workroom at night; we then perceived on all sides the feebly luminous silhouettes of the bottles or capsules containing our products. It was really a lovely sight and one always new to us. The glowing tubes looked like faint, fairy lights."

Marie Curie, Autobiographical Notes [100]

Cherenkov light has a long and interesting history. One of the earlier notes on the chronology of this – at the time unnamed – radiation comes from Marie Curie, who described the observation of pale blue lights emanating from concentrated radium solutions. The described glow was likely Cherenkov radiation.

It would take more than three decades for Pavel Cherenkov to write, in 1934, the first [101] in a series of papers where he would describe his investigations of a blueish light emitted by concentrated radioactive solutions, light which would be named after him. Three years later, a seminal paper by Frank and Tamm [102] would establish the theoretical explanation for the observed phenomena using classical electromagnetic theory. In 1958 the three of them shared the Nobel Prize in Physics for their discovery.

To see the appearance of the Cherenkov ring imaging detectors which are the major scope of this work one would still have to wait until 1977 for the first paper by Ypsilantis and Seguinot [103] describing and predicting the imaging of Cherenkov radiation rings as a particle identification method (based on the idea from A. Roberts in 1960 [104]). Initially referred to as CRID detectors, the adopted acronym would change to RICH a few years later, as a joke on the lack of funding available to pursue the research program [37].

Even though particle identification in high energy physics experiments is the most famous application of the Cherenkov effect and the one focused in this chapter, still it finds applications in many other scenarios, such as fast particle counters in accelerator instrumentation (e.g. BaBar luminosity detector), tracking detectors performing complete event reconstruction in neutrino astronomy (e.g. the large water Cherenkov counters in the Super-Kamiokande), and quantitative radiation measurements in biology and medicine [15].

This chapter is divided in three sections: the first briefly introduces the theory of Cherenkov light emission; the second compares alternative particle identification (PID) techniques and general aspects of Cherenkov detectors; finally, the third section introduces the COMPASS experiment and gives a brief description of the RICH-1 detector.

2.1 The Cherenkov effect

Cherenkov radiation is emitted when a charged particle travels through a medium with refractive index n at a velocity $v = \beta c$ higher than the local speed of light in that medium, $v_c = c/n$ [105], where c is the speed of light in empty space and β a constant. The threshold condition for Cherenkov light emission is therefore:

$$\beta > \frac{1}{n}\,. \tag{2.1}$$

The threshold condition immediately implies that, for a given momentum and a fixed refractive index, some of the heavier particles do not satisfy the minimum velocity condition. That property is used for PID purposes in the Threshold Cherenkov Counters mentioned in section 2.2.

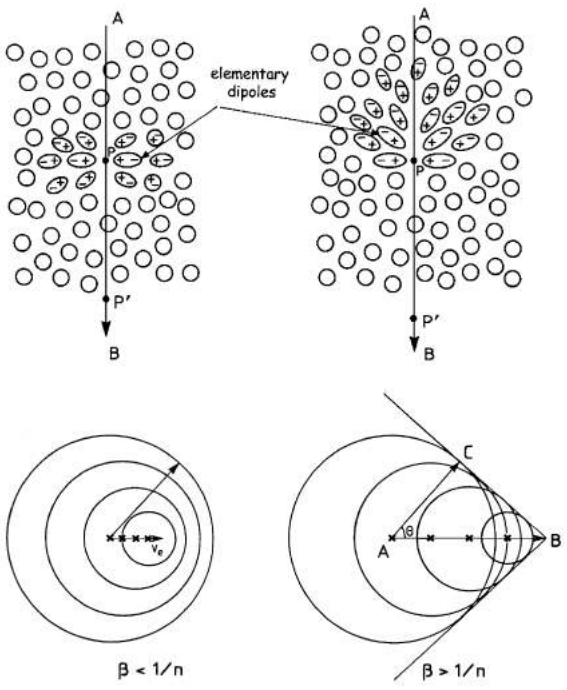

Figure 2.1 Illustration of the Cherenkov effect. The top images illustrate the polarization of the dielectric medium traversed by a negatively charged particle, while at the bottom the corresponding Huygens representation of the spherical wavelets is shown. The left (right) images show a particle below (above) the Cherenkov threshold. [36]

The effect can be interpreted as a polarization of the atoms along the path traveled by the particle, followed by their relaxation. below the Cherenkov threshold, the resulting electromagnetic

field distortions are symmetric, and thus interfere destructively, as illustrated in the left of figure 2.1. If the particle travels fast enough, however, the net dipole field creates a coherent wave front at a specific angle θ relative to the trajectory of the particle, the Cherenkov angle [36]. The Cherenkov angle can be shown to follow the relationship below, where λ represents the wavelenght of the emitted light:

$$\cos\theta = \frac{1}{\beta n(\lambda)}\,. \tag{2.2}$$

The emitted photons, therefore, fall on the cone surface represented by that angle. The measurement of the angle of emission allows the determination of the particle's velocity, the principle behind some of the PID techniques based in Cherenkov radiation, including RICH detectors. For very high momenta, β ~1 and the Cherenkov angle converges to a fixed maximum value, independent of the particle's rest mass (as visible in figure 2.14 at the left). At those momenta the system eventually reaches its angular resolution limit, and particle differentiation is no longer possible.

It can be shown [105] that the dependency of the number of emitted Cherenkov photons N_p in a infinitesimal range of photon energies dE by a particle with charge Ze traveling a length L through a medium is given by,

$$\frac{\mathrm{d}N_p}{\mathrm{d}E} = \frac{\alpha}{\hbar c} Z^2 L \left[1 - \left(\frac{1}{n(E)\beta}\right)^2\right], \tag{2.3}$$

where α is the fine structure constant and $\hbar$ is the reduced Plank's constant. One of the direct implications of this equation is that the emission of Cherenkov photons is favored at higher energies (lower wavelengths). The dependency of n with the energy of the photons (or the wavelength) is typically called the chromaticity of the medium and is important to understand the distribution of Cherenkov light emitted: because n tends to ~1 for higher photon energies, dN_p/dE decreases and eventually light emission ceases beyond the far-UV region.

2.2 PID techniques and Cherenkov counters

Particle identification is a necessary requirement of modern HEP experiments. Visual detection techniques such as bubble chambers are now obsolete, given their limited rate of operation and complexity, but also because digital methods allow much more efficient and versatile analysis.

A distinction between groups of particles is traditionally achieved by the use of trackers and calorimeters, both electromagnetic and hadronic, in physics experiments. Typically, these allow the separation of photons, muons, electrons and hadrons. However, pions, kaons and protons are three very important charged hadrons with identical interactions in such traditional setup, thus requiring additional identification methods [106]. Given that the charge of a particle, as well as its momentum p, can be estimated from its trajectory under the effect of a magnetic field, the determination of the particle's identity is only dependent on the estimation of its mass m via the

measurement of the velocity, through the relation:

$$m = \frac{p}{c\beta\gamma}\,, \tag{2.4}$$

where $\gamma = E/(mc^2)$ is the Lorentz factor for a particle of energy E [36]. It can be shown by error propagation from that equation that the required precision in the velocity measurement ($\Delta\beta/\beta$) when trying to distinguish two particles (m_1,m_2) is inversely proportional to the square of their momenta.

PID is traditionally achieved via one of four alternative methods: ionization energy loss measurement; time-of-flight (TOF); detection of transition radiation; and detection of Cherenkov radiation.

2.2.1 Alternatives to Cherenkov light detection

Time-of-flight techniques are an intuitive solution that consists in measuring the time that it takes for a particle to travel the path between two detectors. Their simplicity is a great advantage: they do not require a large beam line space, have a very quick response and are usually thin and lightweight. However, their performance is mostly dictated by the temporal resolution of the detector systems involved, and for momenta above 2 $\mathrm{GeV/c}$ their π-K separation is usually limited, as illustrated by data from the ATLAS TOF detector at the right of figure 2.2. Nonetheless, the evolution of photodetector technologies led to devices with time resolutions close to the ps level, enabling TOF systems that compare in performance to some of the RICH detectors available, such as the ones using fused silica radiators [14].

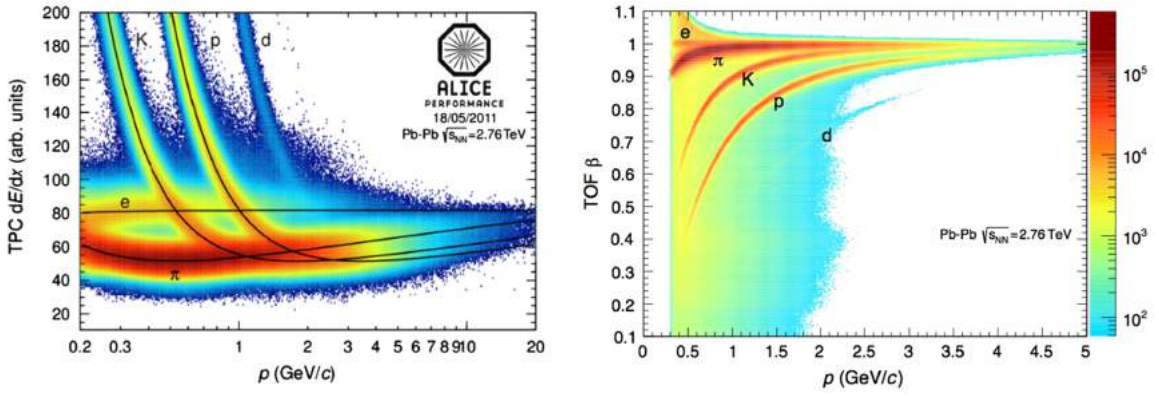

Figure 2.2 Left: ALICE TPC performance showing the measured energy loss as a function of track momentum. Right: ALICE ToF separation as a function of particle momentum. [107]

The techniques involving energy loss measurement, also commonly referred to as $\mathrm{d}E/\mathrm{d}x$, are also viable PID methods based on the energy deposited by particles with different momenta as predicted by the Bethe-Bloch equation (see section 1.1.1). They present very good performance for low p particles, but with increasing momentum values they gradually lose their advantage,

comparing only moderately to the Cherenkov light detection techniques. The large statistical fluctuations of the measurement of deposited energy is a crucial intrinsic limitation. Besides, there are cross-over regions of momentum where differentiation between some particles is not possible (see figure 2.2 at the right).

The transition radiation techniques are based in the measurement of the energy radiated by particles when they cross from one material to another with different dielectric constants. The emission of electromagnetic radiation by this effect is in the X-ray range and its energy is proportional to the Lorentz factor, γ, of the particle instead of its velocity. Additionally, the emission also occurs at an angle determined by γ [11]. This technique is usually confined to electron identification, though, since the minimal velocity required to observe the effect can hardly be achieved by other particles.

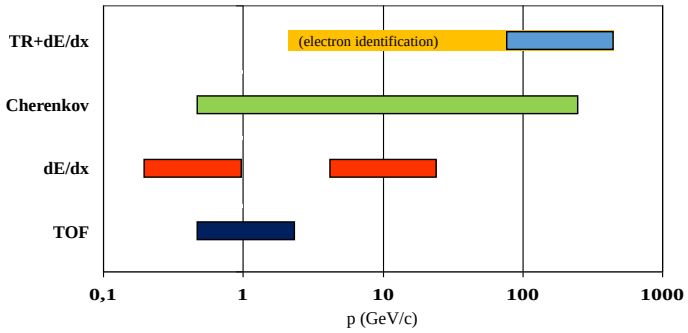

Figure 2.3 Comparison of different PID techniques regarding the range of momenta in which they are effective. Cherenkov radiation detection is the technique that enables efficient PID in the largest range of momenta. [36]

The techniques involving Cherenkov light emission are the most versatile and precise. They allow great angular and momentum acceptance, fast response, and because only a few – typically UV – photons are emitted the energy of the particle is virtually unaffected. Because of that low number of photons, however, the system is as good as its photon generation and detection capability, which, for demanding requirements, may mean an expensive setup. Some examples of PID systems based on Cherenkov light detection are mentioned in the next section.

2.2.2 Cherenkov Detectors

The most basic Cherenkov detection method is the Threshold Cherenkov Counter. The principle of this detector is merely to evaluate if a passing particle emits Cherenkov light on a chosen medium. The radiator – so is called the medium where Cherenkov light is emitted – must be chosen so that for the two types of particles to be distinguished only one of them emits light (or the difference in typical number of photons radiated is large enough). Their performance, however, is relatively poor when compared with more recent developments, mainly because the statistical fluctuations related to the number of photons emitted is high [15].

Differential Cherenkov Counters are in many ways a specialization of the threshold approach, by restricting the detection of light to a very narrow angle relative to the particle's track. They are designed for a very narrow momentum range in which they achieve record velocity resolutions at the order of 10^{-7}. Their use was crucial in the experiment that discovered the antiproton [36].

The problem of the two approaches described above is that their resolution is strictly correlated to their acceptance. By introducing the option to estimate the Cherenkov angle from the imaging of several photons originated by the same particle, the acceptance can be expanded while leaving the velocity determination accuracy depending only on the angular resolution. This is what makes the reconstruction of Cherenkov cones, or their projection in rings, in the RICH detectors so powerful. There are at least three alternative techniques that allow this to be done efficiently: mirror focusing, proximity focusing and the use of total internal reflection (also called pin-hole focusing).

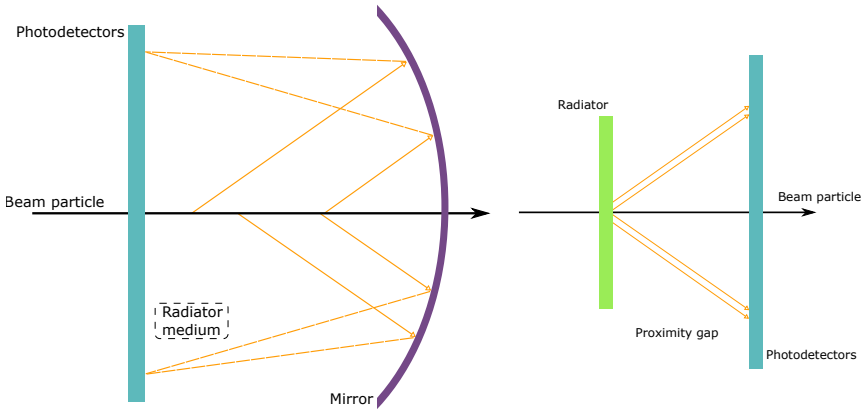

Figure 2.4 Left: illustration of the mirror focused RICH principle. The mirror and the detectors are built so that cones of light production along the particle's track are focused into a single ring. Right: illustration of the proximity focusing configuration. By having a very thin radiator the emission of light itself is approximately confined to a ring.

Mirror focused Cherenkov imaging devices (COMPASS RICH-1 is one of them) use the principle illustrated in figure 2.4 at the left. The particles travel along a long path in the radiator, emitting photons that are reflected in a properly designed mirror (or system of mirrors) that focus all the emitted light into a single ring shape projected on the detector plane. This technique is convenient when using low refractive index radiators, and so requiring a long (a few meters) radiator length. Some designs allow the focusing to be done into detector planes deviated from most of the beam intensity, which is convenient to spare the detectors of background irradiation and to reduce the interference on beam particles.

If one uses a high enough refractive index material for the radiator the number of produced photons is increased, allowing the minimum path that is required for the particle to travel in the medium to be shortened to a point where focusing is no longer required. A distance has to be introduced, however, between the radiator and the imaging plane, so the size of the projected conic section is large enough to be distinguished by the detector's resolution. This is the proximity

focusing approach, illustrated at the right of figure 2.4. Usually when using this technique the photon detectors are put in the way of the traveling particles, which is not ideal.

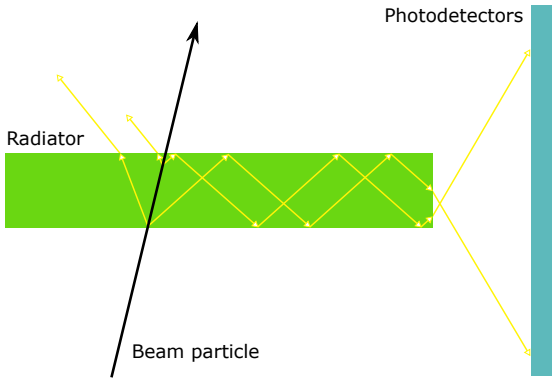

Figure 2.5 Illustration of the DIRC principle, at use in the BaBar experiment.

The DIRC (Detection of Internally Reflected Cherenkov light) is an ingenious approach illustrated in figure 2.5. The radiator is made in a high refractive index material such as quartz, and has a thin light guide geometry, so that when Cherenkov photons are emitted they suffer total internal reflection and are guided along the radiator to a photodetection system [108]. From the position of the detected photons, the Cherenkov angle can be estimated. The DIRC approach led the way to a series of deviations which are very popular topics of research in recent years, namely, the focusing DIRC (FDIRC) and the time of propagation (TOP). It is now one of the most promising approaches for experiments at the low momentum range which favor compact designs [35].

2.2.3 Radiators and Detectors for RICH

The performance of a detector based in Cherenkov ring imaging depends on several variables, namely, the optical properties of the windows used for light transmission, the architecture of the device, the properties of the mirrors or lenses, the timing resolution of the electronic components, the effect of magnetic fields, among other. Two of the most crucial variables are the choice of radiator medium and of photon detection devices [36].

Radiators

The radiator has to be chosen with the overall PID goal in mind, so as to chose proper refractive indexes for the range of momenta and type of particles to be identified. An obvious requirement is that the radiator emits as much Cherenkov light as possible. On the other hand, the material should not emit scintillation light – since that light would probably mask the feeble Cherenkov emission – and should be transparent to the wavelengths of interest for the application.

The chromaticity of the radiator is a strong contribution to the error of the Cherenkov angle measurement, and often defines the PID limit of the technique. Scattering and other dispersion

effects are also negative contributions to the performance of the system.

The choice of radiator material is also intrinsically dependent of the type of RICH device wished for. For instance, proximity focused RICH devices require a sufficient number of photons to be emitted from thin radiators, therefore requiring high n materials. The same is true for DIRC, where the radiator is also a light guide. Instead, mirror focusing allows a larger radiator volume to be used, in which a gaseous medium typically produces enough light.

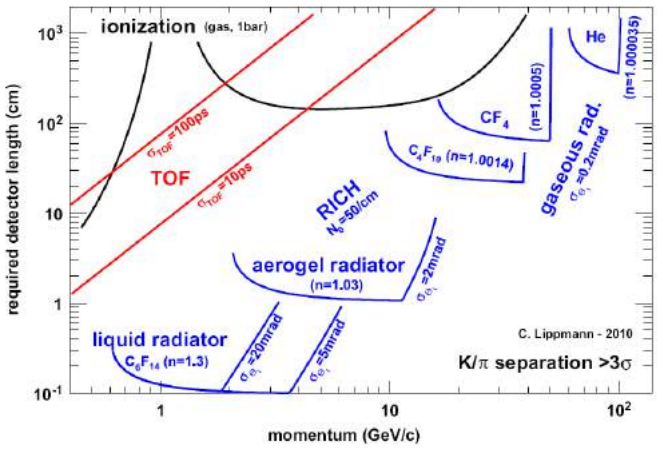

Figure 2.6 Radiators used in RICH systems and the momentum range where they are most effective [106].

A wide range of materials has found applications as Cherenkov radiators, including gases (fluorocarbons mostly), cryogenic liquids of noble elements with low n (He, Ne, Ar), liquids such as water or alcohol, aerogels, and high refractive index solid crystals (quartz, NaF, CaF_2). Figure 2.6 summarizes some of the materials according to the range of momentum of the particles to be identified and required radiator length [106].

Photon Detectors

The evolution of photon detectors in use on RICH applications progressed hand in hand with the research on detection techniques, being one of the propellers of this area of research. In particular, gaseous photodetectors have been a typical choice due, essentially, to their cost-effective ability to cover large areas of detection, and their insensibility to magnetic fields up to 4 T [35], two characteristics that vacuum-based devices such as PMTs, do not share.

Hence, it is not surprising that the first generation of RICH detectors coincided with the development of the first generation of GPDs using photoconverting organic vapors, such as the UV-sensitive TMAE or TEA [36]. This solution implied many technical challenges. For a start, the far-UV region of operation required expensive windows, suffered from large chromatic dispersion, and demanded careful analysis of the gas purity since water and oxygen are very absorbent in that region. Furthermore, these photoconverting vapors required thick volumes of detection, which

besides the loss in resolution also implied a very slow operation. The presence of photon feedback was also a problem.

Despite all this, they were employed with success in some of the largest RICH detectors ever built such as the DELPHI RICH [38] and the SLD's CRID [39], operated between 1987 and 2000 [35]. Other RICH detectors using photoconverting vapors include the Omega RICH [109] and the CLEO-III [110].

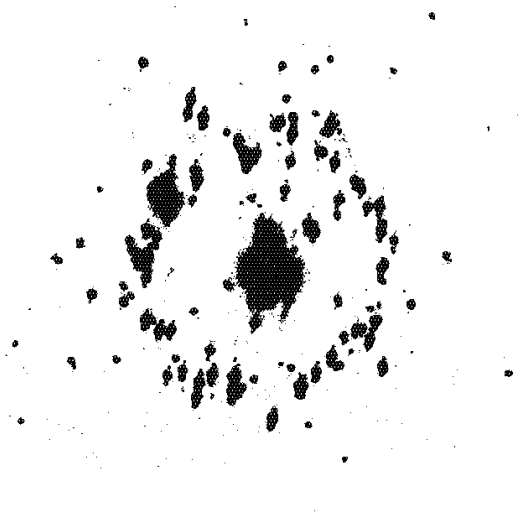

Figure 2.7 Detection of Cherenkov rings using a MWPC detector with TEA as photoconverter. [111]

The second generation of GPDs, developed mostly by the RD26 collaboration at CERN, led to a breakthrough in RICH devices. They consist in the replacement of the photoconverting vapors by solid photocathodes, typically with CsI, while retaining MWPCs as electron multiplier elements. Since CsI is efficient at lower VUV photon energies, the requirement of expensive windows and some of the other effects observed in detectors of the previous generation are not present. Because the photon detection occurs in a thin plane (few hundred nm), parallax errors are eliminated, and the resulting Cherenkov angle resolution is much better. All this is achieved in devices which are fairly easier to operate, and whose timing resolution is greatly improved (down to the ns level) compared to the ones previously available.

MWPCs with solid photocathodes are now used in the majority of large RICH systems: the experiences HADES [112], COMPASS [113], HALL-A [114], and ALICE [115] all use CsI photocathodes coupled to MWPC detectors in their RICH devices [35].

Because the requirements for physics experiments continued to increase, the research on gaseous detectors entered in the third generation, mostly based on MPGDs. The threshold Cherenkov detector at PHENIX already uses a CsI photocathode in a triple GEM detector [68]. In order to continue that evolution, in future RICH devices MPGD-based detectors have to meet a

few requirements:

- short signal formation with time resolution up to 10 ns
- closed geometry to avoid photon feedback
- large gain ($\geq 10^5$) to avoid dependency on the front end electronics thresholds
- efficient photoelectron extraction from the CsI photocathode
- controlled IBF, at the few % level, to reduce aging of the CsI and increase the stability of operation
- stability of response over time and in beam environment conditions

As alternatives to gaseous detectors, PMTs (and Multi Anode PMTs) are a mature solution with great performances in terms of high gains and fast operation. The HERA-B RICH detector [116] and the BaBar DIRC [108] are two examples of RICH systems which employ this solution. They have, particularly over the available gaseous detectors, the big advantage of being very efficient also for photons in the visible range, which allows simpler RICH setups unlike the devices based on VUV detection. Nevertheless, they are costly solutions, especially limiting when the intent is to cover large areas of photon detection. Their sensitivity to magnetic fields is another major drawback.

Solid state detectors such as SiPMs and APDs (Avalanche Photodiodes) have some advantages compared to PMTs, namely by requiring lower supply voltages, being composed of lighter materials and by operating in the presence of magnetic fields [117]. A promising solution seems to be the development of Hybrid Photon Detectors (HPDs) and Hybrid APDs (HAPD), which combine vacuum PMTs with solid photosensors and achieve good sensitivity, energy and spatial resolutions. HAPDs have been chosen for the upgrade of Belle-II's proximity focused RICH [118] and HPDs are implemented in the LHCb RICH [119]. Nonetheless, solid state detectors suffer from other drawbacks including crosstalk between pixels, a trade-off between low temperature operation and higher dark count rate, and generally are not cost effective solutions to cover large areas, especially the ones with good detection efficiency in the VUV region.

2.3 COMPASS RICH-1

2.3.1 COMPASS

COMPASS (NA58) [3, 120] is a high-energy physics experiment at the Super Proton Synchrotron (SPS) at CERN. It first started data taking in 2002 and was, until the start of LHC, the largest running CERN experiment, and remains the biggest at the surface. It counts with the collaboration of well over two hundred physicists and with institutions from more than a dozen countries.

COMPASS aims at a better understanding of the structure of matter at the quantum chromodynamic (QCD) level, namely the understanding of the hadron structure [121]. Within this,

several research topics are of interest. One of the most important is the famous *spin puzzle*: that the spin of hadrons, expected to be a result of the simple contribution of its constituent quarks, was found to be mostly originated from the gluons momenta and other contributions. Little is known about the polarisation of gluons in the nucleon and the transversity Parton Distributions Functions (PDF). In the meson sector the electric and magnetic polarisabilities of pions and kaons can shed light onto their internal dynamics. Finally, hadrons with exotic quantum numbers and double charmed baryons are ideal tools to study QCD.

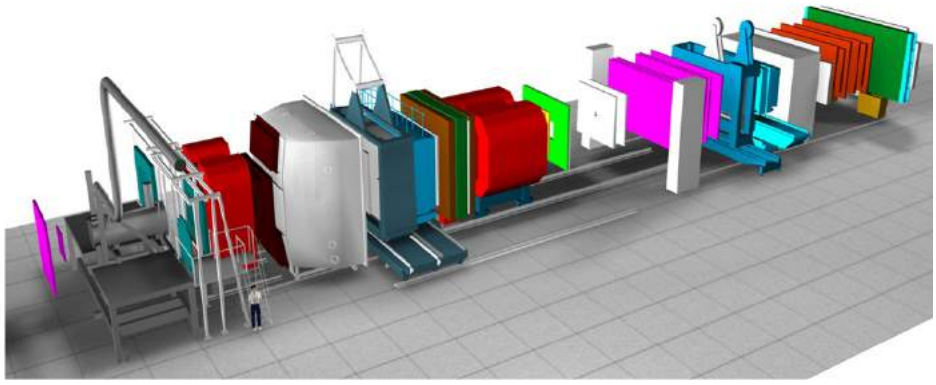

Figure 2.8 Artistic view of the COMPASS experimental setup.

The experiment is based around a fixed target, typically irradiated with high intensity muon (up to 190 $\mathrm{GeV/c}$) or hadron (protons or pions, up to 280 $\mathrm{GeV/c}$) beams from CERN SPS. One or more outgoing particles are detected in coincidence with the incoming muon or hadron. The large polarized target inside a superconducting solenoid is used for the measurements with the muon beam. Fields up to 2.5 T can be applied, for which the target needs to be cooled to as low as 50 mK. Outgoing particles are detected by a two-stage, large angle and large momentum range spectrometer. Particle identification is achieved using the RICH-1 detector in the first stage and hadron and electromagnetic calorimeters in both stages.

The setup is built using several types of tracking detectors (including GEMs, Micromegas, MWPCs, Drift Chambers and Straw tubes), according to the expected incident rate, required space resolution and the solid angle to be covered. Since the detailed description of the COMPASS setup is beyond the goal of this work, a short summary is presented. The reader is referred to references [3, 4, 120] for details.

COMPASS is recognized for it's pioneering efforts in adopting new detector technologies, being among the first experiments to include Micromegas and GEM detectors. It is therefore an interesting and innovative environment, and a perfect place to develop and apply new detector solutions.

2.3.2 RICH-1

The COMPASS experiment requires, for some of the physics under study, very efficient charged particle identification in a wide momentum range and in a very crowded environment at large luminosity. The COMPASS RICH-1 detector is one of the most challenging applications of CsI photon detectors in an experiment, due to the high trigger rates required in a very high-intensity beam.

Due to often using a highly polarized target, a Vertex detector cannot be used to detect the presence of charmed particles, making the use of the RICH essential to allow π-K separation on the COMPASS experiment [2]. The RICH-1 [113] – so called because a second RICH detector was initially planned – is responsible for PID in the momentum range between 3 and 55 $\mathrm{GeV/c}$. This mirror focused RICH, illustrated in figure 2.9, uses C_4F_{10} gas as radiator in the 3 m long, 80 m^3 vessel. C_4F_{10} was chosen due to its low chromaticity and refractive index of 1.0015 at 177 nm [3]. The spherical mirrors (see figure 2.10) cover a 21 m^2 area and focus the Cherenkov light into the 5.5 m^2 photodetection area. The detector has an horizontal angular acceptance of 500 mrad, and 360 mrad vertically.

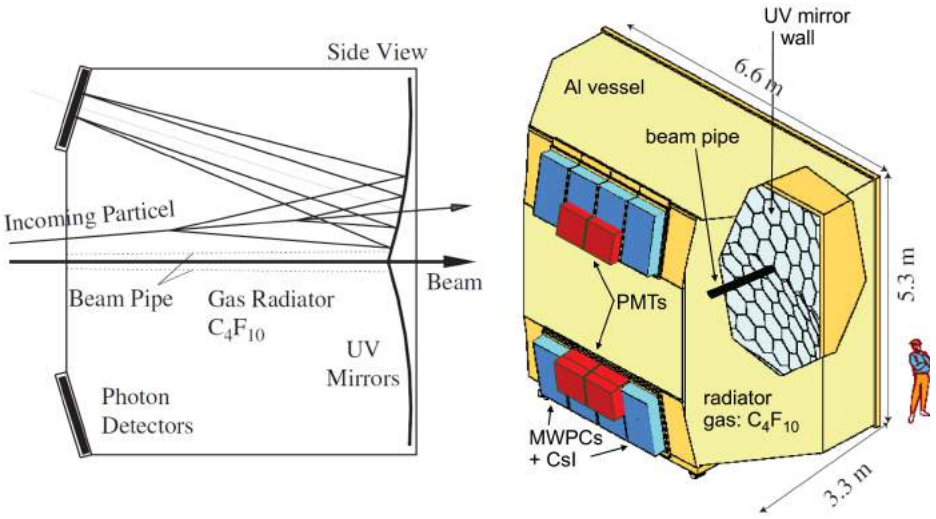

Figure 2.9 Scheme of the RICH-1 mirror focused detector from COMPASS [3] (left) and it's 3D illustration [113] (right).

Originally, the photodetection region was entirely composed of MWPCs with 500 nm thick reflective CsI photocathodes, so the RICH was built having VUV operation in mind: properly chosen mirrors, high purity radiator gas to ensure transparency (contaminations of water and oxygen around 1 ppm and 3 ppm, respectively), and quartz windows for efficient transmission of photons with wavelenghts as low as ~165 nm. Eight MWPCs were installed, each with 576 × 1152 mm^2 of active area and operating in pure methane at atmospheric pressure [113]. The readout of each of the detection elements was a square matrix of 72 × 72 pads, each pad with 8 × 8 mm^2 area. The geometric aspects of this photodetector are illustrated in figure 1.12, in the previous chapter.

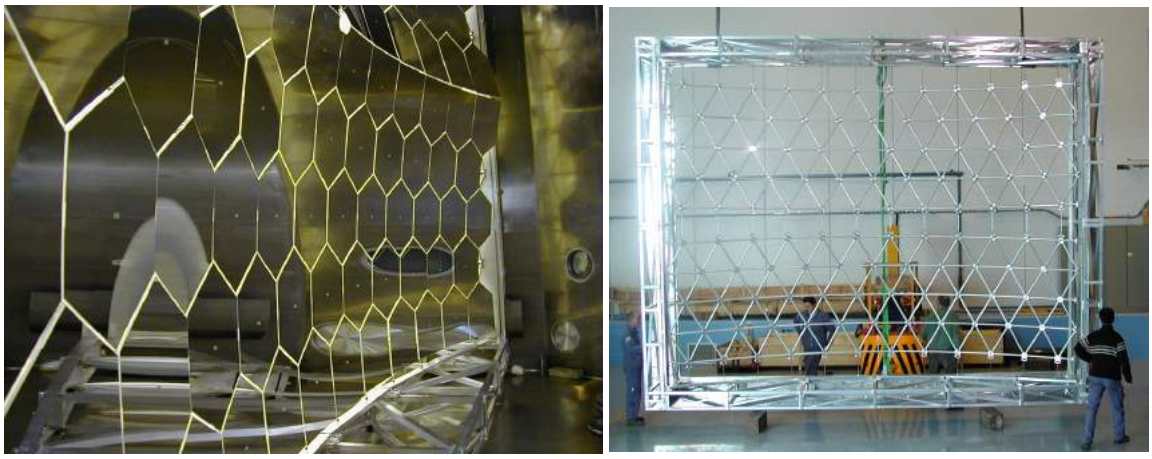

Figure 2.10 Left: photograph of the bottom half of the RICH-1 mirror wall. Right: support frame of the mirror elements, during the assembly in 2001.

The MWPCs in the RICH-1 operate at gains limited to 5×10^4 for several reasons: the high intensity background irradiation decreases the stability of the chambers; in case of a discharge the detectors can take up to one entire day to recover the expected performance; the beam irradiation is responsible for heavy ion bombardment, whose charge is proportional to the gain; and lastly, higher gains increase the possibility of photon feedback effects in these open geometry detectors.

The RICH-1 detector based entirely on MWPCs operated until 2004 showing PID efficiency of ~95% over a wide acceptance, an average ring multiplicity of 14 (number of photons per β~1 particle) and single photon angular resolution of 1.2 mrad, resulting in π-K separation of 2σ at 43 $\mathrm{GeV/c}$.

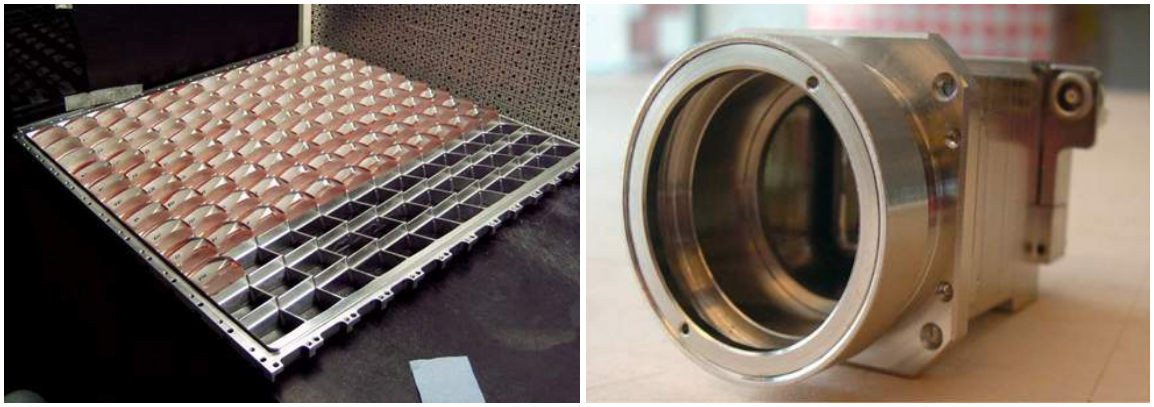

Figure 2.11 Left: array of silica telescope lenses on the support frame, which are placed in front of the MAPMTs, thus effectively increasing the active photodetection area. Right: MAPMT with magnetic shielding. [122]

In 2006, 1.3 m^2 of the central detection region – 25% of the total active area – were equipped with 576 cells consisting of Hamamatsu R7600-03M16 multi-anode photomultiplier tubes (MAPMTs) [122, 123], each with 16 readout pads. The new detectors included a fused silica lens system (see figure 2.11 at the left) that increases the effective active area of detection. The goal of the

substitution was to improve the performance of the affected region, the most limited due to muon background [1], and to handle the increase in beam intensity planned for that period.

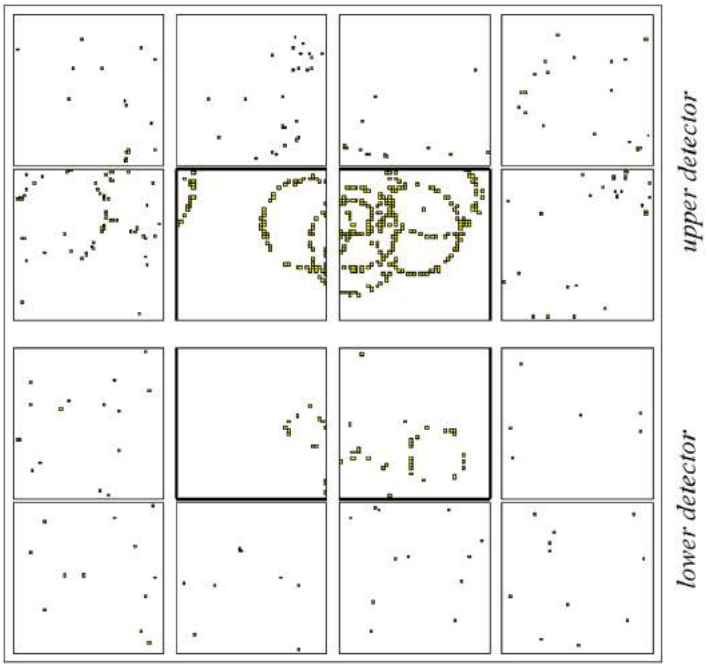

Figure 2.12 Example of Cherenkov ring imaging in the RICH-1, after the 2006 upgrade. The higher efficiency of the central region is evident. [124]

The new detectors operate with gains higher than 10^6 and are stable even under high luminosity conditions. They are characterized by very fast responses and operate in a much larger wavelength range compared to the MWPCs (up to 700 nm), which resulted in the increase of the average number of photons detected per ring to 56, as evidenced by figure 2.12. The 2σ separation with the MAPMT system is now achieved up to 55 $\mathrm{GeV/c}$.

As for the digital readout systems, they are different for the two types of photodetectors. The MAPMTs are operated with a chain of CMAD preamplifier-discriminator chips and DREISAM digital cards with F1-TDC chips [125–127]. Together, they present moderate noise levels (common operation thresholds of 10 fC), high bandwidths up to 5 MHz and a temporal resolution of ~300 ps [128]. During the 2006 upgrade, the digital readout of the MWPCs was also improved [129]. The new readout system is based on the APV25-S1 chip [47], an 128 channel analog preamplifier which can be peaked in a wide time range after a trigger, allowing good operation of slower detectors, as is the case. It also allows noise thresholds at <0.5 fC per channel.

The improvement in PID performance after the 2006 upgrade is particularly evident at the right of figure 2.14, where it is shown that for small polar angles, the kaon identification efficiency is now almost full, which compares to values lower than 60% in some of the acceptance regions before the upgrade.

The MWPCs that make up most of the detection area are still a limitation to the optimal

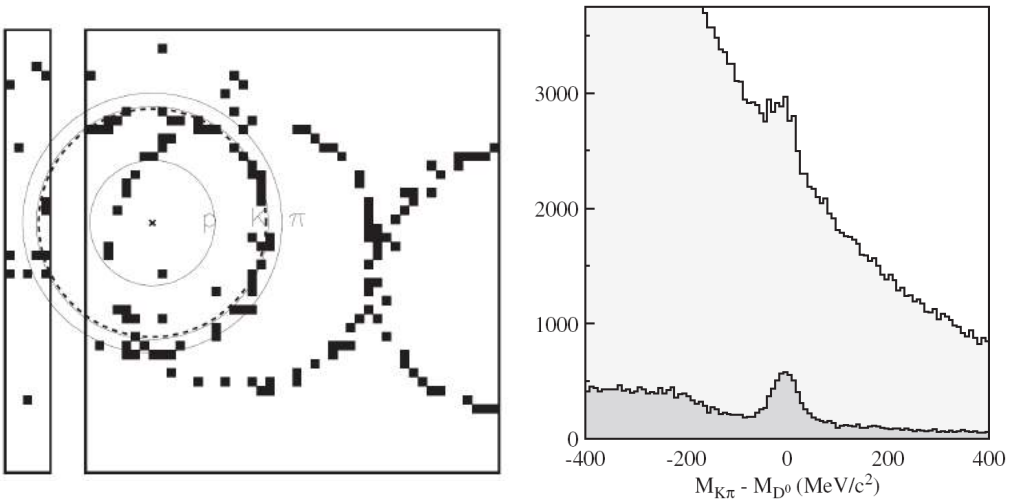

Figure 2.13 Left: partial view of the central region of the RICH with MAPMT photon detectors, showcasing the attempt to identify the particle responsible for the ring at the left (probably a K). Right: data taken in 2006 at COMPASS that demonstrates the big difference between data analysis with (dark grey) and without (light grey) PID. [124]

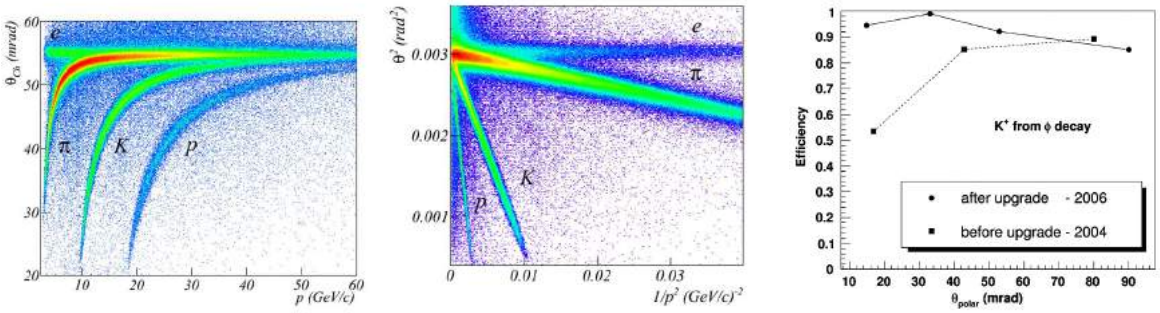

Figure 2.14 Left: measured ring Cherenkov angle versus particle momentum. Center: same data as left but angle squared versus the inverse of the momentum, to display the linear dependence of the variables [128]. Right: comparison of K identification efficiency versus polar angle before and after the upgrade, with the increase in performance clearly visible for smaller angles [130].

operation of the RICH device, even more so considering additional factors such as the CsI aging, and consequent loss of efficiency, due to ion bombardment. The effect of bombardment is particularly evident in figure 2.15, from before the 2006 upgrade.

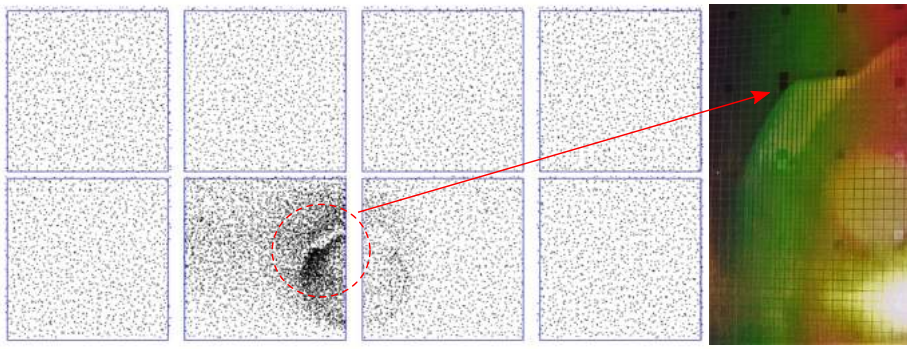

Figure 2.15 Image of the top half of the original COMPASS RICH-1 detection region, composed of MWPCs. The major spot in the lower central region is caused by the beam halo. The picture at the right was taken after an accident that caused air to enter the MWPC chambers. The humidity in the air was more absorbed in the highly bombarded region, which revealed the high deterioration of the central area.

An upgrade of the remaining MWPC detector modules to MAPMTs would be prohibitively expensive for such large area. In recent decades, new generations of gaseous detectors have been developed that offer a promising solution for these applications, some of which have been introduced in the previous chapter. This work, in particular the next chapter, presents the efforts and results of many years of studies of MPGD-based detectors, namely ThGEMs and Micromegas, envisaging such upgrade.

Chapter 3

Development of MPGD-based RICH detectors

This chapter encompasses most of the work done on the development of detectors for the COMPASS RICH-1 upgrade. It includes studies performed on detectors in laboratory conditions, the improvement in production and analysis techniques needed to achieve the necessary upscaling of the detector components, and testifies the most important challenges faced and how they were overcome.

To further evaluate in close-to-work conditions the performance of the detectors developed, tests in radioactive environment under high energy particle beam irradiation need to be performed. Those exercises are important because the detection of real Cherenkov photons is much more delicate than the detection of photons from a light source in laboratory conditions. These tests took place at the installations of the European Organization for Nuclear Research (CERN). In four tests under beam – typically referred to as test beams – the author had direct contributions: two tests with $30 \times 30\,\mathrm{mm}^2$ active area triple ThGEM detectors; one with a $300 \times 300\,\mathrm{mm}^2$ ThGEM-based detector; and a final test beam with Hybrid detectors.

The description and results of the test beam experiments are presented as sections in this chapter, following the sections that deal with the production of the detectors being examined. Naturally, the order by which the sections are introduced being determined by detector size and complexity, the resulting exposition resembles its chronological sequence.

The author joined the research effort in RICH detectors for the COMPASS RICH-1 upgrade after a substantial amount of work had been developed in small area detectors. That research and its main conclusions are summarized in section 3.1, in which the author has no direct contribution. Still, it is included in the present chapter and not in the introductory ones for the sake of coherence, since it led to crucial conclusions that guided the remaining work. In the sections that follow, the author made active contributions, including in the test beams exercises and the respective data treatment.

General experimental considerations

While the specific conditions and instruments used for a particular study are referred in its description, it is convenient to have a few general considerations stated already, to reduce the need for exhaustive repetition throughout the remaining chapter.

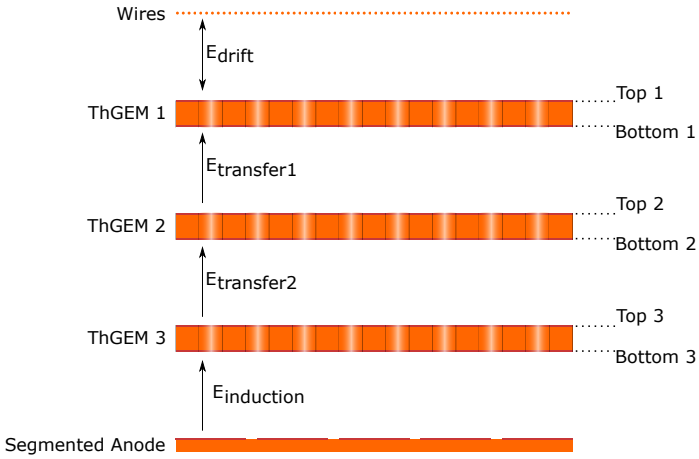

Figure 3.1 Typical nomenclature used for setups presented throughout the present chapter.

Figure 3.1 illustrates a generic ThGEM-based detector. The nomenclature for the different regions is inherited from GEM-based detectors:

- ThGEMs are numbered from top to bottom. The photocathode, if present, is deposited on top of ThGEM1.
- Each ThGEM has two electrodes, Top and Bottom. As an example, one can refer to the Top electrode of ThGEM2 by Top2, and the Bottom of ThGEM3 as Bottom3.
- Between ThGEM1 and the wire plane (typically made with 100 μm wires separated by 2 mm) there is a charge collection volume, called Drift region. The electric field created by the application of a voltage difference between Top1 and the wires is called the Drift field. The Drift field is either null, when operating in single photon detection mode, or positive/pointing upwards (often ~1 kV/cm), in order to collect primary charges created in the Drift region.
- The region between two multiplying elements is the transfer region, where a transfer field is applied. If no other information is provided, the reader can assume this field's strength to be ~1 kV/cm.
- The signal is measured in a segmented PCB anode readout. Between the Bottom of the last ThGEM and the anode there is an Induction region, where the Induction field is applied (typically ~2 kV/cm).

In laboratory conditions, the detectors are studied by exposure to either X-rays or UV light. For the generation of UV light, either the LED-255 by Seoul Optodevice Co. Ltd. (255 nm) or the pulsed PLS 265-10 LED (265 nm), powered with the PDL 800-B by PicoQuant GmbH, are used. The CsI quantum efficiency at those wavelengths is weak, but the intensity of the light source can be increased enough to allow detection at useful rates. The X-ray source used is made of Fe-55, whose emission peak is considered at 5.9 keV.

The establishment of electric fields that guide the electrons through the multiplication process is done by powering the electrodes with high voltage power supplies, most often CAEN N471A modules. Because there is interest in keeping the anode readout at ground level – to protect the chips from high voltages and to reduce the noise level – the polarity of the voltages applied is almost always negative. With the exception of the drift wires (whose voltage varies depending on the type of measurement), the top of ThGEM1 is the electrode at lowest potential, but higher absolute value of voltage. The only occasion where positive polarity voltages will be used is on the capacitive anodes of the Hybrid detectors (section 3.5.3).

The detectors are filled with argon rich mixtures via a *once through* type of gas circuit at atmospheric pressure. The Ar:CH_4 mixture ratio is set by a Bronkhorst gas flow meter. When using Ar:CO_2 either the Bronkhorst system or premixed bottles were used. The flow rates were typically 10 $\mathrm{l/h}$ in the smaller chambers (hosting 30 × 30 $\mathrm{mm^2}$ active area detectors) and 30 $\mathrm{l/h}$ in the larger ones.

The amplified charge signal is collected at the anode readout. The signal can then be processed via a digital or an analog chain. The digital readout chain is used solely in beam exercises, where it will be described. As for the analog chain, it consists, firstly, in a Cremat charge sensitive preamplifier (CR-110 or CR-111) within a CR-150 evaluation board, whose output signal is then further shaped and amplified by an Ortec amplifier (models 590A or 672). The digitalization of the signal is performed by the Amptek MCA8000A multichannel analyzer.

The Cremat board in the analog chain allows an external input – typically a well defined pulse with a known charge – to be introduced in the electronic chain for calibration purposes. An equivalence between ADC channels and charge is thus obtained.

Using the Fe-55 source and the analog chain, a typical spectrum obtained with an argon rich mixture is illustrated in figure 3.2. The full 5.9 keV absorption and the argon 2.9 keV escape peak can be identified. One can estimate (see section 1.2) that the main peak is produced by ~220 initial electrons, which in turn allows one to estimate the gain of the detector.

Using the light source, the gain is estimated by fitting an exponential curve to the spectrum, or more accurately, by fitting a linear curve to the spectrum with counts in logarithmic scale. As explained in section 1.2.2, the slope returned by that fit allows the estimation of the detector's gain.

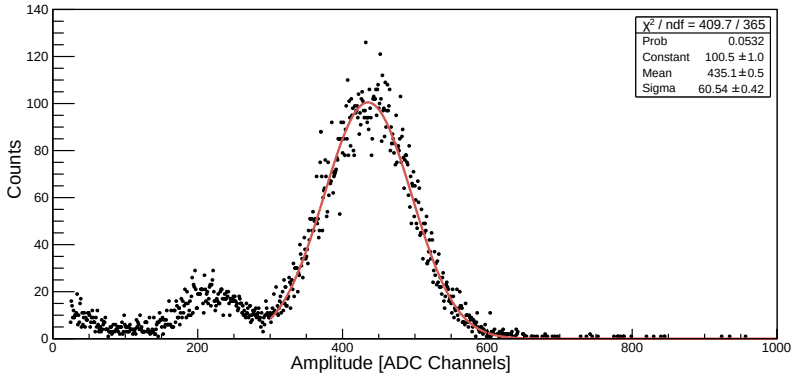

Figure 3.2 Typical spectra obtained with the detectors which will be studied, filled with a argon-based mixture and under irradiation with the Fe-55 source. The full absorption peak (5.9 keV) and the argon escape peak are easily identifiable. After the histogram scale is calibrated, the mean value of the main peak can be used to estimate the gain of the detector.

3.1 Development of 30 × 30 mm^2 ThGEM-based Detectors

As previously mentioned in section 1.4.3, ThGEMs were proposed by several groups, with a great part of the initial development and study achieved by the Weizmann Institute, among others. The group did an extensive body of research regarding the optimization of small – typically 10 × 10 mm^2 of active area – ThGEM detectors, including some studies of their possible use as RICH photodetectors [79, 80, 131]. Building on Weizmann's work, the Trieste section of INFN started a research project focused on ThGEM detectors.

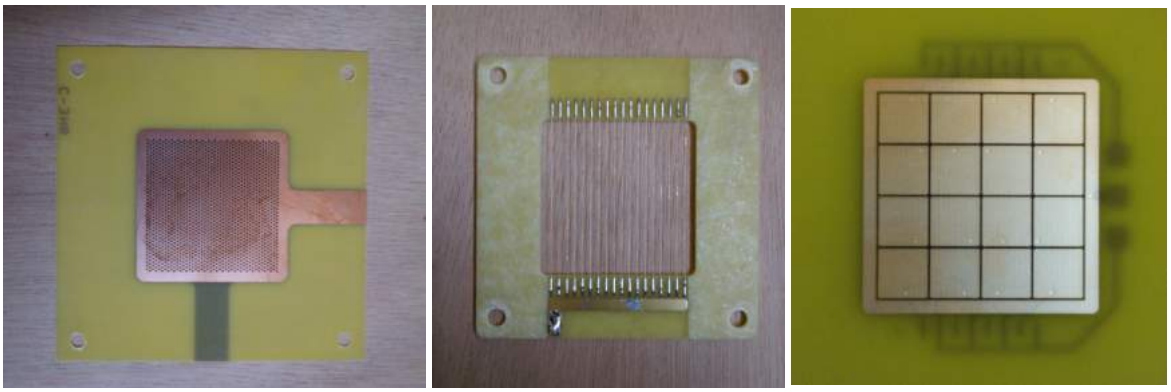

Figure 3.3 Photograph of a typical 30 × 30 mm^2 active area ThGEM (left), a small wire plane structure for defining the drift field (center) and the segmented PCB readout (right).

After initial samples provided by the Photolithography Microconnectics Technologies workshop at CERN, the Italian group decided to work with ELTOS S.p.A., an industrial PCB producer and processing company. A large number of ThGEM pieces with 30 × 30 mm^2 of active area using FR-4 Halogen-free Glass Epoxy Laminate with 35 $\mu\mathrm{m}$ thick Cu layers on both sides were produced along

an extensive list of combinations of different production methods and geometrical parameters of the structures. A picture of a typical ThGEM produced by Eltos is shown at the left of figure 3.3.

Extensive studies were then performed on ThGEM detectors, namely, to find the optimal parameters in order to reduce the Ion Backflow, increase the maximum gain achieved and promote gain stability, as well as guarantee full extraction and collection efficiency of photoelectrons in the case there is a CsI photoconverting layer present.

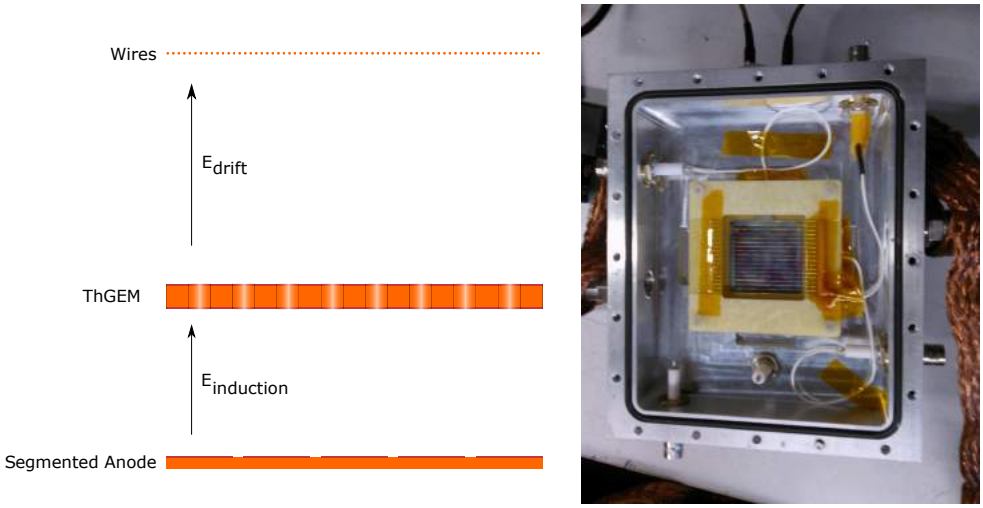

Figure 3.4 Left: scheme of a standard single ThGEM detector. The drift field pointing upwards (positive) is used to collect the primary charge created in the gas by the Fe-55 X-rays. Right: photograph of a typical chamber used for the exercises presented in this section. Inside the chamber, the copper surface of a ThGEM can be seen behind the wires.

A typical detector chamber where single ThGEM studies were performed is shown at the right of figure 3.4, next to a generic scheme of the detector. The signals are collected at the anode plane, a square array of 16 pads, 7.7 × 7.7 mm^2 area each, separated by 0.3 mm gaps, as shown in figure 3.3.

The studies and their conclusions are presented in the following subsections. The separation is used to aid the clarity of the exposition, but the subsections are hardly independent from each other.

3.1.1 ThGEM geometrical parameters

Among the first aspects to be investigated in ThGEMs was the influence of geometrical parameters on the performance of the detectors. The four geometrical parameters that rule the ThGEM behavior are the thickness, hole pitch, hole diameter and rim size. The rim has critical effect on the gain stability which is the main focus of section 3.1.3.

The thickness of the ThGEM is, as would be expected, a parameter that directly influences the maximum voltage that can be applied to the structure before electrical discharges are observed. A thicker ThGEM will require a higher voltage to be applied in order to reach the same electric field

intensity of an equivalent but thinner structure. On the other hand, this thicker piece could have a longer region with fields above the ionization threshold, which should result in a slightly higher measured gain for the same field. These expectations are confirmed experimentally, as shown in the left plot of figure 3.5 and on the plots of figure 3.6. To give one example, roughly 30% higher voltage is required to achieve the same gain when the thickness is doubled from 0.4 to 0.8 mm.

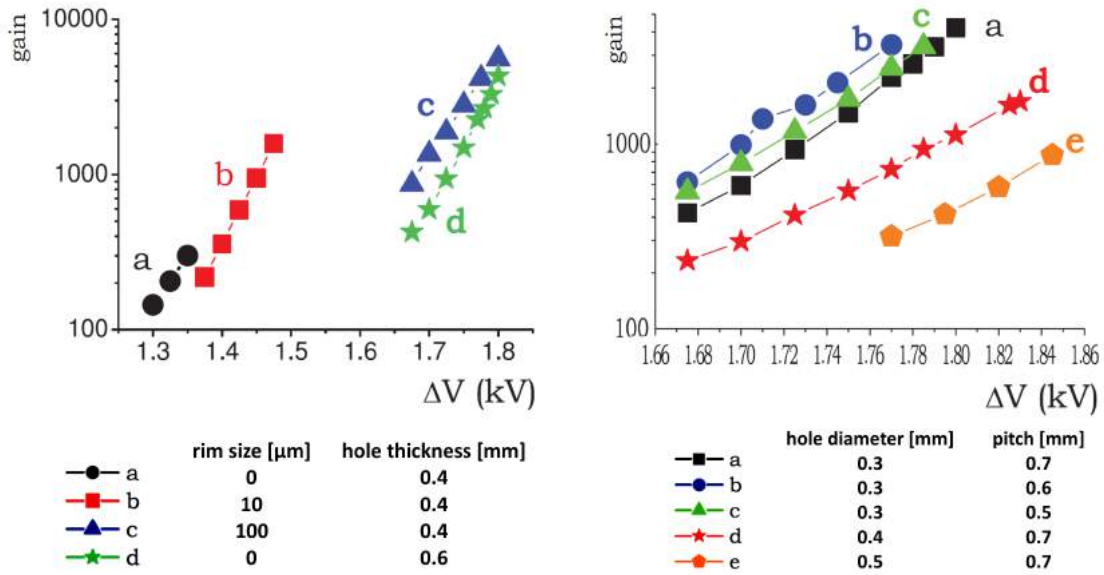

Figure 3.5 Effective gain of ThGEM pieces as function of the voltage difference applied between the electrodes. Left: with 0.3 mm of hole diameter, 0.7 mm pitch and remaining parameters detailed under the chart. Right: fixed thickness of 0.6 mm, no rim, and remaining parameters described under the chart. [132]

The hole diameter is another important parameter to take into account in order to maximize the maximum gain attainable with a ThGEM. A wider hole means that the dipole field on the hole region is weaker for the same voltage difference, which in turn means a lower gain. To match the same gain, a higher voltage has to be supplied. Unlike the increase in thickness however, the larger-hole ThGEMs will only sustain a slightly higher maximum ΔV, insufficient to compensate the gain loss and so in the end wider holes lead to a lower maximum gain. This is corroborated by the right plot of figure 3.5, and leads to the conclusion that to achieve higher gains one should favor smaller holes.

The hole pitch is the parameter which shows the least effect on the gain or maximum voltage sustained, but which has a big importance nonetheless, in particular concerning the choice of ThGEM to be used on top of a cascaded configuration with a CsI photocathode. Not only does the pitch have influence on the electric field present immediately above the photocathode plane (discussed later in subsection 3.1.4), together with the hole diameter it determines the effective area that can receive CsI coating, and therefore the active photodetection area. It can be shown that

establishing a ratio of diameter to pitch around 0.5 leaves more than 80% of the ThGEM surface available for photocathode deposition while satisfying field requirements [133].

The role of the rim is hard to untangle from charging up effects that occur when it is present. In any case, a few assertions can be made on its importance while ignoring the time dependency of the gain. First of all, it is clear that a large rim contributes significantly to reduce the active area of photodetection in the ThGEM's surface. Secondly, the maximum voltage difference that can be applied on the electrodes of the structure before electrical breakdown occurs is higher for larger rims, as would be expected since the electric field is lower. However, if the lower field strength was the sole reason, one would expect similar maximum stable gains even if at different voltage differences, which is not the case: a ThGEM with the slightest rim (<5 $\mu\mathrm{m}$) sustains such higher voltage compared to a structure with no rim, that the maximum stable gains are in fact significantly higher. The reason for this behavior has to do with the elimination of imperfections of the copper edge near the hole during the rim etching process.

3.1.2 The gas medium

The choice of gas medium has a determinant role in essentially two aspects of the detector response: the photoelectron extraction efficiency from CsI photocathodes and the gain.

As already mentioned in the first chapter, the gain achieved by a ThGEM structure for a fixed voltage is essentially determined by the Townsend coefficients of the gases used, which in the cases relevant for this work are essentially the noble elements neon and argon. Within these, argon is strongly favored due to its lower cost, even if it requires the application of higher voltages to the structures in order to achieve high gains. The drawback of using pure noble gases is the low photoelectron extraction efficiency of CsI photocathodes operated in such atmosphere, which is improved with the addition of more complex molecules such as CO_2 or CH_4.

To further understand the optimal medium to be used in our applications, tests were performed on the effect of different gas mixtures in the parameters mentioned. In particular, figure 3.6 shows that for different argon-based mixtures, the use of either CO_2 or CH_4 seems to allow a single ThGEM detector to reach the same approximate maximum stable gain, which with methane mixtures appears also to be independent of the CH_4 fraction used up to 50%.

Nonetheless, the use of Ar:CO_2 stands out as requiring significantly less voltage applied to achieve the same avalanche gain when compared with the equivalent mixture using CH_4. The methane content, on the latter case, is found to be inversely correlated with the gain for a fixed voltage.

If on the other hand one looks at the photoelectron extraction efficiency, methane based mixtures have a clear advantage over carbon dioxide based ones. That conclusion is drawn from studies of the photoelectric current obtained from CsI photocathodes under UV light irradiation, with results such as the ones in figure 3.7. As an example, for a same applied field of 1 $\mathrm{kV/cm}$ the methane mixtures have almost double the efficiency of the Ar:CO_2 alternative.

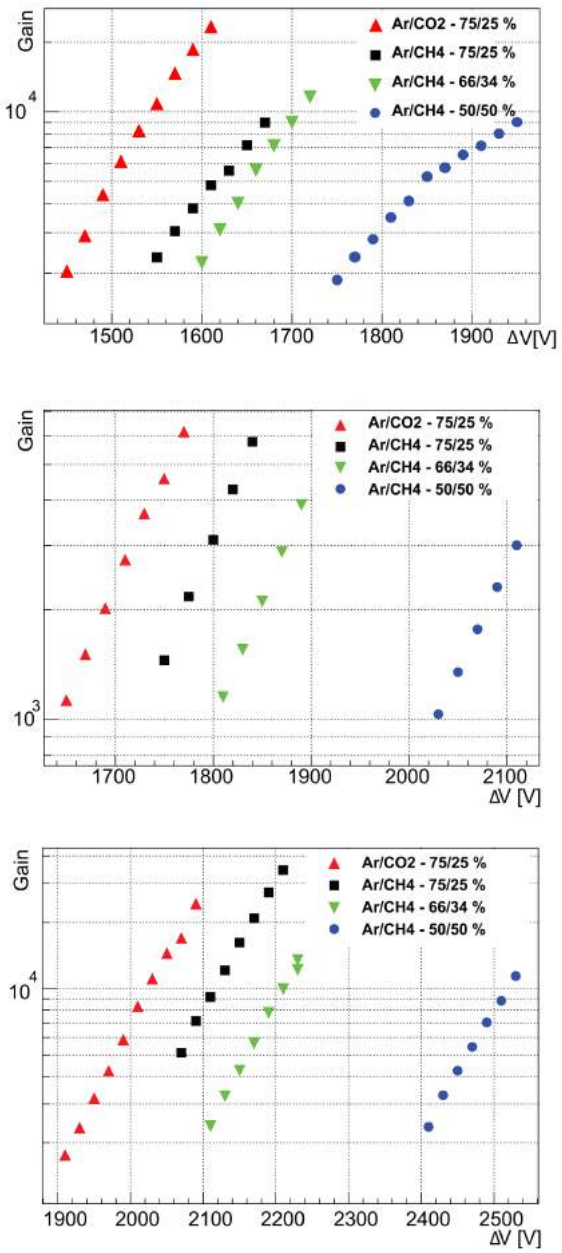

Figure 3.6 Gain achieved, using four argon-based mixtures, for single ThGEMs with 0.4 mm hole diameter, 0.8 mm pitch, and: 0.4 mm thickness and 20 μm rim (top); 0.6 mm thickness and no rim (middle); 0.8 mm thickness and no rim (bottom). [133]

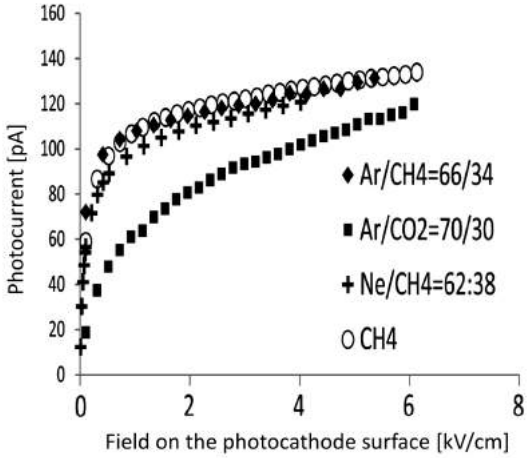

Figure 3.7 CsI photocurrent versus applied electric field in various gas mixtures at atmospheric pressure. [134]

Another important conclusion from the study of figure 3.7 is that a gaseous medium with methane fraction of 1/3 presents the same effectiveness of photoelectron extraction as a pure methane medium. Considering the knowledge of the gain dependency with methane content explained above, this leads us to opt for $ArCH_4$ mixtures with CH_4/Ar ratio close to 33% as a reference for our studies that make use of a CsI photocathode, so that the gain in the electron multiplication process of the ThGEM as well as the extraction efficiency is maximized.

3.1.3 Gain stability – the role of the rim

The rim – the exposed region of PCB around the holes of the ThGEM – is a very important aspect of the structure's behavior, in particular in its gain stability over time. Initially introduced as a way to increase the maximum gain achieved by a ThGEM, it was soon realized that the gain behavior was strongly time-dependent, and that the rim was a key aspect to understand it. A qualitative model of the time dependency of the gain and the effect of the rim took a long time to be developed [135].

The current understanding of the gain stability on ThGEM structures under irradiation is that it consists of two contributions: a fast evolution whose effect is mostly negligible after a few minutes of ThGEM operation and a slow contribution which takes effect over several hours or days.

The fast contribution, depicted on the left of figure 3.8, is usually referred to as the charging-up effect and is better understood. Due to the ThGEM operation and the avalanche multiplication, charges start to accumulate either at the bottom (mainly electrons) or at the top (mainly ions) of the holes of the structure, in the free surfaces of the dielectric, i.e. the hole inner walls and the rim, if present. These charges alter the prevalent field and quickly start to reduce the effective gain, an opposite effect to what had been observed in GEMs [136, 137]. This effect is always present even without rim – usually smaller in that case – and has recently been simulated in agreement with experimental results [138]. The time required to achieve a stabilized configuration depends

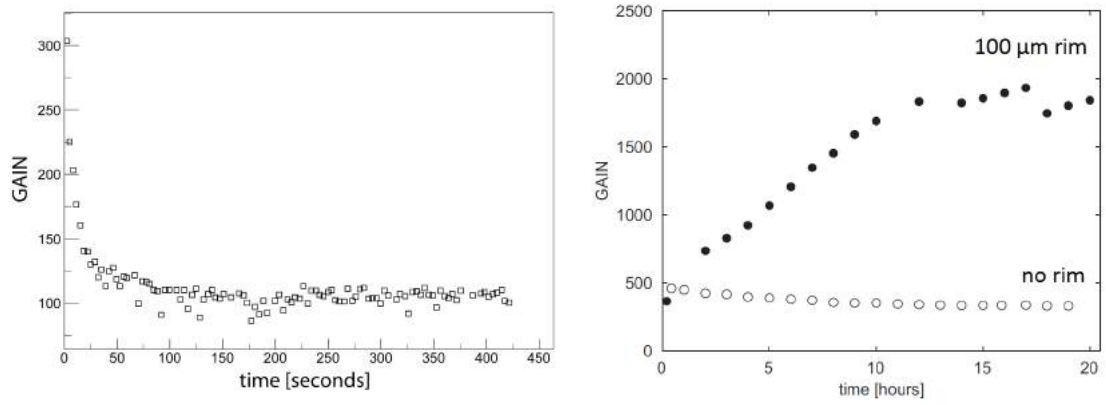

Figure 3.8 Left: short-term time evolution of the gain of a ThGEM structure, 0.2 mm thick, with 0.2 mm diameter holes at 0.4 mm pitch and 40 $\mu\mathrm{m}$ rim. Right: long-term gain evolution of two ThGEMs with 0.4 mm thickness, 0.8 mm pitch and 0.4 mm holes, one with 100 $\mu\mathrm{m}$ rim operated at 1750 V and the other without rim at 1330 V, so that the initial gains for both are similar. Both results were obtained with Ar:CO_2 - 70:30 atmosphere and under Fe-55 source irradiation. [135]

on operational factors, such as the voltage applied on the electrodes and the irradiation rate, and on the geometrical parameters of the ThGEM used, but is typically achieved within minutes.

The long term evolution of the gain, on the other hand, shows a dramatic effect of the presence of a large rim (see figure 3.8 at the right). Gain fluctuations of a factor 5 are seen when a ThGEM with rim is under continuous irradiation, but are negligible if the rim is small. They also have opposite contributions, since large rims increase the gain over hours, while the absence of rim results in a ~20% decrease in the same period.

Depending on the rim's presence and size and on the recent history one can see different aspects of this gain fluctuation. In figure 3.9 it's evident the effect of large rims by comparison of the short term gain evolution of ThGEMs, either operated immediately after a voltage difference is applied to the electrodes, or after several hours at nominal voltage before the measurements. Without rim there is no visible difference between the two cases – it shows no memory. With a large rim and after 10 hours at nominal voltage without irradiation, the gain is initially an order of magnitude higher than the reference without irradiation or voltage history; in the first few minutes of operation the gain then steadily reduces to less than half the starting point. This is the short term behavior of the charging up merging with the long term base line.

It appears from these results that the long term fluctuation is not as much dependent on irradiation history as it is on application of the voltages. The qualitative understanding obtained so far seems to point to the displacement of charges in the PCB fiberglass due to the high voltage set as the cause of the effect. The presence of the rim is dramatic because in its absence the copper electrode shields the upper surface of the insulator, thus limiting the effects of the charge distribution therein.

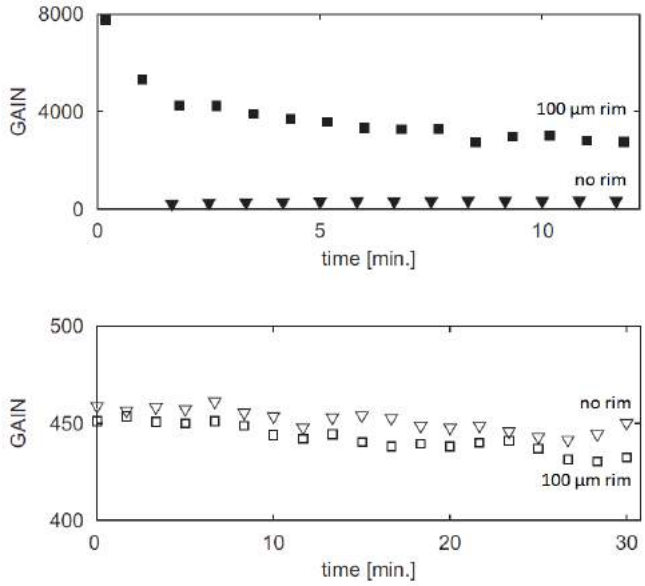

Figure 3.9 Short term gain evolution of two ThGEMs with different rim characteristics when irradiated immediately (bottom), or ten hours (top) after high voltage is applied to their electrodes. The ThGEMs are 0.4 mm thick, have 0.8 mm pitched 0.4 mm holes, and either 100 $\mu\mathrm{m}$ (squares) or no rim (triangles). [139, 140]

The huge gain variation and its dependence on the irradiation history clearly indicates that the use of large rim THGEMs should be avoided.

3.1.4 Electric fields for optimal photoelectron extraction

A ThGEM-based detector's operation and performance is mostly determined by the electric fields to which the electrons are subject to. Notwithstanding the literature having already quite a few insights into the different field regions, their role and the dependency on other aspects of the detector, a few investigations were performed under the scope of the research program to complement the existing knowledge, particularly for the fields that have an immediate relation to the photoelectron extraction efficiency: the drift field and the dipole field of the ThGEM.

The ThGEM dipole field has to be such that, for the chosen geometrical characteristics of the structure, the local electric field at the surface of the photocathode is enough to extract the photoelectrons. The weakest point of extraction is at the critical point, right at the center of the triangle made by neighboring holes, as already mentioned in 1.4.3. COMSOL Multiphysics® simulations were performed [141] that point to the need to use a thinner ThGEM (~0.4 mm) for CsI coating, in order to achieve the required normal field values of ~0.6 $\mathrm{kV/cm}$ at the critical point while keeping the previously set reference value of 1:2 hole diameter to pitch ratio [141]. This would imply that the contribution to the total gain of the detector required from the first multiplication stage is limited. This has the advantage of reducing the flow of ions produced in the avalanche

back to the photocathode.

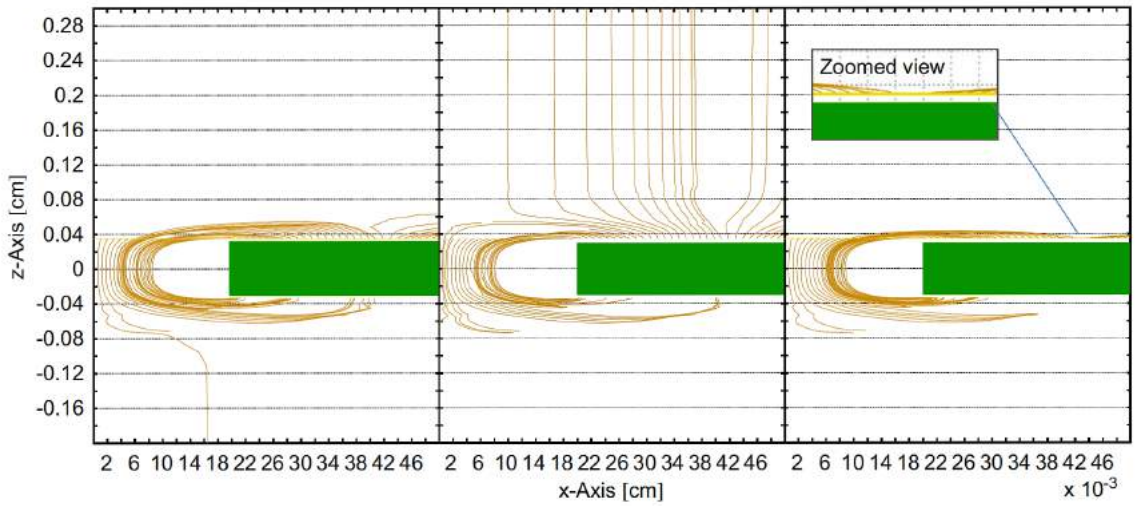

Figure 3.10 Photoelectron trajectories for three drift field configurations over a ThGEM with 0.4 mm holes (no rim), 0.8 mm pitch, 0.4 mm thickness and with an applied dipole field of 1.5 $\mathrm{kV/cm}$ on Ar:CO_2 - 70:30. The trajectories are given by the Garfield package for fields calculated using the Ansys package. Electron multiplication is switched off. Left: 0 $\mathrm{kV/cm}$ drift field. Center: -0.5 $\mathrm{kV/cm}$. Right: +0.5 $\mathrm{kV/cm}$. [142]

The drift field requires a different analysis. As figure 3.10 illustrates with electron trajectories, when the drift field is negative (pointing towards the photocathode) some of the electrons – especially the ones originating at the critical points – have the probability of being collected at the wire plane and are thus lost. On the opposite scenario, with a significant drift field pointing away from the photocathode, the dipole field at the critical point is countered and the effective local field might become too low for efficient photoelectron extraction. Between the two extremes, in a situation where the drift field is weak or lacking, all the field lines at the ThGEM's top surface lead to the holes and the photoelectron extraction efficiency is optimized.

The drift field effect should not be untangled from other defining characteristics of the ThGEM such as the rim or the dipole field set between the electrodes of the structure. Regarding the latter, the drift scans on figure 3.11 show that, as would be expected, a lower dipole field makes the effect of the drift field more pronounced, while higher nominal ThGEM voltages make it possible to apply larger drift fields before the local field at the surface of the photocathode becomes too low. As for the rim, the plots in figure 3.12 show, once again, reasons to favor the presence of small rim regions (or no rim at all) on the ThGEM structures used: when that is the case, the increase in drift field up to moderate values is met with stabilized detector gains and a fair energy resolution; with large rims, the resolution is significantly worse and the gain does not reach a stable value, pointing to incomplete electron collection. Between no rim and small rim configurations, the difference seems to be only significant at large drift field values, where the resolution of no rim ThGEM-based detectors starts to degrade.

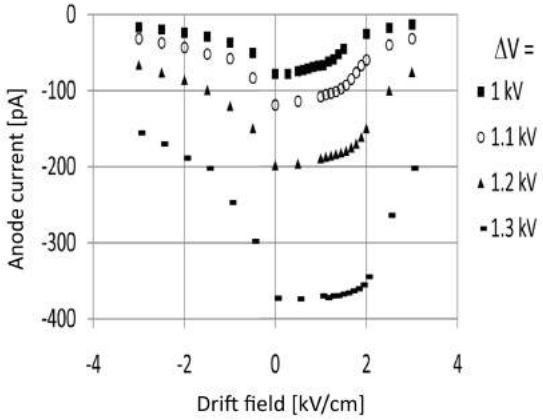

Figure 3.11 Measured current at the anode of a single ThGEM-based Ar:CH_4 - 66:34 flushed detector with a CsI photocathode, as a function of the drift field, for different sets of applied voltages between the electrodes of the structure. [134]

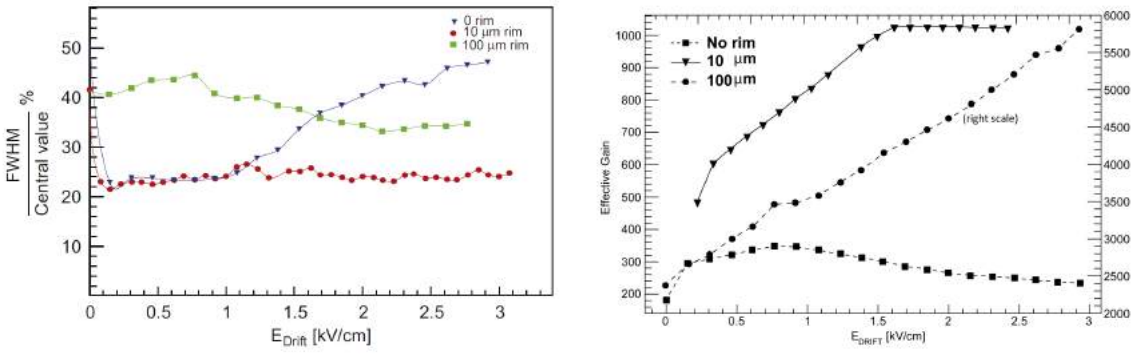

Figure 3.12 Left: energy resolution of the 5.9 keV peak of the spectrum obtained from an Fe-55 source in a single layer ThGEM detector as a function of the drift field, for three ThGEMs with different rims (hole diameter 0.3 mm, pitch 0.7 mm, thickness 0.4 mm). Right: the effective gain curve of the ThGEMs described on the left (the 100 $\mu\mathrm{m}$ rim ThGEM's curve is relative to the scale on the right.) [135, 140]

These studies point to the use, as standard photodetector configuration, of a null drift field to maximize photoelectron extraction. Even so, the studies also showed that the Hadron Blind Detector philosophy mentioned in section 1.4.2 might be applicable to our ThGEM-based detectors, since it was seen that mild reverse drift fields of few tens of $\mathrm{V/cm}$ don't have significant impact on the photoelectron extraction efficiency, but might be useful in reducing the region of collection of electrons resulting from ionizations when operating under MIP irradiation to less than $0.5\ \mathrm{mm}$ [143].

3.1.5 Ion Backflow

As mentioned previously in section 1.3.3, CsI photocathodes suffer from a decrease of quantum efficiency (aging) caused by the bombardment of ions originating in avalanche multiplication. The use of closed geometry detectors with reflective photocathodes naturally reduces the fraction of ions that reach the CsI layer when compared to open geometry detectors such as the MWPC. Among the third generation detectors, cascaded ThGEM structures typically show higher IBF than Micromegas or GEM detectors.

The improvement of IBF figures leads to better performances of the detectors, especially by allowing their operation at higher gains and for longer periods without noticeable degradation. Many options have been suggested to tackle the Ion Backflow issue in thick multipliers, some of which have been investigated [85, 144–146] by the research group in Trieste through experimental methods and simulations:

- the use of a ThCOBRA structure [87], inspired by the MHSP [147], which can replace ThGEM pieces in a cascaded detector. One of the faces of this structure has two electrodes – a cathode and a anode (see figure 3.13 at the left) – which distort the field lines, still enabling electrons to follow their expected path but capturing part of the ions flowing backwards;

- the introduction of a wire plane between ThGEMs, with the same effect of the extra ThCOBRA electrode. By distorting the field lines between cascaded ThGEMs, the ion cloud can be partially collected;

- the misalignment of the middle ThGEM in a triple cascaded configuration, similar to previous attempts with GEMs [148]. As illustrated in figure 3.14, a perfect mismatch between the hole lattice of the middle structure and the other two is established, which connects the field lines originating in the top of a ThGEM to the bottom electrodes of the structure above. Because ions follow the field lines they are trapped, while most electrons still find the path to the holes;

- the use of a *Flower* type of structure, as illustrated in figure 3.13 at the right. By replacing the middle ThGEM with a *Flower* architecture the misalignment between holes is maximized.

The ThCOBRA presented promising results, with IBF reduction to the ~5% level. However, the PCB production technology applied is complex and challenging to extend over the areas which are

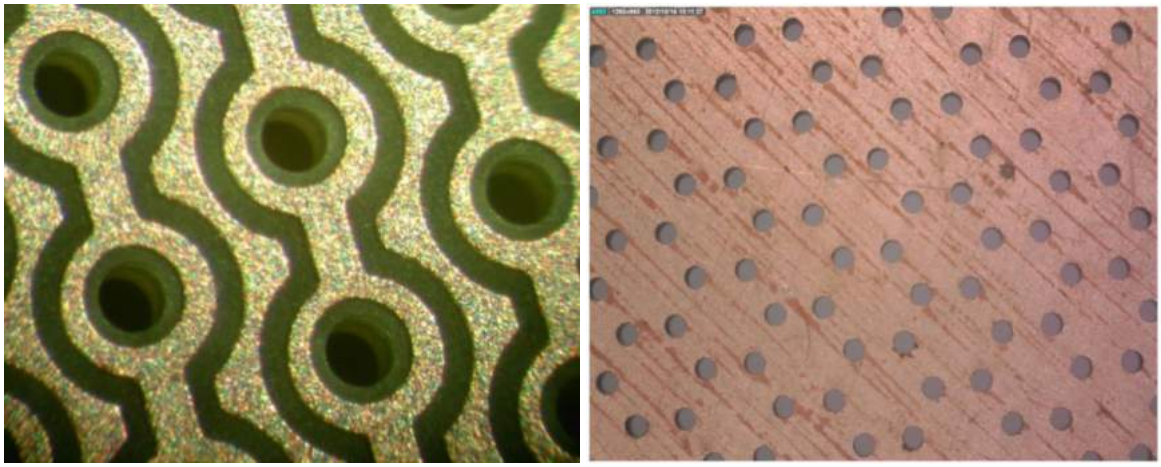

Figure 3.13 Left: photograph of a ThCOBRA structure, as seen from the face with two electrodes. Right: *Flower* ThGEM structure, where the holes are positioned to ensure the misalignment with other two ThGEMs in a cascaded configuration.

envisaged. Besides, it imposes some constrains in the hole diameter to pitch ratio in order to gain room for the separate electrode pistes.

Similarly, the wire plane approach presented acceptable results, but introduces an inconvenient level of complexity in the detector design that, to ensure proper efficiency of a large area device, would be quite limiting.

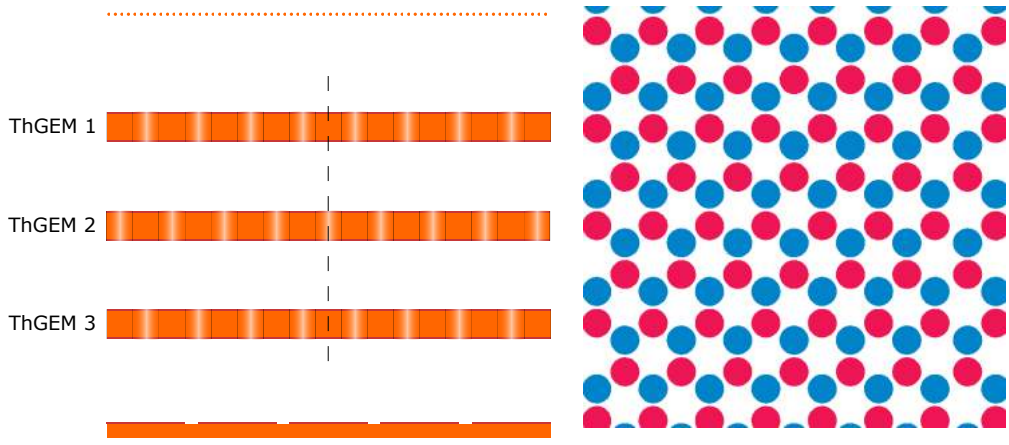

Figure 3.14 The misalignment of the middle ThGEM as show in the scheme at the left, leads to the projected hole pattern illustrated at the right, from a top perspective.

The results of the misalignment approach and of the use of the *Flower* structure are identical in terms of lowest IBF obtained, achieving values lower than 5%. However, the *Flower* configuration results in a diminished efficiency of the detector, with many electrons being also collected by its electrodes.

The best solution seems to be the use of the misaligned middle ThGEM. The IBF results are

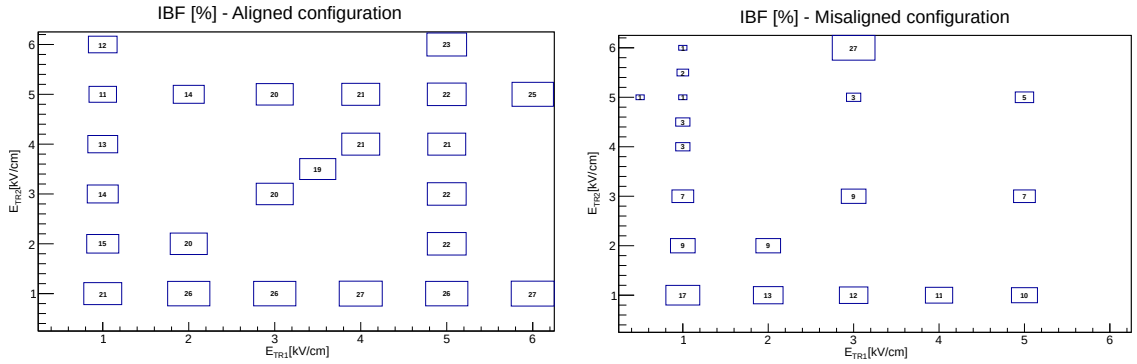

Figure 3.15 Plots of the IBF measurements for different combinations of first (E_{TR1}) and second transfer fields (E_{TR2}) for the aligned (left) and misaligned (right) configurations. For a E_{TR2}/E_{TR1} ratio of 4 in the misaligned configuration, the IBF gets as low as 3%. [85]

further improved by increasing the transfer field between the second and third ThGEMs, up to a value around 4 times higher than the first transfer field, leading to an IBF as low as 3%, as seen in figure 3.15 at the right. The only drawback of the staggering described is a noticed reduction in the gain measured by the detector.

Overall, the results point to the possibility of a cascaded ThGEM-based detector with IBF below 5%, thus able to greatly reduce the ion bombardment rate of CsI photocathodes compared to standard MWPC detectors, even when operated at gains one order of magnitude higher [85].

3.1.6 Conclusions drawn from the laboratory study of small ThGEMs

Considering the knowledge acquired from the results of the investigations undertaken and presented in the previous subsections, one can summarize the main conclusions and aspects to be considered when using ThGEM-based detectors, in particular for RICH applications:

- thicker ThGEMs tend to show higher maximum stable gains;
- the presence of a rim allows a ThGEM to achieve larger maximum stable gains;
- large rims (>40 μm) result in huge long term gain fluctuations, reduce the active photodetection area of the ThGEM and might compromise electron collection efficiency, thus being discarded in favor of smaller rims;
- the electrical fields at the critical points of the photocathode are typically low. To overcome this, thinner ThGEMs should be used for the photoconversion stage;
- a ratio between hole diameter and pitch of ~1/2 ensures >80% active photoconversion area while keeping the field at the photocathode adequate for efficient electron extraction;

- argon-based mixtures with CO_2 show larger avalanche gain than with CH_4, but result in less photoelectron extraction efficiency from the CsI;
- argon-based mixtures with CH_4 fraction higher than 1/3 show extraction figures which are close to optimal (i.e. pure methane);
- the best photoelectron extraction efficiency is obtained when the drift field is set to zero, but small values of tens of $\mathrm{V/cm}$ can be applied without major impact on it;
- the IBF can be kept as low as 5% with a staggered configuration where the middle ThGEM in a triple cascaded detector is misaligned with the other two;

3.2 Performance of 30 × 30 mm^2 ThGEM-based detectors under particle beam irradiation

The first test beams under the scope of this work had the goal of evaluating the performance of 30 × 30 mm^2 active area ThGEM-based detectors under beam conditions. For that purpose, a single detection chamber with room for four small detectors was assembled and used throughout test beam exercises up until 2012. This section compiles the most important results from those endeavors. The changes or differences between the exercises of different years have no relevant effects on the results, but they will be nonetheless clarified ahead when necessary.

The scheme of the chamber used can be seen in figure 3.19. One of the detector elements was a position sensitive R7600 M16 Hamamatsu multi-anode photomultiplier (MAPMT). The MAPMT uses a 18 × 18 mm^2 Bialkali photocathode and has a square array of 16 readout pads. The two side elements were ThGEM-based detectors (the top detector was not used).

In order to choose the ThGEM structures to be used, many were characterized by measuring their gain as a function of the applied voltage, which should increase exponentially (see figure 3.16); the ones achieving higher stable gains were selected. The characterization is done with Fe-55 irradiation of the single ThGEM detector shown in figure 3.4, filled with Ar:CO_2 - 70:30. The drift field was set at ~1 $\mathrm{kV/cm}$ to collect the primaries into the multiplication region. Two different ThGEM types were tested: one with 0.4 mm thickness and ~10 $\mu\mathrm{m}$ rim; the other with 0.8 mm thickness and <5 $\mu\mathrm{m}$ rim. All structures had 0.4 mm holes and 0.8 mm pitch.

The ThGEM-based detectors used in the final chamber are in a triple cascaded configuration, as illustrated on the left of figure 3.19. The second and third structures are 0.8 mm thick, while the first multiplication stage consists of one of the thinner ThGEMs. The reason for the use of a thin top ThGEM has been explained in the previous section, and has to do with the efficient extraction of photoelectrons. The top structures undergo the Ni-Au treatment so the CsI layer can be deposited and used as photocathode.

Before assembling the detector in the final chamber, laboratory tests in triple cascaded configuration are performed. A typical spectrum obtained with the detector in single photon

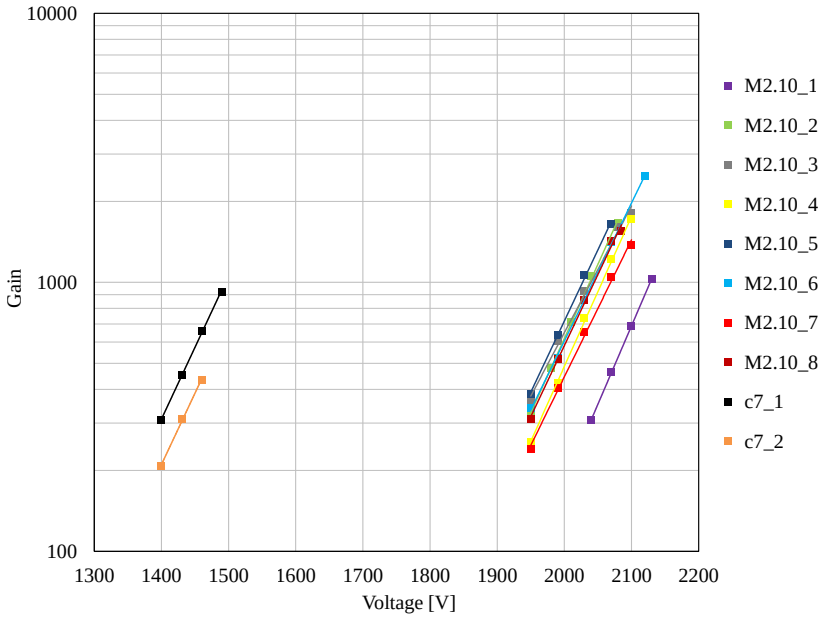

Figure 3.16 Characterization curves of some of the ThGEM pieces available. The two *c7* pieces at left part of the plot had 0.4 mm thickness, while the remaining had 0.8 mm thickness. The curves are obtained irradiating the Ar:CO_2 - 70:30 filled detector with the Fe-55 X-ray source.

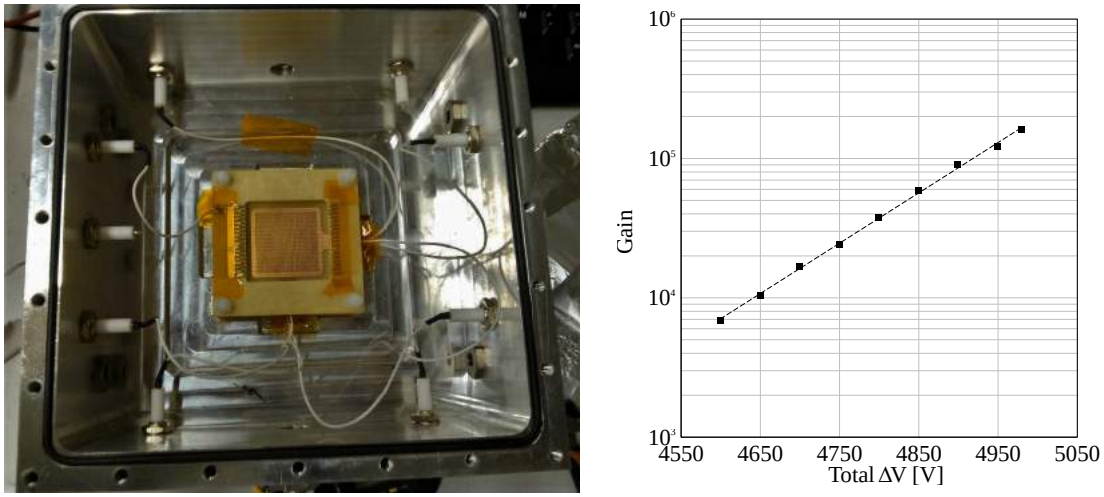

Figure 3.17 Left: photo of the chamber used to characterize the triple cascaded ThGEM detectors. Right: gain (from single photon spectrum) vs sum of the applied voltages on three ThGEMs in cascaded configuration, operated in Ar:CH_4 - 67:33 and with zero drift field applied.

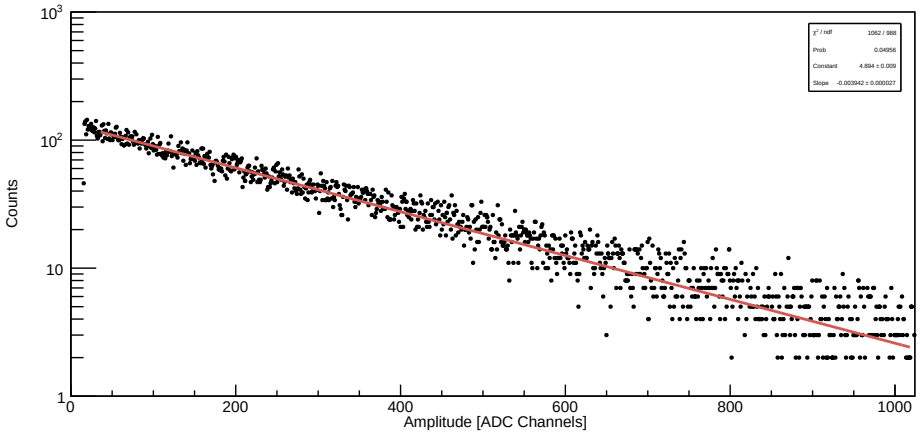

Figure 3.18 Single photon spectrum obtained with the UV LED and using the triple ThGEM cascaded detector. Gain estimated at ~10^5.

operation using UV light is shown in figure 3.18. As an example, figure 3.17 shows the characterization curve of one of the detectors using pulsed UV LED light. The exponential (linear in log scale) dependency of the gain with applied voltage is intact when moving from single to multiple ThGEM arrangements.

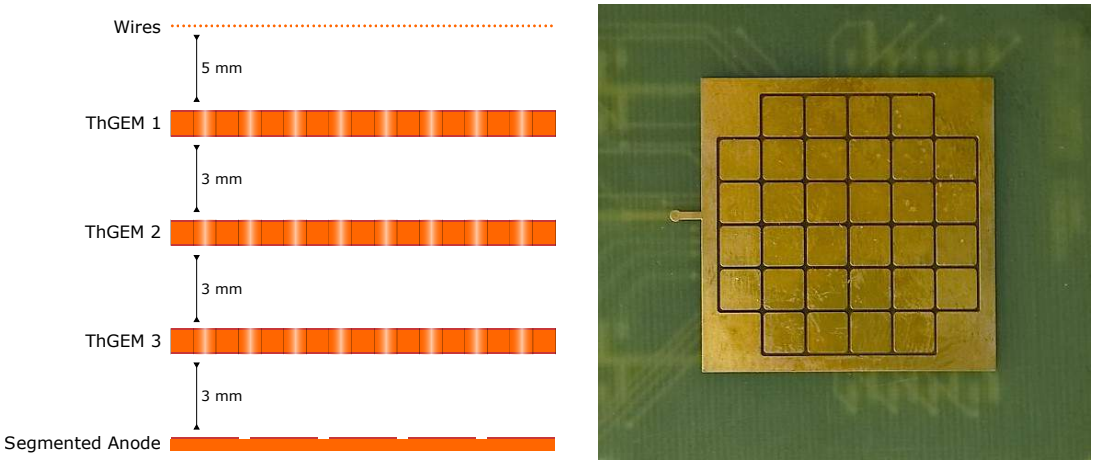

Figure 3.19 Left: the basic scheme of the triple ThGEM detector used in the test beams. Right: anode readout plane consisting of 32 pads, used in each of the ThGEM-based detectors.

3.2.1 Setup

A photo of the interior of the final chamber during detector assembly can be seen in figure 3.20. Missing from the chamber is the front cover which has a hemispheric silica radiator at its center: when the beam is focused in it, Cherenkov UV photons are emitted. The radiator is prepared with transmission slits so that the corona of possible light emission intercepts the center of the

three detectors, as illustrated in figure 3.21. This virtual corona has a radius of 147 $\pm$ 3 mm for wavelengths between 165 nm and 195 nm. The detector placement is such that the center of all detection planes of the three elements are at the same distance from the radiator.

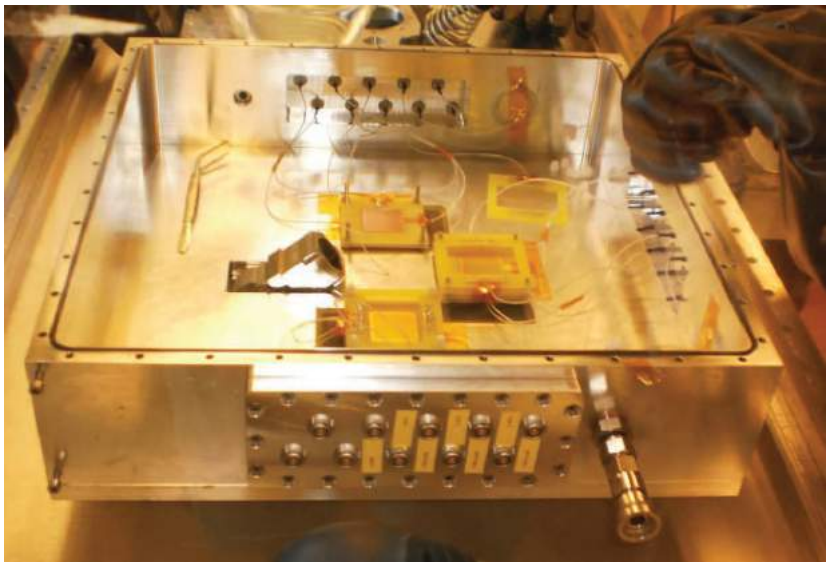

Figure 3.20 The inside of the detection chamber with its components, during the installation of the detectors. The CsI coated THGEMS require that special care is taken to always avoid exposure to air during transport and installation, so the assembly is performed inside a glove box with controlled atmosphere.

To supply the voltage required to establish the electric fields in the ThGEM, either manually controlled CAEN N471A or remotely controled CAEN 1471A power supplies were used. During the initial tests, in order to find the appropriate operation voltages, each electrode would be connected independently so that the voltages could be manually changed. Afterwards, appropriate resistive divider chains would be used: from a single voltage input supplied by a dedicated remote power supply, the chain returns the needed voltage settings to each of the relevant detector points (i.e. drift wires and tops and bottoms of ThGEMs 1, 2 and 3). This has the advantage of reducing the complexity of the whole setup, eliminating the uncertainty in the voltage values arising from the use of separate power supplies and easing the operation of the detector as a whole. Evidently, when an exercise requires the variation of a specific electrical field on the detector the corresponding electrodes are managed separately by dedicated power supply channels.

The analog data acquisition is achieved using the same equipment typically used in laboratory tests and described earlier in this chapter: with Cremat preamplifiers, Ortec amplifiers and Amptek ADMCA digitizers. The digital data acquisition, on the other hand, consists in a different philosophy specific for test beam endeavors, equal to the electronic readout used in the MAPMTs of COMPASS RICH-1: the MAPMT and the two THGEM-based photon detectors are operated at the same time

*The test beam facility is located between the Saleve and the Jura mountains near Geneva, so it was an intuitive nomenclature to use at the time.

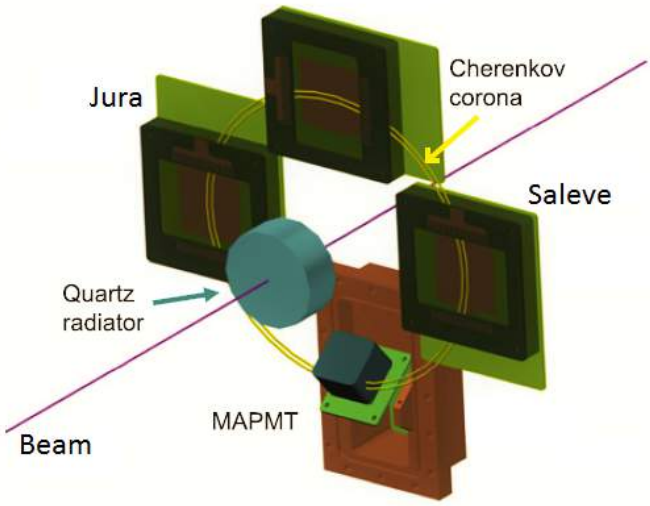

Figure 3.21 Disposition of the key elements used, including the radiator in the virtual beam line and the three detectors (the top detector is not used). From the beam particles point of view, the detector to the right is called Saleve and the one at the left is named Jura*.

using the electronic readout chain based on the CMAD preamplifier/discriminator front end chip and the F1-TDC chip, powered by low voltage power supplies; eight F1-TDC chips are part of one Dreisam board. Between the CMAD chips and the detector anode, protection boards with capacitors are used so the chips are spared in case of discharges. More details on the electronics used can be found in references such as [125], [126] and [127]. A picture of the front-end electronics volume used is shown in figure 3.22, and the modules assembled in the chamber can be seen in figure 3.23.

The digital data acquisition is triggered by using coincidence signals from two sets of scintillators (coupled to small PMTs) in the beam line, illustrated in figure 3.24. One set consists of paddles: two large area (10 × 10 cm^2) square scintillators; one of them is positioned in the front of the setup – it is the first element of the setup that a passing particle intercepts – and another at the very end of it, and they are pre-aligned with the expected beam trajectory. Their large areas allow for a rough alignment of the detection chamber and to measure the beam intensity. The other set consists of *fingers*: four small scintillators, each 5 × 3 mm^2 of cross section and 10 cm long; two of these are positioned after the first paddle, one of them vertically and the other horizontally; other two, in the same configuration, stay just before the last paddle. Their positions are remotely controlled so that, by monitoring the measured rate of signals produced, precise positioning of the beam can be determined, which then can be used for alignment purposes. A photograph showing the same scintillators used in a later exercise is present in figure 3.83.

For some of the tests, the 150 $\mathrm{GeV/c}$ π^+ beam at the CERN H4 line was used. On one occasion though, the chamber was used in the CERN PS T10 test beam facility with a π^+ beam of 6 $\mathrm{GeV/c}$.

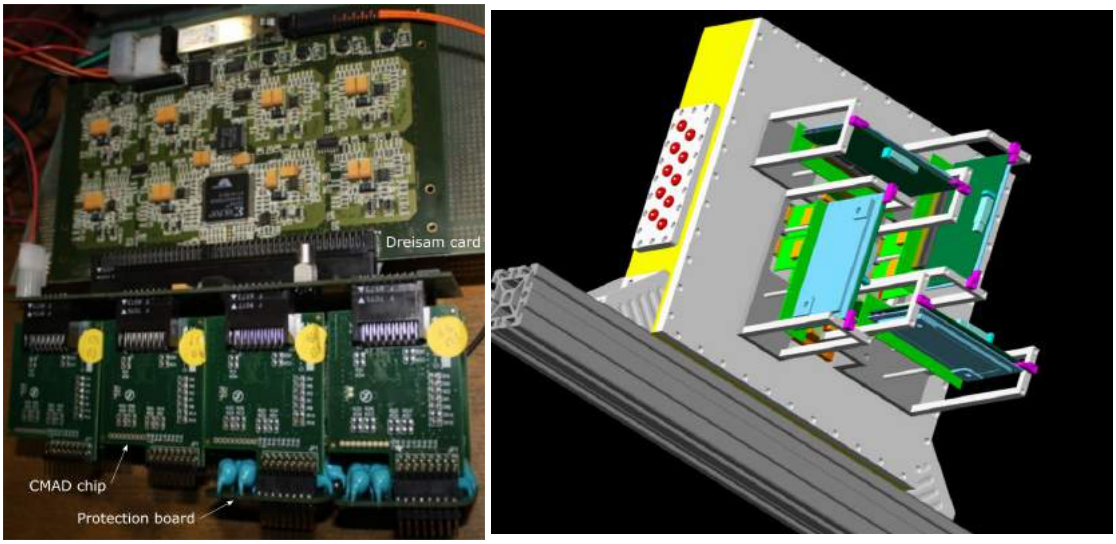

Figure 3.22 Left: picture of a front end electronic unit used with the discharge protections below, the CMAD chips and one Dreisam card above [149]. Right: illustration of the disposition of front end units on the back of the detection chamber.

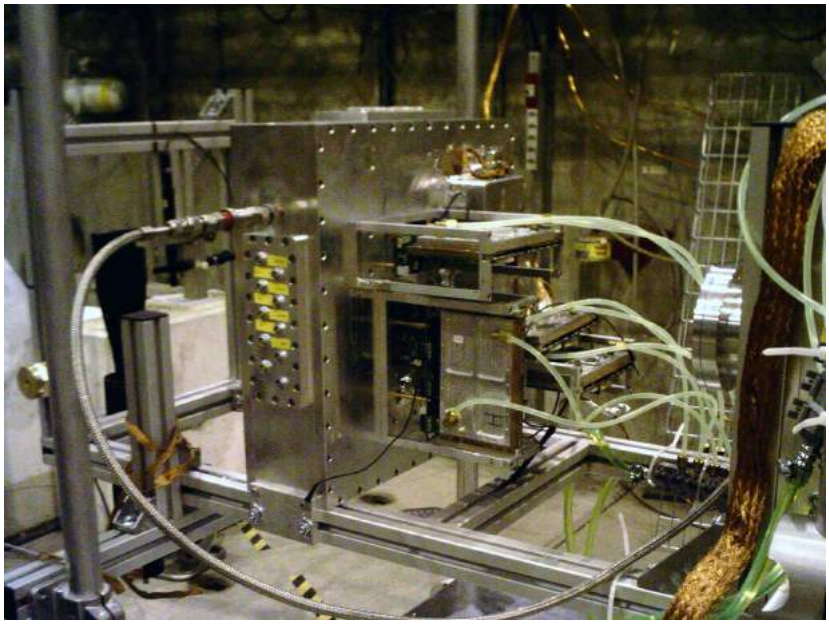

Figure 3.23 Photograph of the front end units on the back of the detector chamber.

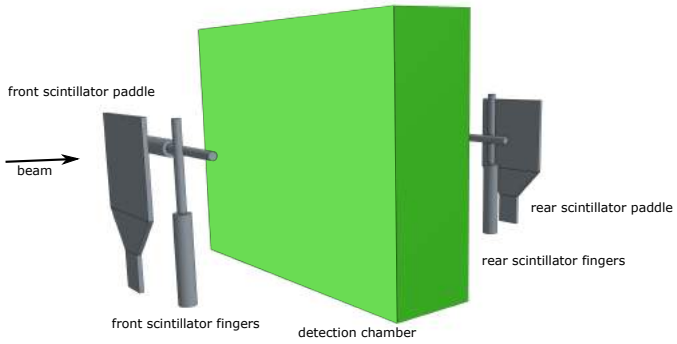

Figure 3.24 Scheme of the disposition of elements in the beam line.

The disposition of elements in the beam line specifically for the latter case is the one illustrated in section 3.4, since in the same exercise a chamber with a large ThGEM-based detector was also tested. Even so, for the present purposes of the exercises concerning the study of small detectors, the beam line can be illustrated by the scheme in figure 3.24.

The beam intensity is typically of the order of 10^3 particles per spill, and the spills usually last only a few seconds. A wire chamber was used to measure the dimensions of the beam profile, indicating that its particles are almost all confined to a spot whose diameter is roughly 3.5 cm.

3.2.2 Results

The ThGEM detectors were operated in stable condition, under beam irradiation, at gains of ~10^5 in mixtures of Ar:CH_4 - 50:50. Such gain is lower than the one achieved in laboratory conditions, an expected result since a small fraction of the beam's particles are anyhow crossing the detectors and make them less stable.

Cherenkov photons emitted from the radiator are clearly detected. Figure 3.25 shows the accumulation of several triggered hits with the 150 $\mathrm{GeV/c}$ π^+ beam centered on the radiator. On the right of that image, a virtual corona of the expected ring is superimposed to the events, matching quite accurately.

A pertinent analysis of the data to confirm the nature of the events detected is the study of the multiplicity, i.e. the number of detected hits per trigger. With the beam aligned with the radiator, the vast majority of its particles cross the chamber far from each detector (right between them), so direct beam particle hits have low probability of occurrence, i.e. should result in low (<<1) multiplicity. Since, according to the histogram of figure 3.26, more than 30% of the events have multiplicity ≥ 1, the hits are most likely Cherenkov photons, especially taking into account their occurrence in the expected position of the corona. The measured multiplicity is an encouraging result if it is taken into account that only a small fraction of the ring is actually being detected.

An important aspect that requires attention is the time response of the detectors. Figure 3.27 shows the time histogram of the events detected by the MAPMT and the ThGEM-based detector:

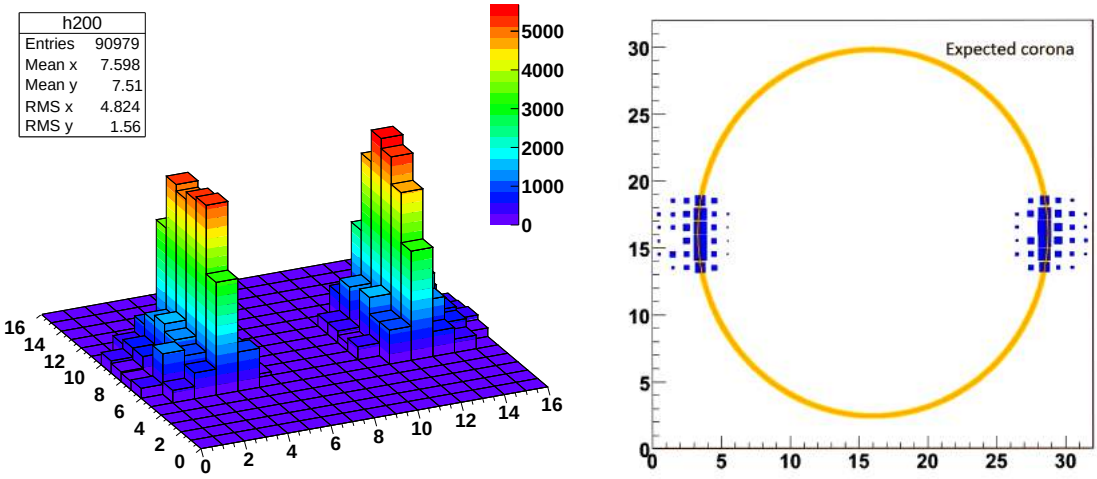

Figure 3.25 Left: 3D pile-up of events collected by the two THGEM-based detectors, with two side arcs of the corona clearly detected [141]. Right: 2D projection of the left histogram with the expected corona of radiator emission superimposed, showing good agreement [150]. The events were collected at ~10^5 gain.

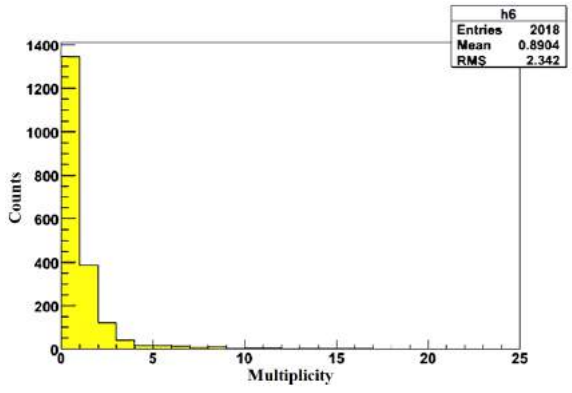

Figure 3.26 Multiplicity histogram of events in the Jura chamber with beam on the radiator and 4.35 kV of total applied ΔV on the three ThGEMs.

the response of the ThGEM detectors is seen to be around 130 ns in respect to the PMT reference. The PMT's time response, on the other hand, is much faster (typically ~12 ns) because the electrons travel in vacuum. The global time response of the ThGEM detector can then be estimated to be around 142 ns. If one considers that the electron speed in a gaseous mixture of the kind used subject to a field of 1.5 $\mathrm{kV/cm}$ is ~8 × 10^6 $\mathrm{cm/s}$ [141], the expected transit time for the detector's vertical size (~1.1 cm) is 138 ns. This is close to the measured time response.

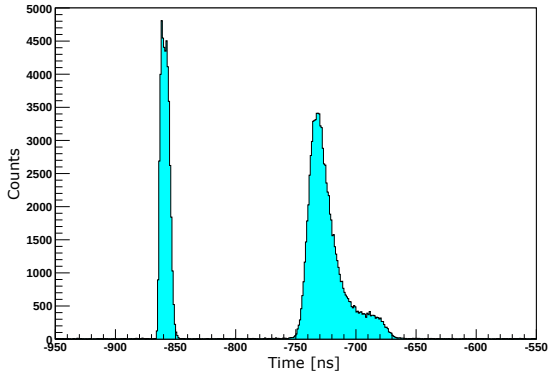

Figure 3.27 Time response of the detectors, in a relative scale. The events detected by the MAPMT appear at the left – i.e. sooner – followed ~130 ns later by the photons detected by the ThGEM. [150]

The profile of the time response of the ThGEM detectors reveal that there is a slower component of the signal after the gaussian peak. By increasing the voltage difference across the CsI coated ThGEM (ThGEM1), one observes a narrowing of the time distribution, with the slower response contribution significantly reduced, as evidenced in the plots in figure 3.28. With that in mind, and considering the knowledge from simulations of the electric fields on the photocathode surface, as well as the expected drift velocity of electrons in the gas mixture used, it seems likely that the slower portion of the signal is related to regions of weak electric field strength, in particular on the critical point of the photocathode. By increasing the voltage difference on the first ThGEM the local field is increased, a faster extraction of photoelectrons is achieved, and the timing resolution is improved down to ~7 ns. Due to the correlation between the field strength at the critical point and the extraction efficiency of the photocathode, the analysis of the timing histograms of the detectors allows one to monitor and ensure that proper photoelectron extraction efficiency is achieved.

To remove any doubt that the effect observed is strictly related to the photoelectron extraction, a test with the LED light source was done whose result can be seen in figure 3.29, with the detector at the same voltages used for the measurement at the left of figure 3.28. The time distribution of LED generated events, despite small differences which are expected, shows the same non-gaussian delayed portion of the signal mentioned above, thus confirming that such effect is present in photon-induced events without beam irradiation.

Confirmed the possibility of Cherenkov light detection with the ThGEM-based detectors, a few

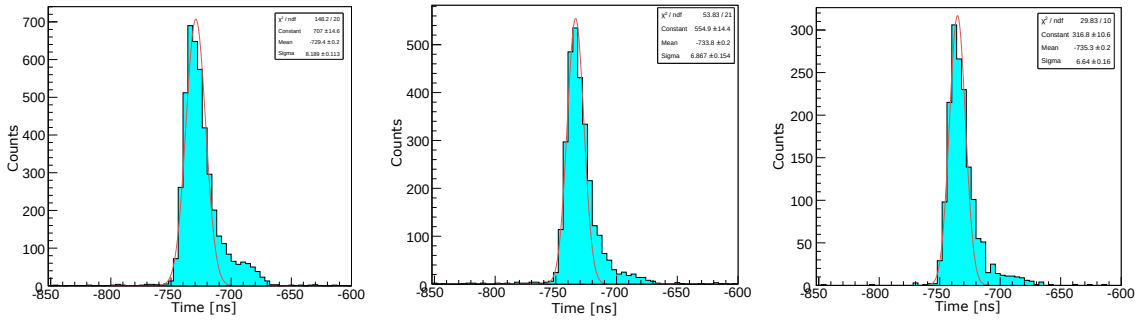

Figure 3.28 Time response of the ThGEM-based detectors for three different voltages across the first ThGEM. A voltage increase of 180 V caused the reduction of the slow component of the signal from 23% to 6% of all the events. The gain of the highest voltage configuration is ~2 × 10^5, and corresponds to a total ΔV of 4.53 kV.

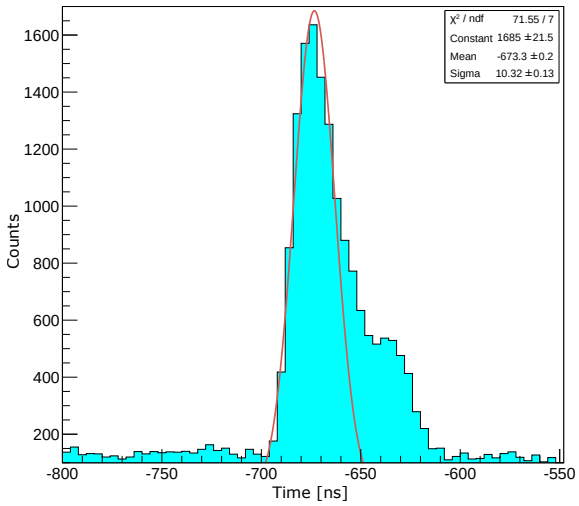

Figure 3.29 Time response of the detector with UV LED irradiation, to be compared with the same plot for Cherenkov photons which can be seen in figure 3.28. The time axis is only to be considered in a relative scale, since the actual values are related to how the triggering is done.

additional inspections were done regarding their operation under MIP irradiation, in particular to study the possibility of using a reverse bias to achieve a hadron blind configuration. The following exercises were performed under 6 $\mathrm{GeV/c}$ π^+ beam and with the detection chamber flushed with Ar:CH_4 - 60:40.

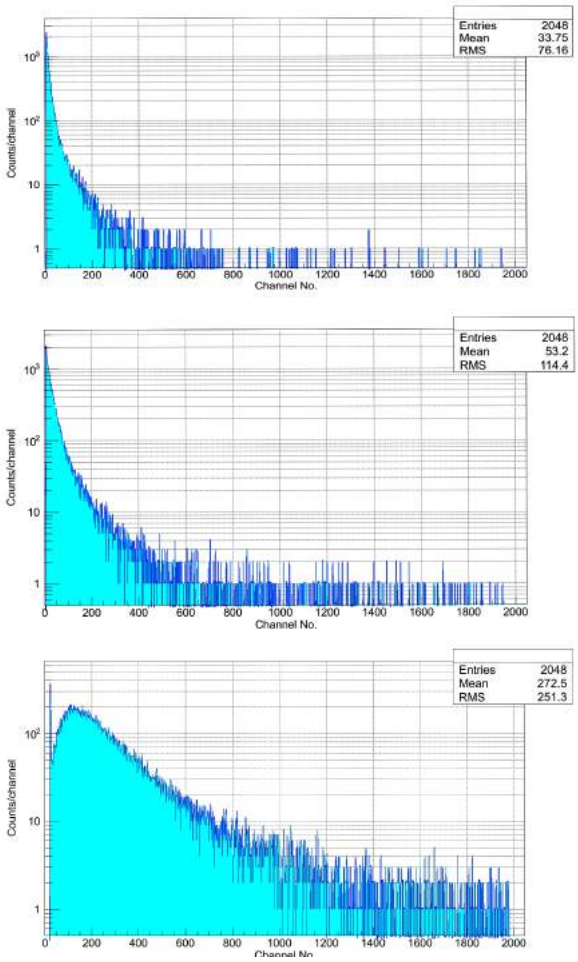

Figure 3.30 Amplitude spectra from the Saleve detector when it is aligned with the beam, for three different drift field configurations of -2 $\mathrm{kV/cm}$ (top), 0 $\mathrm{kV/cm}$ (middle) and +2 $\mathrm{kV/cm}$ (bottom). The last histogram shows a Landau distribution, as expected for the deposition of energy by the beam particles.

The detector was realigned so the beam path is centered on one of the ThGEM-based detectors (Saleve), so no Cherenkov light is produced, only primaries from the interaction of beam particles. In that configuration, a drift scan was performed, varying the voltage applied to the drift wires. To efficiently collect the charge generated by the beam particles, a positive drift field has to be applied (the same was done when using the Fe-55 source on the laboratory). The bottom plot on figure 3.30 is the histogram obtained with the analog readout chain precisely for that configuration. The spectrum follows the expected Landau distribution, with the noticeable peak, or MPV. With a null or reversed field, as anticipated, the majority of the charges generated by the ionization of the gas

are dragged to the drift wires and are not collected, resulting in a less populated spectrum such as the one shown in figure 3.30 at the top.

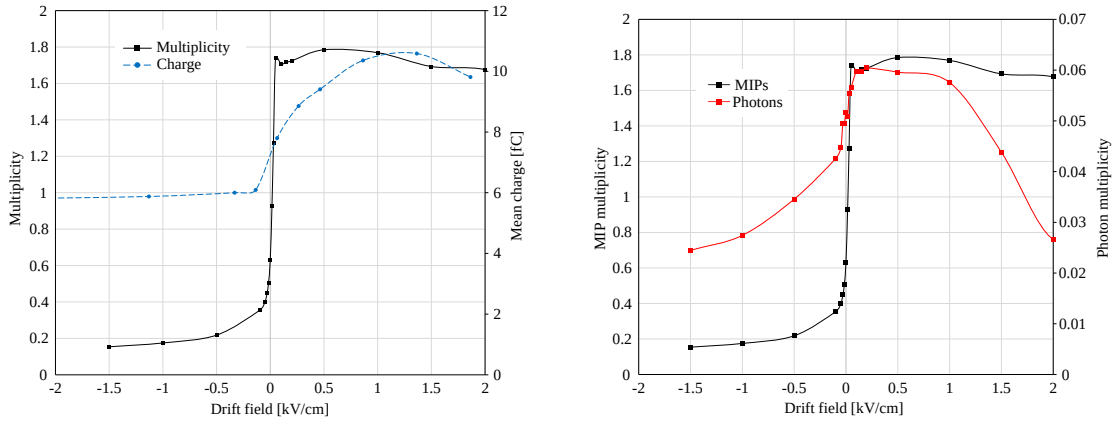

Figure 3.31 Left: drift scans of the ThGEM-based detector with the analog (average charge) and digital (multiplicity) acquisition chains show similar results, even though the average charge seems to increase less abruptly. Right: comparison between MIP and photon multiplicity drift scans points to the validity of the reverse bias approach, since the MIP multiplicity reduction is much sharper.

In many of the spectra – in fact until a positive drift field is applied – the MPV of the Landau is not visible, so in order to perform a drift scan and quantitatively interpret the results a different variable has to be chosen. Figure 3.31 at the left gives two possibilities: with the analog readout chain, the average charge value of the spectrum is used; if, on the other hand, one uses the digital acquisition system, the multiplicity of each trigger event shows similar results. Both curves lead to the same conclusions, but the multiplicity is a more convenient figure because it can also be obtained for Cherenkov light detection with the digital acquisition. Besides, as mentioned earlier, the statistical fluctuations of the average energy deposited by a crossing MIP are very high, which makes the average charge a poor estimate of the Landau's MPV dependency. Figure 3.31 at the right compares the drift scan of the multiplicity of MIP generated events with the multiplicity of Cherenkov photons, the latter obtained with the beam aligned with the radiator. Using a mildly reversed drift field, the photon multiplicity is moderately reduced, while the MIP-generated hits drop sharply.

Concluding, the $30 \times 30\ \mathrm{mm}^2$ active area ThGEM-based detectors successfully operate as RICH counters in beam environments, with satisfying gains. The possibility of implementing the Hadron Blind philosophy in ThGEMs was encouraged by some of the tests performed. As for the time response of the detectors, it raised some concerns regarding the photoelectron extraction efficiency. This can be solved by an increase in the voltage applied to the detector, at the risk of compromising some of its stability.

3.3 Development of 300 × 300 mm^2 ThGEM-based Detectors

Having reached a satisfying understanding of the most important factors determining the performance of 30 × 30 mm^2 ThGEM detectors, research was then oriented towards the up-scaling of the structures, namely in achieving comparable results with 300 × 300 mm^2 active area detectors.

In order to extend the dimensions of the ThGEM pieces one is promptly faced with structural difficulties, since the same thickness of the smaller structures is desired but over a plane a hundred times larger. At that scale some of the PCB self sustainability is lost, so to achieve good planarity some auxiliary holes have to be added to allow for supporting pillars. The pillars, as well as the border blocks later used for the same purpose in the triple cascaded detectors, are made of PEEK (Polyether-Ether-Ketone).

Another issue that arises has to do with the electrostatic characteristics of the pieces. The larger surface of the copper electrodes would imply an increase in capacitance equivalent to the increase in area. This has implications in the detector behavior, namely in terms of danger to the electronic readout chain: a much larger charge is accumulated in the structure; the stored energy, in the event of a discharge, might be channeled to the readout chips with damaging effects; the segmentation of electrodes is thus required. Another advantage of the segmentation is that it allows different voltages to be applied to the sectors: larger structures are often limited in their maximum achieved gain by their weakest points; by keeping those sectors which are frequently discharging at a lower voltage, the ThGEM can still be operated at higher gains on the remaining sectors.

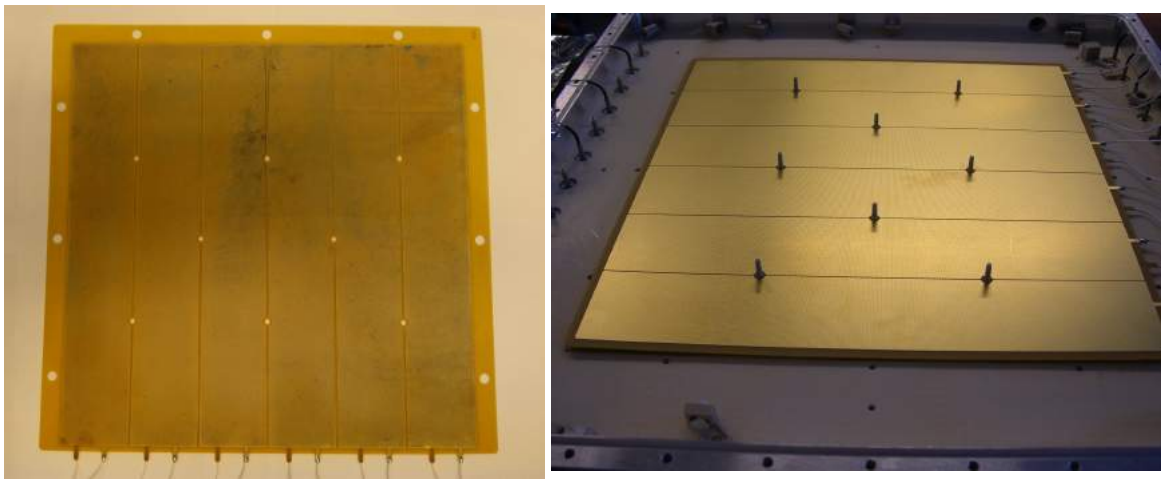

Figure 3.32 Left: photo of a 300 × 300 mm^2 active area ThGEM. Right: ThGEM in the detector chamber, held with supporting pillars.

After studying several pieces with alternative geometries, the design settled in ThGEMs segmented in 6 sectors of 48 mm width, separated by an 0.8 mm copper-free space, thus reducing the electrical coupling and limiting discharge propagations between sectors. Figure 3.32 shows a picture of a typical 300 × 300 mm^2 ThGEM developed. It was produced by Eltos S.p.a. using FR-4

Halogen-free Glass Epoxy Laminate [†] with 35 μm thick copper surfaces.

After receiving and testing the first batches of larger area ThGEMs industrially produced, it was apparent that the success achieved in the production of high quality small pieces was still far from being extrapolated to bigger areas while keeping under control the presence of defects and the uniformity. It was particularly evident that the maximum voltage the pieces were able to sustain without frequent discharges was far from what the smaller prototypes had exhibited, clearly below expectations.

To progress further, several steps of the production of larger ThGEMs were taken under control of the research group, in particular, the selection of the PCB boards used to produce the ThGEMs, the choice of production techniques and finally, the establishment of post-production treatments that remove imperfections and remains left by the industrial production process.

3.3.1 PCB foil selection

One of the most important factors that influences the quality of a large ThGEM is the gain uniformity over its area, since it is not only an indicator of uneven response of the future detector, but also because the maximum voltage that one can apply to the whole structure might be limited by the thickness of a small section. Because of that, producing ThGEMs with very even thickness over all their area is an important goal, which requires assuming control over the selection of the PCB boards that are then used to produce the structures.

The thickness uniformity of large 700 × 400 mm^2 PCB boards was inspected with a Mitutoyo digital micrometer in a setup that can be seen at the left of figure 3.33. Due to the mechanical mounting structure and the measurement procedure, the overall precision of the setup is in the order of 5 μm. A total of 75 foils of PCB with thicknesses of 0.4, 0.6 and 0.8 mm were measured in equally distributed points over their area. The relative thickness range, *(Maximum thickness - Minimum thickness) / Minimum thickness*, was defined as the *figure of merit* for the foils.

The results of the measurements confirmed the existence of relevant variations in thickness of the PCB boards used – frequently >5% – which then translate to the produced ThGEMs. It is interesting to note that such non uniformities are not random irregularities between neighbor points, but instead almost always a smooth monotonic gradient over the whole area of the PCB board. This points to a systematic bias in the production of the foils. It is also apparent that the quality of the produced foils is not independent of the nominal thickness: for foils of 0.4 mm nominal thickness only 3 of 26 foils present variation below 2%; for 0.8 mm thickness there are 2, while for 0.6 mm there are 8 good pieces. As an example, the histogram of the variance found after the inspection of some 0.4 mm thick PCB foils is shown in figure 3.35. After careful measurement and evaluation of the results, only a few of the foils were approved for use: the ThGEMs were produced from PCB boards with <3% of thickness tolerance.

[†] R-1566W by Panasonic Corporation or DURAVER-E-Cu 156 ML by Isola GmbH

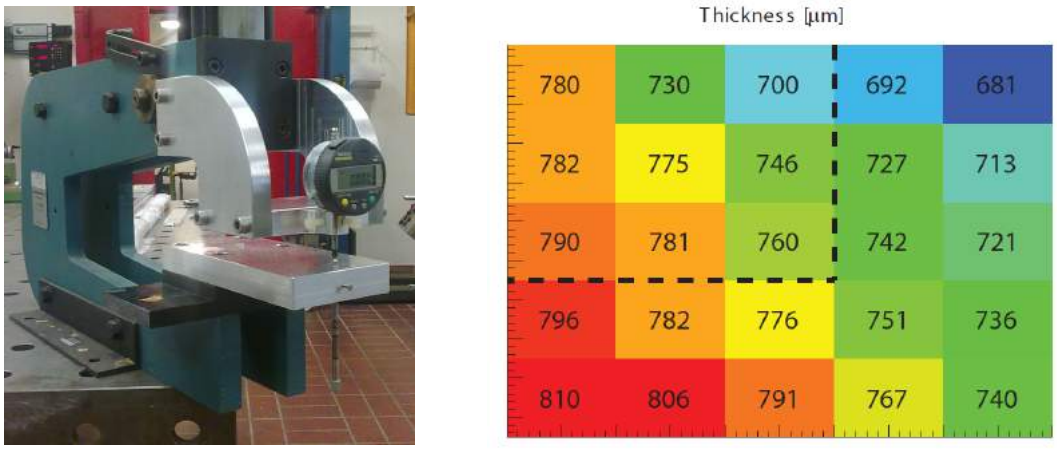

Figure 3.33 The PCB boards are measured using a Mitutoyo C112B digital micrometer with aligned sphere-to-sphere contact (left). At the right, example of a uniformity plot measured with the micrometer, and detail of a section selected for ThGEM production.

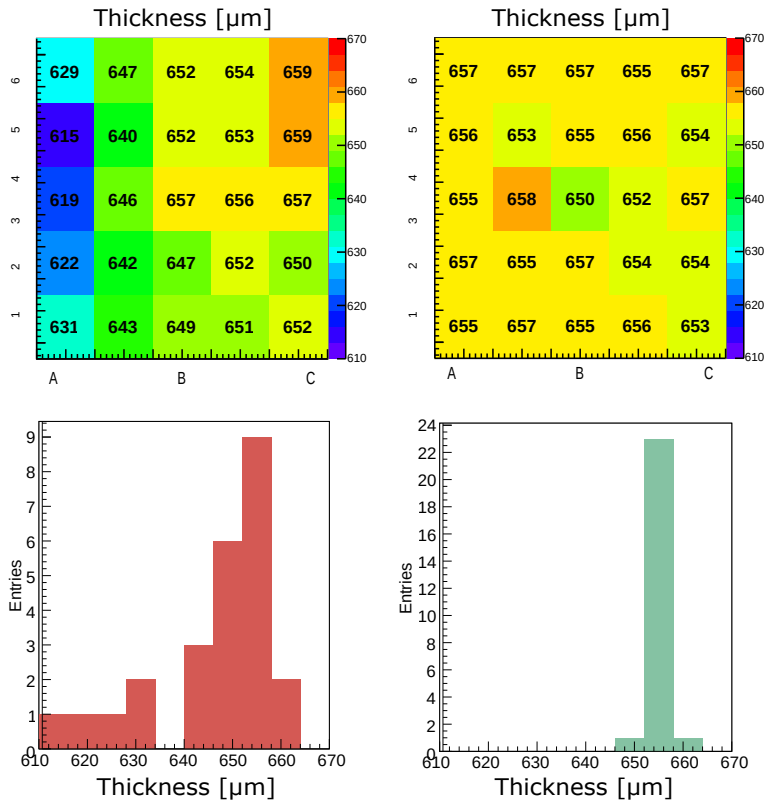

Figure 3.34 Examples of two inspected 0.6 mm thick PCB foils. Some pieces can have huge gradients of thickness, such as the one on the left, while a few are very uniform (right).

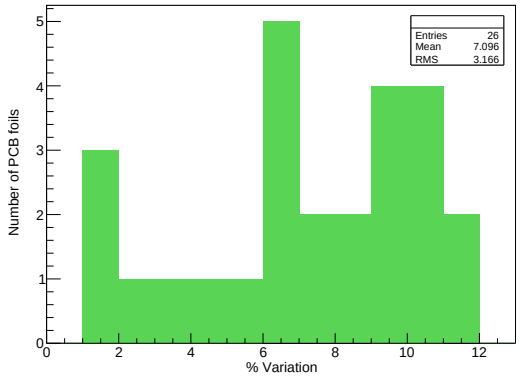

Figure 3.35 Histogram of the thickness variation of 0.4 mm thick PCB foils. Only 3 pieces among 26 show variance below 3%.

Studies regarding the choice of the insulator material were also performed. The production of ThGEMs with different types of Halogen-free epoxy laminated fiberglass was tried, specifically the following materials:

- ISOLA FR4, type Duraver E-CU 156;
- Panasonic FR4, type R-1551W;
- Permaglass CEM3, TE 630;
- APICAL[‡], type AV.

The pieces produced with APICAL AV (similar to Kapton®) showed poor stiffness and self sustaining properties. As for Permaglass, the production method limits the thickness of the foils to a minimum value of 1 mm, so the boards then have to be milled to the intended ThGEM thickness. This, and the requirement of a special glue to attach the copper electrodes, increases the cost of the foil production and makes it a poor choice for our goals, even if the resulting boards are very uniform. Therefore, these two insulator materials were rejected. In the end, no major difference between using ISOLA and Panasonic fiberglass was seen for the tested applications, so the distinction was made based on secondary criteria, and the choice fell on Panasonic for most of our 300 × 300 mm^2 pieces.

3.3.2 ThGEM production

After the measurement and selection of the best PCB boards, they are sent to Eltos S.p.a. to produce the ThGEM structures. There are three important alternative production methods that were considered as possible solutions to achieve the best large area structures. The most traditional method, illustrated at the left of figure 3.36, consists in the application of a photoresist (light blue)

[‡]Kaneka Corporation

followed by etching of electrodes and the rim region. Only after this step the holes are drilled. The resulting large area ThGEM is often defective, showing a persistent misalignment between the etched rim circumferences and the center of the holes, as visible in figure 3.37 at the left, and so it must be discarded.

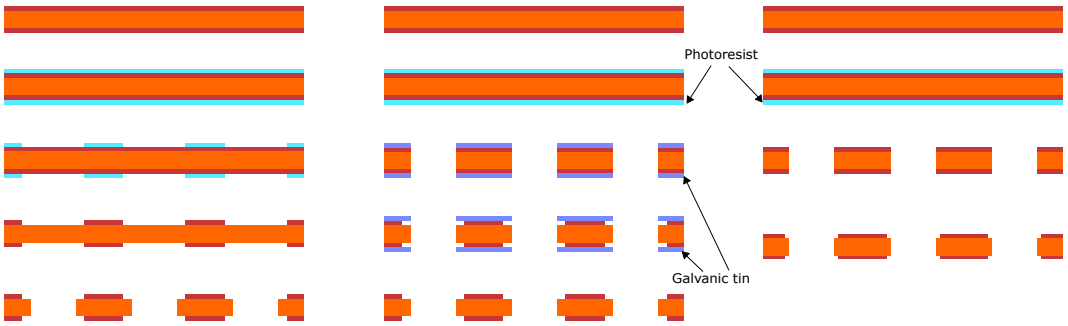

Figure 3.36 Illustration of the different ThGEM production methods: traditional (left), small rim (center) and global micro-etching (right). The one adopted for the production of large structures is the global etching procedure. See text for descriptions.

Production techniques for large rims are not ideal due to the gain instability their presence introduces (see section 3.1.3). On the other hand, a small rim technique (see center of figure 3.36) is available where the drilling of the ThGEM holes is done before the electrode etching. Then, the photoresist is replaced by a 20 $\mu\mathrm{m}$ galvanic tin layer, and the piece is subject to a chemical etching attack which slowly erases the exposed regions of copper near the holes, creating the rims. This results in much better hole/rim alignment than in the traditional method. However, rim size uniformity is limited to small regions not bigger than 30 × 30 mm^2. Attempting to use this technique in bigger structures leads to non-uniformity of the rim dimensions over the surface and between samples.

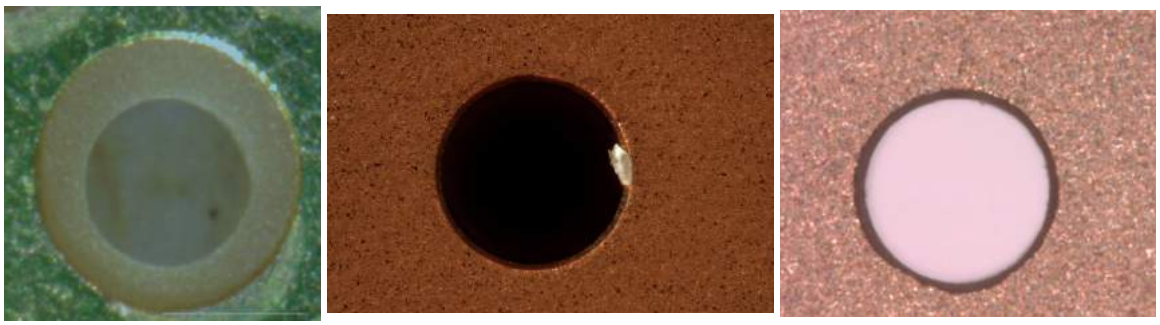

Figure 3.37 Examples of production defects: misaligned rims (left), metallic remnants (center) and rim irregularities caused by glue remnants which interfere in the etching process (right).

The technique of global micro-etching, illustrated in figure 3.36 at the right, was found to be the best option. It is quite reliable and produces very good results in small samples. The printed circuit

board with copper in each side is covered with a photoresist and the electrode shapes are etched, with the different sectors and connection pistes, but no holes. After removing the photoresist the holes are drilled, with the drilling head being replaced every 1000 holes for optimal results. Finally, the piece is subject to a mild etching procedure to remove drill remnants, simultaneously creating a tiny rim (~10 μm) ideal for our applications. A final desmearing procedure is used to remove the glue left from the copper gluing. Large area ThGEMs produced by global micro-etching are of high quality in terms of geometrical uniformity, but still reveal the presence of some remnants and imperfections (see figure 3.37 at the center and right for two examples). Partially as a consequence of that, the maximum voltage that the piece could sustain with moderate discharge rate was far below expectations.

In order to solve those issues, post-production treatments had to be sought in order to remove the said remnants and irregularities. One treatment considered in the attempts to increase the performance of ThGEMs, and studied by other groups as well, was the coating of the structures with a polyurethane mask. In principle, this organic insulator coating masks some of the weak points of the electrodes and stretches the maximum voltage that the ThGEM can handle in stable conditions, but the tests pointed to undesirable side effects to this approach, such as charging-up effects. Since no significant improvement was verified, this solution was discard.

With the help of the TS-DEM-PMT[§] laboratory at CERN, a post-production treatment was implemented consisting in chemical etching with acidic baths and thermal processes [151]. The treatment has the effect of reducing significantly the presence of remains and irregularities on ThGEMs, but the resulting structures are nonetheless far from the expected performance (see the next subsection for details on how the ThGEMs are evaluated).

Figure 3.38 Left: polishing of a ThGEM with pumice poweder to smoothen hole edges and reduce defects. Right: after the ultrasonic bath, the ThGEM is washed in demineralized water.

[§]Technical Support Department, Development of Electronic Modules, Photolithography and Microconnectics Technologies

A complementary procedure was then adopted based on a harsh surface treatment by a long polishing process: the ThGEMs are brushed (see at the left on figure 3.38) with Hinrichs pumice powder of typical grain size thinner than 40 $\mu\mathrm{m}$. At the end, a high pressure water bath is required to clean the piece and remove the powder residuals. It is followed by a long – roughly one hour – ultrasonic bath at 50 $^{\circ}\mathrm{C}$ in a strongly basic aqueous solution of Sonica PCB, responsible for a mild chemical attack to the copper surface, smoothening the hole edges and removing possible metallic residuals which may have been left by the processes. The procedure concludes with a bath in demineralized water (see the right of figure 3.38) followed by 24 hours on a oven where the ThGEM dries at ~80 $^{\circ}\mathrm{C}$.

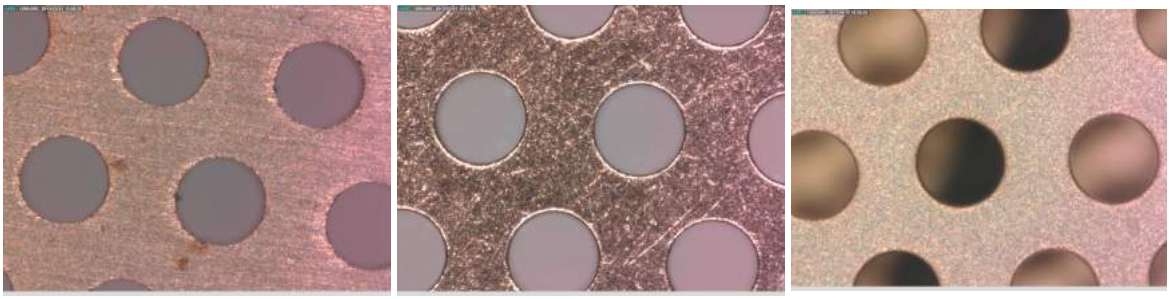

Figure 3.39 Comparison of the aspect of the ThGEM surface throughout the treatment process, seen on the microscope. The original piece after production (left) sees the hole irregularities soften by the polishing treatment (center), and the ultrasonic bath finally leads to a smooth electrode surface (right).

Figure 3.39 shows the effect of the additional polishing treatment seen on the microscope: after each step, the holes become more uniform and even with dull edges and the copper surface gets smoother. The results on figure 3.40 prove that the treatment is effective in increasing the maximum voltage that the ThGEMs can sustain to values close to the Paschen limit (details in the next subsection).

3.3.3 Characterization of 300 × 300 mm^2 ThGEMs

A set of tests was implemented to evaluate the merit of the treatments being introduced, and later to choose the best 300 × 300 mm^2 ThGEMs to be used in triple cascaded detectors and tested in beam conditions. These tests included careful and systematic optical inspection with a Dino-Lite AM7013 MZT microscope to detect defects and non uniformities.

One of the most crucial tests to evaluate the quality of a ThGEM piece, used throughout this work, is the check of maximum voltage that the piece can sustain without recurrent electrical discharges. Typically, this test was performed in air, in a box specific for the purpose, where two connectors allow for the application of high voltages from a CAEN N471A channel to a ThGEM's sector. As the voltage is increased past a certain threshold, the frequency of electric discharges or *trips* raises: the maximum stable voltage is typically defined as the one at which the ThGEM sparks

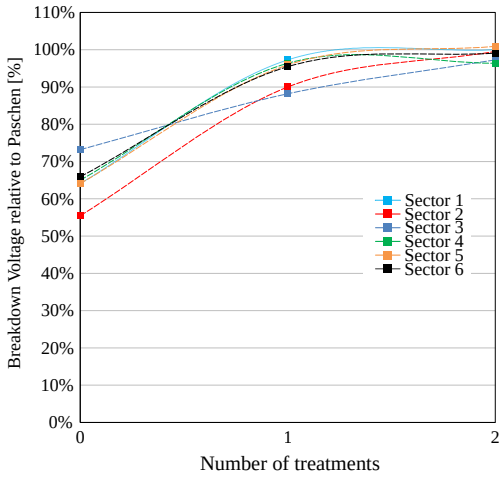

Figure 3.40 Effect of two consecutive treatments, evaluated with the Paschen test. For this test, the Paschen limit was expected to be ~2200 V.

only twice within one minute.

This test is commonly referred to as a Paschen check, since the goodness of a ThGEM piece is usually compared to the voltage predicted by Paschen's law. This law states that the breakdown voltage V_{bd} (in kV) between two electrodes in a specific gas medium is a function of the product of gas pressure p (in torr) and the distance that separates the electrodes d (in cm) [152, 153]. The actual $V_{bd}(pd)$ curve over a wide domain of pd values has a complex shape, but for the case at hand – air at standard temperature and pressure conditions and gaps above 200 $\mu\mathrm{m}$ – Paschen's law can be stated as follows [152]:

$$V_{bd} = \frac{24.22pd}{760} + 6.08\sqrt{\frac{pd}{760}}\,. \tag{3.1}$$

From the above equation, at standard atmospheric pressure, a 0.4 mm gap could be expected to stand ~ 2.2 kV. One can then take this value as reference for a 0.4 mm thick ThGEM, even if it should be taken into account the approximation that is implicit in this approach, the fact that in experimental conditions atmospheric pressure fluctuates, and that humidity and temperature affect the actual value measured. In the lab, when performing these tests, those variables are measured and taken into account in interpreting the results.

Even if it is a blunt tool, the Paschen check is useful because it can be done without a controlled atmosphere, and so is quick, practical and gives a good first-hand indication of the effects of the treatments being implemented and which pieces qualify to proceed to a more careful characterization. Figure 3.40 shows how through two instances of the post production treatment the structures present increasingly higher maximum stable voltages, until values for all sectors reach figures very close to the expected Paschen limit.

As a final test, much like the single test chamber built for the evaluation of the smaller ThGEMs,

a larger version was assembled to allow the operation of single 300 × 300 mm^2 active area ThGEMs. Due to their increased size, one is no longer interested in merely measuring a single gain value from one spectrum, but instead to obtain a map of the gains in different sections and evaluate the non uniformity of the structures.

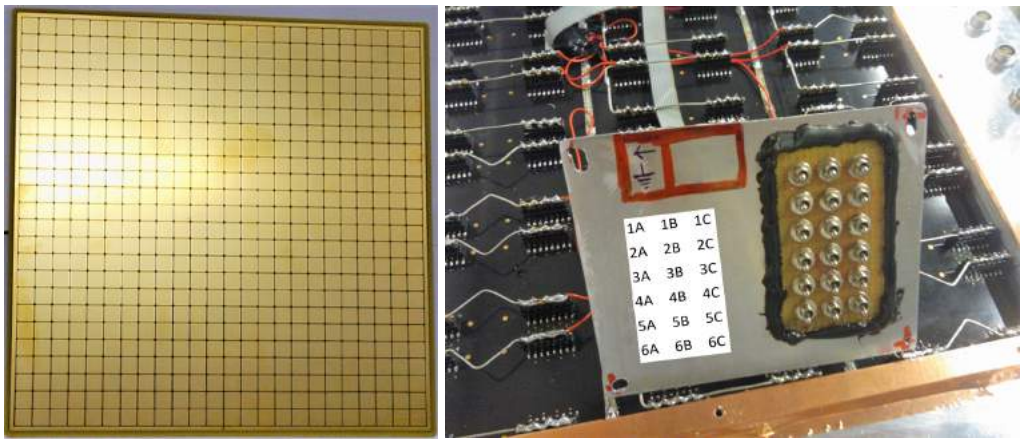

Figure 3.41 Left: large 300 × 300 mm^2 anode used in the large detectors, with 576 readout pads of 12 × 12 mm^2 area. Right: switch board for anode section selection.

To allow the evaluation of the full active area of the new ThGEM pieces the anode had to be scaled accordingly. The new anodes used, produced by TVR srl, are similar in concept to the smaller version, but consist in 576 (24 × 24) readout pads, each being 12 × 12 mm^2 with a 0.5 mm gap between them. A picture of one large anode used is shown in figure 3.41, at the left.

In order to obtain an appropriate mapping of the performance of the ThGEM, one has to choose the number of pads that should be grouped and whose signal should be read together (the smaller ThGEM-based detectors used a single group of 6 pads). If the divisions are too small, the rate of events that can be measured using the Fe-55 source is too low, the complexity of those connections would be high and the time it would take to complete a full scan would be long. If on the other hand one groups too many pads, the noise level is increased – it is proportional to the capacitance – and the mapping lacks detail. For the purposes intended, it was decided that a division of the readout in 18 sections would be ideal: the anode is mapped in six numbered rows matching the ThGEM sectors (1 to 6, couting downwards), each of them divided in three columns (A, B and C, from left to right, from the perspective of the detector cover). Therefore, each of the resulting sections connects a matrix of 8 × 4 pads. The selection of which anode region to read at a given time is done with a set of electronic switches (see figure 3.41 at the right) placed before the signal is propagated to the usual analog chain, in particular to the CR-110 preamplifier.

The readout sectors are matched on the cover of the chamber by holes made in a copper foil that is shown in figure 3.42, thus allowing the easy alignment of the Fe-55 source with the sector whose switch is enabled. The window of the detector is a single kapton® foil that covers the whole active area and is not in direct contact with the copper foil. The acoustic effects of that big membrane

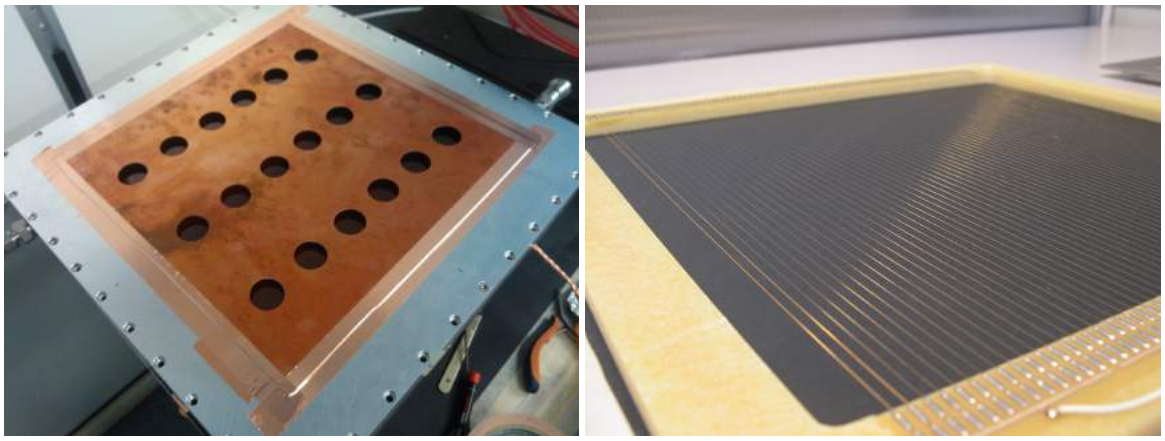

Figure 3.42 Left: cover of the large single ThGEM test chamber with holes in the copper mask for positioning of the Fe-55 source. Right: wire plane that sets the drift region in the test chamber.

introduce negative consequences on the noise level of the chamber, with acquisition thresholds often close to 2 fC. The drift field is established by a plane of wires that covers the whole active region of the ThGEMs, as depicted at the right of figure 3.42.

The same gaseous mixtures already used in previous characterization exercises of small ThGEMs, namely Ar:CO_2 - 70:30 and Ar:CH_4 - 70:30, were again used for the tests. The HV power supply system is still based on CAEN N471A units. To simplify the connections and the powering procedures, all six bottom electrodes are grouped so their voltages can be set from a single power supply channel, via a splitter. This leads to the adoption of a simpler routine to increase the ΔV applied to the ThGEM, by initially setting the top and the bottom electrodes at the same voltage value in seven PS channels, and then lower the absolute value of the voltage applied to the bottoms by controlling a single channel (the polarity is negative – the anode is at ground – so the real value of the voltage at the bottoms is actually being raised).

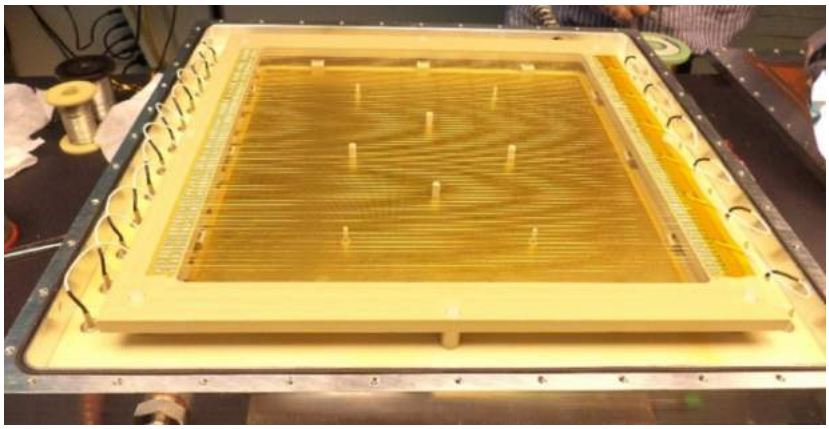

Figure 3.43 Picture of the single ThGEM evaluation chamber open.

The characterization exercise starts with the slow increase of the voltage differences applied to

the ThGEM electrodes, to evaluate the maximum that can be applied, in the gas medium used, to all sectors in stable conditions; this is somewhat similar to a Paschen check for a different gaseous mixture. After that limiting value is found, a ThGEM piece deemed good by the previous exercises should be at a condition where the gain from the voltage difference applied is enough to allow the acquisition of a spectrum of the Fe-55 source. Once again, a small positive drift field is applied to help directing the primary charge towards the ThGEM holes. From a typical spectrum presenting the full absorption peak of the 5.9 keV Fe-55 X-ray emission, the gain of each section is estimated.

With the help of the single ThGEM test chamber one can, first of all, appreciate the improvement achieved by the careful selection procedure of the PCB foils. In figure 3.44 it is shown the result of the characterization of a ThGEM both with and without PCB foil pre-selection. The non uniformity diagnosed in the PCB thickness measurements is clearly projected to the gain characterization, with a noticeable trend towards one side of the piece, leading to gains in different sections varying by up to a factor of 3. When the ThGEM is produced from a PCB foil selected within our uniformity criterion, the gain variation is typically reduced in half, as illustrated at the bottom of the same figure.

The non-uniformities in gain can be further limited by taking advantage of the segmentation of the ThGEM. Applying different voltages to the top of each sector in order to equalize their average gain, the discrepancies go down to ~25%.

The characterization of the new ThGEM structures was a crucial step to improve the performance of the larger area detectors. The large triple cascaded ThGEM-based detector used in the next section, for tests in beam environment, used three pieces previously characterized and which had shown the best performances.

3.4 Performance of 300 × 300 mm^2 ThGEM-based detectors under particle beam irradiation

Once more, to evaluate the performance of the new large ThGEMs for Cherenkov light detection, tests in beam environment are required. To perform such tests, a chamber was built to accommodate a single detector of 300 × 300 mm^2 active area using three cascaded ThGEMs. Figure 3.45 at the left illustrates the disposition of the elements, with the relevant geometrical specifications.

The spacings between ThGEMs are set to 3 mm while the induction region is 2.5 mm. The drift region is 5.2 mm. The unusual use of two planes of wires is to ensure a better uniformity of the drift field. The ThGEMs used had a 0.8 mm pitch of 0.4 mm diameter holes with ~5 $\mu\mathrm{m}$ rims. The CsI coated ThGEM1 (which underwent the Ni-Au treatment as usual) was 0.4 mm thick, while the other two had 0.8 mm thickness. As mentioned in the previous section, precise positioning and planarity of the ThGEMs is achieved via the use of insulator spacers in the inner columns and border blocks, both made of PEEK, and fixed by insulator screws allowing easy mounting and dismounting

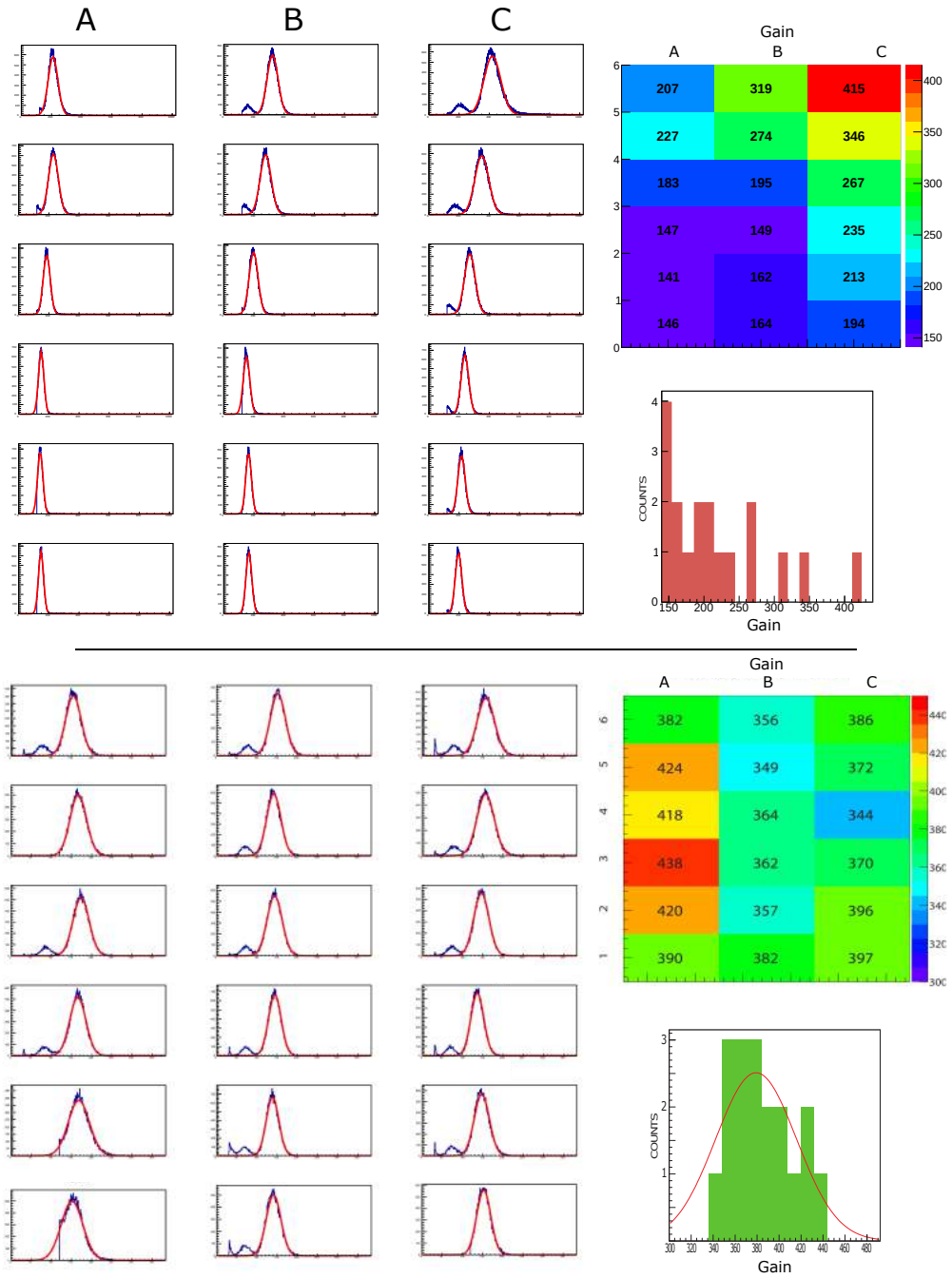

Figure 3.44 Comparison between the characterization results of a ThGEM produced with a non uniform PCB foil (upper half) and the same exercise with a ThGEM obtained from a good PCB (lower half). Both ThGEMs are 0.4 mm thick and are characterized in Ar:CO_2 - 70:30. The maximum gain is similar in both pieces, but in the lower uniformity piece several sectors stand only a very moderate gain.

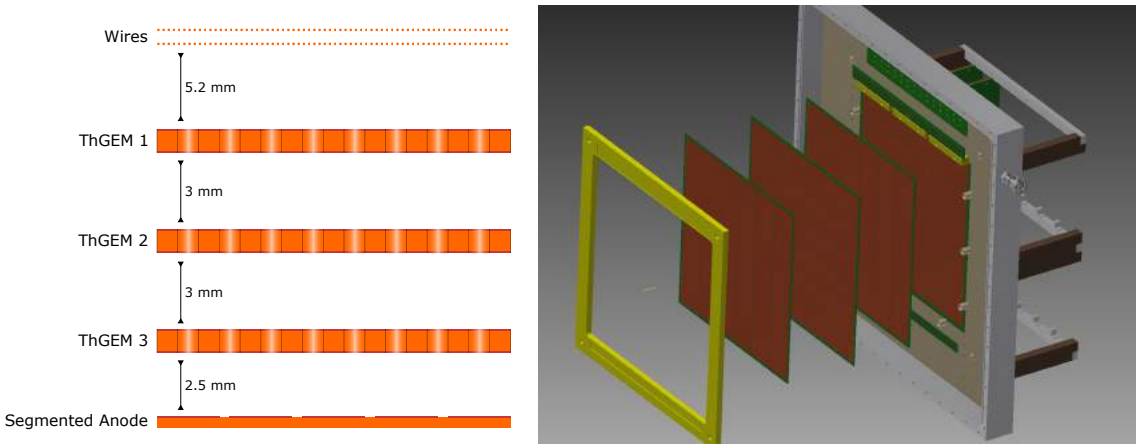

Figure 3.45 Left: scheme of geometric disposition of elements in the detector. Right: 3D representation of the components of the detector.

operations.

The high voltage is supplied by six separate channels for each of the detector's sectors from a A1526N board on an SY1527 mainframe, both from CAEN. The different *vertical* voltages in the detector – the voltage drop across the drift region, ThGEM tops and bottoms, transfer and induction regions – are obtained with a resistive divider chain as in the small detectors. Resistive divider boards for each sector were produced and can be seen in figure 3.46 at the left.

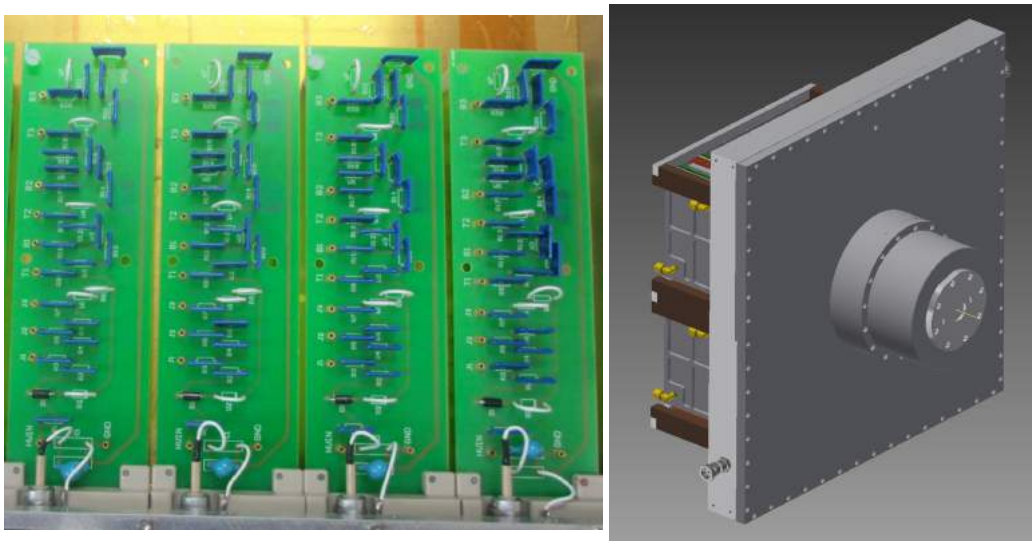

Figure 3.46 Left: photograph of some of the resistive divider boards. Right: representation of the detection chamber seen from the front cover, with front end electronics installed.

The detector, flushed with Ar:CH_4 - 60:40, was characterized using light from the UV LED, transmitted through a small quartz window in the cover of the chamber. The result of the characterization (of a single readout section) is plotted in figure 3.47 as a function of the sum of

the voltage differences applied to the three ThGEMs. The curve obtained for the 300 × 300 mm^2 ThGEM-based detector is compatible with the ones obtained with the smaller prototypes, which are also included in the plot for comparison (gray data points). However, It is noticeable how the maximum voltage that the larger chamber can sustain is slightly lower than the one achieved with the previous smaller prototypes, leading to a maximum gain below 10^5.

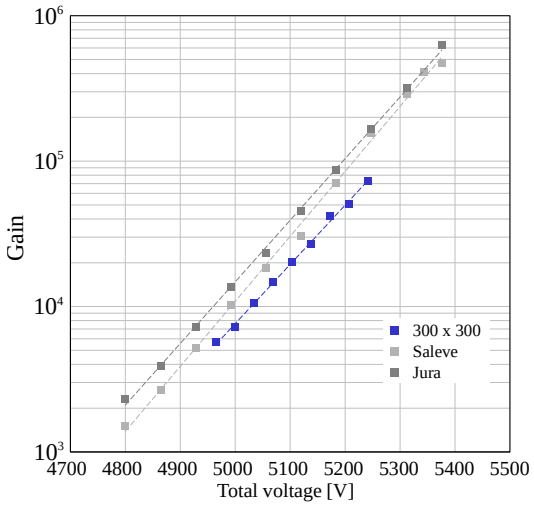

Figure 3.47 Gain obtained with the detector irradiated with UV light as a function of the sum of voltages applied to the three ThGEMs, with null drift field (blue). For comparison, the results of the same test performed in the two small area triple ThGEM detectors is shown as well (gray).

3.4.1 Setup

The set of studies under beam was performed at CERN in November 2012, this time at the PS T10 Beam line, with a π^+ beam of 6 $\mathrm{GeV/c}$. The beam line disposition of elements, illustrated in figure 3.48, is in practice equivalent to the one used in the exercises with small ThGEM-based detector prototypes. In particular, the trigger system is almost identical to the one described on that exercise (see section 3.2), but one of the larger scintillators was found to be redundant, and so the new configuration is now a 5-fold scintillator coincidence (the frontal paddle was removed). Besides the large detector chamber under study, a second chamber was also present with small ThGEM-based detectors, whose discussion was already given in section 3.2 and which does not interfere in any way with the behavior of the large chamber.

The analog readout, when used, is still the traditional one for laboratory tests and previous beam exercises. The same is true for the digital readout electronics, still based on the chain using current protection, CMAD and F1-TDC chips, just in a more dense and larger arrangement to accommodate all the elements needed to read the signal from all the pads of the anode. A picture of the electronic readout chain is shown in figure 3.49.

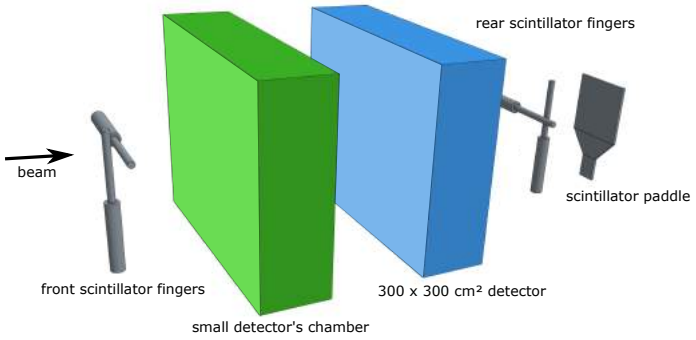

Figure 3.48 Disposition of elements in the 2012 beam line exercise.

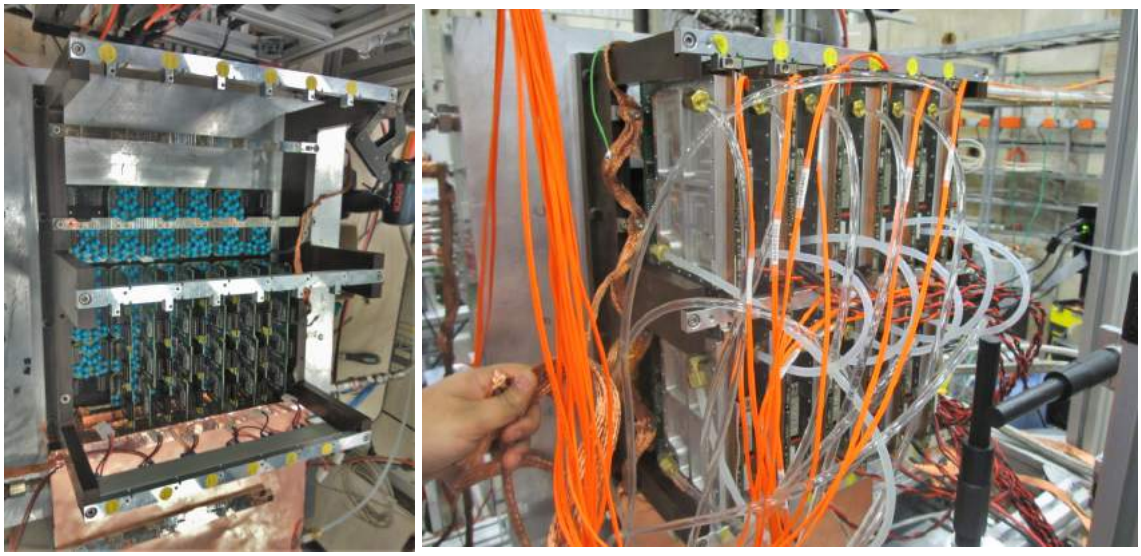

Figure 3.49 Photographs of the electronic readout setup during (left) and after (right) being mounted.

For the emission of Cherenkov photons, a new truncated conical radiator of fused silica was used on the beam axis equipped with a remotely controlled cylindrical interceptor. This radiator illuminates over a complete corona of Cherenkov photons that hit all the sectors of the top ThGEM. A photograph of the radiator can be seen in figure 3.50. Because the radiator is centered in the active detection area, the beam will be crossing at full intensity the central sectors of the ThGEMs, which did not happen in the case of the chamber with the small prototypes. This is, therefore, a demanding test for the ThGEM-based detector's stability.

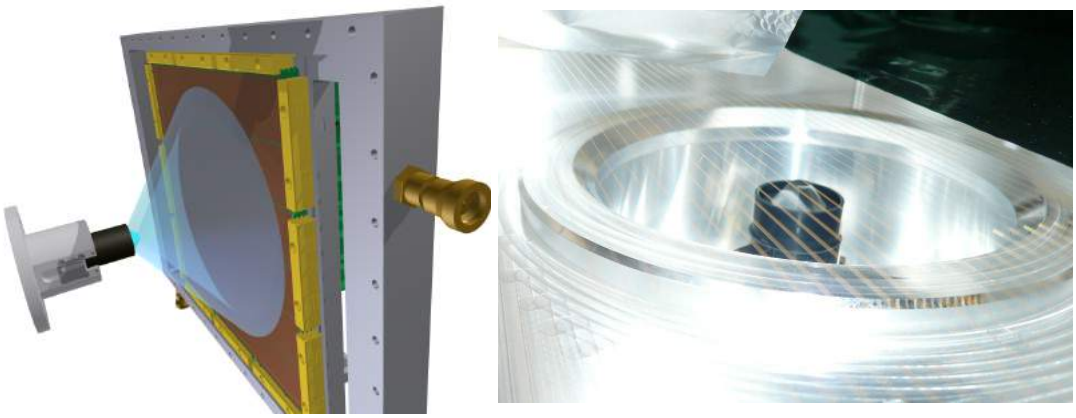

Figure 3.50 Left: scheme of the radiator positioning relative to the ThGEM detectors, and representation of the light emission. Right: photograph of the conical radiator in the cover of the chamber, and of one wire plane.

3.4.2 Results

The detector, flushed with Ar:CH_4 - 60:40, was operated under beam particle flux aligned with the radiator in order to look for Cherenkov light. The voltages of each sector were slightly tuned so the gain would be more uniform over the whole area of the detector and the stability improved: on average, the total voltage applied to the sectors of the three ThGEMs is ~5.1 kV. Figure 3.51 shows the result obtained from the pile up of events detected during a typical run. Figure 3.52 shows the same super-imposition of events but from a longer run. The visible rings correspond to the expected Cherenkov corona, while the central bins show high counts resulting from the interaction of the beam itself.

As an example, two single events – each generated by one particle activating the trigger – are shown in figure 3.53, where 8 and 9 hits are detected, i.e. the multiplicity of both is ~8.5. The hits are due to the detection of Cherenkov photons, considering their positioning near the expected corona also represented in the same plots, even if there is a finite probability that some of them are due to random noise.

The stability of the detector in the conditions used to obtain the events illustrated is rather limited, with several trips experienced during data taking. Even when the voltage at the four central sectors – where the beam intensity is higher – is slightly reduced by 30 V, the histogram of the

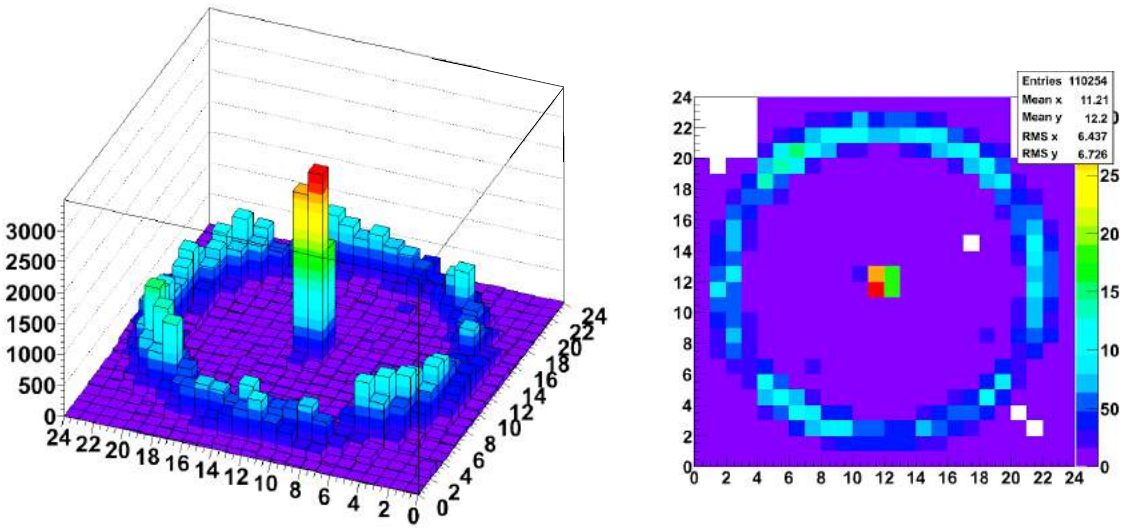

Figure 3.51 Pile up of events detected during a typical run. 3D (left) and 2D (right) views show the central point where the beam crosses the detector.

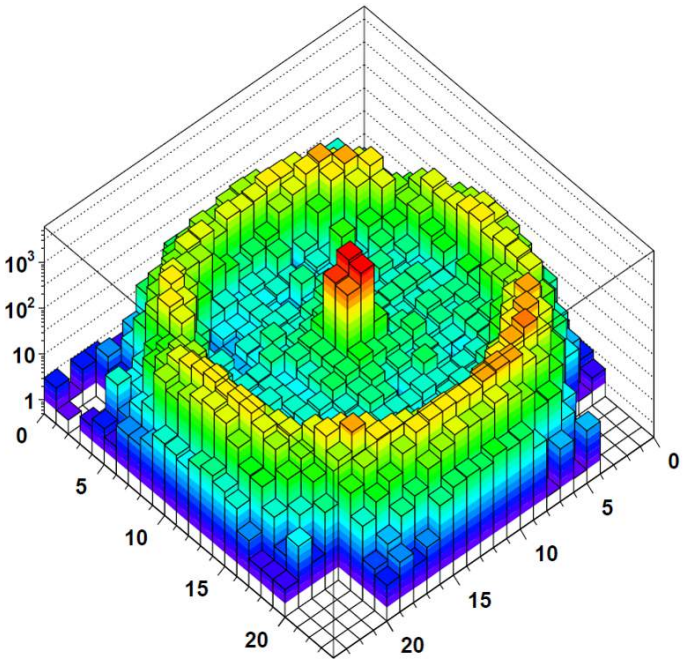

Figure 3.52 Super-imposition of events from a long run. The ring-like distribution is evident, and matches the expected position of the corona of light.

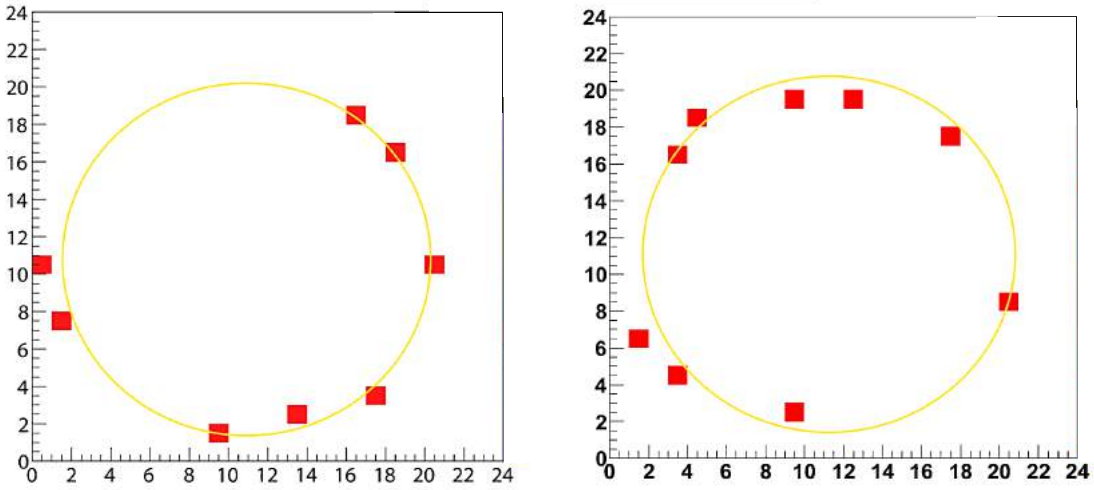

Figure 3.53 Two examples of Cherenkov rings, each generated by a single beam particle.

average multiplicity of each spill, presented in figure 3.54 at the left, shows several drops in the performance of the detector, which can be attributed to discharges of the detector. By comparison, in the same figure at the right, the detector operated with all sectors at 5030 V of total voltage shows satisfying stability of the response.

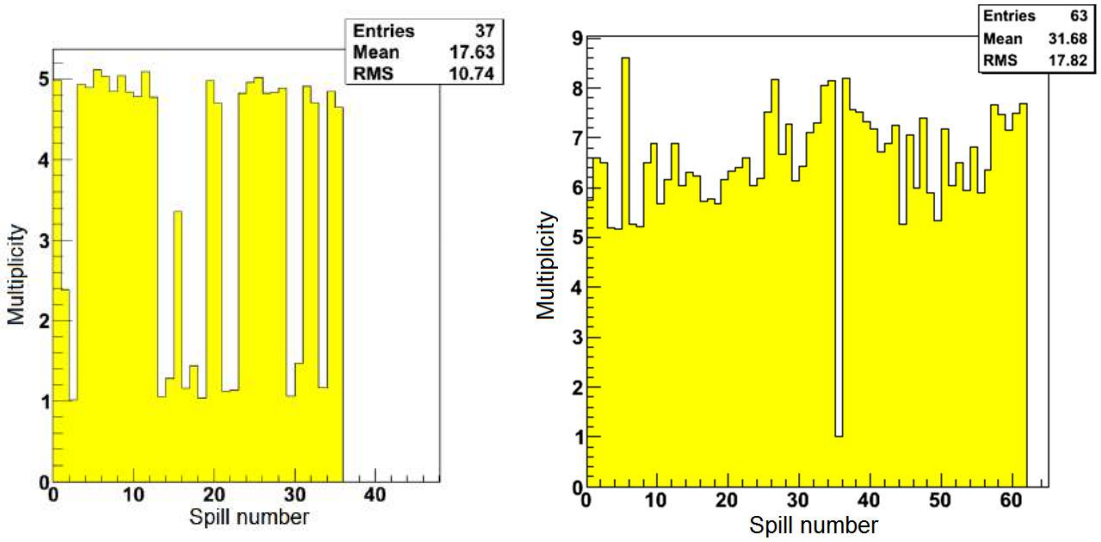

Figure 3.54 Average multiplicity per spill. At the left, the detector is at a total ΔV of 5.07 kV (gain ~2 × 10^4), except in the two lateral sectors where it is at 30 V more. At the right, all the sectors are at 5.03 kV, resulting in increased stability.

Operating at the lower voltages that ensure stability introduces issues with the time response, resembling what was observed in the test beam exercises of the small prototypes. The time distribution of the detected photons, illustrated in the histograms of figure 3.55 for a single sector,

are highly dependent on the voltages applied on the detector. It can be seen in those histograms that a well resolved gaussian time distribution peak is only achieved at voltages incompatible with stable operation of the full detector. Therefore, efficient collection of the photoelectrons generated by the Cherenkov light is not guaranteed.

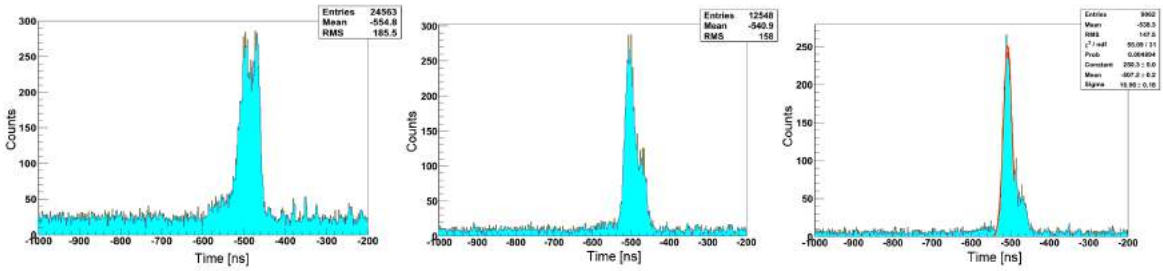

Figure 3.55 Time response of the detector for three different total voltages across the ThGEMs. The histograms are obtained with most sectors kept at unusually low total voltages (4.96 kV), so that a single sector can be pushed to 5.1 kV (left), 5.24 kV (center), and 5.37 kV (right).

A final check to confirm the nature of the events detected can be performed by monitoring the multiplicity of each event while scanning the position of the interceptor of Cherenkov light attached to the radiator. The results, plotted in figure 3.56, prove that the interceptor is indeed reducing the number of hits collected per trigger, a definitive indication that Cherenkov light is the source of the events. The different values of multiplicity per sector are, most likely, related to the non uniformity of the gain, as well as noise level, over the detector's area.

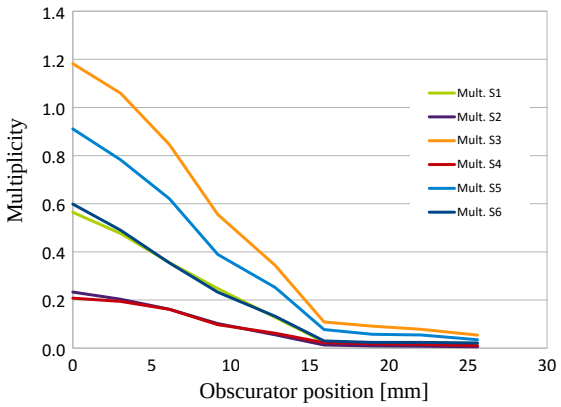

Figure 3.56 Multiplicity of events as function of the interceptor position.

From a global perspective, the results of this Test Beam are not great. The detection of Cherenkov rings is an achievement in itself, but the inefficient photoelectron extraction raises concerns. The efficient detection of photons, and a good time resolution, requires the establishment of voltages in which the detector is not stable. The gain sustained, slightly above the order of 10^4, is below the intended goals, and it seems unlikely that this could be solved in the larger devices

required, maintaining the configuration used so far.

3.5 Development of Hybrid Detectors

The tests performed allowed insightful conclusions to be extracted regarding the operation of the ThGEM-based detectors. However, it was also true that the evolution of the ThGEM technology was not occurring at a fast enough pace, with limitations in the maximum stable gains achieved. Probably of more concern, the efficient photoelectron extraction from the CsI photocathodes seemed to come at the expense of the detector stability. These issues need to be overcome before the evolution of the detectors to 600 × 600 mm^2 active areas can be considered.

Another limitation of the triple ThGEM configuration was related to the control of the Ion Backflow. To limit the IBF to values of few %, besides the misalignment of ThGEMs, a transfer field of ~4 $\mathrm{kV/cm}$ in the second transfer region is required. As a result, the absolute voltages that need to be applied to the detector, especially to the Drift wires, often get to values greater than 8 kV. This is a common limit for the conventional power supplies and would also imply the change of many components related to the supply system, such as the HV cables and connectors.

With those considerations in mind, the research group decided for a change in the typical detector architecture studied so far: the replacement of the ThGEM responsible for the third multiplication stage by a Micromegas. The Micromegas is expected to reach higher stable gains, which in turn allows the shift to a gaseous mixture with higher methane content. This should, as a consequence, improve the photoelectron extraction efficiency from the CsI. Furthermore, the Micromegas requires applied voltages which are less than half the ones used in a ThGEM to obtain the same gains. Even better is the implementation of the capacitive anode, as will be demonstrated in section 3.5.3, which allows the operation of the Micromegas with the micromesh at electric ground by applying a positive bias voltage to the anode.

3.5.1 30 × 30 mm^2 Hybrid Prototype

The Micromegas is a well researched structure, already described in section 1.4.1, and has been successfully operated in detectors while coupled to either a GEM or a ThGEM structure, as mentioned in section 1.4.4. Still, the hybrid concept lacks the extensive studying that their standalone components underwent.

To prove that no drawbacks are introduced due to its operation in hybrid configuration, the concept was first studied in a small area prototype. A Micromegas produced by Bulk technology for the CEA Saclay group was used (see figure 3.57) and a new chamber was designed and built to include it. This detector had an active area of 60 × 100 mm^2, and is characterized by a distance between the micromesh and the anode (amplification gap) of 128 $\mu\mathrm{m}$. The chamber allowed the use of two alternative covers, one with a Kapton® window fit for the use of our Fe-55 X-ray source

and another with a quartz window to ensure transparency to UV light produced by the LED, used later with the integration of the ThGEM element.

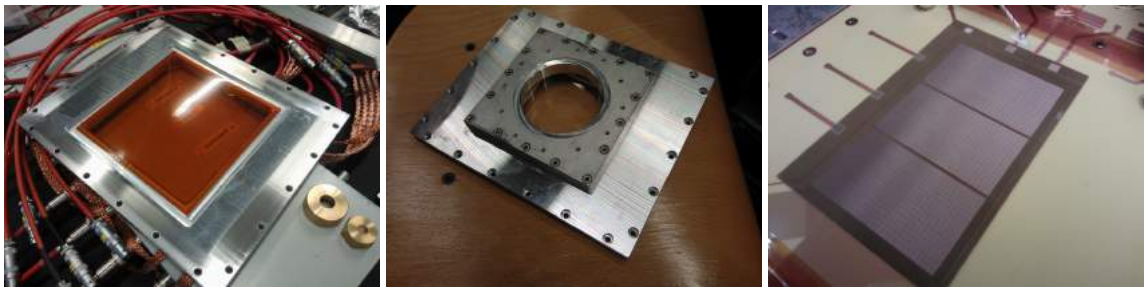

Figure 3.57 Left: Kapton® cover of the small hybrid chamber. Center: quartz cover. Right: Bulk Micromegas used in the small hybrid detector.

For the hybrid configuration, a 0.6 mm thick, 0.4 mm hole diameter, 0.8 mm pitch ThGEM was initially used. The first configuration used in the detector is illustrated at the left on figure 3.58. When only the Micromegas is being studied, the configuration is equivalent but without the ThGEM contribution, meaning that the distance between the micromesh and the drift wires – the conversion region – is 20 mm.

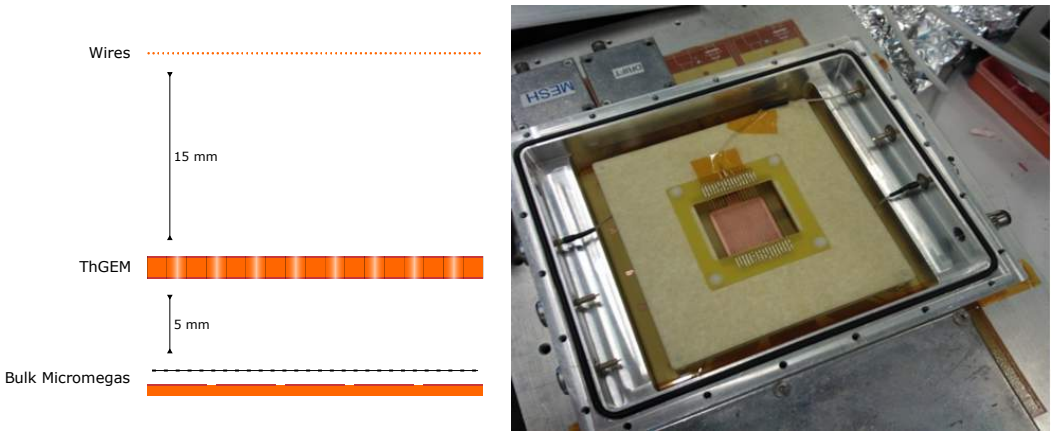

Figure 3.58 Left: configuration used in the single ThGEM hybrid detector (in the Micromegas detector, the ThGEM is absent). Right: photograph of the chamber holding the single ThGEM hybrid detector whose scheme is illustrated at the left.

To analyze the effect of adding a ThGEM element to the Micromegas detector, both configurations were operated with Ar:CO_2 - 70:30 atmosphere. The tests monitored how the rate of events, the gain and the energy resolution of the Fe-55 source spectra depended on the ratio between the amplification and conversion fields of the Micromegas (ξ). This means changing the conversion (drift) field for the Micromegas standalone configuration, or modifying the transfer field between the two electron multipliers in the hybrid configuration, while the amplification field is kept constant.

Like the ThGEM electrodes, the micromesh is polarized with negative voltages, since the anode

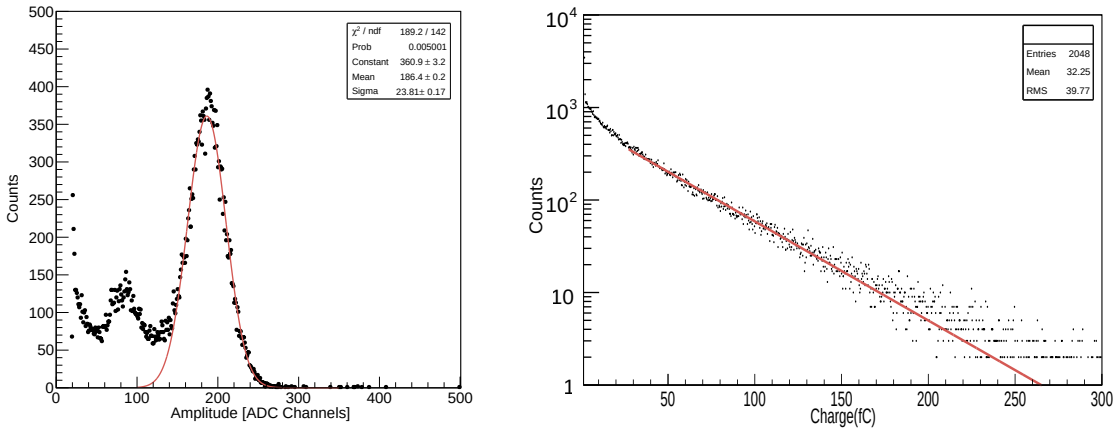

Figure 3.59 Left: spectrum obtained with the Fe-55 source by the single ThGEM hybrid detector; the energy resolution is ~30%. Right: single photon spectrum with the same detector. The gains are respectively ~10^5 and ~10^6.

is at electric ground. The exercises were done for a fixed micromesh voltage of -620 V ($E_{\text{amplification}}$ of 48 kV/cm) and -590 V (46 kV/cm) for the standalone and hybrid configurations, respectively. The ThGEM in the hybrid detector was operated with a voltage difference between the electrodes of 1400 V. Figure 3.59 shows two typical spectra obtained with the hybrid prototype, with the Fe-55 source and using the UV LED. The gains achieved were respectively ~10^5 and ~10^6.

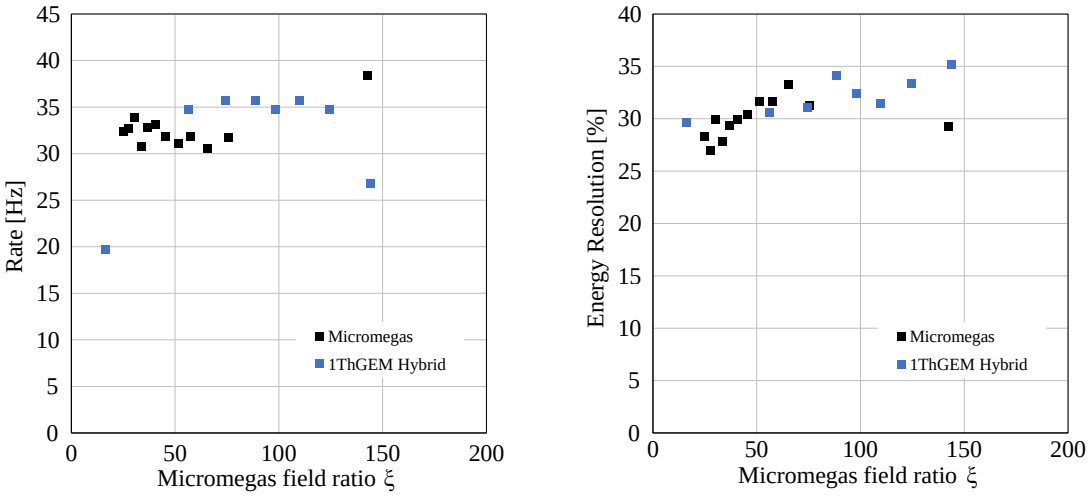

Figure 3.60 Comparison of the rate (left) and energy resolution (right) achieved with the Micromegas and the single ThGEM hybrid detector, in Ar:CO_2 - 70:30 and with fixed micromesh voltages of -620 V and -590 V, respectively. [146]

The comparison between the performance of the detectors using the Micromegas (standalone) and the hybrid prototype is shown in figure 3.60. The results show little difference between

the two configurations: the energy resolution of both approaches is similar and so is the rate achieved. Naturally, the gain in the two architectures is quite different since there is an additional multiplication stage in the hybrid case. The only relevant difference verified during the measurements was that, for the hybrid prototype, the gain is seen decreasing as ξ increases. Since in this case the increase of field ratio is actually a result of the decrease in the transfer field between the two elements, it's reasonable to attribute this drop in gain to the reduction of the electron transparency between the elements.

A complementary test was done by introducing another ThGEM structure above the existing one, creating a double ThGEM hybrid prototype. Gains of ~2 × 10^6 were observed while still conserving the remaining operation properties of the detector.

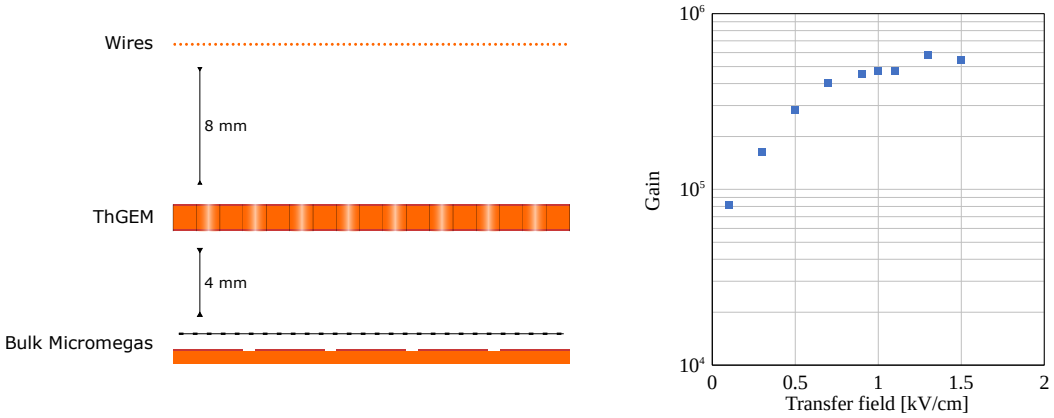

Figure 3.61 Left: second configuration used with a single ThGEM hybrid detector, with a thinner ThGEM (0.4 mm) and smaller drift region. Right: gain of the hybrid setup as a function of the transfer field between ThGEM (at 1600 V of ΔV) and Micromegas (with the micromesh at -600 V); the gas medium was Ar:CH_4 - 60:40.

The chamber was then adopted for a second setup, again with single ThGEM stage, for the characterization in methane rich mixtures. The scheme of the elements in the new hybrid detector is illustrated in figure 3.61, at the left. The main differences reside in a thinner ThGEM (0.4 mm thick) and in the reduction of the drift space to 8 mm.

The effect of the transfer field between the two multiplication elements was studied in Ar:CH_4 - 60:40. The dependency of the gain of the detector with the transfer field is shown in figure 3.61 at the right, and shows that full transfer of charge between the two elements is guaranteed at 1 kV/cm.

The detector was characterized in Ar:CH_4 - 10:90 atmosphere, with a fixed ThGEM voltage difference set to 1950 V and varying the Micromegas voltage. The results plotted in figure 3.62 show that the exponential response of the Micromegas is achieved at fields higher than 40 kV/cm, before which the structure is still not operating optimally. The Micromegas achieves such strong electric fields in the amplification region that high gain operation in pure methane, with a CsI

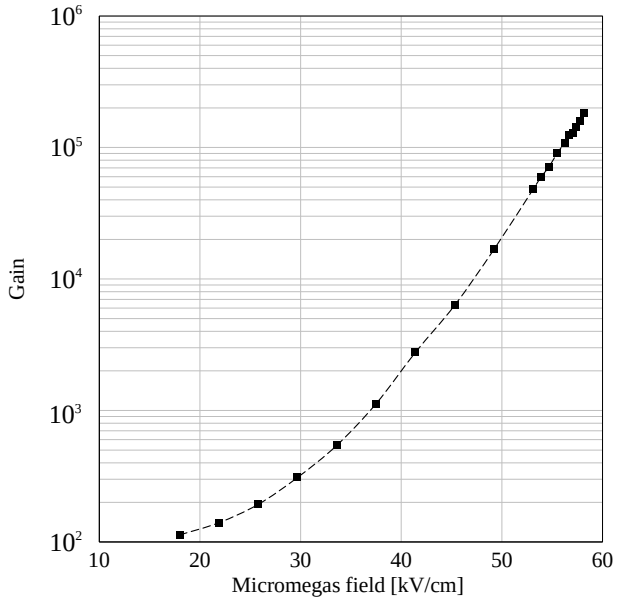

Figure 3.62 Micromegas characterization curve obtained with Ar:CH_4 – 10:90 atmosphere, for a fixed ThGEM voltage difference of 1950 V and using the Fe-55 source.

coated ThGEM and UV light, was perfectly possible.

If, on the other hand, one sets a fixed micromesh voltage and varies the voltage difference between the electrodes of the ThGEM, the gain evolution follows a curve spanning two separate regimes. This happens because, at low ThGEM voltages, the dipole field is not enough for the onset of Townsend avalanche, so the structure acts as transparent to electrons (unitary gain), and the measured gain of the detector is fairly constant and determined by the Micromegas. After that plateau, the fields become strong enough to produce electron multiplication, and the lines converge to the characterization curves of the ThGEM being used. Figure 3.63 shows this behavior in three curves of gain as a function of the ThGEM voltage, for three different $ArCH_4$ mixtures. The curves show how the increasing methane content delays the start of the ThGEM multiplication to higher voltage differences, and lowers the resulting gain, as expected.

By comparing the characterization curves of each element (figures 3.62 and 3.63) one also confirms that the Micromegas structure has a gain slope which is much steeper than the ThGEMs: as a rule of thumb, a 100 V increase in the voltage applied to the Micromegas increases the gain by a factor 10, while the same increase would merely double the ThGEM's gain.

Lastly, the IBF of the hybrid prototype was estimated with a set of picoammeters, yielding results of ~4%. Altogether, these sets of tests were convincing and motivated the will to proceed in the investigations of hybrid architectures by increasing the size of the prototypes being studied to 300 × 300 mm^2 of active area.

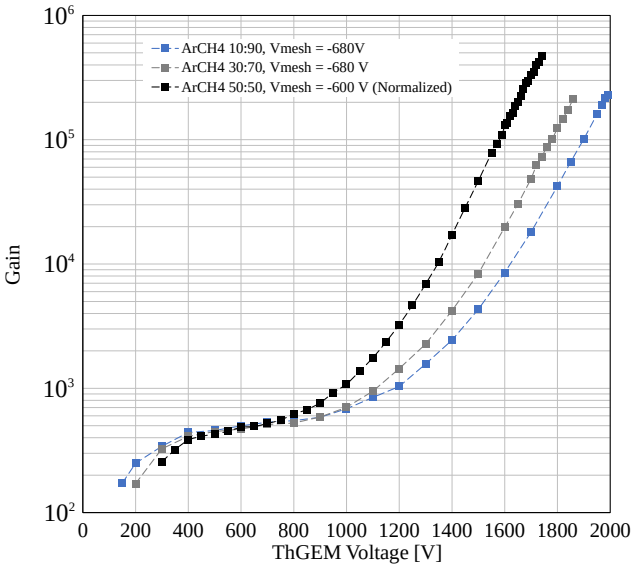

Figure 3.63 Hybrid detector gain as a function of the voltage applied to the ThGEM, for three $ArCH_4$ mixtures, under Fe-55 source irradiation. Two of the curves were obtained with the mesh set at -680 V, while the Ar:CH_4 – 50:50 curve was obtained with the mesh at -600 V. The Ar:CH_4 – 50:50 curve was normalized so the plateau, corresponding to the Micromegas gain, leads to the same gain of the other two curves.

3.5.2 300 × 300 mm^2 Hybrid Detectors

The 300 × 300 mm^2 active area Micromegas are produced by Bulk technology at the CERN TS-DEM-PMT[¶] workshop. They are integrated in the 300 × 300 mm^2 anode readouts manufactured by TVR srl. The first version of the large Micromegas produced and studied can be seen in the pictures of figure 3.64. It uses a conventional anode, identical to the ones in the large ThGEM-based detectors.

The new large area hybrid detectors require new chambers to be built and properly tested. For the first detector studied, the chamber assembled is pictured in figure 3.65. The cover features a Kapton® window to allow the irradiation of part of the detector with the X-ray source. As for the readout part, the switch system previously used was replaced since it contributed negatively to the noise level. The readout pads are now joint in groups of 16 (4 by 4), which are read through LEMO connectors, grounded with 50 Ω terminations when not in use. Because the divisions now cover 16 pads each – instead of 32 as previously – the number of virtual sectors is doubled (36), in a square array of 6 × 6. The matrix is labeled according to the convention in figure 3.68 at the left, from the perspective of the chamber's cover. The only difference between this arrangement and the one existing in the ThGEM-based detectors is the three additional columns: D, E and F.

Before progressing with the assembly of the hybrid detector, the Micromegas alone was tested

[¶]Technical Support Department, Development of Electronic Modules, Photolithography and Microconnectics Technologies

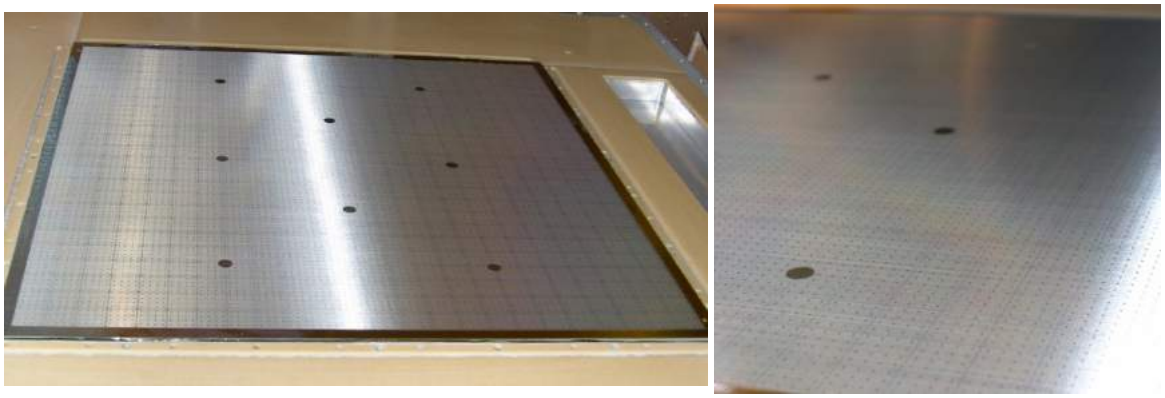

Figure 3.64 Pictures of a 300 × 300 mm^2 active area Bulk Micromegas produced at CERN on top of a standard anode. One can see the spots were the pillars that support the ThGEMs will be glued, the microscopic pillars which support the mesh wires, and even the anodic pad contours can be distinguished with some effort.

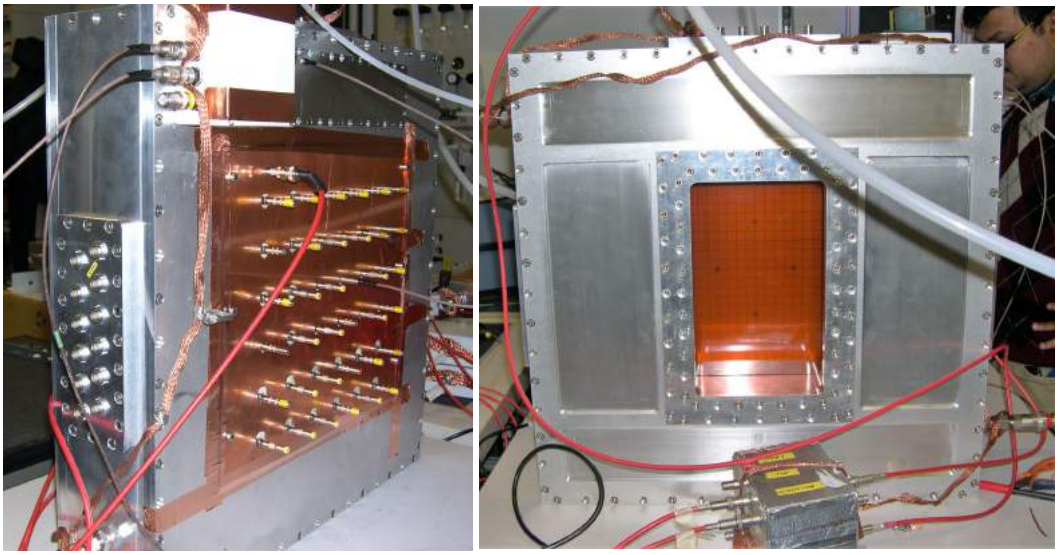

Figure 3.65 Picture of the back (left) and front (right) covers of the large hybrid detector chamber. On the back, the 50 Ω terminations can be seen coming out of a copper plate used to improve the grounding of the detector, leading to noise levels below 2 fC.

to evaluate its performance. The characterization was done with the detector illustrated in the scheme of figure 3.66, for one single readout sector, and the resulting curve is plotted in figure 3.67, next to a typical spectrum in such configuration. The results of the characterization show a slope of the gain curve which is similar to the one obtained for the smaller version of the Micromegas. The difference in gain obtained for the same field is explained by the use of a different gas mixture, in this case Ar:CO_2 - 70:30.

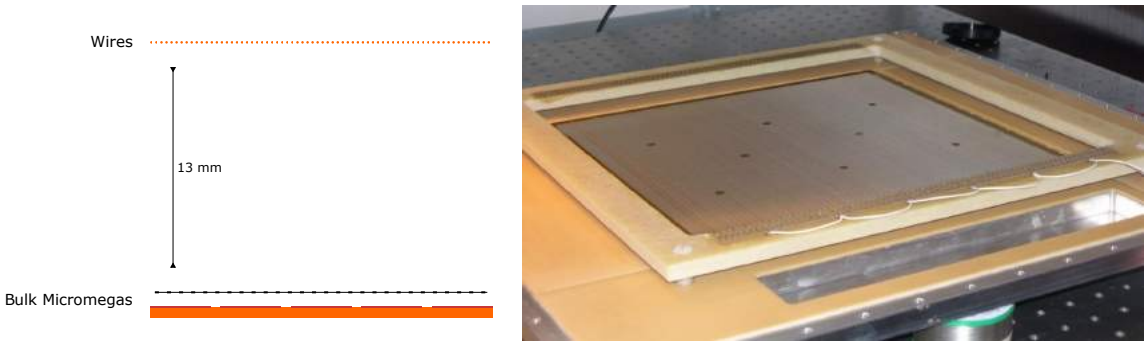

Figure 3.66 Left: scheme of the disposition of elements in the Micromegas standalone detector. Right: picture of the Micromegas detector with the plane of wires on top.

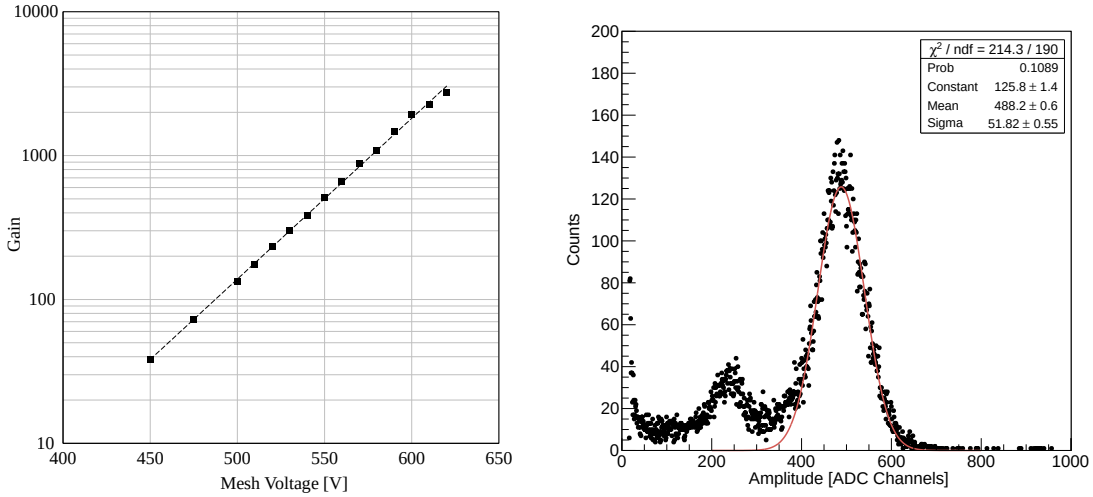

Figure 3.67 Left: gain of the 300 × 300 mm^2 Micromegas detector as a function of the voltage applied to the micromesh, in Ar:CO_2 – 70:30, irradiated by the Fe-55 source and with a conversion field of 1 $\mathrm{kV/cm}$. Right: example of a typical spectrum obtained with the described architecture; the energy resolution is ~25%.

The gain of the Micromegas was then inspected in several points to perceive the uniformity of its response with a fixed voltage. The results, illustrated in figure 3.68 at the center and right, show a variation of 20% between minimum and maximum gain values in that fraction of the total area. This is much lower than the non uniformities measured in ThGEMs, and was already expected from

the theoretical considerations presented in section 1.4.1.

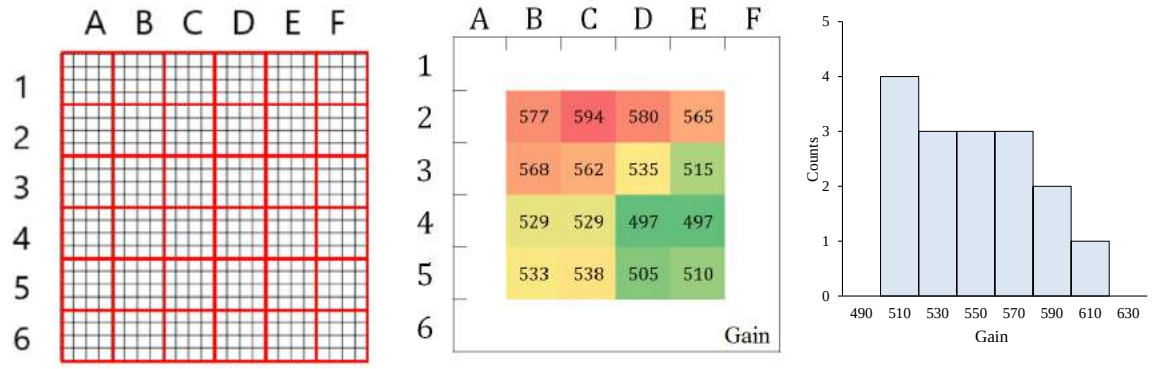

Figure 3.68 Left: mapping convention used for the large hybrid detectors, with 36 readout sections. Center: gain uniformity map of the central region of the Micromegas (standard anode), with the micromesh at -550 V. Right: Histogram of the gain uniformity measurement in the center.

Having tested the Micromegas element alone, the detector was then adopted to the hybrid configuration illustrated in figure 3.69. A typical 300 × 300 mm^2 ThGEM with 0.4 mm thickness, 0.4 mm hole diameter, 0.8 mm pitch and <5 $\mu\mathrm{m}$ rim was used. The ThGEM was produced following the procedures described in section 3.3, and was selected for its good uniformity, besides having reached maximum stable voltages in all sectors close to the predicted Paschen limit.

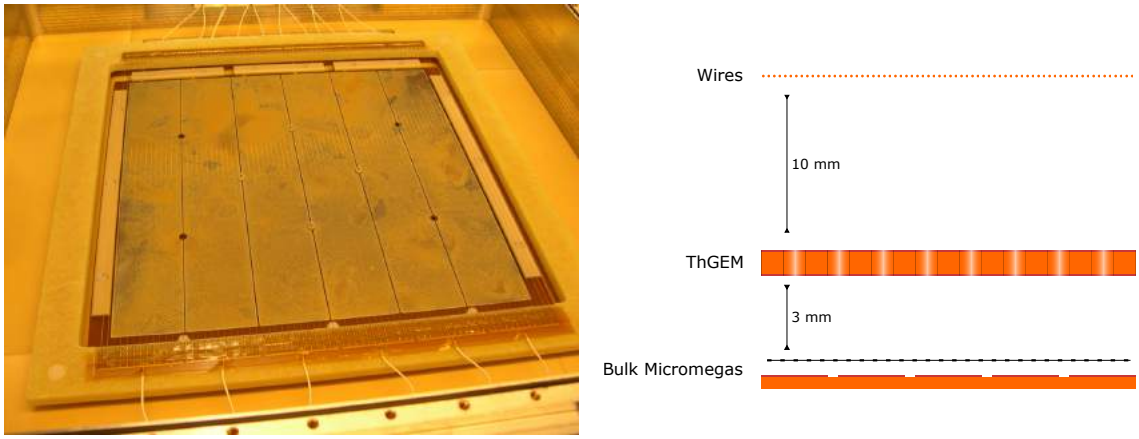

Figure 3.69 Left: picture of the 300 × 300 mm^2 active area hybrid detector with one ThGEM. Right: scheme of the elements in the single ThGEM hybrid detector.

Following the procedure implemented in the smaller hybrid chambers, the detector was characterized in terms of gain and stability in Ar:CH_4 - 30:70 gas medium. The HV is supplied, once again, using CAEN N471A power supplies, with the top electrodes being operated independently while the bottoms are powered via a single HV channel using a splitter. The curves on figure 3.70 show the result of the characterization of the detector for six readout sections in different sectors, varying the voltage applied to the ThGEM and keeping the Micromegas amplification field constant.

Each curve resembles the one obtained for the small area single ThGEM hybrid prototype (see figure 3.63) with an initial plateau followed by the characteristic exponential curve of the ThGEM. Most curves are quite compatible, with the exception of the one for sector 4, which was measured at a weak point of the Micromegas. Despite that, all sectors reached similar maximum stable gains.

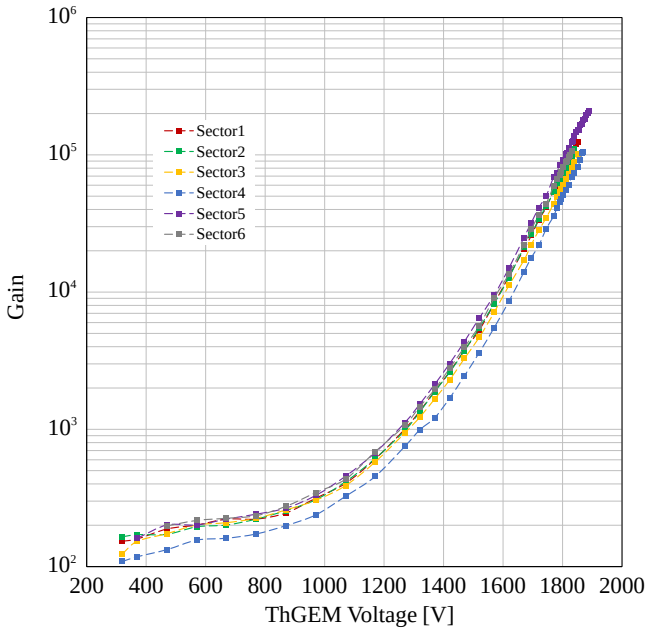

Figure 3.70 Characterization of the hybrid detector as a function of the voltage difference applied between ThGEM electrodes, for a fixed mesh voltage of 640 V, in Ar:CH_4 - 30:70 and using the X-ray source.

A second ThGEM, identical to the first one, was also added to create the final version of the hybrid detector. This chamber was operated, within the stability criterion, at a maximum of ~6×10^4 of gain, in the Ar:CH_4 - 30:70 atmosphere. A spectrum taken with the detector in such configuration can be seen in figure 3.71, with a slightly worse energy resolution (~38%) compared to the single ThGEM hybrid. One particular feature of the histogram is a small peak at the left portion of the plot, which can be identified as a full absorption peak of X-rays from the Fe-55 source converted in the transfer region between the two ThGEMs. The observation of that peak is possible because the gain contribution of the first ThGEM is limited, and is useful because it allows the disentanglement of the gain contributions of each multiplier element.

3.5.3 Capacitive Anode and new ThGEM design

During the development of the hybrid detector detailed in the previous subsection, a different Micromegas was idealized which uses a less conventional anode readout. The new type of anode, which will be called capacitive to distinguish it from the standard/conventional one, appears as

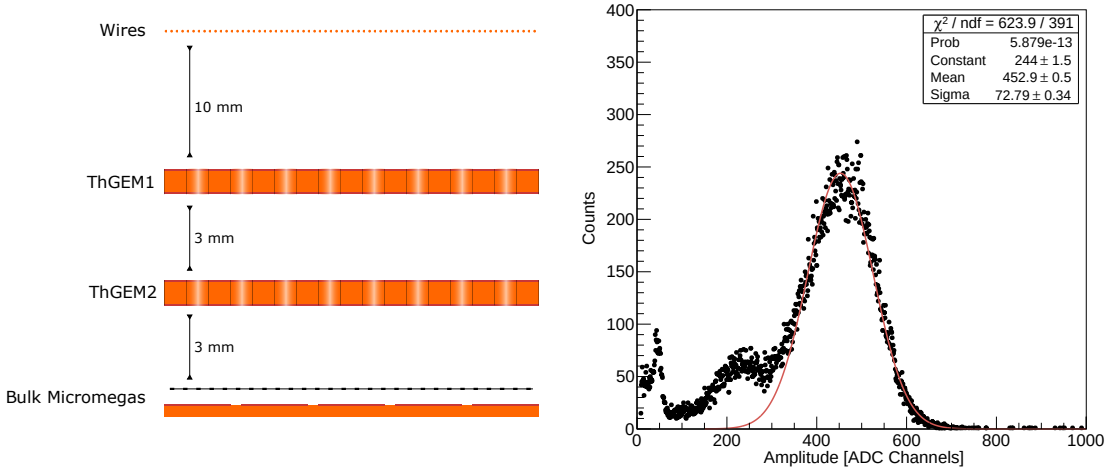

Figure 3.71 Left: configuration of the standard anode hybrid detector with two ThGEMs. Right: typical spectrum obtained with the configuration of the left, with Fe-55 irradiation in Ar:CH_4 - 30:70; the gain is ~3 × 10^4 and the energy resolution is ~38%.

a natural way to answer some of the issues experienced with the detectors tested so far and to improve their performance.

The new anode comes as an answer to reduce the risk created by electric discharges on the electronic readout components, especially the ones used in the digital acquisition systems. This problem is also faced by many research groups, and a typical solution found in the literature is the so called resistive anode [154, 155]. However, the production techniques for the typical resistive anodes have poor results when applied to large areas, and so another alternative had to be contemplated.

The capacitive[‖] anode is conceptually inspired in the resistive anode introduced by the MAMMA project [156, 157] but uses an insulating layer of standard fiberglass (FR4) instead of the resistive coating, creating a capacitive coupling between the segmented anode and the readout (see figure 3.72). By using standard fiberglass the uniformity of the layer for surfaces of 300 × 300 mm^2 and larger can be achieved with more certainty.

As the scheme at the left of figure 3.73 illustrates, the new anode is made with two aligned planes of metallic pads in each side of the insulator. The top pads (blue) act as the effective detector anode; the voltage difference between them and the micromesh defines the Micromegas amplification field. The signal is actually measured from the bottom pads (red), induced by the capacitive coupling with the top ones. In practice the readout chain is operated in much the same way the standard anode hybrid chamber does: with the analog chain, the signal from a group of 16 pads is collected through LEMO connectors to the preamplification board, or terminated with resistors when idle; the digital acquisition, on the other hand, reads the signal from each bottom pad individually.

An advantage of the capacitive anode is that one can change the way the HV is applied to

[‖]It remains a resistive anode in the sense that there is a coupling mediated by a resistor, but to distinguish it from the common resistive anodes we focus on its capacitive coupling

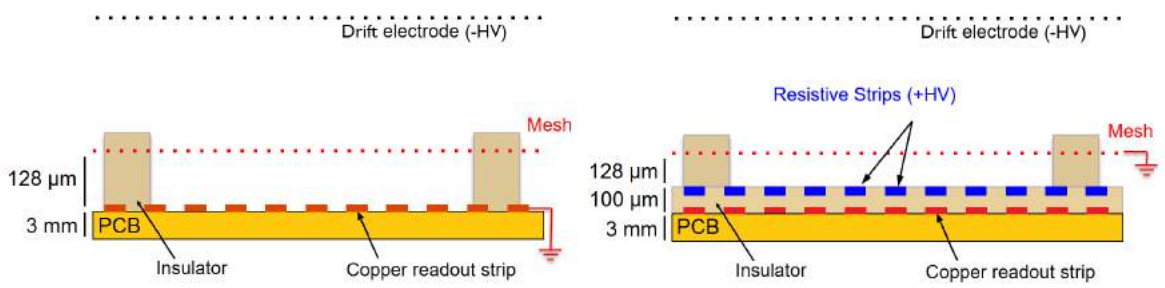

Figure 3.72 Comparison between the standard (left) and capacitive (right) anode architectures. The use of the grounded mesh in the latter case is not required by its design, but merely the illustration of the choice used in our case.

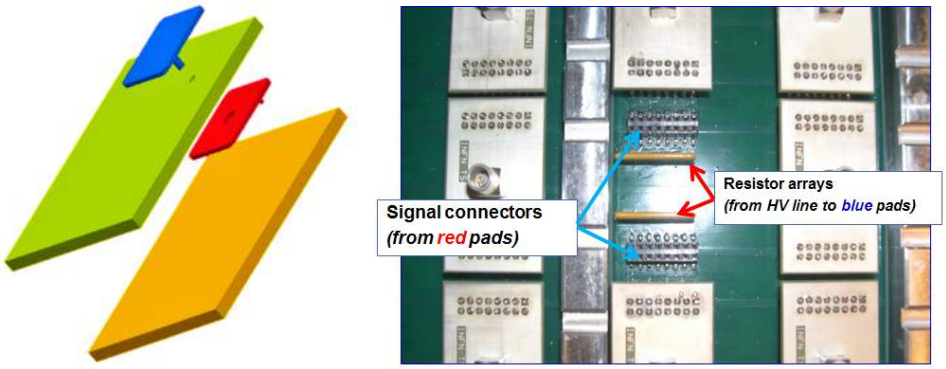

Figure 3.73 Left: illustration of the elements in a single pad of the capacitive anode, where the blue pads face the micromesh and have their voltage set by a connection through a hole in the red pads; the red pads give the signal output to the readout chain. Right: picture of the back of the chamber where the desired coupling resistance can be placed between the readout pins.

the Micromegas, since the electric anode and the readout pads are now separate components. Therefore, the mesh of the Micromegas can now be connected to the electrical ground, and a positive HV bias can be supplied to the top (blue) anode pads. As a consequence, the whole hybrid detector can be operated at lower absolute voltages in each electrode. The HV is supplied to the anode pad through a hole in the readout pad (bottom/red). The connection between the anode pad and the power supply is mediated by a 100 $\mathrm{M}\Omega$ resistor, introduced in the back of the chamber between the pin connectors, as shown in the right of figure 3.73. The value of the resistance was chosen to minimize collateral effects of discharges and propagation of noise signals between neighbor pads.

A Micromegas was built by the CERN workshop using as substrate the new type of anode, manufactured by TVR srl**. Macroscopically, the distinction between the two types of Micromegas is very difficult. A second chamber, very similar to the already described above, but to host the capacitive hybrid detector, was assembled and characterized. The chamber features a Kapton® window over the full active area of the detector, as can be seen in figure 3.74.

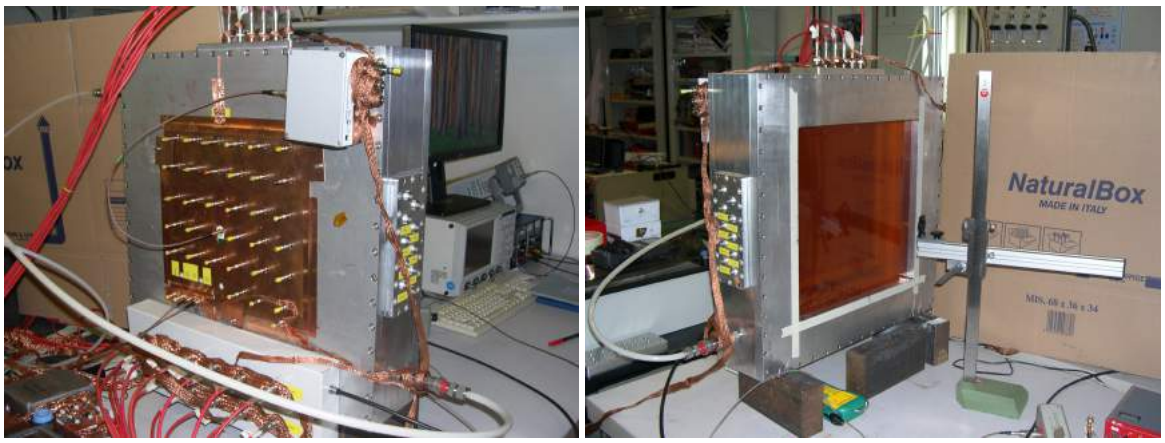

Figure 3.74 Picture of the back (left) and front (right) covers of the chamber with the capacitive anode hybrid detector.

The usual steps for the characterization were followed, so first the chamber including just the Micromegas detector is operated and tested. The result of the Micromegas characterization is plotted in figure 3.75 at the left, this time by varying the positive HV bias applied to the anodic pads while keeping the mesh grounded. The gain curve is perfectly compatible with the ones observed with the standard anode, but is surprising that the maximum value that can be achieved in stable conditions is much higher: gains up to ~10^4 are measured. A typical spectrum obtained during the exercise is shown in the same figure at the right.

Regarding the uniformity of the gain measured, the results obtained and illustrated in figure 3.76 show a variation of ~45% between lowest and highest gain spots. This value is not as good as the one obtained by performing similar measurements on the standard anode Micromegas, but is

**TVR srl, Schio, Italy

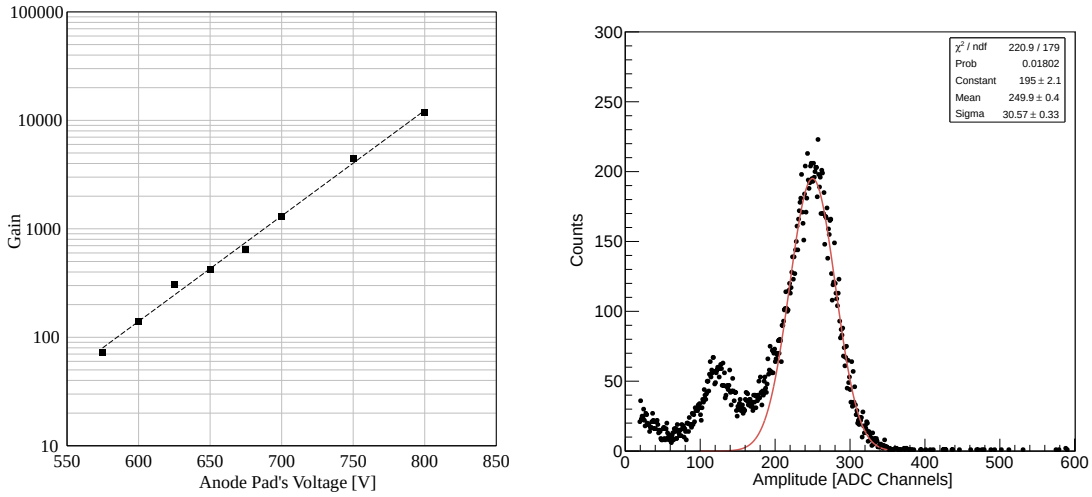

Figure 3.75 Left: characterization of the gain of the 300 × 300 mm^2 Micromegas as a function of the positive voltage applied to the anodic pads in the capacitive anode architecture. Right: example of a spectrum obtained during the characterization of the Micromegas with capacitive anode, with Ar:CH_4 - 30:70 under irradiation with the Fe-55 source. The mesh itself is grounded, while the anode pads are positively biased so that the Micromegas amplification field is ~55 $\mathrm{kV/cm}$. The energy resolution is 29% for a gain of ~2 × 10^3.

still a lot better than the gain uniformity of typical ThGEM structures.

The detector was then completed with the addition of two ThGEMs, as expected. Here however, the ThGEMs used had the implementation of two small changes that were designed to improve their performances and stability. During laboratory tests, it was often noticed that a high number of discharges occurred at the edges of the sectors of ThGEMs. In order to reduce that contribution and obtain structures which are more stable at higher voltage differences, a new design was implemented that removes the last line of holes at the edges of the electrodes. The second adaptation, illustrated in figure 3.77, was to increase the spacing between the electrodes of the ThGEM to 1.2 mm, and even in some of the pieces also to remove the major portion of the exposed insulator. That should reduce the capacitive coupling between the sectors and avoid discharge propagations.

The final capacitive anode hybrid detector was assembled using ThGEMs with 1.2 mm separation between sectors and no holes in the edges. The top ThGEM (ThGEM1) had the fiberglass removed from the intervals (see figure 3.82). Figure 3.78 shows a typical spectrum obtained with the detector described. The detector was then characterized in Ar:CH_4 - 30:70 by varying the voltages applied to all the three multipliers. All the characterization curves plotted in figure 3.79 match the expected behavior of the detector. In particular, one verifies that the variation of voltage difference applied in one ThGEM is indistinguishable from the same variation on the other. The detector

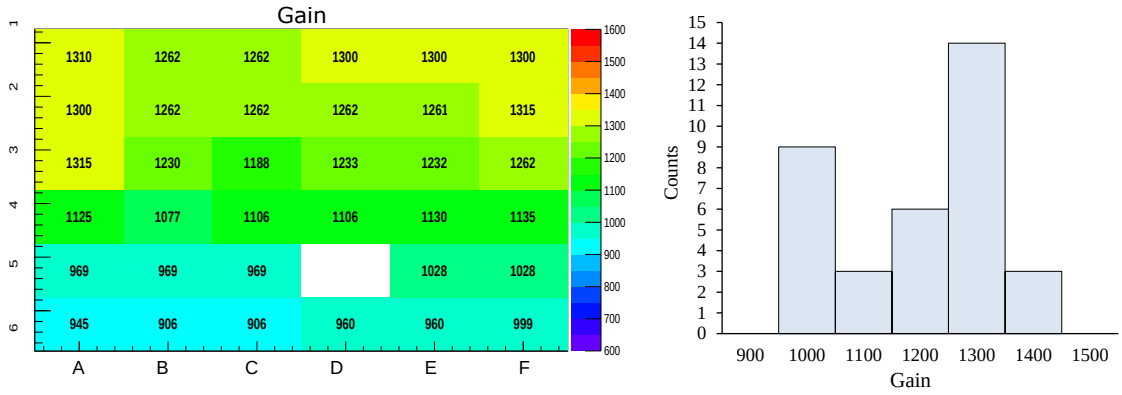

Figure 3.76 Left: map of the effective gain on the virtual sections of the capacitive anode Micromegas. Right: Histogram of the uniformity map presented at the left.

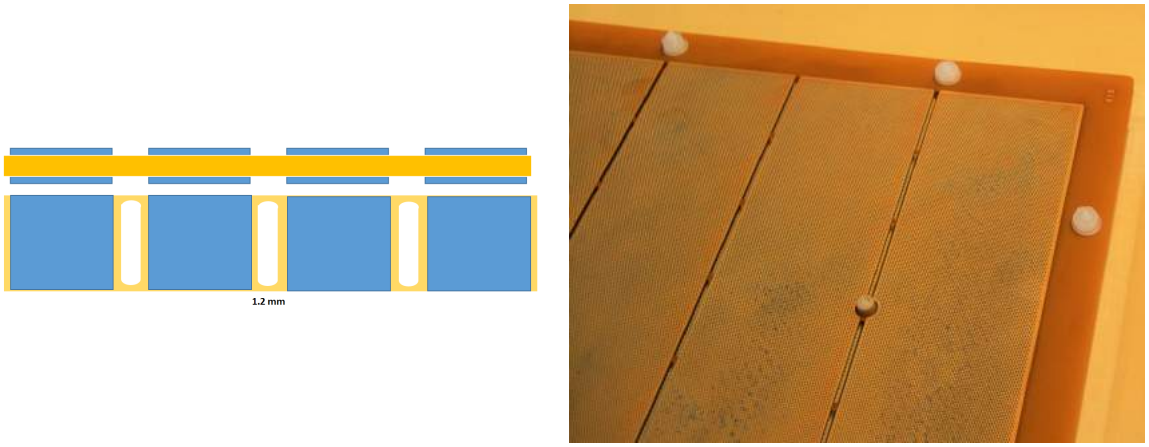

Figure 3.77 Left: schematic illustration of the new ThGEM architectures with larger (1.2 mm) separation between sectors and void of fiberglass in those regions. Right: photograph detailing the new design, with larger fiberglass-free intervals between electrodes.

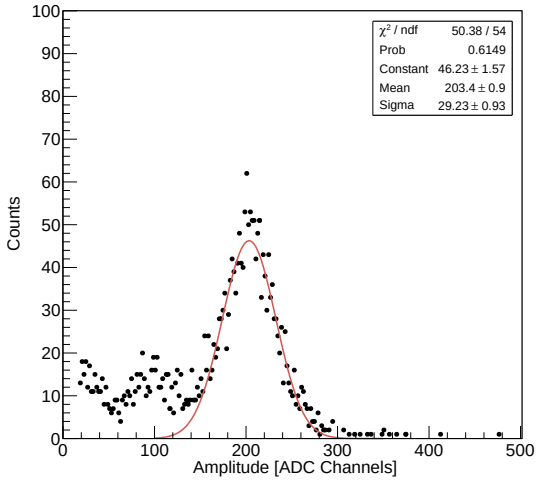

Figure 3.78 Example of a spectrum obtained with the 300 × 300 mm^2 capacitive anode hybrid detector with double ThGEM, with Ar:CH_4 - 30:70 under irradiation with the Fe-55 source.

achieved gains up to ~2 × 10^5 in stable conditions with Fe-55 irradiation.

3.6 Performance of 300 × 300 mm^2 Hybrid detectors under particle beam irradiation

The last test beam under the scope of this work had the purpose to evaluate the progress achieved in the production of large hybrid detectors. This test occurred, once more, at CERN's PS T10 beam line. The tests took place between August and September 2014 and used 5 $\mathrm{GeV/c}$ π^- particles.

3.6.1 Setup

Under scrutiny were the two large chambers whose study has been detailed in the previous section. As mentioned, all ThGEMs were produced under the procedures detailed in section 3.3, with careful inspection and characterization. The two detectors are very similar, but one uses a standard anode and the other the recently developed capacitive anode.

The disposition of the detection chambers in the beam line is illustrated in figure 3.81, while the configuration of the elements inside both detectors is illustrated in figure 3.82, on the left. The two ThGEM's holes are misaligned to reduce the IBF of the detectors, as prescribed by the analysis presented in section 3.1.5. The misalignment is achieved using properly designed spacers and border blocks and is verified using a laser guide, as shown at the right of figure 3.82.

Regarding the chamber covers, the Kapton® ones used in the laboratory tests are replaced by front covers including conical radiators identical to the one used in the previous test beam exercise (of 300 × 300 mm^2). One of the covers includes a remotely controled interceptor system as well.

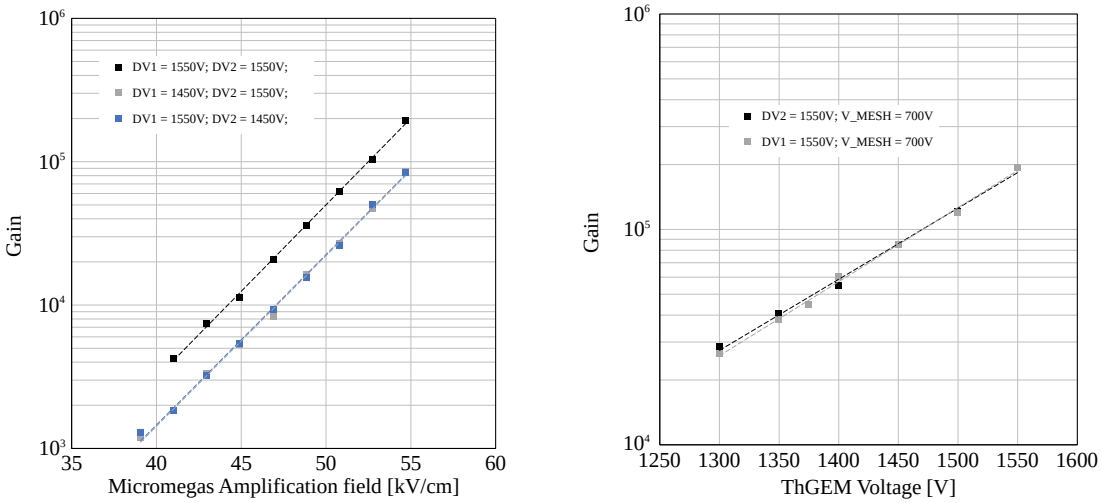

Figure 3.79 Left: characterization curves of the Micromegas in the capacitive hybrid detector for three different voltages applied to the ThGEMs. Right: characterization of the ThGEMs used in the capacitive hybrid detector, for a fixed positive voltage applied to the anode pads of 700 V. In both plots the two ThGEMs have indistinguishable behaviors.

Figure 3.80 Chamber containing the double ThGEM hybrid detector with capacitive anode.

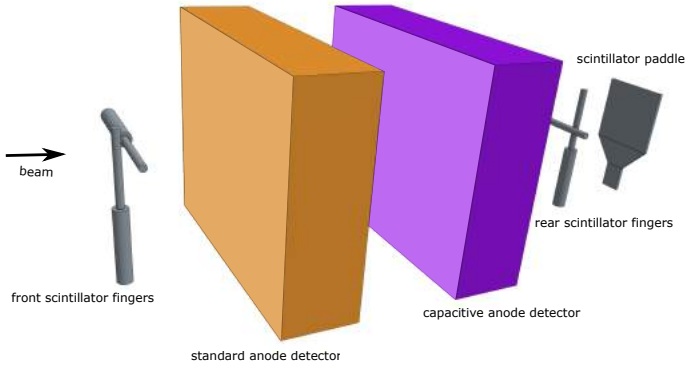

Figure 3.81 Scheme of the disposition of elements in the 2014 beam line.

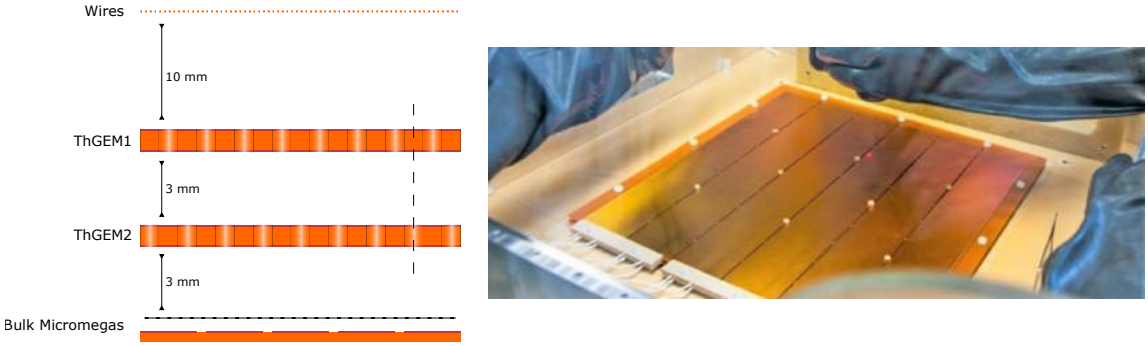

Figure 3.82 Left: scheme of the configuration used in the detectors under test. Right: photograph taken during the misalignment procedure, which is ensured with laser light.

Figure 3.83 Photographs of the beam setup with the chambers (left) and trigger scintillators (right).

The scintillator-based trigger system is identical to the one described in the 2012 test beam (see section 3.4). The same is true for the digital acquisition system, which is the standard CMAD chip plus the F1-TDC boards already described in the other beam exercises. It is, however, for the first time that two large detectors are simultaneously present in the beam area, while the front end electronics setup cannot be assembled in more than one chamber, thus limiting the digital data acquisition to a single detector at a time. A photograph of the chambers in the beam site, with the Dreisam boards already mounted on the capacitive detector, is shown in figure 3.83 at the left. In the capacitive anode chamber the protection boards for the electronics are not used, since the anode itself acts as capacitive shielding between the detector and the CMAD chip.

As for the analog data acquisition, besides the conventional Amptek MCA, in this test beam exercise a GANDALF [158] ADC system was also tested and used. This digitizer has several advantages including faster response, timing information retrieval, possibility of inspection and calibration of noise pedestals and the setting up of complex triggers, giving it a digital-like approach and versatility. Most of the analog data reported in this section was acquired with this device.

The chambers were continuously flushed with Ar:CH_4 - 30:70. During the test beam period, the temperature and pressure of the chambers was continuously monitored and frequent measurements of the gain of the detectors in predefined control voltages were done. This allows the compensation of performance fluctuations induced by changes in the environmental conditions.

The HV is supplied to the detectors from CAEN N1471H (remotely controlled) or CAEN N471A power supplies, and the top sectors of each ThGEM are powered independently, while the bottoms are fed via a HV splitter. The resistive dividers used before were abandoned in favor of increased flexibility in the voltage control. The Micromegas with capacitive anode has the field established by application of a positive HV bias in the anodic pads while keeping the micromesh grounded, as tested in the previous section with good results.

3.6.2 Results

The initial operation of the detectors under beam particle irradiation was first directed towards their characterization and evaluation of performance using the analog chain. The gain curves of both chambers were similar to the ones obtained from the laboratory tests, with the capacitive anode chamber showing a much better performance in terms of the maximum stable gain achieved. The standard anode chamber seemed to be limited in performance, not only due to the maximum field that could be applied to its Micromegas, but also in the first stage ThGEM, which possibly suffered some degradation when applying the Ni-Au treatment before CsI deposition. The major problem affecting the capacitive anode chamber was a erratic current leak measured in the anode pads when the HV was applied to them. This was eventually solved by flushing the high voltage connection boxes, on the back of the chamber, with warm nitrogen gas.

Figure 3.84 shows the histograms obtained while focusing the beam on one of the lateral sectors of the capacitive anode detector, for three different voltages applied to the Micromegas, and with

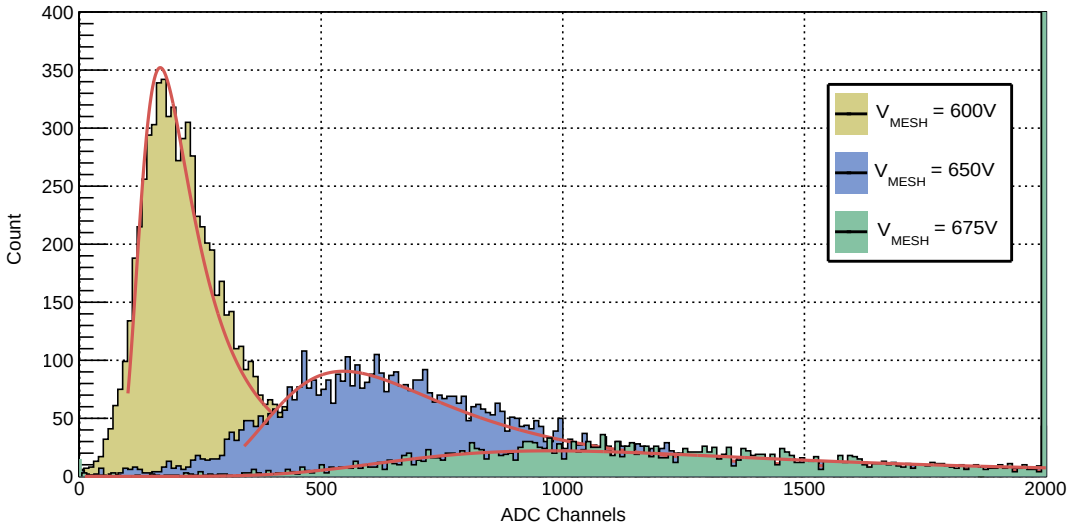

Figure 3.84 Spectra of MIP induced signals on the capacitive anode detector, acquired using the GANDALF ADC triggered by the 5-fold scintillation system, for three different voltages on the anode pads. The red lines are Landau fits of the histograms. A positive drift field was applied so the charges resulting from the ionization could be directed towards the amplification region. As a reference, the gain of the left spectrum is ~4 × 10^3.

a drift field guiding the charge to the amplification regions. The spectra clearly resemble Landau distributions. The absence of noise pedestals in the histograms means that for each trigger signal from a passing beam particle the corresponding charge produced is collected and amplified, i.e. the detector shows full detection efficiency for MIPs.

Drift scans, like to the ones performed in the test beams of the smaller ThGEM-based detectors, were repeated to consolidate the knowledge obtained then. Two typical spectra are shown in figure 3.85, one for a mild negative drift field and another for a strong positive one. The results clearly indicate that most of the MIP generated charge is suppressed in the first case. In fact, as can be seen on the results of the drift scans plotted in figure 3.86, with a positive drift voltage below 100 $\mathrm{V/cm}$ the drop of signal amplitude is drastic. This result holds true for both hybrid chambers. Notwithstanding this difference regarding the tests with the smaller prototypes, the shape of the plots is quite resemblant of the ones obtained and shown in figure 3.31 in section 3.2, which show similar measurements. It is also very similar to equivalent results obtained by the PHENIX HBD [70].

Having concluded that the capacitive anode chamber was the one performing better (achieving higher gains while maintaining stability) the front end electronics was then installed on this detector and some tests were performed, still using the beam focused on a lateral sector. Figure 3.87 shows how the digital acquisition system confirms the high detection efficiency of beam particles: on the plot at the right, the multiplicity of events is at least 1 for >80% of the triggers. In those conditions, the stability of the detector is illustrated on the left plot, where only one drop in

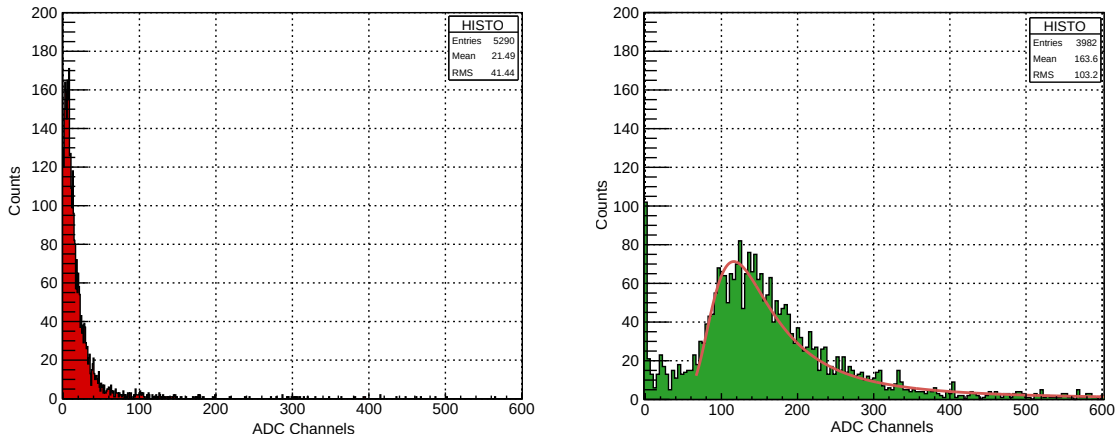

Figure 3.85 Spectra of MIP generated events with the detector operated with -100 $\mathrm{V/cm}$ (left) and +1000 $\mathrm{V/cm}$ (right) of drift field. The gain was roughly 10^3.

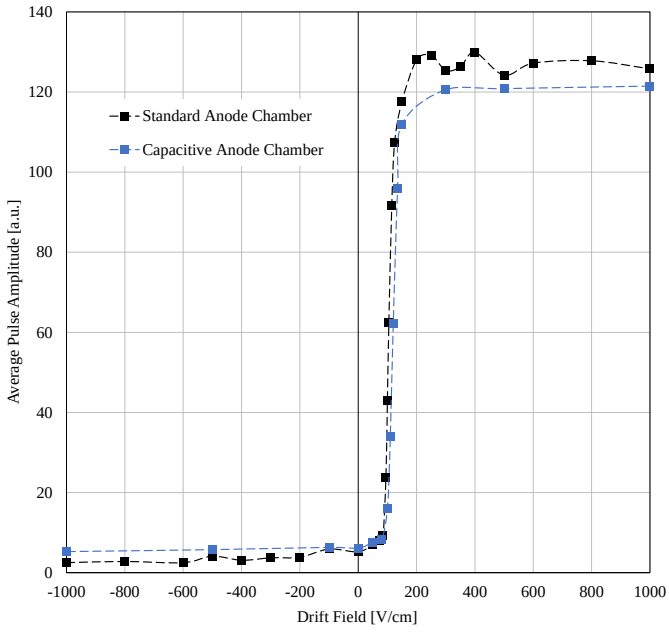

Figure 3.86 Results of the drift scan performed in each of the detectors. The average pulse amplitude is used as the monitored variable (vertical axis) since for lower fields the MPV of the Landau cannot be estimated.

detection efficiency is detected over 50 beam spills, with the average multiplicity being quite stable. The drop is most likely due to a discharge of the detector.

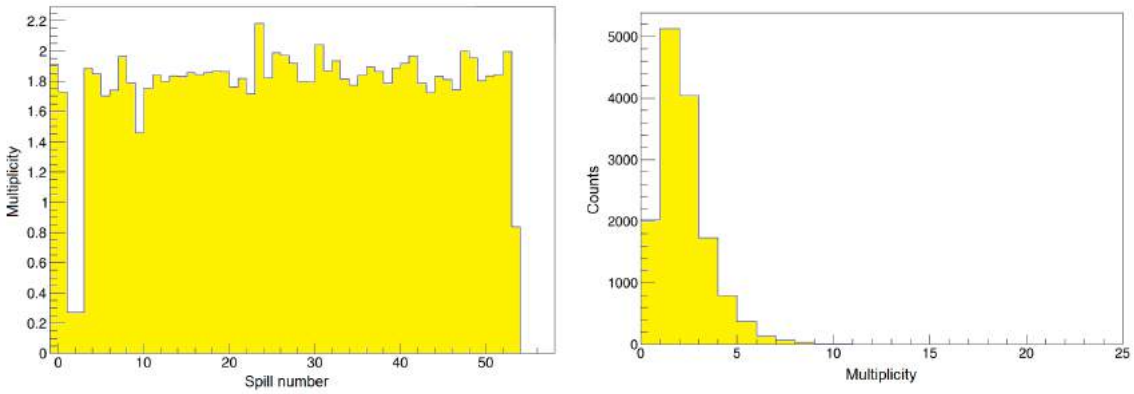

Figure 3.87 Left: average multiplicity of events detected per beam spill, with the capacitive anode hybrid detector. Right: histogram of the multiplicity of the events detected in the run of the left histogram.

The noise level for the digital measurements described above was unusually high. As a comparison, in the 2012 test beam exercise with large ThGEM-based detectors the amplitude thresholds set for the digital acquisition were ~3 fC, while in this exercise they stayed close to 15 fC. Even assuming that the large capacitance of the Micromegas now in use is a factor, it should not be the sole explanation for the exceptionally high noise level difference. A great effort was put into finding the origin of this problem. Firstly, it was noticed that the remotely controlled CAEN N1471H power supplies were significantly contributing to the noise level, and were promptly replaced by N471A models. A test was also done by mounting the front end electronics in the standard anode chamber, but the same noise figures were still present, which points to problems in the digital system itself. In the end, it was concluded that it was impossible to run with all the Dreisam boards active, and the worst sections of the readout in terms of noise level were disconnected.

With those constrains, the ability of the capacitive anode hybrid detector to detect Cherenkov light was evaluated. Figure 3.88 shows the result of the superposition of several events detected with the beam focused in the radiator of the detector, while the drift field is now set to zero. A large portion of the area of the detector readout is not active, but where the it is, a partial ring with very similar aspect to the one detected in the other beam exercises is seen, despite the very high amplitude threshold. That information is complemented with the spectrum in figure 3.89, obtained with the analog setup in a single readout section (16 pads). The Cherenkov light detected produced a typical single photon exponential histogram that allows the gain to be estimated at ~1.3×10^5, a remarkable result for detectors of this size under direct beam irradiation.

The great performance of the detector is also evident in the time response. If one recalls past beam exercises, the time histogram of the detected light had often a delayed contribution, indicating inefficient extraction of photoelectrons. However, as shown in figure 3.90 at the left, this

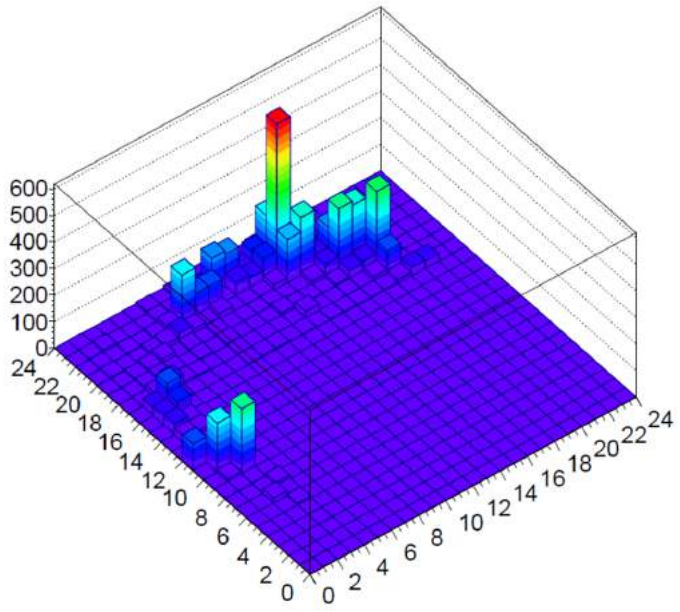

Figure 3.88 Accumulation of events detected with the beam focused on the radiator, with an amplitude threshold of ~12 fC, and zero drift field. The partial corona of light that is seen matches the expected position for Cherenkov light detection.

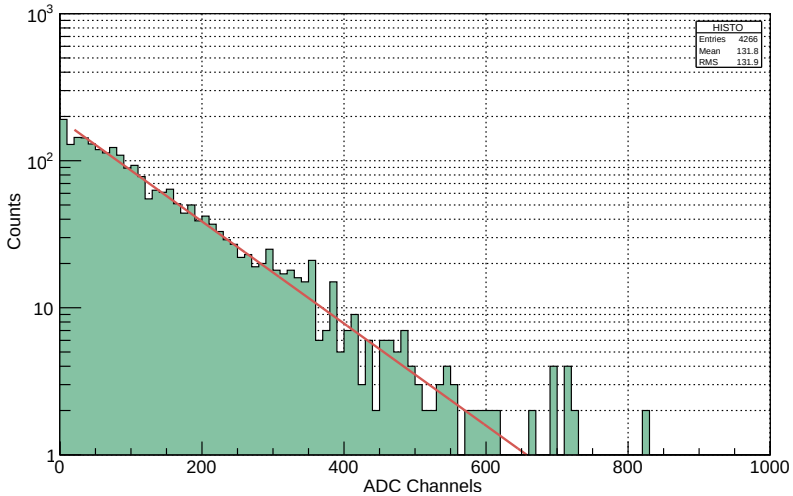

Figure 3.89 Cherenkov light spectrum obtained with the hybrid detector, with null drift field. The estimated gain is at ~1.3 × 10^5. The data was collected via the analog chain.

time the timing resolution is ~7.2 ns and the time response is very symmetric, indicating efficient photoelectron extraction. The corresponding partial ring from the same run is shown at the right of the same figure. Even though only part of the readout is active, one can still extrapolate that the rest of the detector shows a similar response. The reason for such improved performance in extraction efficiency is most likely due to the use of a gaseous mixture with a higher methane content compared to previous test beams.

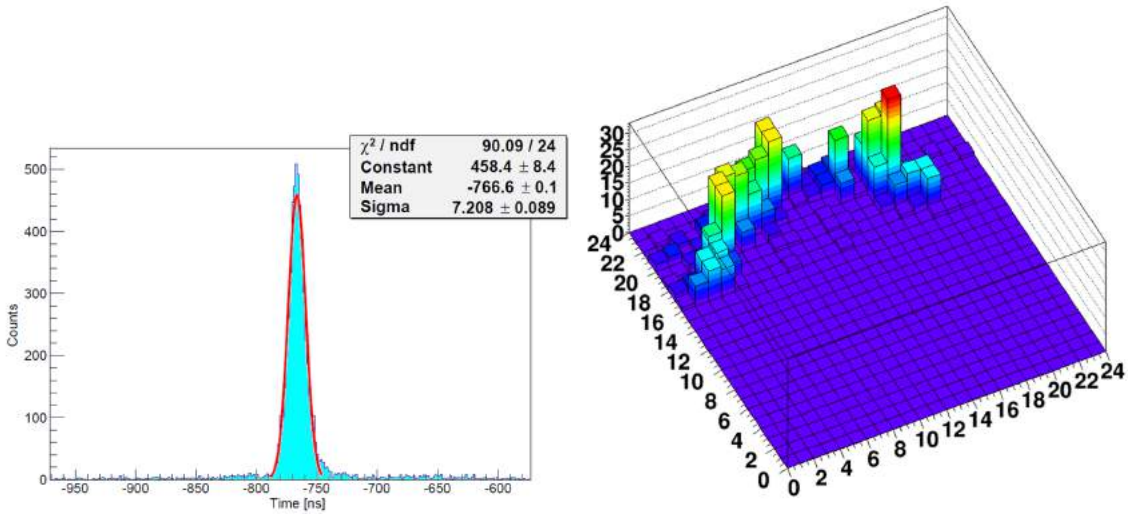

Figure 3.90 Time response of the detector in the optimal operation conditions described in the text during one long run (left) and respective 3D illustration of the superimposition of the events (right).

During a very long run the photon detection multiplicity was evaluated, with good results confirming the efficient operation in Cherenkov light mode. The histogram of the multiplicity is shown in figure 3.91 at the left, and shows ~80% of the triggers leading to the detection of one or more hits. Considering that less than half of the detector's area is being read and the high threshold used, this is better than expected. In the same figure at the right the average multiplicity per beam spill is shown, so the detector stability can be studied. In the 400 spill run, only 10% of the spills suffered from performance loss due to electrical discharges.

A final exercise was done, using the remotely controlled interceptor and the analog readout chain, to confirm the nature of the events detected: the interceptor is designed so its movement crosses the expected corona of light emitted by the radiator, so if the events detected are indeed due to Cherenkov light as expected, a drop in the measured multiplicity must occur when changing the interceptors position. Figure 3.92 shows the result of the test, confirming that the events are originated by Cherenkov light detection.

Finally, to prove the possibility of the reversed drift field configuration in the hybrid detector, a photon multiplicity drift scan is also performed. The results, shown in figure 3.93, once again point to a maximum efficiency of photon detection when the drift field is very weak, and dropping only

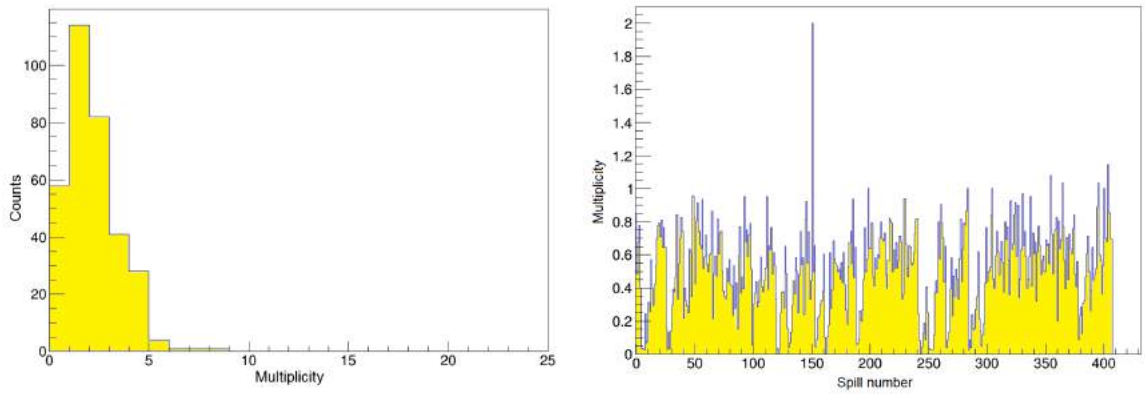

Figure 3.91 Left: hit multiplicity of the events detected during a long run. Right: stability of the multiplicity of events over a long run.

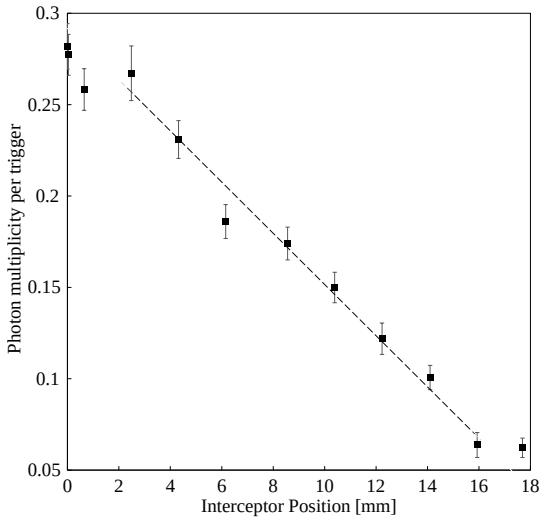

Figure 3.92 Monitoring of the multiplicity of events as a function of the position of the interceptor, showing a behavior compatible with Cherenkov light detection.

mildly when a reverse bias is applied. The result confirms expectations and is a good indication for the future adoption of the Hadron Blind principle.

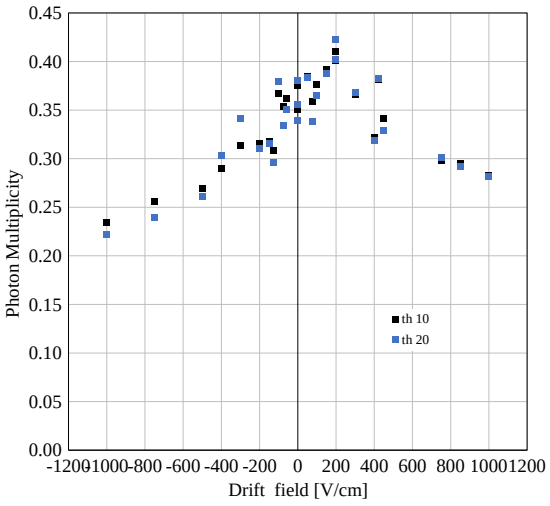

Figure 3.93 Photon multiplicity per trigger as a function of the drift field.

Concluding, the results of this test beam exercise were compromised by a defective performance of the digital acquisition system, with thresholds set at levels which are far from the ones expected in normal working scenarios. That said, the possibility that with such predicaments the detectors still presented acceptable data was a good indication. The fact that detectors of 300 × 300 mm^2 active area successfully detected Cherenkov light with high efficiency, under direct beam particle irradiation, in stable conditions, at an estimated gain higher than 10^5, is a very motivating result. With such results, the choice to use double ThGEM hybrid detectors with capacitive anodes for the RICH-1 upgrade was settled.

3.7 Towards 600 × 600 mm^2 Hybrid Detectors

Envisaging the first phase of the RICH-1 upgrade, four 600 × 600 mm^2 active area detectors have to be produced and assembled. Those detectors will be larger versions of the ones tested in the previous section, in particular of the chamber with capacitive anode, which produced the best results. The last months covered by this work were devoted to the development of 600 × 600 mm^2 active area hybrid detectors, including the characterization of larger ThGEM structures.

Due to the proven benefits of the approach followed for the expansion to 300 × 300 mm^2 detectors described in section 3.3, the same steps will be adopted. The larger area of the detectors envisaged, however, make some of the methods used unpractical, such as the PCB thickness measurement with a micrometer. Instead, a Mitutoyo EURO CA776 coordinate measuring machine with a ruby touch probe (figure 3.94 at the right) will be used to evaluate the uniformity of the PCB foils. This system allows the fast measurement, with $\mu\mathrm{m}$ precision, of the thickness of 70 × 70 cm^2

foils. The result of one of such measurements is illustrated in figure 3.94 at the left, with the corresponding histogram of gain distributions at the center. It shows a foil with 2.3% of variation between thinner and thicker points.

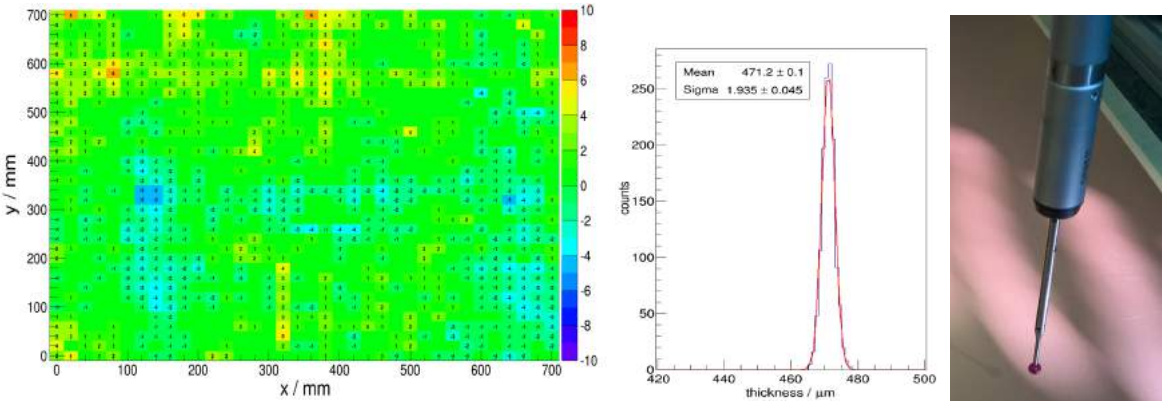

Figure 3.94 Left: thickness variation in μm, relative to the average, of a 70 × 70 cm^2 foil, measured at 2 cm steps with the Mitutoyo EURO CA776 machine, showing a variation of 11 μm (~2.3%) at the most. Center: histogram of the thickness measurement at the left. Right: ruby probe used in the machine.

After a large number of foils is inspected, the ones which obey the uniformity requirements of <3% variance (see figure 3.95 at the top right) were selected for ThGEM production. The full 600 × 600 mm^2 active area of the detectors is achieved by using two ThGEMs of 300 × 600 mm^2, side by side; the production and subsequent characterization of 600 × 600 mm^2 ThGEM pieces with the quality required would be unpractical and hard to achieve in useful time. The new ThGEMs are divided in 12 sectors 600 mm long; this way, the capacitance of each sector remains roughly the same as in the 300 × 300 mm^2 active area ThGEMs with 6 sectors. The distance between sectors is 0.6 mm of copper-free insulator material (the designs with void spaces introduced in the later pieces did not show any evidence of improvements, and therefore were discarded). As for the hole pattern, it remains mostly the same with the exception of the border holes at the edges of sectors: new calculations have demonstrated that instead of removing that line of holes to increase stability, the electric field uniformity is enhanced by replacing the standard 0.4 mm diameter holes by 0.5 mm at the periphery of the active region, as can be seen in the photograph of figure 3.95 at the bottom right. Two 300 × 600 mm^2 ThGEMs can be seen at the left of the same figure.

The characterization of the larger ThGEMs produced can, once more, be done by establishing readout sections to be read with the analog setup, which are irradiated using the Fe-55 source. A test chamber for single 300 × 600 mm^2 ThGEMs was built, as seen on the photograph of figure 3.96. In the same figure at the center and right, the result of a random ThGEM characterization exercise is shown, with maximum gain variations of 14%.

It can be seen that, even grouping pairs of ThGEM sectors, the number of divisions is high and a whole ThGEM requires therefore a long time to be characterized by such method. For that

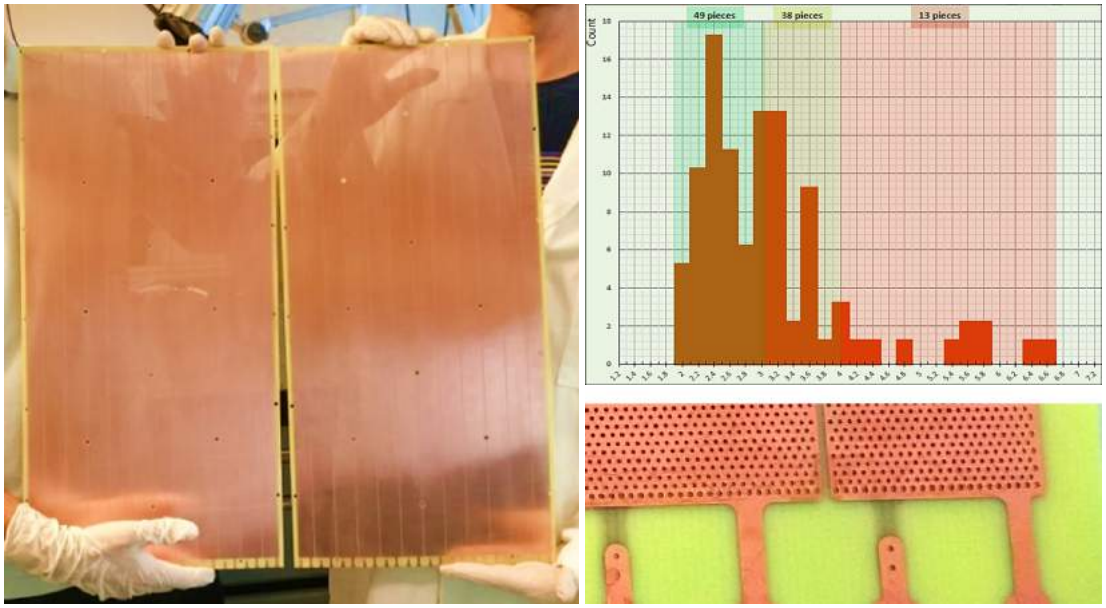

Figure 3.95 Left: two 300 × 600 mm^2 ThGEMs produced from selected PCB foils. Top right: histogram of the measured PCB foils uniformity, with 49 found to be below 3% of maximum variation. Bottom right: detail of the enlarged holes in the edges of the sectors of the new ThGEMs.

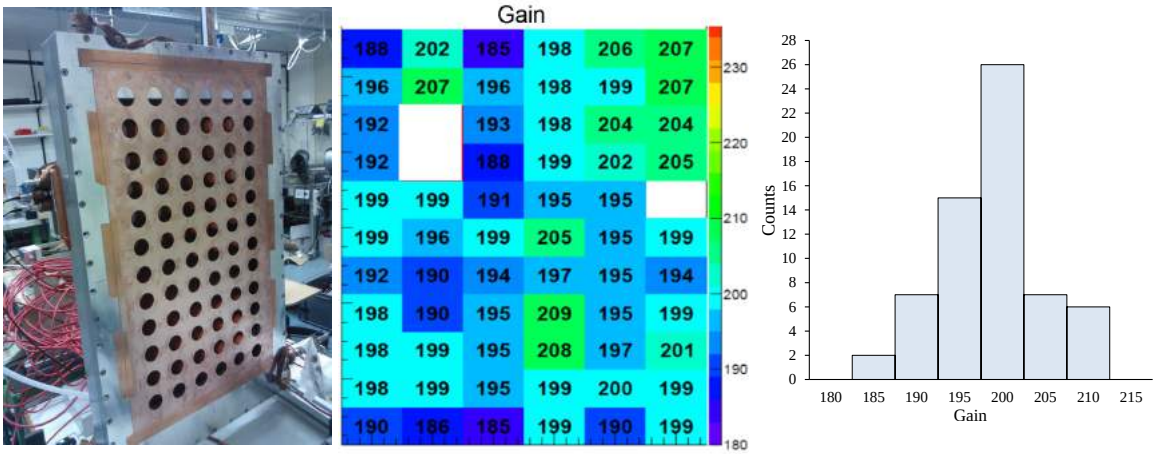

Figure 3.96 Left: photograph of the front of the characterization chamber for 300 × 600 mm^2 ThGEMs. Center: result of gain uniformity measurement of a ThGEM using the Fe-55 source and the analog chain (blank spaces due to noisy connectors). The gain variance measured in this particular case is 14%. The histogram of the gain is shown at the right.

reason, a more efficient method of characterization has been conceived by using an Amptek Mini-X X-Ray Tube System with gold target as radiation source, allowing the simultaneous irradiation of the full ThGEM area. Instead of the analog readout, a digital setup based on APV25 chips [47, 129] is used, which allows the acquisition at the single anode pad level. The back of the characterization chamber with 8 APV chips in the readout can be seen in the photograph of figure 3.97. At the right, a preliminary result of the characterization of a ThGEM using this system, allowing an irradiation rate of ~5 $\mathrm{kHz/cm^2}$. The characterization of ThGEMs is ongoing at the time of writing.

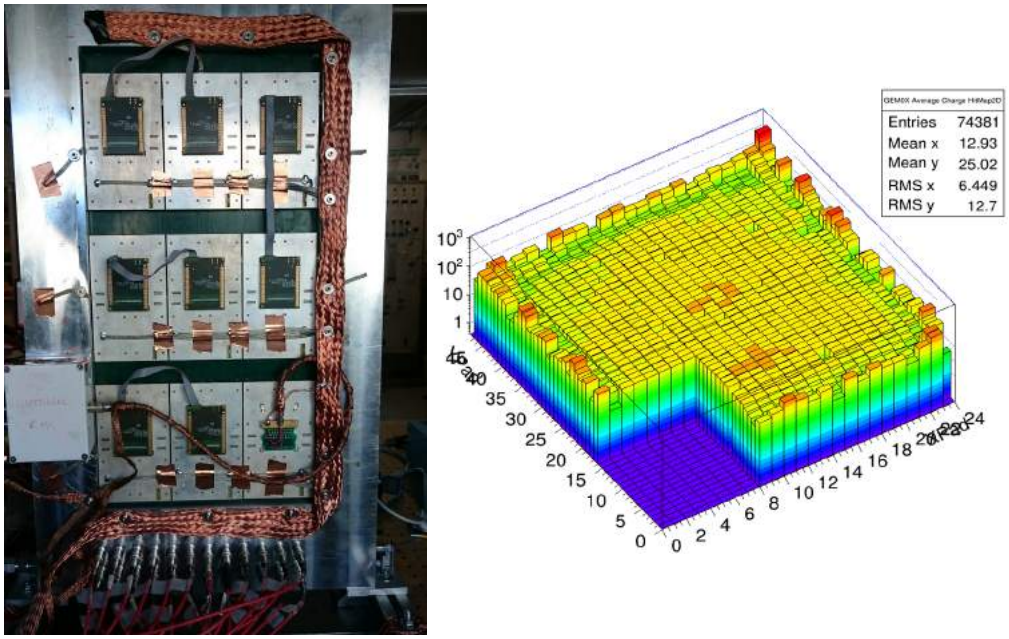

Figure 3.97 Left: photograph of the back of the characterization chamber with 8 APVs connected for use in the X-ray characterization setup. Right: preliminary result of the characterization of a ThGEM using the X-ray system at 15 kV and 200 mA. Using the Cu filter the result is a 8 keV X-ray peak, uniformly illuminating the detector at a rate of ~5 $\mathrm{kHz/cm^2}$. The 2D histogram shows the distribution of the average charge measured by the APV readout.

Meanwhile, a 600 × 600 $\mathrm{mm^2}$ detection chamber was built with two 300 × 600 $\mathrm{mm^2}$ Bulk Micromegas detectors with a standard anode (see figure 3.98). This chamber is a prototype to test the configuration of the final detectors to be implemented in the RICH-1, even though the capacitive version of the anode will be used. The use of two separate Micromegas detectors is preferred because it confines defects and discharges to half of the area. Besides, since each Micromegas will be coupled with a separate set of two ThGEMs, there is more freedom to optimize each half of the detector to obtain the best performance.

The large chamber just with the two Micromegas has been characterized with the standard analog chain and the Fe-55 source. The results, namely as the uniformity plot and corresponding histograms in figure 3.99, show that at the same voltage applied to the pads there is a ~6% discrepancy between the average gain of the two halves of the chamber corresponding to the two

Figure 3.98 Front cover of the 600 × 600 mm^2 active area chamber prototype (left) using two Micromegas detectors (center). At the right, the back part of the chamber showing the anode connections.

Micromegas structures, which is within the power supply tolerance. Each separate Micromegas shows a gain uniformity of ~14%.

Both the new ThGEMs and the Micromegas produced are showing improved uniformities and the possibility of achieving high stable gains. In the meantime, the production of the new large area capacitive anode Micromegas has been completed. The issue reported in the last beam exercise, where leak currents were measured when applying voltage to the anode pads, has been fixed: this problem was caused by a minor production defect of the high voltage pistes, which let them exposed to air; the humidity in the environment would then cause current leaks. The capacitive anode Micromegas will be characterized soon, and final tests of the new double ThGEM hybrid detectors will then follow. From then on, the first phase of the upgrade can proceed.

3.8 Conclusions

The studies reported along this chapter were initially focused on 30 × 30 mm^2 active area triple cascaded ThGEM-based detectors. The major principles that guide their operation were studied and some basic rules of their geometry and configuration were deduced. This allowed the detection of Cherenkov light under beam irradiation, even if with moderate performances, especially regarding the photoelectron extraction efficiency.

The partial success of the small prototypes justified the move to larger detectors, requiring the development of production and quality control procedures so 300 × 300 mm^2 active area ThGEMs with uniform thickness could be obtained. The introduction of a polishing treatment along with a chemical bath produced pieces with breakdown voltages close to the ones expected by the Paschen curve.

The test of the larger triple cascaded ThGEM detectors in beam environment allowed the detection of Cherenkov rings, a success in itself. However, once again the extraction efficiency was below expectations, as indicated by the asymmetric time response of the detectors. Also

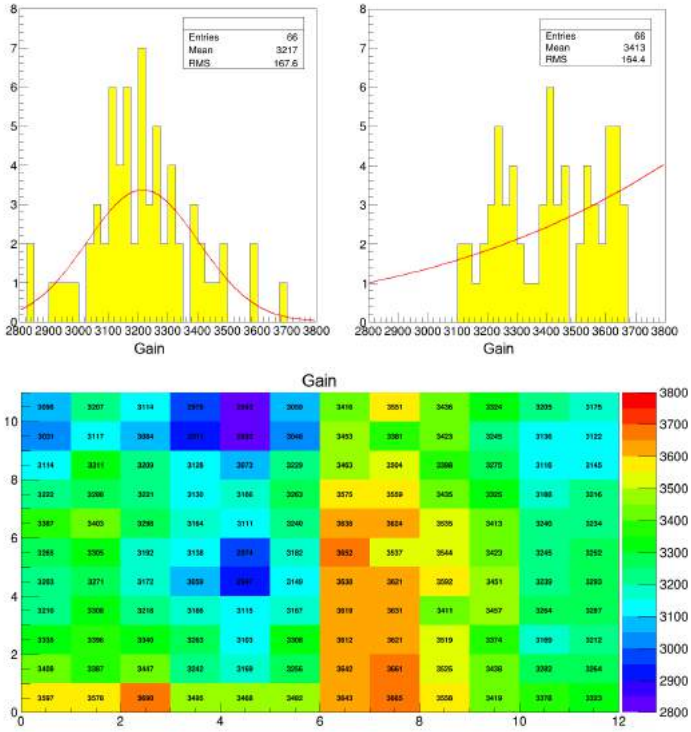

Figure 3.99 Gain uniformity of the two 300 × 600 mm^2 Micromegas detectors, each presenting a ~14% variation of gain, and a 6% discrepancy between them.

unsatisfying was the maximum gain achieved (~10^4).

The study of Hybrid detectors, composed of ThGEMs and Micromegas, showed very promising results with small prototypes reaching gains as high as 10^7 for single photon detection in laboratory conditions. Furthermore, the Hybrid detectors have an intrinsic ion entrapment capability, further increased by the misalignment of ThGEMs.

Two 300 × 300 mm^2 Hybrid chambers, one with a capacitive anode, were tested in beam environment. The detection of Cherenkov light was possible, namely in the capacitive chamber at gains higher than 10^5 while retaining stable operation and efficient photoelectron extraction as measured by the time response of the detector (temporal resolution ~7.2 ns). The increased efficiency can be justified by the use of gaseous mixtures richer in methane, while the gain is kept exceptionally high by the remarkable performance of the Micromegas. The tests also confirmed the possibility of using soft negative drift fields to attenuate MIP signals while retaining efficient single photon detection. The performance was mostly limited by electronic noise interfering with the digital acquisition.

These results were a definitive motivation to adopt hybrid detectors as the choice for the upcoming RICH-1 upgrade. For that purpose, the production and characterization of 300 × 600 mm^2 ThGEM structures has began. After the characterization of a sufficient number of ThGEMs is successful, the best pieces will be chosen for laboratory test in hybrid configuration. Finally, four 600 × 600 mm^2 hybrid detectors will be assembled in four 1200 × 600 mm^2 modules at the RICH-1

detector. Each module will remain with half of its detection area consisting of MAPMTs while the MWPCs in the other half will be replaced. As for the readout electronics, the APVs in use with the MWPCs will be installed on the new chambers, since they allow lower signal amplitude thresholds to be defined.

Chapter 4

Towards a Gaseous Compton Camera

Within the scope of the RD51 collaboration [9], gaseous detectors, namely MPGDs, are studied and developed for a wide range of applications beyond HEP. Nuclear Medical Imaging is one such application, where high interest exists in detection systems which can improve the performances of available PET and SPECT techniques [159], or possibly deliver more cost effective solutions. The major advantage of gaseous detectors is the competitive price, but they also offer fair energy resolution and great position resolution. The recently developed MPGD-based detectors can be operated under strong magnetic fields, making them good candidates for integrated operation with MRI devices.

The SPECT (Single Photon Emission Computed Tomography) is a very useful medical imaging exam. This functional imaging technique consists in the administration of a radionuclide to the patient which decays by emission of γ-rays. Very often Tc-99m is used, which emits 140 keV photons. The goal is then to obtain an image of the radiation emission distribution, conventionally using detection systems based in the Gamma Camera, or Anger Camera [160]. This imaging device uses a collimator to filter the direction of incoming γ-rays (as illustrated in figure 4.1), thus projecting an image in the detector, which usually consists of scintillator crystals and PMTs.

One of the major limitations of the Gamma Camera is the use of the collimator, which implies that a great fraction of the emitted photons is absorbed there and does not contribute to the image formation. Typically, only one out of every ten thousand photons emitted by the radioisotope crosses the collimator, i.e. the efficiency is often limited to 10^{-4}. Besides, the material of the collimator can be chosen so it is effective for a specific energy – such as 140 keV – but creates image artifacts if used with higher energy sources [159].

The Compton Camera was introduced independently by K. Pinkau in 1966 [161] and R. S. White in 1968 [162] for astronomy applications. Up to date, that remains the most relevant application of these systems, since for the higher energies of cosmic rays the limitations of the system are less relevant. The medical application of such systems was idealized by Todd et al. in 1974 [163]. The advantage of the Compton Camera is that it forms an image without the need of a collimator, presenting higher efficiency and therefore possibly enabling the reduction of the irradiation to

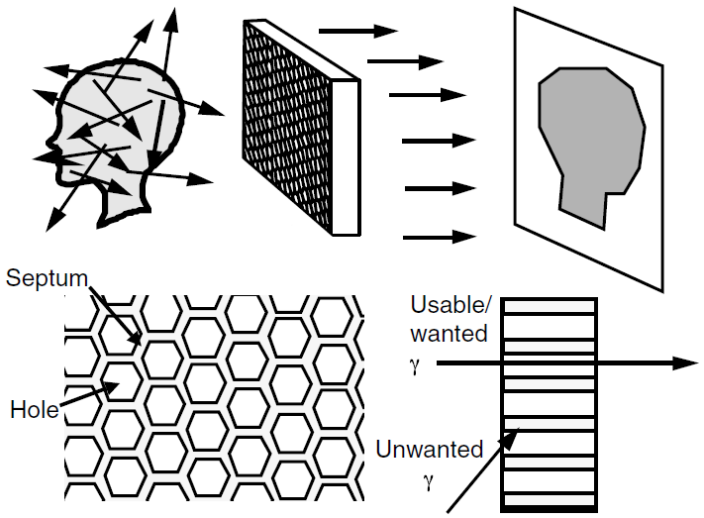

Figure 4.1 Illustration of the principle of collimation. By allowing rays to pass only in one direction the image is projected in the detector plane. [159]

which the patient needs to be subjected. Furthermore, It opens the way to the use of radioactive tracers such as I-131 or In-113m, which are currently not used due to the limited efficiency of the Anger camera for the energies of their decays (364 keV and 392 keV, respectively), or to the development of new ones [159].

This chapter analyzes the progress towards the development of a gaseous Compton Camera detector. The first section will introduce the basic principles of this type of imaging devices and where the device which is proposed fits in the state-of-the-art. The second section will present a few simulations and calculations, undertaken by the author, to estimate the performance and optimal parameters of a Compton Camera based in a gaseous detection medium. The third section will show the steps of development of this detector, and its initial characterization. The last section shows complementary studies on the possibility of incorporating a CsI photocathode in the detection medium, namely its implications for the statistical fluctuations of the efficiency; the last section is also a direct contribution by the author of this thesis.

4.1 Compton Cameras

4.1.1 Principle of Operation

A Compton Camera bases its working principle in kinematic (also called electronic) collimation. Instead of limiting the direction of the rays that are detected, the interaction of the photons in the detector medium by Compton scattering is analyzed and the original direction is reconstructed.

In a Compton scattering interaction, a photon (energy E_γ) is scattered by an inelastic collision with an electron (mass m_0, charge e), resulting in a new photon being emitted with a different energy (and direction) and the increase of kinetic energy of the electron. The classical analysis

regarding momentum and energy conservation of a two solid body collision leads to a general expression for the scattered photon's energy, $E_{\gamma'}$ [15]:

$$E_{\gamma'} = \frac{E_\gamma}{1 + E_\gamma(1 - \cos\theta)/m_0c^2}\,, \tag{4.1}$$

where c is the speed of light in empty space and θ is the angle between the scattered photon's direction and the initial trajectory, also called the Compton angle: θ = 0 for an unscattered ray, and θ = π in a backscattering event. The electron is assumed to be free and initially at rest, an approximation that often is not accurate enough and which will be discussed later in section 4.2. After the event, the recoil electron's kinetic energy is equal to the energy difference between scattered and original photon, $E_{e^-} = E_{\gamma'} - E_\gamma$, as conservation of energy dictates.

The differential scattering cross section for Compton events in a material with atomic number Z is described, with the assumptions made above, by the Klein-Nishina formula [12],

$$\frac{\mathrm{d}\sigma}{\mathrm{d}\Omega} = \frac{Zr_e^2}{2}\left(\frac{1}{1+\alpha(1-\cos\theta)}\right)^2\left(1+\cos^2\theta+\frac{\alpha^2(1-\cos\theta)^2}{1+\alpha(1-\cos\theta)}\right)\,, \tag{4.2}$$

where $\alpha = E_\gamma/(m_0c^2)$, and $r_e = e^2/(m_0c^2)$ is the classical electron radius, approximately 2.82 × 10^{-13} cm. The formula predicts a proportional dependence of the cross section with Z, and a decrease of the cross section value with increasing E_γ. As for the dependency on the scattering angle, it is best illustrated by the polar plot in figure 4.2 at the left: the cross section is higher for lower scattering angles, but for lower incident photon energies the backscattering probability increases.

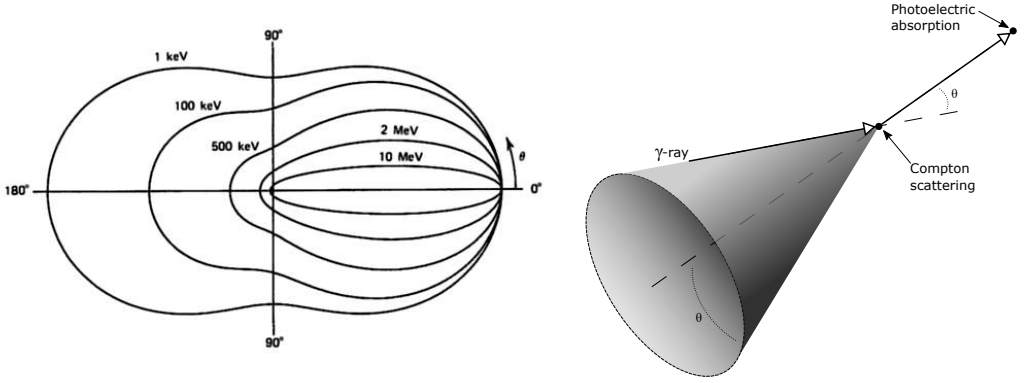

Figure 4.2 Left: polar plot of the scattering cross section as a function of the scattering angle, for different γ-ray energies [12]. Right: scheme of the principle behind kinematic collimation.

Kinematic collimation is obtained by studying a Compton scattering interaction that occurs in a detector. The recoil electron will quickly interact and deposit its kinetic energy in the detector, allowing the measurement of the position of the scattering event and the energy lost by the photon. Then, the scattered photon needs to be collected so its energy and position can also be

retrieved. That is accomplished in a photoelectric interaction with the medium, where the resulting photoelectron will convey its energy (~$E_{\gamma'}$) and position to the detector.

The position information allows the reconstruction of the scattered photon's trajectory, while the energies deposited in each interaction allow the deduction of the initial Compton angle by adaptation of the formula from equation 4.1 to:

$$\cos\theta = 1 - \frac{m_0 c^2 E_{e^-}}{(E_{\gamma'} + E_{e^-})E_{\gamma'}}\,. \tag{4.3}$$

The angle estimated by the above equation implies that the direction of the initial photon must have originated within the surface of a cone with vertex at the point of Compton interaction, whose axis is the direction of scattered photon and with aperture of θ. The process is illustrated at the right of figure 4.2. The intersection of several cones obtained with multiple events will result in an image of the source distribution with 3D information, unlike the conventional method using a collimator that only reproduces a planar image. An illustration of the principle and an example of a reconstructed image with a Compton Camera are given in figure 4.3.

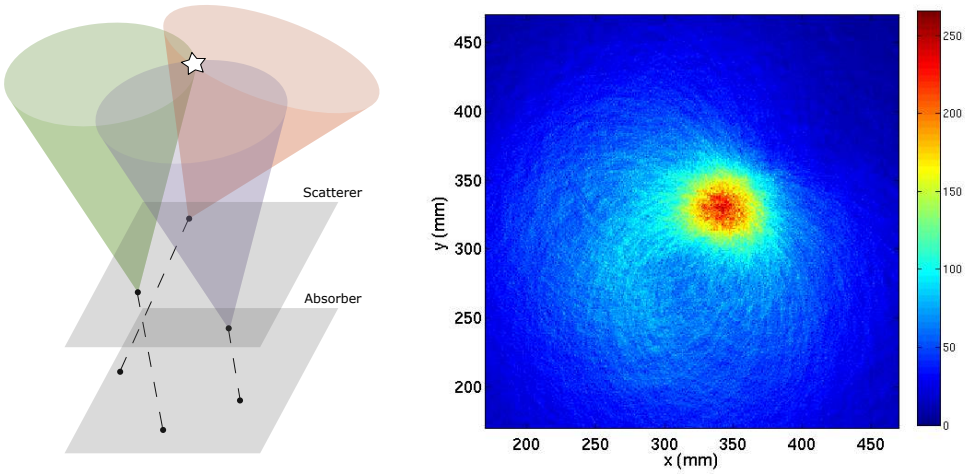

Figure 4.3 Left: illustration of the principle of reconstruction in a Compton camera, where the intersection of multiple cones should occur in the radiation sources. Right: example of a reconstructed projection image from a Compton Camera [164].

4.1.2 Compton Camera detectors

The most conventional Compton Camera, by far, uses two stages of semiconductor detectors: a scatterer detector where Compton interactions take place and an absorber where the scattered photon is collected [164–169]. A typical detector in such configuration is illustrated in figure 4.3 at the left. There are two major reasons for the separation of the device in two steps: first, the identification of the events becomes virtually unambiguous, since even in the low probability that a γ-ray would backscatter in the absorber detector and is absorbed in the first stage, by performing basic analysis taking into consideration Compton kinematics one is able to exclude such

occurrences; second, each interaction process has competing requirements, with heavier (higher Z) materials being preferred as absorbers due to higher cross section of photoelectric effect, and lighter elements not only having higher Compton scattering probability but also presenting less Doppler broadening (an effect discussed in the next section).

Semiconductor detectors are of recognized importance for this application because of their intrinsic excellent energy resolution, and potential to achieve great position resolutions by using segmentation and pulse shape analysis techniques [166]. Among them, the notable high purity germanium (HPGe) detectors stand out [164, 165, 167]. Besides HPGe, Cadmium Zinc Telluride (CZT) [168] and Cadmium Telluride (CdTe) [170] are also very promising due to high photoelectric absorption cross section. HPGe has the drawback of needing cooling systems or liquid nitrogen to operate properly, but most of the alternatives have low charge carrier mobility and shorter life time. Semiconductor crystals of Sodium Iodide (NaI) [169, 171] and Caesium Iodide (CsI) [166] are also investigated as absorber materials, which can be used coupled to photosensor arrays. For scatter detectors, Silicon (Si) [171–173] and Lithium drifted Silicon (Si(Li)) [165] are common choices, along with HPGe as well [164]. Silicon, not only is a great scatterer due to low atomic number, also presents the lowest Doppler broadening among alternatives such as Ge or even the gaseous Ne [174].

Besides the more popular two stage detectors, some attempts have been made to obtain a single stage detector to use as a Compton camera [175–177]. That raises the need to find an intermediate material that at the same time shows good Compton scattering and photoelectric absorption coefficients. Besides, it requires more complex routines and analysis to obtain efficient event identification. On the other hand, a single detector has the advantage of being more compact, easy to produce and since it acts as both scatterer and absorber can potentially detect photons that scatter in any angle θ, resulting in increased sensitivity. This type of devices commonly uses either Ge [175] or CZT [176, 177].

Compton Cameras with gaseous detectors

Since the introduction of the Compton camera concept that gaseous detectors have been suggested as alternatives to solid state devices since they would allow the use of large detection volumes. Noble gases, and particularly xenon, were the main choice for this application with drift chambers, but their limitation in energy resolution limited their application to astrophysics, for energies higher than 1 MeV [159].

An interesting approach using gaseous detectors has been more recently suggested envisaging medical imaging [178–181]. It consists in a two stage Compton Camera where the absorbers are scintillator crystals such as NaI(Tl) [178] or GSO [179] surrounding a gaseous scatter. The scatter is in fact a time projection chamber (TPC) with charge multiplication performed by a GEM structure. Besides the unconventional geometry, this detector is also remarkable for being able to track the direction of the scattering electron that originates from the Compton event, hence named

Electron Tracking Compton Camera (ETCC). That additional information limits the surface of the Compton cone to a specific direction, greatly improving the quality of the reconstructed images. An illustration of this system can be found in [180].

In general an ETCC may not be as sensitive as a solid state detector, but it allows the increase of the volume of the detector without too much effort and cost. A 30 × 30 × 30 cm^3 chamber with Xe or CF_4 at high pressure (several atm) provides detection efficiency on the order of a few percent for 500 keV γ radiation, much better than a common SPECT system [179]. Besides, the performance of the ETCC is the same in every direction, an advantage over small animal PET systems. An ETCC within a compact camera on a movable table has been demonstrated, with multi-tracer imaging capability and good spatial resolution. It is one of the best implementations of a Compton camera incorporating gaseous detectors so far, allowing the acquisition of impressive images from tests in small animals [181].

A single volume gaseous Compton Camera was achieved with the use of a Scintillation Drift Chamber (SDC) by Bolozdynya et al. [182, 183]. It uses the intrinsic multiplication of light in the detector by using low threshold electroluminescence noble gases, in particular Xe. In these detectors, the charge produced in the gas by a γ photon is accelerated by an electric potential beyond the ionization threshold, to an energy sufficient to produce electroluminescence, as explained in section 1.2.2. That light is then detected by photosensitive devices such as PMTs and gives 3D information about the location of charge generation, besides energy of interaction (see Figure 4.4). Due to the intrinsic multiplication process, a gaseous detector with 1000 cm^2 matches the energy resolution of a 1 cm^2 semiconductor detector at room temperature [159].

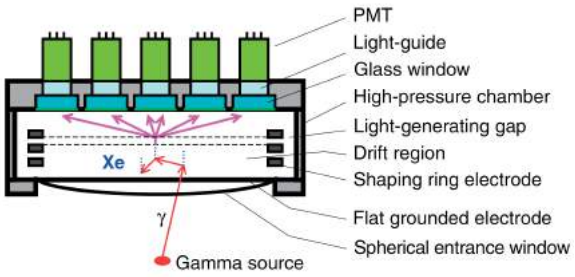

Figure 4.4 Schematics of the scintillation drift chamber proposed by Bolozdynya [159].

The compactness and performance of the semiconductor detectors is hard to match. Still, gaseous detectors can offer fair performances at much more reasonable costs. Also, because charge mobility is not a limiting factor, higher detection volumes can be designed, with the corresponding increase in sensibility. The SDC is the most promising solution to implement a Compton Camera with a single gaseous volume, for a variety of reasons:

- allows 3D position measurements for low-energy interactions;

- low detection threshold (~1 keV) of Compton scattering events;
- competitive energy resolution;
- a flexible design for building detectors with very large field-of-view;
- operation at high magnetic fields.

This is the motivation behind the attempt to create a gaseous Compton Camera based in the Bolozdynya design. The question of which gas medium allows a better compromise between Compton cross section without significant Doppler broadening and good photoelectric absorption probability is discussed in the next section, and some calculations presented.

4.2 Calculations of Compton Camera performance with different gases

Even though dismissed so far in this chapter, one of the most limiting characteristics of a Compton Camera is the uncertainty introduced by the Doppler broadening effect. This effect occurs because the electron which undergoes Compton scattering is not really at rest in the laboratory environment. Even though in some cases it can be negligible, the electron has a finite kinetic energy to start with, related to its orbital motion. In practical applications such as Compton Cameras this uncertainty in the initial electron energy means that instead of well defined Compton angles, there is a statistical distribution around the expected electron-at-rest value. This then translates to the image reconstruction, with the position resolution of the devices being severely affected in some cases.

The Doppler broadening tends to be worse in higher Z materials. As examples, Ge detectors lead to large broadening, while diamond is a very good material in this regard. Silicon is an intermediate option, as is the noble gas Neon [159].

Due to the importance of the effect, calculations were performed to study how different gases compare taking it into account. They are partly inspired by previous works [184, 185] where also solid state detectors are analyzed. However, the data regarding noble gases is not sufficient and often includes assumptions like detector geometry which are not intrinsic to the problem and do not fit the detector envisaged. Therefore, and in sake of more freedom of analysis, the calculations were made from scratch keeping the previous works as a reference.

To calculate the Doppler broadening effect, one has to consider a generalized version of the Klein-Nishina formula (equation 4.2) which does not assume an electron at rest. One of such equations, a relativistic Double Differential Cross Section (DDCS), was derived by Ribberfors [186], and can be stated as follows:

$$f_{\Omega} = \frac{\mathrm{d}^2\sigma}{\mathrm{d}\Omega \mathrm{d}E_{\gamma'}} = \frac{m_0 r_e^2}{2} \frac{E_{\gamma'}}{E_{\gamma}} \frac{\bar{X}_{KN}}{\Delta_k} J(p_z)\,, \tag{4.4}$$

where

$$\bar{X}_{KN} = \frac{E_\gamma}{E_{\gamma'}} + \frac{E_{\gamma'}}{E_\gamma} - \sin^2\theta\,, \tag{4.5}$$

$$\Delta_k = \sqrt{E_\gamma^2 + E_{\gamma'}^2 - 2E_\gamma E_{\gamma'}\cos\theta}\,, \tag{4.6}$$

and most other variables already defined in equation 4.2. As for $J(p_z)$, it is the Compton profile, a crucial variable which implicitly introduces the Doppler broadening effect to the results. The Compton profiles are obtained from available literature relative to the elements one wishes to analyze, and applied by calculating p_z as

$$p_z = \frac{E_\gamma E_{\gamma'}(1-\cos\theta) - m(E_\gamma - E_{\gamma'})}{\Delta_k}\,. \tag{4.7}$$

In fact, one can obtain the profiles $J_n(p_z)$ for each n-subshell of an atom, and thus analyze the DDCS for each. The profile for the atom as a whole can be calculated by the sum of each shell's profile weighted by the expected number of electrons in that shell. For the present work, the $J_n(p_z)$ values used in the calculations were obtained from reference [187].

It is often more practical to deal with the Compton angle θ defined in the plane of scattering than with the solid angle Ω. In that case, one can rewrite the DDCS as

$$f_\theta = \frac{\mathrm{d}^2\sigma}{\mathrm{d}\theta\mathrm{d}E_{\gamma'}} = 2\pi\sin\theta f_\Omega\,. \tag{4.8}$$

The calculations presented below were performed with the software Matlab®, by Mathworks®. They consist in the creation of a matrix M_{f_θ} indexed by values of $E_{\gamma'}$ in one coordinate and θ in the other, for each subshell of an element. The matrix value $M_{f_\theta}(\theta, E_{\gamma'})$ corresponds to the differential cross section for those conditions, i.e. to the probability that a photon with energy E_γ interacts in a Compton event with an electron from the shell, being scattered at an angle θ with energy $E_{\gamma'}$. The matrix obtained for xenon irradiated with 140 keV γ-rays is illustrated in figure 4.5.

The DDCS derived by Ribberfors uses the so called impulse approximation, which relies on the assumption that the energy transmitted to the recoil electron by the γ-ray is far greater than its binding energy to the atom. For elements such as Xe, with large shell binding energies, and for events with small Compton angles those conditions might not be met and the precise calculation and simulation of such interactions is complex. Therefore, a selection criterion was adopted where an atom's shell can only contribute to a Compton interaction which deposits in the recoil electron the required energy to extract such electron. The shell binding energies for the different elements were obtained from reference [188].

The result of implementing the shell selection criterion is illustrated in figure 4.6 at the left. The curves are obtained by calculating, for each Compton angle, the corresponding scattered γ-ray energy using the electron-at-rest approximation (equation 4.1). Then, the DDCS matrix is evaluated at such energy, producing the Doppler broadening profile centered in the Compton angle (as illustrated in figure 4.7 for θ = 60°); the standard deviation of the angle distribution can thus be obtained. It is observed that by using the binding criterion the Doppler broadening is reduced

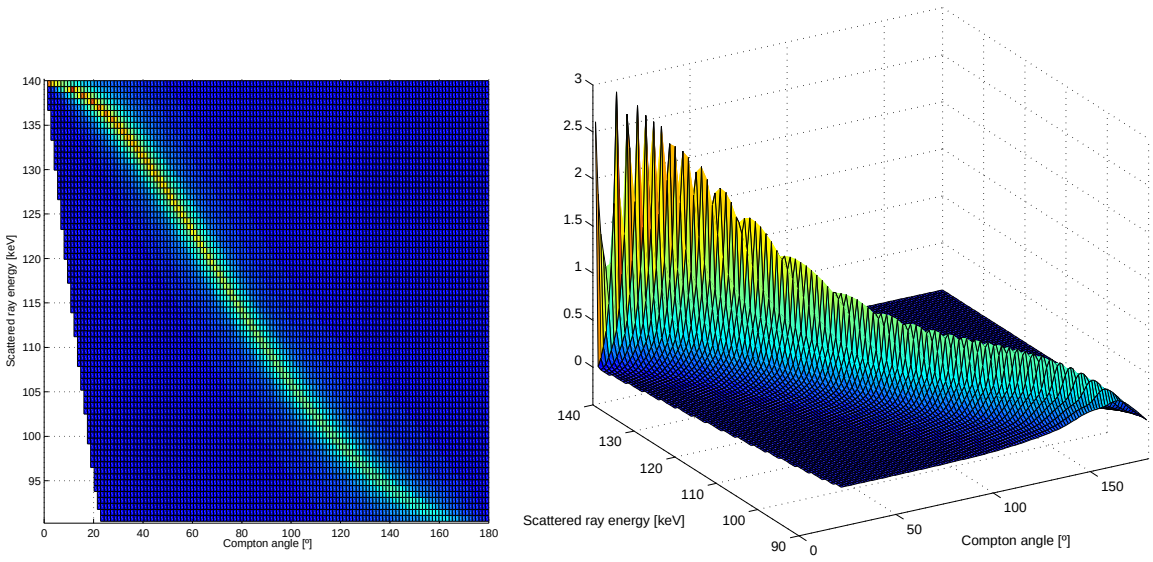

Figure 4.5 DDCS matrix calculated with Matlab®, for xenon and 140 keV incident γ-rays. The matrix values represent the probability of a scattering with the respective θ and $E_{\gamma'}$ parameters. The matrix is shown in a colored 2D projection (left) and three dimensionally (right).

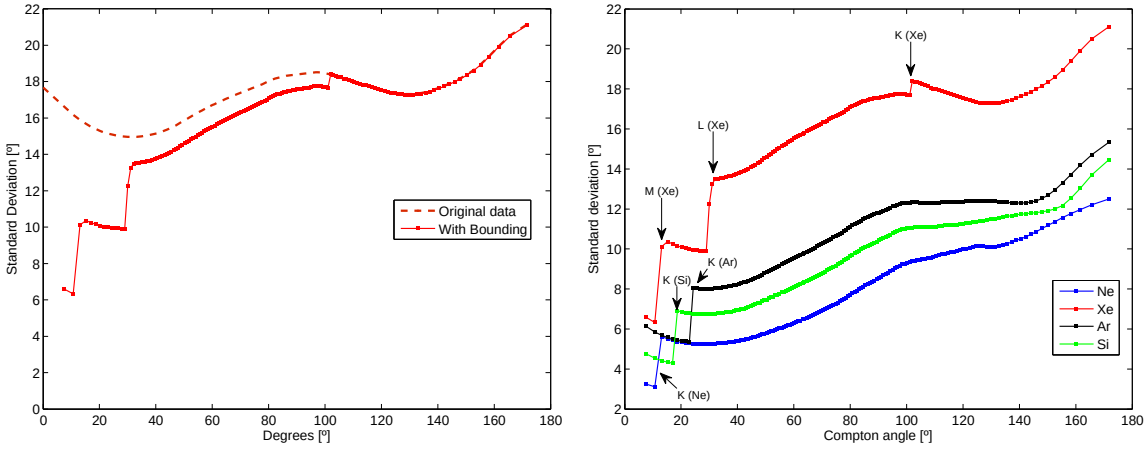

Figure 4.6 Left: standard deviation of the angle distribution caused by Doppler broadening, as a function of the Compton angle, for the original DDCS matrix (dashed line) and with the inclusion of the electron binding selection criterion. Right: standard deviation of the angle distribution caused by Doppler broadening, as a function of the Compton angle, for the noble gases Ne, Ar, Xe and for silicon. Labels indicate the shells responsible for the edges.

at angles where inner shells do not contribute to the process. This is a consequence of having broader Compton profiles for such shells, such as K or L. At the angles where certain shells start to contribute, a sharp edge is observed in the standard deviation.

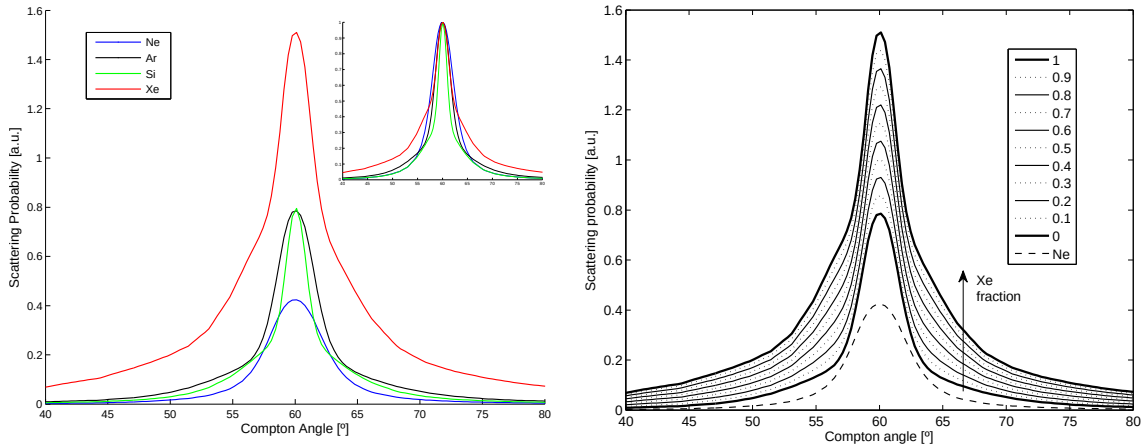

Figure 4.7 Left: Doppler broadening effect around a 60º Compton angle, for Ne, Ar, Xe and Si (the inset shows the plot normalized at the peak). Right: evaluation of the Compton profile at 60º for Xe fractions of a Ar:Xe gaseous mixture (0 is pure argon).

At the right of figure 4.6 the Doppler broadening effect is compared between Ne, Ar and Xe, as well as Si. The curves show that xenon's Doppler broadening is more pronounced, especially for scattering angles higher than ~30º when the L-shell contribution becomes dominant. This is evident by looking at the actual profiles for a chosen Compton angle, such as 60º, as plotted in figure 4.7. The shape of the curves is a convolution of the profiles of each contributing shell, and the normalization (inset) allows the observation that the more central portion of the profile does not differ much between elements; it is the broad contribution of xenon's L-shell that widens the profile at the sides.

One can use the calculated data from each element and estimate how the Doppler broadening compares in gaseous mixtures, by weighting the profiles of each gas by their fraction in the mixture. One pertinent example is the Ar:Xe mixture, whose 60º Compton profile for different Xe fractions is plotted at the right of figure 4.7. The plot shows how the addition of Xe steadily broadens the profile from pure Ar, but also how the area – i.e. the cross section – is increasing as well.

To determine how the different gases compare for application in a Compton camera one should take into account both the Doppler broadening and the interaction probabilities (cross sections). To do that, a quality factor (QF) is introduced to transpose into one *figure of merit* the standard deviation of the profiles ($SD(\theta)$) and the respective Compton cross sections ($\sigma(\theta)$). Inspired by the definition of decoding penalty [189, 190] – a similar concept for the comparison of performances of Compton and Anger cameras – QF is defined as the ratio between the variance of the profile and

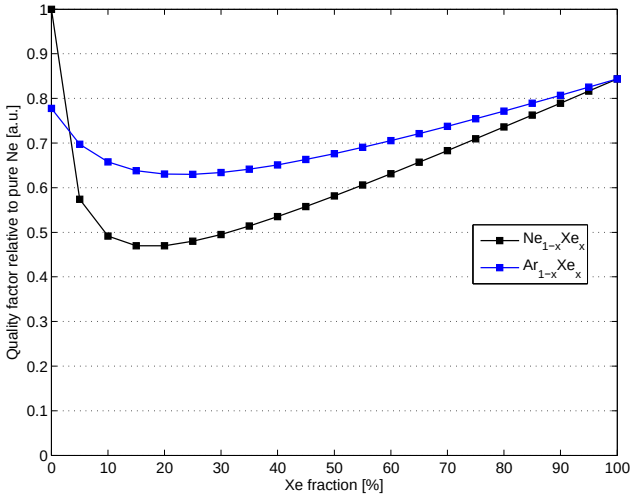

Figure 4.8 Quality factor of Ar:Xe and Ne:Xe gaseous mixtures as a function of xenon's fraction.

its area:

$$QF = \frac{SD^2(\theta)}{\sigma(\theta)} \,. \tag{4.9}$$

Figure 4.8 shows the curves obtained for QF, calculated at θ = 60°, for the gaseous mixtures Ne:Xe and Ar:Xe as a function of xenon's content, normalized to the value of pure Ne. The plot shows that the addition of small fractions (<20%) of Xe sharply reduces QF in either mixture, since the profile is immediately broadened by the interaction with Xe atoms. Nonetheless, as xenon's fraction continues to increase, the Compton cross section of the medium gets higher while $SD^2(\theta)$ converges, leading to an increase of QF. Pure Xe shows a QF above pure Ar and merely 15% lower than pure Ne.

To make a better prediction of the gaseous Compton camera's performance, other aspects of the detector must be considered as well. One of them is the attenuation coefficients for the photoelectric and Compton interactions, illustrated in figure 4.9 at the left, for the gases of interest. Xenon has the higher values of both coefficients: at 100 keV its photoelectric effect probability is two orders of magnitude higher than in argon, while its Compton coefficient is double. Therefore, the number of interactions in a chamber filled with that gas will be much higher than using the alternatives. A more precise prediction can be made considering the probabilities of useful events, i.e. the probability of a single Compton interaction followed by photoelectric absorption of the scattered ray. Assuming $X_{\text{p.e.}} = P_{\text{p.e.}}/P_{\text{total}}$ as the fraction of total interactions which are of photoelectric nature, and that all other events are Compton ($X_{\text{compt}} = 1 - X_{\text{p.e.}}$), a rough *figure of merit* can be defined as $F = X_{\text{compt}} \times X_{\text{p.e.}}$. From that It can be easily deduced that the maximization of F is obtained when the probability for both types of interactions is similar. With such consideration in mind, the curves of figure 4.9 at the left point to a preference for argon if the energy of the photons is up to 100 keV, but for the use of xenon if dealing with γ-rays of 200 keV and above.

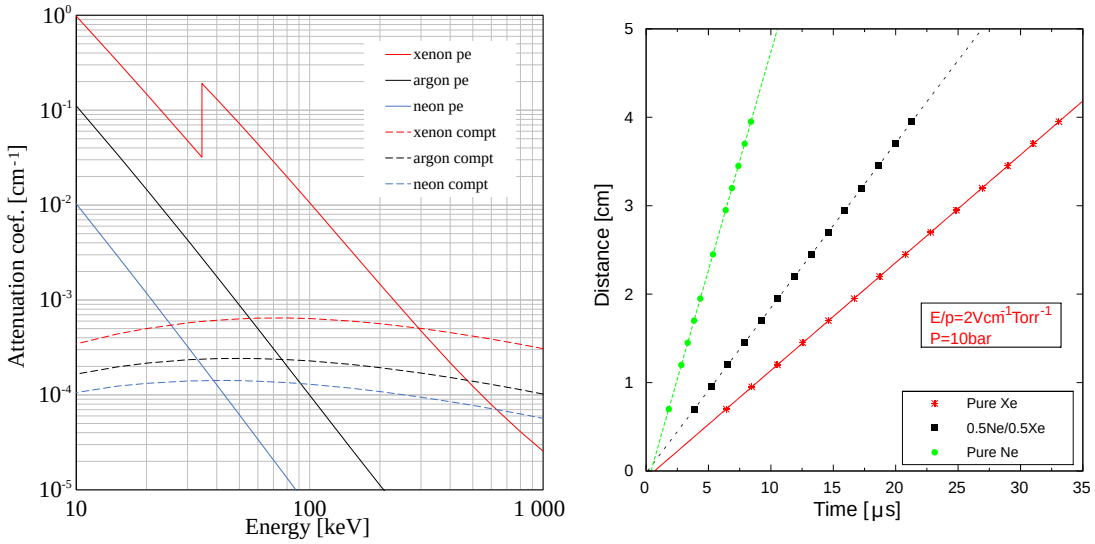

Figure 4.9 Left: attenuation coefficients for photoelectric and Compton interactions for Ne, Ar and Xe (data from [16]). Right: simulations (using Garfield simulation package) of drift distance as a function of time for electrons in pure Ne, Xe, and Ne:Xe - 50:50 mixtures, under a mild drift electric field and at high pressure (10 bar) [10].

Other two aspects lead to the final choice of Xe as gas medium, and both are related to the spacial resolution of the detector. Firstly, as the plot at the right of figure 4.9 shows, the drift velocity of electrons in Xe is much lower than in Ne, and the same is true for Ar. Because one of the coordinates of the interaction positions will be estimated from the drift time of electrons, a slower drift velocity leads to better spacial resolution, even if it eventually limits the maximum rate of acquisition ($\lesssim$ 10 kHz for a 10 cm vertical space). Secondly, the interactions with the detector medium will produce primary electron clouds. The spatial dispersion of these charges is the lowest in Xe [191, 192] compared to either Ar or Ne, allowing better determination of interaction position and hence spatial resolution.

A proof of principle of the gaseous Compton camera was done by simulating all the steps of detector operation and reconstructing cones from the generated signals. A 3D view of three selected cones reconstructed from simulated data in a Xe filled camera irradiated with a 140 keV source is shown at the left of figure 4.10. A slice projection of the cones at the plane of the source is shown at the right of the same figure.

4.3 Operation of the Gaseous Compton Camera

4.3.1 Description of the proposed detector

Gaseous detectors using signal amplification by electroluminescence were first introduced in 1967 [193] and were thoroughly investigated in the years that followed [194]. In 1981 the research led to the introduction of the Scintillation Drift Chamber (SDC) [195], one of the most successful

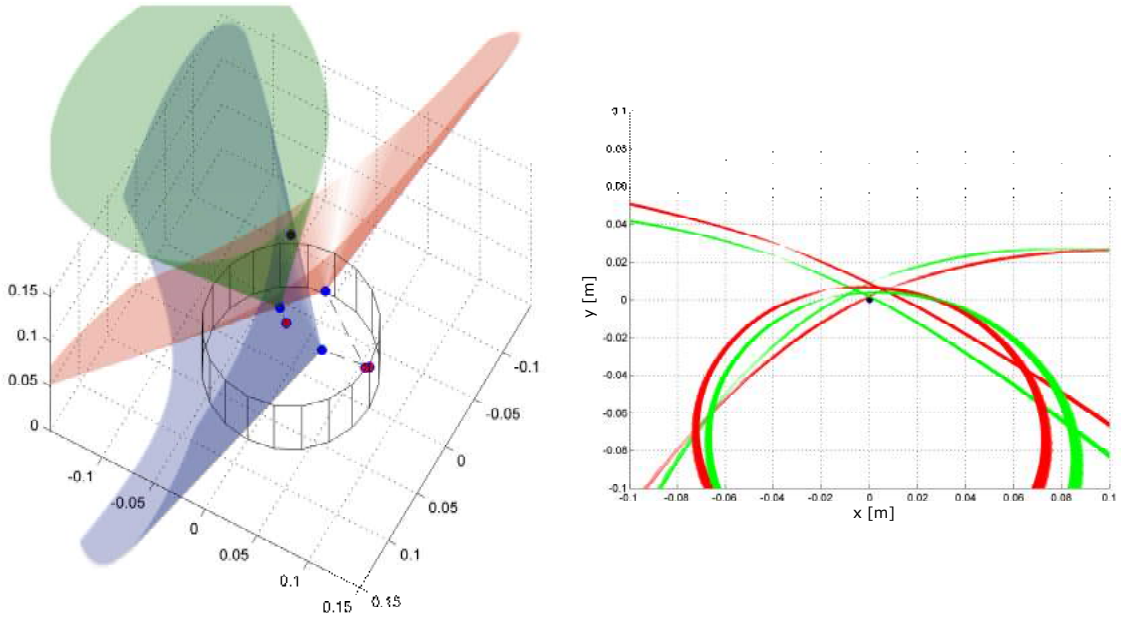

Figure 4.10 Left: 3D view of three cones reconstructed from simulated data in a Xe filled camera irradiated with a 140 keV source. Right: slice of the reconstructed cones at the plane of the source, without knowing its energy (red) or using the information of the incident γ-rays energy (green).

implementations of the principle. The gaseous Compton Camera here proposed [10], inspired by the design of Bolozdynya et al. [182, 183], is a High Pressure Scintillation Chamber (HPSC) based in the SDC principle.

The SDC presents limitations related to the 2D localization performed by the photodetector array. The PMTs typically used present limited position resolution; there are ways to improve it, such as using smaller units, but the costs quickly become prohibitive. Gaseous Photomultipliers (GPMs), on the other hand, have demonstrated large-area coverage and imaging capability with very high position resolution at low cost. In particular, recent results shown the successful implementation of a gaseous photodetector with imaging capability consisting of a ThCOBRA combined with THGEMs, obtaining single photon position resolutions as low as 300 $\mu\mathrm{m}$ in Ne:5%CH_4 [196, 197].

For the Compton Camera proposed, whose configuration is illustrated in figures 4.11 and 4.12, the PMT array will be replaced with a position sensitive GPM based in ThCOBRA/ThGEM structures. Between the HPSC and the GPM, a quartz window will allow the transmission of Xe scintillation light (~173 nm [19]). To ensure the purity of the gas atmosphere, getters will be used in the high pressure chamber, while the GPM will most likely be operated within a *once through* gas flow system.

The development of a single useful Compton event in the camera volume will occur as follows:

1. the Compton scattering of a γ-ray in the HPSC volume leads to the release of a recoil electron;

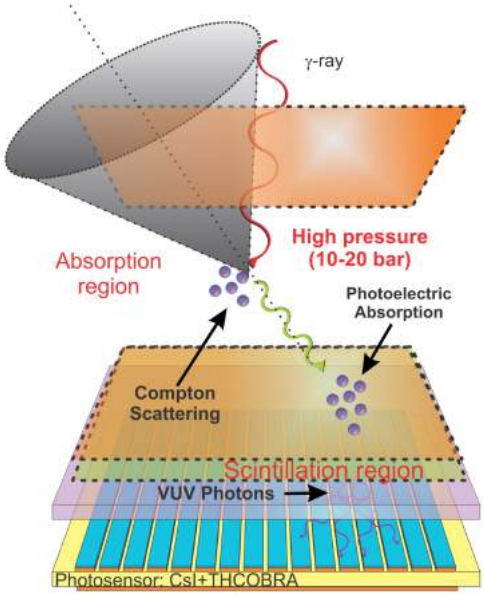

Figure 4.11 Scheme of the High Pressure Scintillation Chamber operation principle as a Compton camera, coupled to a CsI coated ThCOBRA for imaging of the produced light.

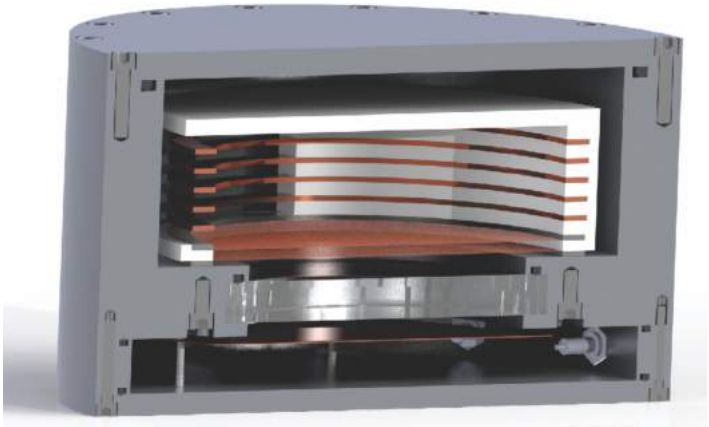

Figure 4.12 3D illustration of the detection chamber built for use as a gaseous Compton camera, hosting the High Pressure Scintillation Chamber proposed.

2. the kinetic energy of the electron is then converted by interaction with the atoms of the gaseous medium. While most of its energy will cause the ionization of the atoms and the creation of an electron cloud, a few primary scintillation photons will be emitted in the UV range, representing a negligible fraction of the electron's energy. This light is detected by the photosensor;

3. the scattered γ-ray travels a certain distance before it undergoes photoelectric interaction, being fully absorbed by the medium with the emission of a photoelectron. Once more, besides the creation of ion pairs by the photoelectron, a few photons will be emitted by primary scintillation and then detected by the photonsensor;

4. The charges of both electron clouds (created in 2. and 3.) are drifted by the electric field towards the scintillation region. There, they will generate the electroluminescence photons in number proportional to their charge, which will be detected by the photosensor.

The acquisition is started by the detection of the few primary scintillation photons (2. and 3.). The two electron clouds drift towards the light amplification region and electroluminescence occurs: the emitted light intensity is measured and allows the determination of the energies of the scattered photon and recoil electron; at the same time, the 2D position of the Compton and photoelectric interactions is estimated by combination of the *center-of-gravity* method – weighting each measurement position by the respective number of photons detected – and the resistive charge division method – which measures the intensity of a signal in two ends of a resistive line [198–200]. The Z coordinate is obtained by the time difference between the detection of primary scintillation light and electroluminescence light.

From the position and energy of each interaction, one should be able to reconstruct the Compton angle, and therefore the cone of γ-ray origin. However, in single volume detectors there is no clear method to unmistakably distinguish the scattering and absorption events, since they can occur in any position within the chamber volume and the time difference between the two is too short. Therefore, to distinguish the events one has to look at the possibilities allowed by Compton kinematics. In particular, one can predict the minimum energy fraction of the scattered photon allowed from a source with energy E_γ by solving equation 4.1 for the case of backscattering,

$$\frac{E_{\gamma'}(\theta=\pi)}{E_\gamma} = \frac{1}{1+2E_\gamma/m_0c^2}\,, \tag{4.10}$$

and correspondingly calculate the maximum recoil electron energy, $E_\gamma - E_{\gamma'}(\theta=\pi)$. It can then be observed that, for any source whose energy E_γ is lower than 256 keV, the recoil electron will always have less energy than the scattered photon, thus allowing a straightforward identification protocol for such cases. If the use of higher energy sources is intended one shall look to probabilistic methods of identification such as the ones already developed for single crystal Compton Cameras [177, 201].

4.3.2 Characterization of the HPSC

The HPSC component of the Compton camera has been assembled and characterized. The drift/absorption region is 18 cm in diameter and 4.2 cm in length. The electric field in this region is established by 5 copper ring electrodes, uniformly spaced with peek spacers, whose voltage is set by a resistive divider chain. The field at the top is set by a copper roof. As for the amplification region, the fields required to generate light by electroluminescence are established by two parallel meshes, which consist of a stainless steel grid made of 80 $\mu\mathrm{m}$ wires with a 400 $\mu\mathrm{m}$ pitch. This scintillation region is 0.4 cm in length. Figure 4.13 shows photographs of the chamber elements, including the shaping ring electrodes and the grids; at the right, the copper roof can be seen through the grid wires.

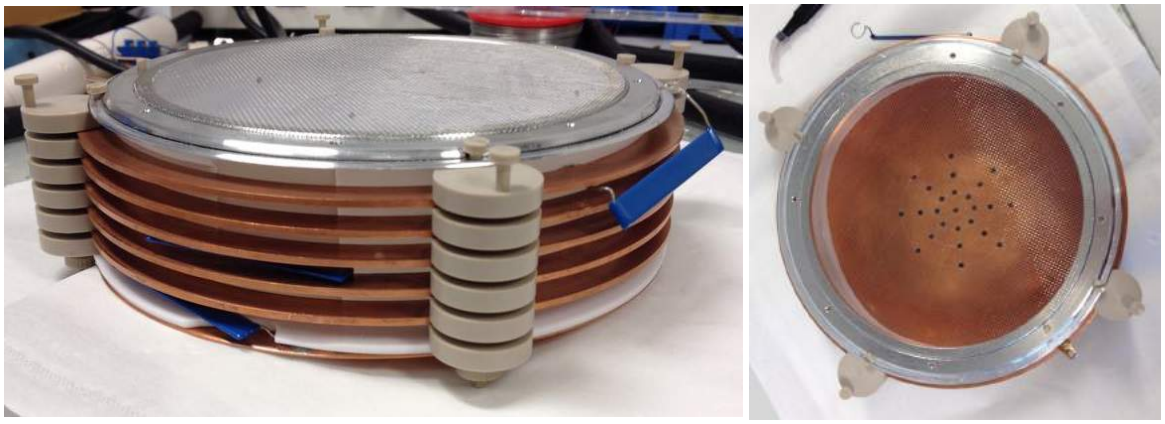

Figure 4.13 Photograph of the HPSC components assembled outside the detector chamber, namely the shaping copper electrodes, the peek spacers and the meshes.

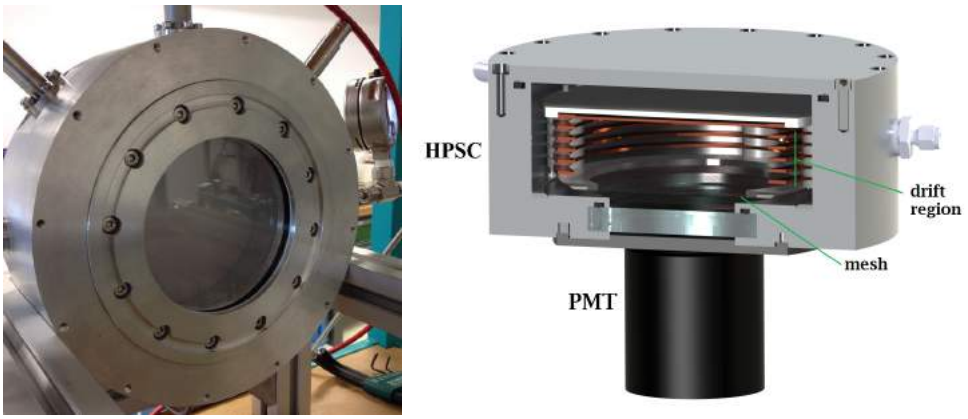

Figure 4.14 Left: photograph of the outside of the detector without the photosensor component, with the quartz window visible. Right: schematic representation of the setup used for the characterization exercise.

The outside of the chamber can be seen in figure 4.14 at the left, in particular the quartz window. The characterization of the chamber here presented was performed using a commercial PMT with

sensitivity in the VUV range, coupled to the bottom part of the chamber, as the scheme at the right of said figure illustrates. The space between the Spectrosil-B window and the PMT is filled with Argon so that optical transparency in the VUV is assured. The HPSC itself is filled with Xe and studied at various pressures with an Am-241 γ-ray source, emitting characteristic 59.6 keV photons.

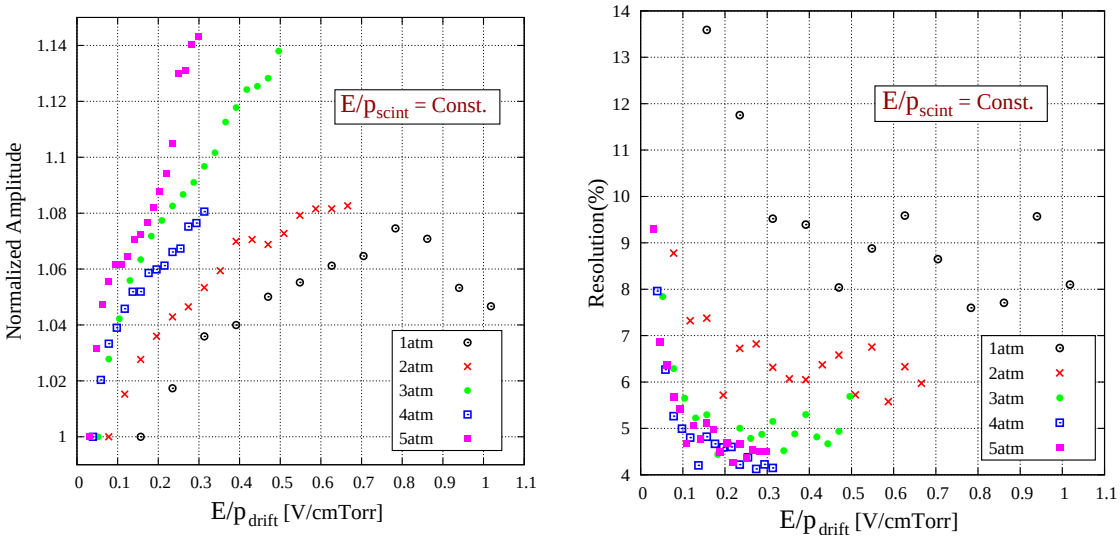

Figure 4.15 Characterization of the pulse amplitudes (left) and energy resolution (right) as a function of the reduced electric field in the drift region, for a fixed amplification field (scintillation region) of 3.3 $\mathrm{Vcm^{-1}torr^{-1}}$.

Figure 4.15 presents the results of the drift field characterization in terms of light yield (gain) and energy resolution. The decrease in amplitude at 1 atm for reduced electric fields higher than 0.8 $\mathrm{Vcm^{-1}torr^{-1}}$ is caused by limitation of the resistive chain that establishes the electric field in the drift region: the electric field in the last shaping ring is also dependent on the cathode's voltage; therefore, it is not possible to keep constant or fine tune the field strength between the last shaping ring and the mesh; this means that, when increasing the drift field, the electric field between the last copper ring and the scintillation mesh will also increase, thus reducing the mesh's electron transparency.

Figure 4.16 at the left presents the light yield characterization of the amplification stage from 1 to 5 atm, confirming its linear nature. The increase in pressure allows the detector to reach significantly higher gains, assuming the proportionally higher electric fields are supplied. Since the increase in pressure also results in a more confined electron cloud, it will be also beneficial in the final detector for the Compton camera event reconstruction, allowing a better spacial resolution in determining the interaction points [192].

As for the energy resolution in the same conditions (see figure 4.16 at the right), the results show poor performance of the chamber at lower pressures (up to 2 atm). For higher pressures, the resolution is, naturally, improved by the higher gains achieved, and values as low as 4% are obtained.

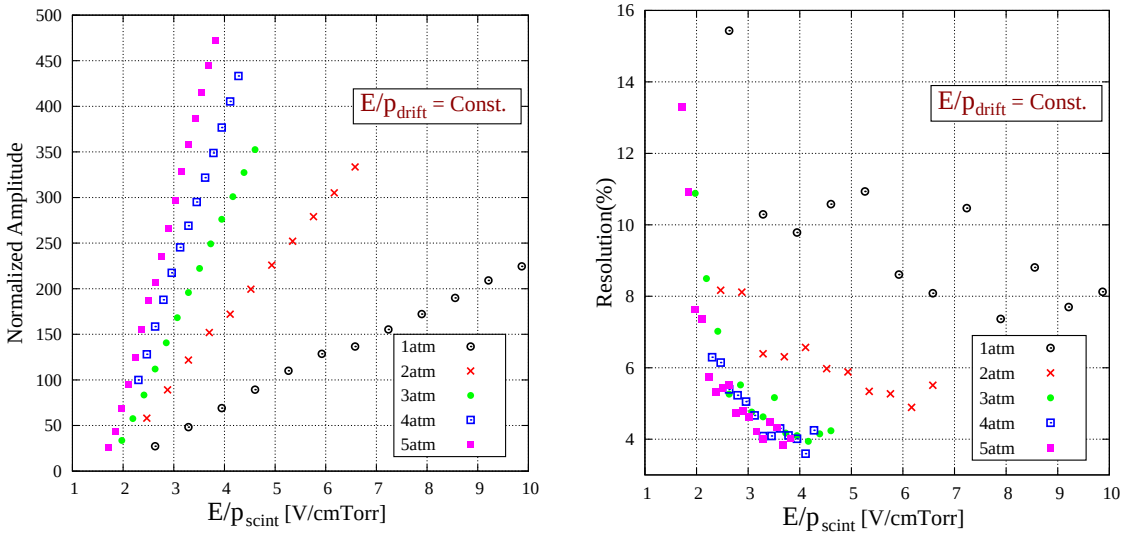

Figure 4.16 Characterization of the pulse amplitudes (left) and energy resolution (right) as a function of the reduced electric field in the amplification (scintillation) region.

This is a very promising result, since the spacial resolution of a Compton Camera is intrinsically related to the energy resolution of the device.

Figure 4.17 shows a spectrum obtained with the chamber under simultaneous irradiation of Am-241 and Co-57 sources, which points to the possibility of identifying multiple sources of radiation. Another feature of this spectrum is the background originated by Compton scattering of the higher energy photons.

In the near future the PMT will be replaced by the GPM element with imaging capability. After that, the study and characterization of the detector as a Compton camera can take place.

4.4 Statistical fluctuations of CsI photocathodes

The proposed Compton Camera requires a photodetector to be coupled to the main HPSC detector, with the light transmitted through a quartz window. However, a possible future iteration of the proposed device might consider the integration of the photodetector inside the chamber volume. That would lead to improvements in detector design and it would avoid the inclusion of the window, maximizing the number of photons measured.

However, the operation of CsI photocathodes in high pressure Noble gases introduces other concerns related to the photoelectron extraction efficiency. These issues have been subject to investigation (see for example [202]) mostly motivated by the proposal to use CsI photocathodes and pressurized noble GPMs for future experiments based on rare event detection, namely Dark Matter [89, 90, 99, 203] and Double Beta Decay [204] research, which are faced with the problem of the prohibitive costs of the use of PMTs [205]. A note-worthy example is the research on single and

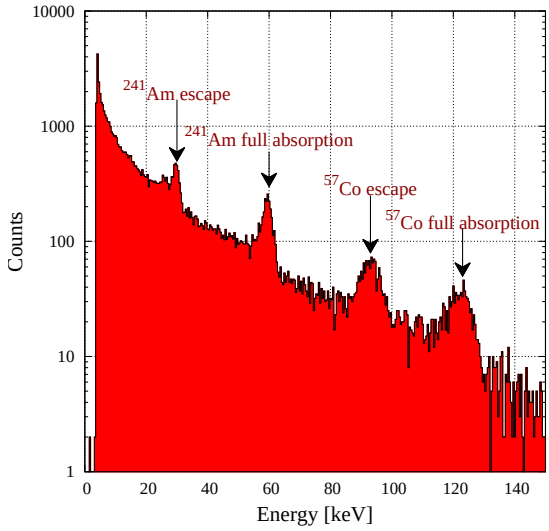

Figure 4.17 Spectrum obtained with the HPSC with two sources used simultaneously. Besides the two main full absorption peaks from the Am-241 and Co-57 sources – 64 keV and 122 keV, respectively – the respective escape peaks are also present at 30 keV lower energy, as predicted by xenon's characteristic fluorescence X-ray.

double-phase noble gas detectors, especially Ar and Xe [91, 206, 207].

Some general conclusions regarding this subject have already been mentioned in section 1.3.3. If the backscattering effect of photoelectrons and the consequent drop in extraction efficiency in high pressure media is now generally understood, there is no study of the implications for the statistical uncertainties related to the effect, as far as the author is aware. In the case of Compton Cameras, for example, one can easily understand how a loss of accuracy in the counting of few photons originating from a low energy scattering event can lead to performance limitations of the detector as a whole. Studies of the statistical fluctuations associated are, therefore, pertinent.

Experimental measurements

The motivation to understand the statistical effects imposed on CsI photoelectron extraction in high pressure noble gases led to a series of experimental studies and simulations which are presented next. They are related to a previous set of studies performed by Covita et al. [208]. The results from that precursor study, some of which are illustrated in figure 4.18, allowed a few conclusions: the photoelectron extraction efficiency from CsI photocathodes in pure argon is ~1/3 of the value obtained in vacuum; the curves for different pressures up to 10 bar as a function of the reduced field (E/p), are indistinguishable up to the electroluminescence (excitation) threshold (~1.0 $\mathrm{Vcm^{-1}torr^{-1}}$); Xe shows an even lower efficiency, ~1/2 of argon's value.

The results here presented are obtained with an adaptation of the setup from that study, since in that case the measurements were performed in current mode with a picoammeter. For the evaluation of statistical effects the ability to control very precisely the number of photons that

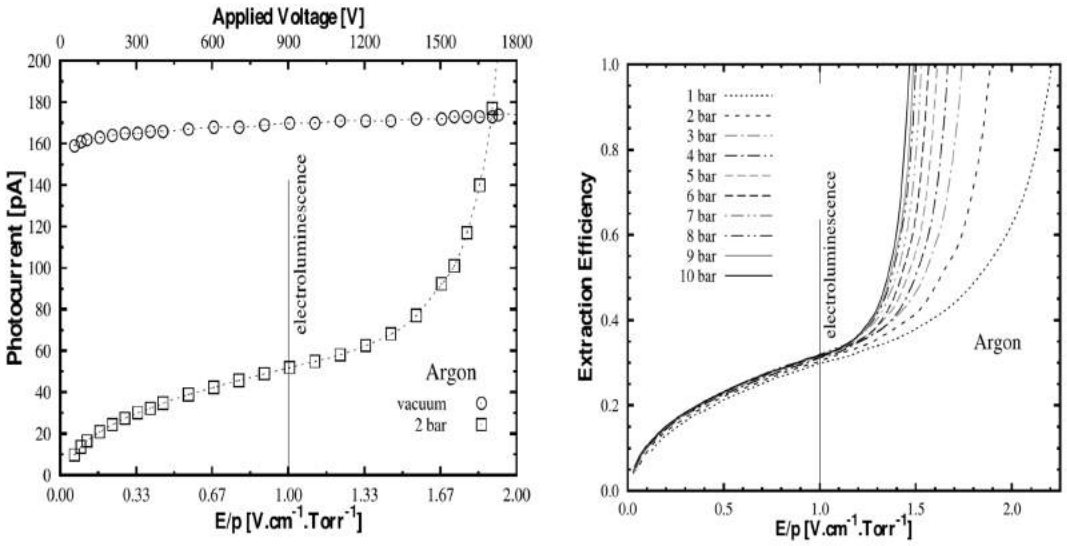

Figure 4.18 Photoelectron extraction efficiency of CsI photocathodes. At the left, the comparison between operation in vacuum and Ar at 2 bar; at the right, the curves for argon at pressures between 1 and 10 bar. [208]

irradiate the photocathode is required, and the data acquisition in pulse mode is more adequate. The experimental setup is illustrated at the right of figure 4.19, next to a photograph. A 500 nm CsI film, deposited in a Kapton® sheet with Ni-Au layer, is irradiated by a Hg(Ar) UV lamp with emission peak at 185 nm. The field above the photocathode is established by polarizing with a positive bias the thin (semitransparent) aluminum layer deposited in the quartz window, 6 mm above the photoconverting film, which is at ground. A CAEN N471A power supply is used for that.

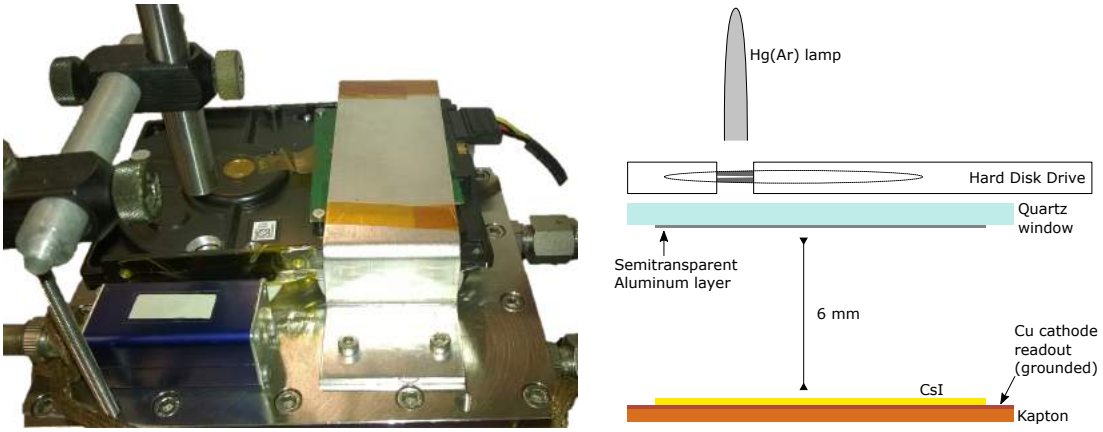

Figure 4.19 Schematic diagram (right) and photograph (left) of the setup used for the measurements of the statistical fluctuations of photoelectron extraction efficiency.

To generate a pulsed light source with very low variation in the number of emitted photons between each pulse, a 7200 rpm hard disk drive (HDD) was adapted with a slit and positioned

between the lamp and the chamber's window. This allows the generation of very constant pulses with a precision which can be estimated at the ~0.04% level from the timing histogram (see figure 4.21 at the left). The pulses result in the extraction of electrons from the CsI layer, with a corresponding electric signal induced in the electrode. The signal is then fed to a Canberra 2006 preamplifier and measured by a CAEN V1724 digitizer. To avoid that a fixed threshold trigger influences the timing of the measurements, the acquisition of the CAEN board is triggered by a constant fraction discriminator (CFD) Ortec 934. Most of the curves presented are obtained varying the intensity of light, which is achieved by changing the distance of the UV lamp to the detector. For each amplitude, typical measures consist of 3 minutes of data taking at 120 Hz (dictated by the 7200 rpm speed of the disk), producing a gaussian-shaped histogram from which the variance is extracted.

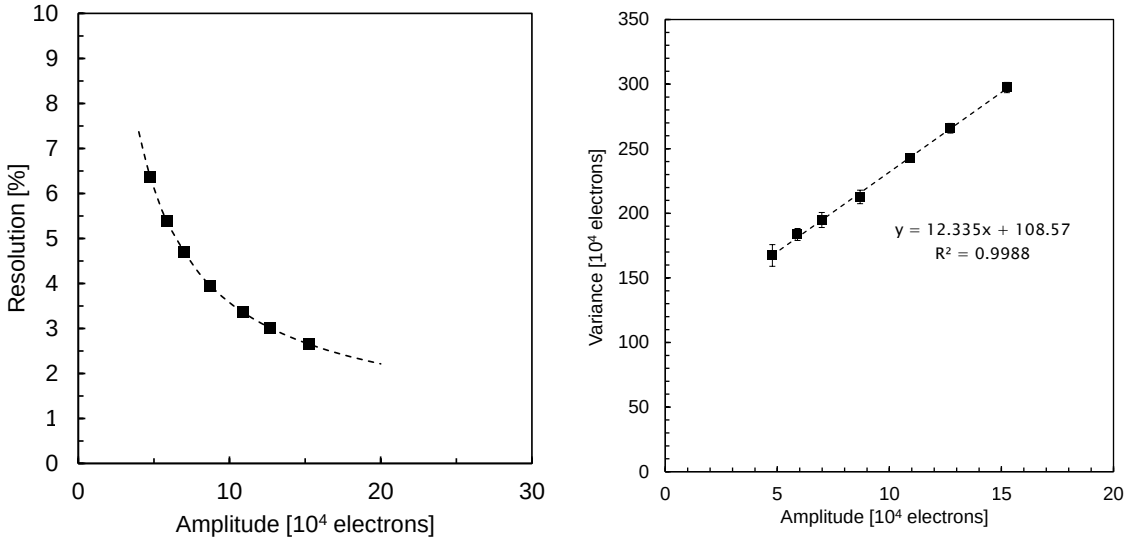

Figure 4.20 Left: resolution as a function of the pulse amplitudes (number of extracted electrons) in vacuum. Right: variance as a function of the pulse amplitudes in vacuum.

Figure 4.20 at the right shows that the statistical behavior of the system, in vacuum (~10^{-7} mbar), is described by a linear dependency between the variance and the average of the pulse amplitudes (number of extracted electrons), a poissonic characteristic. However, the verification of a significant value of variance at the origin is not an expected characteristic of the photoelectric process being studied, and is interpreted as a result of the electronic noise that affects the system, to which the vibration of the hard disk contributes significantly. For that reason, the data analysis presented hereafter will show curves corrected by the offset of each line at the origin. As an example, the data points from the plot of figure 4.20 at the right would be subtracted by 108.57 (x 10^4 electrons). In any case, the conclusions presented would be the same if no such correction was applied. The resolution of the electron extraction measurement in vacuum is between 2.5% and 6.5%, as shown at the left of that figure.

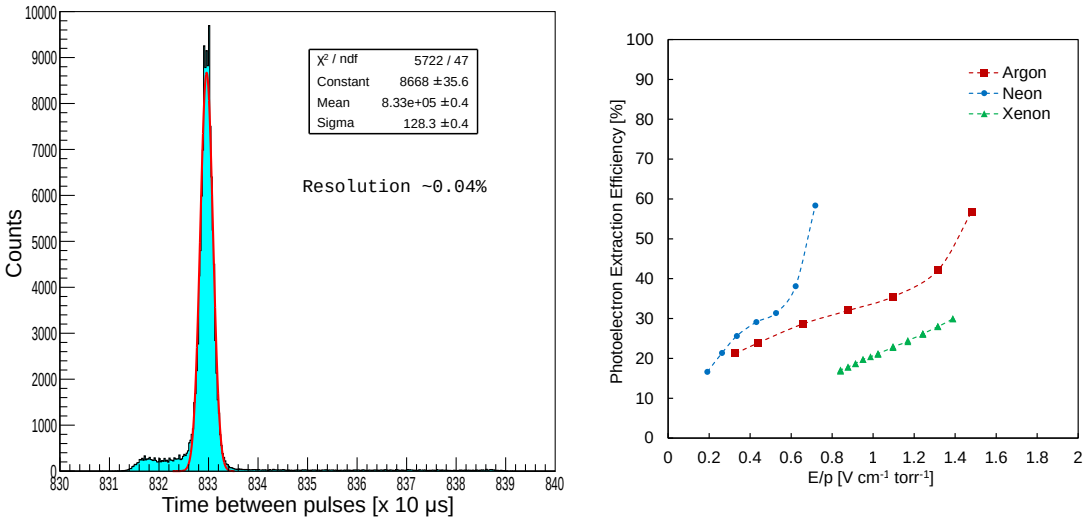

Figure 4.21 Left: histogram of the time difference between two consecutive events, confirming the high precision of the velocity of the HDD. Right: extraction curves for Ar, Xe, and Ne, at 1 atm obtained in pulse mode, presenting comparable results to the same curves in current mode obtained by Covita et al..

The measurements with gaseous atmosphere are done at the plateau points of the curves seen in figure 4.21 at the right, ensuring the maximum extraction efficiency before the electroluminescence threshold (~1.0 $\mathrm{Vcm^{-1}torr^{-1}}$ for argon). These curves for Ar and Xe match the expected from the previous studies in current mode.

Figure 4.22 shows how the values of the variance as a function of the measured number of extracted electrons compares between the CsI in vacuum and in pure argon at 1 atm. Argon exhibits a smaller uncertainty of number of photoelectrons, even if the amplitude is significantly reduced, i.e. points at the same value of the X coordinate are obtained with different light intensities, a consequence of the diminished electron extraction efficiency. The same figure at the right compares two profiles of typical pulses, illustrating the difference.

The study of several gaseous elements led to the consistent finding that all of them show a lower statistical fluctuation of number of electrons measured, when compared to vacuum (figure 4.23). In fact, xenon and neon show an even lower statistical fluctuation of the process when compared to argon. Some doubts may be raised regarding the results found for Ne, since the lower excitation threshold of that gas might lead to unwanted electroluminescence light emission, and be a contributing factor to lower the measured fluctuations; but for the remaining gases where the electroluminescence occurs later, this process is more accurately controlled. There seems to be an intrinsic selection process, occurring at the level of the backscattering of photoelectrons at the time of extraction, that leads to an increase in accuracy of the measurements.

The same results are found at any pressure of the gas medium, as the plot in figure 4.24 shows. The data is, once again, obtained at the plateaus of maximum photoelectric extraction, and so at the

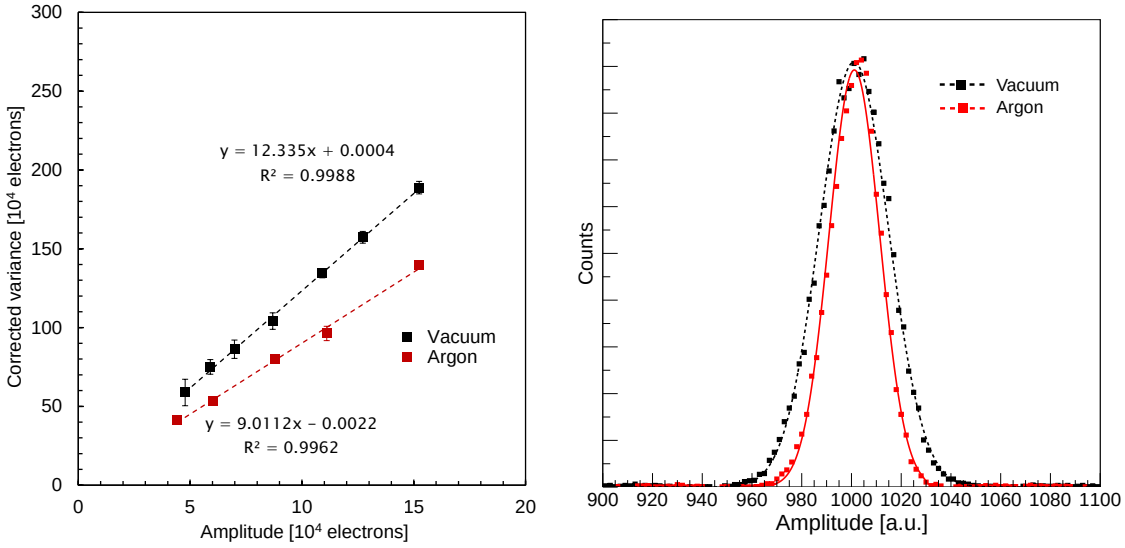

Figure 4.22 Left: variance as a function of the pulse amplitudes in vacuum and in argon, showing lower statistical fluctuations of the latter. Right: comparison of two typical histograms in vacuum and in Ar atmosphere, obtained at the same amplitude (number of extracted photoelectrons) and normalized.

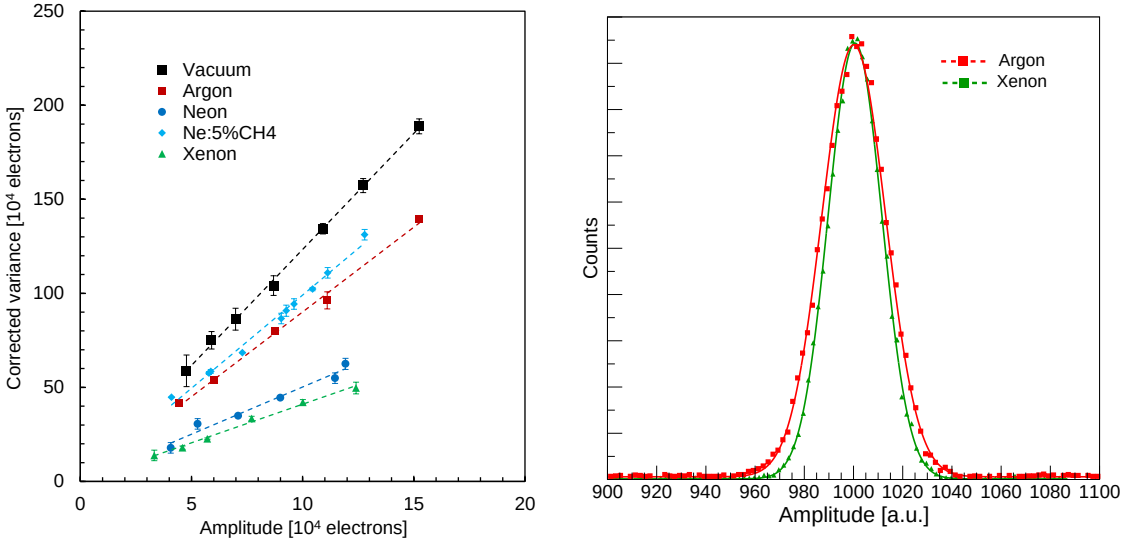

Figure 4.23 Left: variance as a function of the pulse amplitudes in vacuum and in Ar, Xe, Ne and Ne:5%CH_4, showing lower statistical fluctuations of all gases, and especially lower in xenon. Right: comparison of two typical histograms in Xe and in Ar atmosphere, obtained at the same amplitude (number of extracted photoelectrons) and normalized.

same reduced electric fields (~1.0 $\mathrm{Vcm^{-1}torr^{-1}}$) in all curves. Considering that the photoelectron extraction efficiency is also solely dependent of the reduced electric field, the same observation regarding its variance is no surprise.

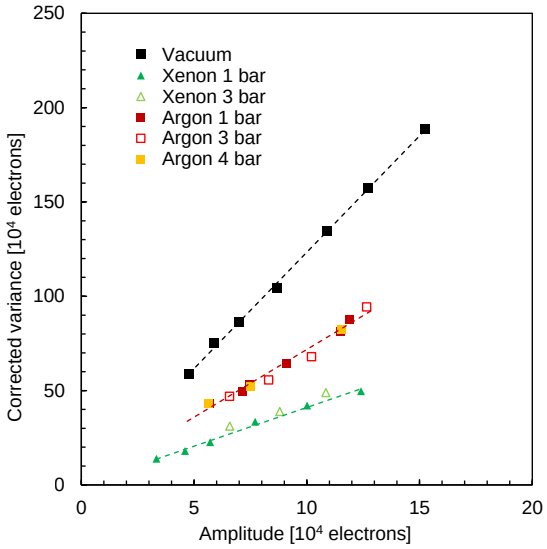

Figure 4.24 Variance as a function of the pulse amplitudes in vacuum and in argon and xenon at various pressures. No significant influence of the pressure is seen.

Simulations

The results obtained with the experimental setup revealed a lower statistical fluctuation of photoelectron extraction from CsI photocathodes operated in noble gases, and specially in xenon, when compared to vacuum. The explanation for such results is not clear but should be related to the statistic aspects of the backscattering process. A possible way to test such hypothesis is to simulate the process using a simulation tool such as Garfield, whose calculations take into account interaction cross sections of electrons with different gases.

To simulate the process of photoelectron extraction using Garfield, electrons are generated in a plane, initially at rest, and subject to a constant drift field equal to the one applied in the experimental measurements (at the extraction plateau). The number of electrons is generated according to a gaussian distribution whose variance (double black line in the plot of figure 4.25) matches the one measured in vacuum in the experiments.

The electrons, subject to the electric field, drift towards a collection plane through a series of collisions with the medium's atoms, in a erratic path. The process of backscattering that reduces the number of collected electrons is mimicked by introducing a virtual intermediate plane above the plane of electron generation: any electron crossing the intermediate plane and eventually returning to the plane of generation is considered reabsorbed; the distance at which the intermediate plane is defined is chosen so that the measured photoelectron extraction efficiency (the number of electrons

that escape) is consistent with the experimental measurements. It is observed that the same distance defined for argon and xenon leads to the correct values of extraction efficiency (~33% and ~16%, respectively), an indication that the crude method conceived is accurately simulating the physical process.

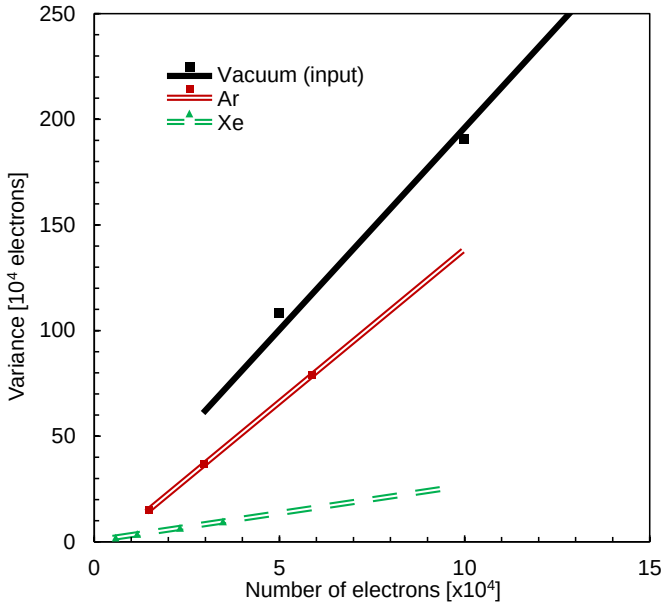

Figure 4.25 Variance of the number of extracted electrons as a function of the average, obtained by simulation with the Garfield software. The preliminary results show agreement with the experimental curves.

The results of variance of the number of extracted electrons as a function of the average, obtained by the simulation described above for argon and xenon, are plotted in figure 4.25, along with the variance of electrons generated (similar to vacuum values). Each point is the result of 100 simulated events. The lines thus obtained are comparable to the experimental results and so give further confidence that they are based in a physical process at the extraction level. They imply that the use of CsI photocathodes in high pressure noble gas media results in less statistical uncertainty in the number of counted photons, even if reducing the extraction efficiency. This has implications to the energy resolution of GPMs, such as the ones which will be implemented in the gaseous Compton camera.

4.5 Conclusions

This chapter reported the study of several aspects related to the development of a gaseous Compton Camera.

Calculations were performed to study the effect of Doppler broadening in a gaseous medium. The results confirm that, in this regard, gases such as neon show a performance similar to silicon,

a common standard for Compton camera devices. To compare between different gases one should take into account the cross sections for the interactions of interest: such analysis revealed that, despite its larger Doppler broadening, xenon's increased attenuation coefficient for both Compton and photoelectric effect make him the preferred choice.

The High Pressure Scintillation Chamber which will compose the proposed Compton camera detector has been assembled and characterized with a PMT, showing energy resolution as low as 4% for 60 keV γ-rays. Operation up to 5 atm in pure Xe has been confirmed with good energy resolution.

Finally, the contribution of statistical fluctuations in photoelectron extraction from CsI photocathodes in noble gases has been studied. Tests using pulsed UV light show that the statistical uncertainty of extraction efficiency in high pressure Ar and Xe are consistently below vacuum values. The result seems to be replicated in a simulation of the backscattering process of electrons in such gases. The results may prove to be relevant for the use of high pressure or double-phase noble gaseous photomultipliers where energy resolution is demanding, as in gaseous Compton cameras.

Conclusions and future work

The development and testing of triple cascaded ThGEM detectors showed that gains could be reached of the order of 10^4 while detecting Cherenkov photons under beam environment. Also, experience with the aforementioned detectors showed a fast recovery from electrical discharges, in the order of seconds, a great improvement if compared to MWPCs. To the good results reached with $300 \times 300\ \mathrm{mm}^2$ ThGEMs, namely the improvement in gain uniformity and maximum stable voltage, contributed the careful production, quality control and characterization procedures developed and adopted.

However, limitations in controlling the Ion Backflow, unsatisfying detector stability and the will to increase even further the maximum gains obtained led to the adoption of a Micromegas final multiplication stage. With the hybrid prototype, the maximum stable gain was increased by an order of magnitude. The performance of those detectors was limited by aspects which are exterior to the detector itself, namely the noise level of the digital frontend electronics.

The final detectors assembled allowed gains in the order of 10^5 to be reached in stable conditions under particle beam irradiation, and the detection of Cherenkov light. They show fast response, high efficiency of single photon detection at high rates and a constricted IBF at less than 4% level, reducing the aging effect on the photocathode. The introduction of a mild reverse drift field allows the suppression of signals created by the passage of beam particles in the detector. At the same time, the capacitive/resistive nature of the anode protects the electronics from electrical discharges. Therefore, they will be major improvements to the current MWPCs used on COMPASS RICH-1 up to now.

At the time of writing this conclusion, the preparations for the first stage of the upgrade is in progress, where four MWPC detection chambers of the RICH-1 will be replaced by capacitive anode hybrid detectors of $60 \times 60\ \mathrm{cm}^2$ of active area. The larger Micromegas with capacitive anodes have been produced and are being characterized. They will be joined by two ThGEMs, and the double ThGEM hybrid detectors will be subject to final checks of performance. The upgrade is expected to be completed in the first quarter of 2016.

Additionally, a gaseous detector was simulated and characterized envisaging its application as a Compton Camera. The results of the calculations justified the decision to use pure xenon in the detection volume. The simulations and initial characterization point to a prototype being capable of offering promising performances. As far as the author is aware, it would be the first Compton

Camera purely based in gaseous detectors, and probably a very competitive solution cost-wise.

However, the work here reported is a very modest first step towards the assembly and successful operation of the gaseous Compton camera. One wishes, first of all, to replace the PMT by a GPM based in the ThCOBRA structure as its photosensor. How this will affect the measured position and energy resolution of the device needs to be studied. Secondly, the detector will require the development of a complex data analysis and image reconstruction software. The creation of such scripts and tools will demand a deep understanding of the physics of the interactions involved and can contribute crucially to the performance of the final detector. Compton kinematics, detector geometry, resolution, energy of the γ-ray source and probabilistic considerations are just a few of the vast number of aspects that can be introduced to such reconstruction methods to improve their results.

At last, regarding the measurements of statistical fluctuations of photoelectron extraction, the studies should be extended to other gaseous media, higher pressures and possibly double phase (or liquid) detectors. Besides, a crucial confirmation of the results would be a more accurate simulation of the effect, for example taking into account the distribution of kinetic energies of extracted electrons from the photocathode.

Bibliography

[1] S. Dalla Torre, "*Status and Perspectives of Cherenkov Imaging Counters*", In *Astroparticle, Particle and Space Physics, Detectors and Medical Physics Applications-Proceedings of the 11th Conference on Icatpp-11*, 2010.

[2] D. Websdale, "*Review of Cherenkov imaging devices in particle and nuclear physics experiments*", Nuclear Instruments and Methods in Physics Research Section A: Accelerators, Spectrometers, Detectors and Associated Equipment, vol. 595, no. 1, pp. 12–18, 2008.

[3] P. Abbon, E. Albrecht, V. Alexakhin, Y. Alexandrov et al., "*The COMPASS experiment at CERN*", Nuclear Instruments and Methods in Physics Research Section A: Accelerators, Spectrometers, Detectors and Associated Equipment, vol. 577, no. 3, pp. 455–518, 2007.

[4] COMPASS collaboration and F. Gautheron, "*COMPASS-II Proposal*", 2010 .

[5] R. Chechik and A. Breskin, "*Advances in gaseous photomultipliers*", Nuclear Instruments and Methods in Physics Research Section A: Accelerators, Spectrometers, Detectors and Associated Equipment, vol. 595, no. 1, pp. 116–127, 2008.

[6] M. Hoch, "*Trends and new developments in gaseous detectors*", Nuclear Instruments and Methods in Physics Research Section A: Accelerators, Spectrometers, Detectors and Associated Equipment, vol. 535, no. 1, pp. 1–15, 2004.

[7] A. Breskin, R. Alon, M. Cortesi, R. Chechik et al., "*A concise review on THGEM detectors*", Nuclear Instruments and Methods in Physics Research Section A: Accelerators, Spectrometers, Detectors and Associated Equipment, vol. 598, no. 1, pp. 107–111, 2009.

[8] Y. Giomataris, P. Rebourgeard, J. P. Robert and G. Charpak, "*MICROMEGAS: a high-granularity position-sensitive gaseous detector for high particle-flux environments*", Nuclear Instruments and Methods in Physics Research Section A: Accelerators, Spectrometers, Detectors and Associated Equipment, vol. 376, no. 1, pp. 29–35, 1996.

[9] RD51 Collaboration, "*Development of Micro-Pattern Gas Detector Technologies*", 2008 .

[10] C. Azevedo, F. Pereira, T. Lopes, P. Correia et al., "*A Gaseous Compton Camera using a 2D-sensitive gaseous photomultiplier for Nuclear Medical Imaging*", Nuclear Instruments and Methods in Physics Research Section A: Accelerators, Spectrometers, Detectors and Associated Equipment, vol. 732, pp. 551–555, 2013.

[11] C. Grupen, B. Shwartz and H. Spieler, "*Particle Detectors*", Cambridge University Press, 2008.

[12] G. Knoll, "*Radiation Detection and Measurement*", John Wiley & Sons, 2010.

[13] K. A. Olive and P. D. Group, "*Review of particle physics*", Chinese Physics C, vol. 38, no. 9, pp. 090001, 2014.

[14] B. Ratcliff, "*Advantages and limitations of the RICH technique for particle identification*", Nuclear Instruments and Methods in Physics Research Section A: Accelerators, Spectrometers, Detectors and Associated Equipment, vol. 595, no. 1, pp. 1–7, 2008.

[15] C. Grupen and I. Buvat, "*Handbook of Particle Detection and Imaging*", Springer, 2011.

[16] M. Berger, J. Hubbell, S. Seltzer, J. Chang et al., "*XCOM: Photon cross sections database (version 1.5) [Online, accessed Nov. 2015]*", NIST Standard reference database, vol. 8, 2013.

[17] W. Blum, W. Riegler and L. Rolandi, "*Particle Detection with Drift Chambers*", Springer Berlin Heidelberg, 2008.

[18] E. Aprile, A. Bolotnikov, A. Bolozdynya and T. Doke, "*Noble Gas Detectors*", Wiley, 2007.

[19] C. A. B. d. Oliveira, "*Monte Carlo study of electroluminescence in gaseous detectors*", 2011.

[20] C. Monteiro, L. Fernandes, J. Lopes, L. Coelho et al., "*Secondary scintillation yield in pure xenon*", Journal of Instrumentation, vol. 2, no. 05, pp. P05001, 2007.

[21] V. Peskov and P. Fonte, "*Research on discharges in micropattern and small gap gaseous detectors*", arXiv preprint arXiv:0911.0463, 2009.

[22] M. Cortesi, V. Peskov, G. Bartesaghi, J. Miyamoto et al., "*THGEM operation in Ne and Ne/CH4*", Journal of Instrumentation, vol. 4, no. 08, pp. P08001, 2009.

[23] H. Raether, "*Electron avalanches and breakdown in gases*", 1964.

[24] A. Bressan, M. Hoch, P. Pagano, L. Ropelewski et al., "*High rate behavior and discharge limits in micro-pattern detectors*", Nuclear Instruments and Methods in Physics Research Section A: Accelerators, Spectrometers, Detectors and Associated Equipment, vol. 424, no. 2, pp. 321–342, 1999.

[25] Y. Ivaniouchenkov, P. Fonte, V. Peskov and B. Ramsey, "*Breakdown limit studies in high-rate gaseous detectors*", Nuclear Instruments and Methods in Physics Research Section A: Accelerators, Spectrometers, Detectors and Associated Equipment, vol. 422, no. 1, pp. 300–304, 1999.

[26] J. Byrne, "*Statistics of electron avalanches in the proportional counter*", Nuclear Instruments and Methods, vol. 74, no. 2, pp. 291–296, 1969.

[27] J. Va'Vra, "*Photon detectors*", Nuclear Instruments and Methods in Physics Research Section A: Accelerators, Spectrometers, Detectors and Associated Equipment, vol. 371, no. 1, pp. 33–56, 1996.

[28] S. Dalla Torre, "*Status and perspectives of gaseous photon detectors*", Nuclear Instruments and Methods in Physics Research Section A: Accelerators, Spectrometers, Detectors and Associated Equipment, vol. 639, no. 1, pp. 111–116, 2011.

[29] F. Tokanai, T. Sumiyoshi, H. Sugiyama, T. Okada et al., "*Development of gaseous PMT with micropattern gas detector*", Nuclear Instruments and Methods in Physics Research Section A: Accelerators, Spectrometers, Detectors and Associated Equipment, vol. 610, no. 1, pp. 164–168, 2009.

[30] G. Charpak, C. Zupancic, R. Bouclier, T. Bressani et al., "*The use of multiwire proportional counters to select and localize charged particles*", Nucl. Instrum. Methods, vol. 62, pp. 262–268, 1968.

[31] F. Sauli, "*Principles of Operation of Multiwire Proportional and Drift Chambers*", 1987.

[32] G. Charpak and F. Sauli, "*Multiwire proportional chambers and drift chambers*", Nuclear Instruments and Methods, vol. 162, no. 1, pp. 405–428, 1979.

[33] A. Di Mauro and CsI-RICH Collaboration, "*RD-26 Status Report*", CERN/DRDC, pp. 94–49, 1994.

[34] E. Nappi, G. Tomasicchio, E. G. Chesi, R. Ferreira-Marques et al., "*Development of a large area advanced fast rich detector for particle identification at the Large Hadron Collider operated with heavy ions*", 1992 .

[35] A. Di Mauro, "*Status and perspectives of gaseous photon detectors*", Nuclear Instruments and Methods in Physics Research Section A: Accelerators, Spectrometers, Detectors and Associated Equipment, vol. 766, pp. 126–132, 2014.

[36] E. Nappi and J. Seguinot, "*Ring Imaging Cherenkov Detectors: The state of the art and perspectives*", Rivista del Nuovo Cimento, vol. 28, no. 8-9, 2005.

[37] J. Séguinot and T. Ypsilantis, "*A historical survey of ring imaging Cherenkov counters*", Nuclear Instruments and Methods in Physics Research Section A: Accelerators, Spectrometers, Detectors and Associated Equipment, vol. 343, no. 1, pp. 1–29, 1994.

[38] E. Albrecht, G. Van Apeldoorn, A. Augustinus, P. Baillon et al., "*Operation, optimisation, and performance of the DELPHI RICH detectors*", Nuclear Instruments and Methods in Physics Research Section A: Accelerators, Spectrometers, Detectors and Associated Equipment, vol. 433, no. 1, pp. 47–58, 1999.

[39] J. Va'Vra and R. CRID Collaboration, "*Long-term operational experience with the barrel CRID at SLD*", Nuclear Instruments and Methods in Physics Research Section A: Accelerators, Spectrometers, Detectors and Associated Equipment, vol. 433, no. 1, pp. 59–70, 1999.

[40] F. Piuz, "*Ring Imaging CHerenkov systems based on gaseous photo-detectors: trends and limits around particle accelerators*", Nuclear Instruments and Methods in Physics Research Section A: Accelerators, Spectrometers, Detectors and Associated Equipment, vol. 502, no. 1, pp. 76–90, 2003.

[41] A. Breskin, "*CsI UV photocathodes: history and mystery*", Nuclear Instruments and Methods in Physics Research Section A: Accelerators, Spectrometers, Detectors and Associated Equipment, vol. 371, no. 1, pp. 116–136, 1996.

[42] A. Buzulutskov, "*Gaseous photodetectors with solid photocathodes*", Physics of Particles and nuclei, vol. 39, no. 3, pp. 424–453, 2008.

[43] A. Breskin, A. Buzulutskov, R. Chechik, A. Di Mauro et al., "*Field-dependent photoelectron extraction from CsI in different gases*", Nuclear Instruments and Methods in Physics Research Section A: Accelerators, Spectrometers, Detectors and Associated Equipment, vol. 367, no. 1, pp. 342–346, 1995.

[44] H. Hoedlmoser, A. Braem, G. De Cataldo, M. Davenport et al., "*Production technique and quality evaluation of CsI photocathodes for the ALICE/HMPID detector*", Nuclear Instruments and Methods in Physics Research Section A: Accelerators, Spectrometers, Detectors and Associated Equipment, vol. 566, no. 2, pp. 338–350, 2006.

[45] H. Hoedlmoser, A. Braem, G. De Cataldo, M. Davenport et al., "*Long term performance and ageing of CsI photocathodes for the ALICE/HMPID detector*", Nuclear Instruments and Methods in Physics Research Section A: Accelerators, Spectrometers, Detectors and Associated Equipment, vol. 574, no. 1, pp. 28–38, 2007.

[46] A. Braem, G. De Cataldo, M. Davenport, A. Di Mauro et al., "*Results from the ageing studies of large CsI photocathodes exposed to ionizing radiation in a gaseous RICH detector*", Nuclear Instruments and Methods in Physics Research Section A: Accelerators, Spectrometers, Detectors and Associated Equipment, vol. 553, no. 1, pp. 187–195, 2005.

[47] M. French, L. Jones, Q. Morrissey, A. Neviani et al., "*Design and results from the APV25, a deep sub-micron CMOS front-end chip for the CMS tracker*", Nuclear Instruments and Methods in Physics Research Section A: Accelerators, Spectrometers, Detectors and Associated Equipment, vol. 466, no. 2, pp. 359–365, 2001.

[48] F. Sauli and A. Sharma, "*Micropattern gaseous detectors*", Annual Review of Nuclear and Particle Science, vol. 49, no. 1, pp. 341–388, 1999.

[49] F. Sauli, "*Micro-pattern gas detectors*", Nuclear Instruments and Methods in Physics Research Section A: Accelerators, Spectrometers, Detectors and Associated Equipment, vol. 477, no. 1, pp. 1–7, 2002.

[50] A. Oed, "*Position-sensitive detector with microstrip anode for electron multiplication with gases*", Nuclear Instruments and Methods in Physics Research Section A: Accelerators, Spectrometers, Detectors and Associated Equipment, vol. 263, no. 2-3, pp. 351–359, 1988.

[51] F. Sauli, "*Recent topics on gaseous detectors*", Nuclear Instruments and Methods in Physics Research Section A: Accelerators, Spectrometers, Detectors and Associated Equipment, vol. 623, no. 1, pp. 29–34, 2010.

[52] F. Sauli, "*GEM: A new concept for electron amplification in gas detectors*", Nuclear Instruments and Methods in Physics Research Section A: Accelerators, Spectrometers, Detectors and Associated Equipment, vol. 386, no. 2, pp. 531–534, 1997.

[53] Y. Giomataris, "*Development and prospects of the new gaseous detector "Micromegas"*", Nuclear Instruments and Methods in Physics Research Section A: Accelerators, Spectrometers, Detectors and Associated Equipment, vol. 419, no. 2, pp. 239–250, 1998.

[54] G. Charpak, J. Derre, Y. Giomataris and P. Rebourgeard, "*Micromegas, a multipurpose gaseous detector*", Nuclear Instruments and Methods in Physics Research Section A: Accelerators, Spectrometers, Detectors and Associated Equipment, vol. 478, no. 1, pp. 26–36, 2002.

[55] P. Colas, I. Giomataris and V. Lepeltier, "*Ion backflow in the Micromegas TPC for the future linear collider*", Nuclear Instruments and Methods in Physics Research Section A: Accelerators, Spectrometers, Detectors and Associated Equipment, vol. 535, no. 1, pp. 226–230, 2004.

[56] I. Giomataris, R. De Oliveira, S. Andriamonje, S. Aune et al., "*Micromegas in a bulk*", Nuclear Instruments and Methods in Physics Research Section A: Accelerators, Spectrometers, Detectors and Associated Equipment, vol. 560, no. 2, pp. 405–408, 2006.

[57] S. Andriamonje, D. Attie, E. Berthoumieux, M. Calviani et al., "*Development and performance of Microbulk Micromegas detectors*", Journal of Instrumentation, vol. 5, no. 02, pp. P02001, 2010.

[58] F. Thibaud, P. Abbon, V. Andrieux, M. Anfreville et al., "*Performance of large pixelised Micromegas detectors in the COMPASS environment*", Journal of Instrumentation, vol. 9, no. 02, pp. C02005, 2014.

[59] M. Iodice, "*Micromegas detectors for the Muon Spectrometer upgrade of the ATLAS experiment*", Journal of Instrumentation, vol. 10, no. 02, pp. C02026, 2015.

[60] S. Anvar, P. Baron, M. Boyer, J. Beucher et al., "*Large bulk Micromegas detectors for TPC applications*", Nuclear Instruments and Methods in Physics Research Section A: Accelerators, Spectrometers, Detectors and Associated Equipment, vol. 602, no. 2, pp. 415–420, 2009.

[61] M. Titov, "*Perspectives of micro-pattern gaseous detector technologies for future physics projects*", arXiv preprint arXiv:1308.3047, 2013.

[62] S. Dalla Torre, "*MPGD developments: historical roadmap and recent progresses in consolidating MPGDs*", Journal of Instrumentation, vol. 8, no. 10, pp. C10020, 2013.

[63] F. Sauli, "*Development and applications of gas electron multiplier detectors*", Nuclear Instruments and Methods in Physics Research Section A: Accelerators, Spectrometers, Detectors and Associated Equipment, vol. 505, no. 1, pp. 195–198, 2003.

[64] F. Sauli, "*The gas electron multiplier (GEM): Operating principles and applications*", Nuclear Instruments and Methods in Physics Research Section A: Accelerators, Spectrometers, Detectors and Associated Equipment, vol. 805, pp. 2–24, 2016.

[65] T. Meinschad, L. Ropelewski and F. Sauli, "*GEM-based photon detector for RICH applications*", Nuclear Instruments and Methods in Physics Research Section A: Accelerators, Spectrometers, Detectors and Associated Equipment, vol. 535, no. 1, pp. 324–329, 2004.

[66] A. Breskin, A. Buzulutskov and R. Chechik, "*GEM photomultiplier operation in CF 4*", Nuclear Instruments and Methods in Physics Research Section A: Accelerators, Spectrometers, Detectors and Associated Equipment, vol. 483, no. 3, pp. 670–675, 2002.

[67] A. Milov, W. Anderson, B. Azmoun, C. Chi et al., "*Construction and expected performance of the hadron blind detector for the PHENIX experiment at RHIC*", Journal of Physics G: Nuclear and Particle Physics, vol. 34, no. 8, pp. S701, 2007.

[68] C. Aidala, B. Azmoun, Z. Fraenkel, T. Hemmick et al., "*A hadron blind detector for PHENIX*", Nuclear Instruments and Methods in Physics Research Section A: Accelerators, Spectrometers, Detectors and Associated Equipment, vol. 502, no. 1, pp. 200–204, 2003.

[69] W. Anderson, B. Azmoun, A. Cherlin, C. Chi et al., "*Design, construction, operation and performance of a Hadron Blind Detector for the PHENIX experiment*", Nuclear Instruments and Methods in Physics Research Section A: Accelerators, Spectrometers, Detectors and Associated Equipment, vol. 646, no. 1, pp. 35–58, 2011.

[70] Z. Fraenkel, A. Kozlov, M. Naglis, I. Ravinovich et al., "*A hadron blind detector for the PHENIX experiment at RHIC*", Nuclear Instruments and Methods in Physics Research Section A: Accelerators, Spectrometers, Detectors and Associated Equipment, vol. 546, no. 3, pp. 466–480, 2005.

[71] A. Austregesilo, F. Haas, B. Ketzer, I. Konorov et al., "*First results of the PixelGEM central tracking system for COMPASS*", Nuclear Physics B-Proceedings Supplements, vol. 197, no. 1, pp. 113–116, 2009.

[72] M. Quinto, M. Berretti, E. David, F. Garcia et al., "*The TOTEM GEM telescope (T2) at the LHC*", Nuclear Physics B-Proceedings Supplements, vol. 215, no. 1, pp. 225–227, 2011.

[73] C. Lippmann and A. T. Collaboration, "*A continuous read-out TPC for the ALICE upgrade*", Nuclear Instruments and Methods in Physics Research Section A: Accelerators, Spectrometers, Detectors and Associated Equipment, 2015.

[74] P. Jeanneret, "*Time projection chambers and detection of neutrions*", 2001.

[75] L. Periale, V. Peskov, P. Carlson, T. Francke et al., "*Detection of the primary scintillation light from dense Ar, Kr and Xe with novel photosensitive gaseous detectors*", Nuclear Instruments and Methods in Physics Research Section A: Accelerators, Spectrometers, Detectors and Associated Equipment, vol. 478, no. 1, pp. 377–383, 2002.

[76] P. Barbeau, J. Collar, J. Miyamoto and I. Shipsey, "*Toward coherent neutrino detection using low-background micropattern gas detectors*", Nuclear Science, IEEE Transactions on, vol. 50, no. 5, pp. 1285–1289, 2003.

[77] R. Chechik, A. Breskin, C. Shalem and D. Mörmann, "*Thick GEM-like hole multipliers: properties and possible applications*", Nuclear Instruments and Methods in Physics Research Section A: Accelerators, Spectrometers, Detectors and Associated Equipment, vol. 535, no. 1, pp. 303–308, 2004.

[78] C. Shalem, R. Chechik, A. Breskin and K. Michaeli, "*Advances in Thick GEM-like gaseous electron multipliers – Part I: atmospheric pressure operation*", Nuclear Instruments and Methods in Physics Research Section A: Accelerators, Spectrometers, Detectors and Associated Equipment, vol. 558, no. 2, pp. 475–489, 2006.

[79] C. Azevedo, M. Cortesi, A. Lyashenko, A. Breskin et al., "*Towards THGEM UV-photon detectors for RICH: on single-photon detection efficiency in Ne/CH4 and Ne/CF4*", Journal of Instrumentation, vol. 5, no. 01, pp. P01002, 2010.

[80] A. Breskin, V. Peskov, M. Cortesi, R. Budnik et al., "*CsI-THGEM gaseous photomultipliers for RICH and noble-liquid detectors*", Nuclear Instruments and Methods in Physics Research Section A: Accelerators, Spectrometers, Detectors and Associated Equipment, vol. 639, no. 1, pp. 117–120, 2011.

[81] J. Escada, L. Coelho, T. Dias, J. Lopes et al., "*Measurements of photoelectron extraction efficiency from CsI into mixtures of Ne with CH4, CF4, CO2 and N2*", Journal of Instrumentation, vol. 4, no. 11, pp. P11025, 2009.

[82] G. Hamar and D. Varga, "*High resolution surface scanning of Thick-GEM for single photo-electron detection*", Nuclear Instruments and Methods in Physics Research Section A: Accelerators, Spectrometers, Detectors and Associated Equipment, vol. 694, pp. 16–23, 2012.

[83] A. Breskin, M. Cortesi, R. Alon, J. Miyamoto et al., "*The THGEM: A thick robust gaseous electron multiplier for radiation detectors*", Nuclear Instruments and Methods in Physics Research Section A: Accelerators, Spectrometers, Detectors and Associated Equipment, vol. 623, no. 1, pp. 132–134, 2010.

[84] A. Lyashenko, A. Breskin, R. Chechik, J. Veloso et al., "*Further progress in ion back-flow reduction with patterned gaseous hole-multipliers*", Journal of Instrumentation, vol. 2, no. 08, pp. P08004, 2007.

[85] M. Alexeev, R. Birsa, F. Bradamante, A. Bressan et al., "*Ion backflow in thick GEM-based detectors of single photons*", Journal of Instrumentation, vol. 8, no. 01, pp. P01021, 2013.

[86] A. Lyashenko, A. Breskin, R. Chechik, J. Veloso et al., "*Advances in ion back-flow reduction in cascaded gaseous electron multipliers incorporating R-MHSP elements*", Journal of Instrumentation, vol. 1, no. 10, pp. P10004, 2006.

[87] J. Veloso, C. Santos, F. Pereira, C. Azevedo et al., "*THCOBRA: Ion back flow reduction in patterned THGEM cascades*", Nuclear Instruments and Methods in Physics Research Section A: Accelerators, Spectrometers, Detectors and Associated Equipment, vol. 639, no. 1, pp. 134–136, 2011.

[88] V. Peskov, G. Bencze, A. Di Mauro, P. Martinengo et al., "*First observation of Cherenkov rings with a large area CsI-TGEM-based RICH prototype*", Nuclear Instruments and Methods in Physics Research Section A: Accelerators, Spectrometers, Detectors and Associated Equipment, vol. 695, pp. 154–158, 2012.

[89] L. Baudis, "*DARWIN dark matter WIMP search with noble liquids*", In *Journal of Physics: Conference Series*, 2012.

[90] L. Kaufmann and A. Rubbia, "*The ARDM project: a dark matter direct detection experiment based on liquid Argon*", In *Journal of Physics: Conference Series*, 2007.

[91] C. Cantini, L. Epprecht, A. Gendotti, S. Horikawa et al., "*Performance study of the effective gain of the double phase liquid Argon LEM Time Projection Chamber*", Journal of Instrumentation, vol. 10, no. 03, pp. P03017, 2015.

[92] S. Dalla Torre, "*Micro Pattern Gas Detector Technologies and Applications-the work of the RD51 Collaboration*", PoS, pp. 002, 2014.

[93] R. Bouclier, W. Dominik, M. Hoch, J. C. Labbé et al., "*New observations with the gas electron multiplier (GEM)*", Nuclear Instruments and Methods in Physics Research Section A: Accelerators, Spectrometers, Detectors and Associated Equipment, vol. 396, no. 1, pp. 50–66, 1997.

[94] S. Kane, J. May, J. Miyamoto, I. Shipsey et al., "*A study of a combination of MICROMEGAS+ GEM chamber in Ar-CO 2 gas*", In *Nuclear Science Symposium Conference Record, 2001 IEEE*, 2001.

[95] S. Kane, J. May, J. Miyamoto and I. Shipsey, "*An aging study of a MICROMEGAS with GEM preamplification*", Nuclear Instruments and Methods in Physics Research Section A: Accelerators, Spectrometers, Detectors and Associated Equipment, vol. 515, no. 1, pp. 261–265, 2003.

[96] S. Duval, A. Breskin, H. Carduner, J. P. Cussonneau et al., "*MPGDs in Compton imaging with liquid-xenon*", Journal of Instrumentation, vol. 4, no. 12, pp. P12008, 2009.

[97] S. Duval, A. Breskin, R. Budnik, W. Chen et al., "*On the operation of a micropattern gaseous UV-photomultiplier in liquid-Xenon*", Journal of Instrumentation, vol. 6, no. 04, pp. P04007, 2011.

[98] S. Duval, L. Arazi, A. Breskin, R. Budnik et al., "*Hybrid multi micropattern gaseous photomultiplier for detection of liquid-xenon scintillation*", Nuclear Instruments and Methods in Physics Research Section A: Accelerators, Spectrometers, Detectors and Associated Equipment, vol. 695, pp. 163–167, 2012.

[99] K. Giboni, X. Ji, H. Lin and T. Ye, "*On Dark Matter detector concepts with large-area cryogenic Gaseous Photo Multipliers*", Journal of Instrumentation, vol. 9, no. 02, pp. C02021, 2014.

[100] M. Curie, "*Pierre Curie: With Autobiographical Notes by Marie Curie*", Dover Publications, 2013.

[101] P. A. Cherenkov, "*Visible emission of clean liquids by action of γ radiation*", Doklady Akademii Nauk SSSR, vol. 2, pp. 451, 1934.

[102] I. Frank and I. Tamm, "*Coherent visible radiation from fast electrons passing through matter*", CR Acad. Sci. USSR, vol. 14, pp. 109–114, 1937.

[103] J. Séguinot and T. Ypsilantis, "*Photo-ionization and Cherenkov ring imaging*", Nuclear Instruments and Methods, vol. 142, no. 3, pp. 377–391, 1977.

[104] A. Roberts, "*A new type of Čerenkov detector for the accurate measurement of particle velocity and direction*", Nuclear Instruments and Methods, vol. 9, no. 1, pp. 55–66, 1960.

[105] T. Ypsilantis and J. Séguinot, "*Theory of ring imaging Cherenkov counters*", Nuclear Instruments and Methods in Physics Research Section A: Accelerators, Spectrometers, Detectors and Associated Equipment, vol. 343, no. 1, pp. 30–51, 1994.

[106] C. Lippmann, "*Particle identification*", Nuclear Instruments and Methods in Physics Research Section A: Accelerators, Spectrometers, Detectors and Associated Equipment, vol. 666, pp. 148 - 172, 2012.

[107] N. Harnew, "*Alternative particle identification techniques to Cherenkov detectors*", Nuclear Instruments and Methods in Physics Research Section A: Accelerators, Spectrometers, Detectors and Associated Equipment, vol. 766, pp. 274–282, 2014.

[108] I. Adam, R. Aleksan, L. Amerman, E. Antokhin et al., "*The DIRC particle identification system for the BaBar experiment*", Nuclear Instruments and Methods in Physics Research Section A: Accelerators, Spectrometers, Detectors and Associated Equipment, vol. 538, no. 1, pp. 281–357, 2005.

[109] H. W. Siebert, W. Beusch, J. Engelfried, F. Faller et al., "*The omega RICH*", Nuclear Instruments and Methods in Physics Research Section A: Accelerators, Spectrometers, Detectors and Associated Equipment, vol. 343, no. 1, pp. 60–67, 1994.

[110] M. Artuso, R. Ayad, K. Bukin, A. Efimov et al., "*Construction, pattern recognition and performance of the CLEO III LiF-TEA RICH detector*", Nuclear Instruments and Methods in Physics Research Section A: Accelerators, Spectrometers, Detectors and Associated Equipment, vol. 502, no. 1, pp. 91–100, 2003.

[111] G. Charpak, S. Majewski, G. Melchart, F. Sauli et al., "*Detection of far-ultraviolet photons with the multistep avalanche chamber. Application to Cherenkov light imaging and to some problems in high-energy physics*", Nuclear Instruments and Methods, vol. 164, no. 3, pp. 419–433, 1979.

[112] K. Zeitelhack, A. Elhardt, J. Friese, R. Gernhäuser et al., "*The hades rich detector*", Nuclear Instruments and Methods in Physics Research Section A: Accelerators, Spectrometers, Detectors and Associated Equipment, vol. 433, no. 1, pp. 201–206, 1999.

[113] P. Abbon, M. Alexeev, H. Angerer, G. Baum et al., "*The experience of building and operating COMPASS RICH-1*", Nuclear Instruments and Methods in Physics Research Section A: Accelerators, Spectrometers, Detectors and Associated Equipment, vol. 639, no. 1, pp. 15 - 19, 2011.

[114] F. Garibaldi, E. Cisbani, S. Colilli, F. Cusanno et al., "*A proximity focusing RICH detector for kaon physics at Jefferson Lab Hall A*", Nuclear Instruments and Methods in Physics Research Section A: Accelerators, Spectrometers, Detectors and Associated Equipment, vol. 502, no. 1, pp. 117–122, 2003.

[115] A. Gallas, "*Performance of the high momentum particle identification CsI-RICH for ALICE at CERN-LHC*", Nuclear Instruments and Methods in Physics Research Section A: Accelerators, Spectrometers, Detectors and Associated Equipment, vol. 553, no. 1, pp. 345–350, 2005.

[116] I. Arino, J. Bastos, D. Broemmelsiek, J. Carvalho et al., "*The HERA-B ring imaging Cherenkov counter*", Nuclear Instruments and Methods in Physics Research Section A: Accelerators, Spectrometers, Detectors and Associated Equipment, vol. 516, no. 2, pp. 445–461, 2004.

[117] D. Renker and E. Lorenz, "*Advances in solid state photon detectors*", Journal of Instrumentation, vol. 4, no. 04, pp. P04004, 2009.

[118] S. Nishida, I. Adachi, N. Hamada, K. Hara et al., "*Aerogel RICH for the Belle II forward PID*", Nuclear Instruments and Methods in Physics Research Section A: Accelerators, Spectrometers, Detectors and Associated Equipment, vol. 766, pp. 28–31, 2014.

[119] M. Moritz, G. A. Rinella, L. Allebone, M. Campbell et al., "*Performance study of new pixel hybrid photon detector prototypes for the LHCb RICH counters*", Nuclear Science, IEEE Transactions on, vol. 51, no. 3, pp. 1060–1066, 2004.

[120] COMPASS collaboration webpage: `http://wwwcompass.cern.ch`.

[121] P. Abbon, C. Adolph, R. Akhunzyanov, Y. Alexandrov et al., "*The COMPASS setup for physics with hadron beams*", Nuclear Instruments and Methods in Physics Research Section A: Accelerators, Spectrometers, Detectors and Associated Equipment, vol. 779, pp. 69–115, 2015.

[122] P. Abbon, M. Alexeev, H. Angerer, R. Birsa et al., "*Design and construction of the fast photon detection system for COMPASS RICH-1*", Nuclear Instruments and Methods in Physics Research Section A: Accelerators, Spectrometers, Detectors and Associated Equipment, vol. 616, no. 1, pp. 21–37, 2010.

[123] P. Abbon, M. Alexeev, H. Angerer, R. Birsa et al., "*The COMPASS RICH-1 fast photon detection system*", Nuclear Instruments and Methods in Physics Research Section A: Accelerators, Spectrometers, Detectors and Associated Equipment, vol. 595, no. 1, pp. 23–26, 2008.

[124] P. Abbon, M. Alexeev, H. Angerer, G. Baum et al., "*Particle identification with COMPASS RICH-1*", Nuclear Instruments and Methods in Physics Research Section A: Accelerators, Spectrometers, Detectors and Associated Equipment, vol. 631, no. 1, pp. 26–39, 2011.

[125] M. Chiosso, O. Cobanoglu, G. Mazza, D. Panieri et al., "*A fast binary front-end ASIC for the RICH detector of the COMPASS experiment at CERN*", In *Nuclear Science Symposium Conference Record, 2008. NSS'08. IEEE*, 2008.

[126] P. Abbon, M. Alexeev, H. Angerer, R. Birsa et al., "*The fast readout system for the MAPMTs of COMPASS RICH-1*", Nuclear Instruments and Methods in Physics Research Section A: Accelerators, Spectrometers, Detectors and Associated Equipment, vol. 595, no. 1, pp. 204–207, 2008.

[127] P. Abbon, M. Alexeev, H. Angerer, R. Birsa et al., "*Read-out electronics for fast photon detection with COMPASS RICH-1*", Nuclear Instruments and Methods in Physics Research Section A: Accelerators, Spectrometers, Detectors and Associated Equipment, vol. 587, no. 2, pp. 371–387, 2008.

[128] F. Tessarotto, P. Abbon, M. Alexeev, R. Birsa et al., "*Long term experience and performance of COMPASS RICH-1*", Journal of Instrumentation, vol. 9, no. 09, pp. C09011, 2014.

[129] P. Abbon, E. Delagnes, H. Deschamps, F. Kunne et al., "*Fast readout of the COMPASS RICH CsI-MWPC photon chambers*", Nuclear Instruments and Methods in Physics Research Section A: Accelerators, Spectrometers, Detectors and Associated Equipment, vol. 567, no. 1, pp. 104–106, 2006.

[130] P. Abbon, M. Alexeev, H. Angerer, R. Birsa et al., "*Particle identification with the fast COMPASS RICH-1 detector*", Nuclear Instruments and Methods in Physics Research Section A: Accelerators, Spectrometers, Detectors and Associated Equipment, vol. 623, no. 1, pp. 330–332, 2010.

[131] R. Chechik, A. Breskin and C. Shalem, "*Thick GEM-like multipliers – a simple solution for large area UV-RICH detectors*", Nuclear Instruments and Methods in Physics Research Section A: Accelerators, Spectrometers, Detectors and Associated Equipment, vol. 553, no. 1, pp. 35–40, 2005.

[132] M. Alexeev, M. Alfonsi, R. Birsa, F. Bradamante et al., "*Development of THGEM-based photon detectors for Cherenkov Imaging Counters*", Journal of Instrumentation, vol. 5, no. 03, pp. P03009, 2010.

[133] M. Alexeev, F. Barbosa, R. Birsa, F. Bradamante et al., "*Detection of single photons with THickGEM-based counters*", Journal of Instrumentation, vol. 7, no. 02, pp. C02014, 2012.

[134] M. Alexeev, R. Birsa, F. Bradamante, A. Bressan et al., "*Micropattern gaseous photon detectors for Cherenkov imaging counters*", Nuclear Instruments and Methods in Physics Research Section A: Accelerators, Spectrometers, Detectors and Associated Equipment, vol. 623, no. 1, pp. 129–131, 2010.

[135] M. Alexeev, R. Birsa, F. Bradamante, A. Bressan et al., "*The gain in Thick GEM multipliers and its time-evolution*", Journal of Instrumentation, vol. 10, no. 03, pp. P03026, 2015.

[136] B. Azmoun, W. Anderson, D. Crary, J. Durham et al., "*A study of gain stability and charging effects in GEM foils*", In *Nuclear Science Symposium Conference Record, 2006. IEEE*, 2006.

[137] P. Correia, C. Oliveira, C. Azevedo, A. Silva et al., "*A dynamic method for charging-up calculations: the case of GEM*", Journal of Instrumentation, vol. 9, no. 07, pp. P07025, 2014.

[138] P. M. M. Correia, "*Studies in gaseous radiation detectors: GEM, THGEM and Compton camera*", Universidade de Aveiro, 2013.

[139] M. Alexeev, R. Birsa, F. Bradamante, A. Bressan et al., "*The quest for a third generation of gaseous photon detectors for Cherenkov imaging counters*", Nuclear Instruments and Methods in Physics Research Section A: Accelerators, Spectrometers, Detectors and Associated Equipment, vol. 610, no. 1, pp. 174–177, 2009.

[140] E. Rocco, "*Development of a gaseous photon detector for Cherenkov imaging applications*", Turin U., 2010.

[141] M. Alexeev, F. Barbosa, R. Birsa, F. Bradamante et al., "*Detection of single photons with THickGEM-based counters*", Nuclear Instruments and Methods in Physics Research Section A: Accelerators, Spectrometers, Detectors and Associated Equipment, vol. 695, pp. 159 - 162, 2012.

[142] M. Alexeev, R. Birsa, F. Bradamante, A. Bressan et al., "*Progress towards a THGEM-based detector of single photons*", Nuclear Instruments and Methods in Physics Research Section A: Accelerators, Spectrometers, Detectors and Associated Equipment, vol. 639, no. 1, pp. 130–133, 2011.

[143] M. Alexeev, R. Birsa, F. Bradamante, A. Bressan et al., "*Thick GEM-based detectors of single photons for Cherenkov imaging applications*", In *Nuclear Science Symposium and Medical Imaging Conference (NSS/MIC), 2012 IEEE*, 2012.

[144] M. Alexeev, C. Azevedo, R. Birsa, F. Bradamante et al., "*Ion back flow reduction in a THGEM based detector*", In *Nuclear Science Symposium and Medical Imaging Conference (NSS/MIC), 2012 IEEE*, 2012.

[145] M. Alexeev, R. Birsa, F. Bradamante, A. Bressan et al., "*Thick GEM-based detectors of single photons for Cherenkov imaging applications*", In *Nuclear Science Symposium and Medical Imaging Conference (NSS/MIC), 2012 IEEE*, 2012.

[146] C. A. F. d. Santos, "*Thick-microstructures for MPGDs: simulations and experimental studies*", 2014.

[147] J. Veloso, J. Dos Santos and C. Conde, "*A proposed new microstructure for gas radiation detectors: The microhole and strip plate*", Review of Scientific Instruments, vol. 71, no. 6, pp. 2371–2376, 2000.

[148] F. Sauli, L. Ropelewski and P. Everaerts, "*Ion feedback suppression in time projection chambers*", Nuclear Instruments and Methods in Physics Research Section A: Accelerators, Spectrometers, Detectors and Associated Equipment, vol. 560, no. 2, pp. 269–277, 2006.

[149] M. Alexeev, R. Birsa, F. Bradamante, A. Bressan et al., "*Status and progress of novel photon detectors based on THGEM and hybrid MPGD architectures*", Journal of Instrumentation, vol. 8, no. 12, pp. C12005, 2013.

[150] M. Alexeev, R. Birsa, F. Bradamante, A. Bressan et al., "*Development of THGEM-based Photon Detectors for COMPASS RICH-1*", Physics Procedia, vol. 37, pp. 781 - 788, 2012.

[151] M. Alexeev, R. Birsa, F. Bradamante, A. Bressan et al., "*Progresses in the production of large-size THGEM boards*", Journal of Instrumentation, vol. 9, no. 03, pp. C03046, 2014.

[152] M. S. Naidu and V. Kamaraju, "*High voltage engineering*", Tata McGraw-Hill Education, 2013.

[153] C. Wadhwa, "*High voltage engineering*", New Age International, 2007.

[154] M. S. Dixit, J. Dubeau, J. P. Martin and K. Sachs, "*Position sensing from charge dispersion in micro-pattern gas detectors with a resistive anode*", Nuclear Instruments and Methods in Physics Research Section A: Accelerators, Spectrometers, Detectors and Associated Equipment, vol. 518, no. 3, pp. 721–727, 2004.

[155] M. Dixit and A. Rankin, "*Simulating the charge dispersion phenomena in Micro Pattern Gas Detectors with a resistive anode*", Nuclear Instruments and Methods in Physics Research Section A: Accelerators, Spectrometers, Detectors and Associated Equipment, vol. 566, no. 2, pp. 281–285, 2006.

[156] T. Alexopoulos, G. Iakovidis and G. Tsipolitis, "*Study of resistive micromegas detectors in a mixed neutron and photon radiation environment*", Journal of Instrumentation, vol. 7, no. 05, pp. C05001, 2012.

[157] T. Alexopoulos, J. Burnens, R. De Oliveira, G. Glonti et al., "*A spark-resistant bulk-micromegas chamber for high-rate applications*", Nuclear Instruments and Methods in Physics Research Section A: Accelerators, Spectrometers, Detectors and Associated Equipment, vol. 640, no. 1, pp. 110–118, 2011.

[158] S. Bartknecht, H. Fischer, F. Herrmann, K. Königsmann et al., "*Development of a 1GS/s high-resolution sampling ADC system*", Nuclear Instruments and Methods in Physics Research Section A: Accelerators, Spectrometers, Detectors and Associated Equipment, vol. 623, no. 1, pp. 507–509, 2010.

[159] M. Wernick and J. Aarsvold, "*Emission Tomography: The Fundamentals of PET and SPECT*", Elsevier Academic Press, 2004.

[160] H. O. Anger, "*Scintillation camera*", Review of scientific instruments, vol. 29, no. 1, pp. 27–33, 1958.

[161] K. Pinkau, "*Die Messung solarer und atmosphärischer Neutronen*", Zeitschrift für Naturforschung A, vol. 21, no. 12, pp. 2100–2101, 1966.

[162] R. White, "*AN EXPERIMENT TO MEASURE NEUTRONS FROM SUN*", In *BULLETIN OF THE AMERICAN PHYSICAL SOCIETY*, 1968.

[163] R. Todd, J. Nightingale and D. Everett, "*A proposed gamma camera*", Nature, vol. 251, pp. 132–134, 1974.

[164] S. Moon, B. Arnés, A. Boston, H. Boston et al., "*Compton imaging with AGATA and SmartPET for DESPEC*", Journal of Instrumentation, vol. 6, pp. C12048, 2011.

[165] L. Harkness, D. Judson, H. Kennedy, A. Sweeney et al., "*Semiconductor detectors for Compton imaging in nuclear medicine*", Journal of Instrumentation, vol. 7, pp. C01004, 2012.

[166] L. Harkness, A. Boston, H. Boston, R. Cooper et al., "*Optimisation of a dual head semiconductor Compton camera using Geant4*", Nuclear Instruments and Methods in Physics Research Section A: Accelerators, Spectrometers, Detectors and Associated Equipment, vol. 604, no. 1-2, pp. 351–354, 2009.

[167] R. Cooper, A. Boston, H. Boston, J. Cresswell et al., "*SmartPET: applying HPGe and pulse shape analysis to small-animal PET*", Nuclear Instruments and Methods in Physics Research Section A: Accelerators, Spectrometers, Detectors and Associated Equipment, vol. 579, no. 1, pp. 313–317, 2007.

[168] D. Porgamrays Collaboration Judson, A. Boston, P. Coleman-Smith, D. Cullen et al., "*Compton imaging with the PorGamRays spectrometer*", Nuclear Instruments and Methods in Physics Research A, vol. 652, pp. 587–590, 2011.

[169] A. Studen, D. Burdette, E. Chesi, V. Cindro et al., "*First coincidences in pre-clinical Compton camera prototype for medical imaging*", Nuclear Instruments and Methods in Physics Research Section A: Accelerators, Spectrometers, Detectors and Associated Equipment, vol. 531, no. 1, pp. 258–264, 2004.

[170] S. Watanabe, T. Tanaka, K. Oonuki, T. Mitani et al., "*Development of CdTe pixel detectors for Compton cameras*", Nuclear Instruments and Methods in Physics Research Section A: Accelerators, Spectrometers, Detectors and Associated Equipment, vol. 567, no. 1, pp. 150–153, 2006.

[171] J. LeBlanc, N. Clinthorne, C. Hua, W. Rogers et al., "*A Compton camera for nuclear medicine applications using* ^{113m}In", Nuclear Instruments and Methods in Physics Research Section A: Accelerators, Spectrometers, Detectors and Associated Equipment, vol. 422, no. 1, pp. 735–739, 1999.

[172] C. Uche, W. Round and M. Cree, "*Effects of energy threshold and dead time on Compton camera performance*", Nuclear Instruments and Methods in Physics Research Section A: Accelerators, Spectrometers, Detectors and Associated Equipment, 2011.

[173] S. An, H. Seo, J. Lee, C. Lee et al., "*Effect of detector parameters on the image quality of Compton camera for* ^{99m}Tc", Nuclear Instruments and Methods in Physics Research Section A: Accelerators, Spectrometers, Detectors and Associated Equipment, vol. 571, no. 1, pp. 251–254, 2007.

[174] E. Cochran, "*PHD thesis: Silicon Detectors for PET and SPECT*", 2010.

[175] L. Mihailescu, K. Vetter, M. Burks, E. Hull et al., "*SPEIR: a Ge Compton camera*", Nuclear Instruments and Methods in Physics Research Section A: Accelerators, Spectrometers, Detectors and Associated Equipment, vol. 570, no. 1, pp. 89–100, 2007.

[176] D. Xu, Z. He, C. Lehner and F. Zhang, "*4π Compton imaging with single 3D position sensitive CdZnTe detector*", In *Proc. of SPIE Vol*, 2004.

[177] C. E. Lehner, Z. He and F. Zhang, "*4π Compton imaging using a 3-D position-sensitive CdZnTe detector via weighted list-mode maximum likelihood*", Nuclear Science, IEEE Transactions on, vol. 51, no. 4, pp. 1618–1624, 2004.

[178] A. Takada, K. Hattori, H. Kubo, K. Miuchi et al., "*Development of an advanced Compton camera with gaseous TPC and scintillator*", Nuclear Instruments and Methods in Physics Research Section A: Accelerators, Spectrometers, Detectors and Associated Equipment, vol. 546, no. 1, pp. 258–262, 2005.

[179] S. Kabuki, K. Hattori, R. Kohara, E. Kunieda et al., "*Development of Electron Tracking Compton Camera using micro pixel gas chamber for medical imaging*", Nuclear Instruments and Methods in Physics Research Section A: Accelerators, Spectrometers, Detectors and Associated Equipment, vol. 580, no. 2, pp. 1031–1035, 2007.

[180] M. Takahashi, S. Kabuki, K. Hattori, N. Higashi et al., "*Development of an Electron-Tracking Compton Camera using CF4 gas at high pressure for improved detection efficiency*", Nuclear Instruments and Methods in Physics Research Section A: Accelerators, Spectrometers, Detectors and Associated Equipment, vol. 628, no. 1, pp. 150–153, 2011.

[181] S. Kabuki, H. Kimura, H. Amano, Y. Nakamoto et al., "*Electron-tracking Compton gamma-ray camera for small animal and phantom imaging*", Nuclear Instruments and Methods in Physics Research Section A: Accelerators, Spectrometers, Detectors and Associated Equipment, vol. 623, no. 1, pp. 606–607, 2010.

[182] A. Bolozdynya, V. Egorov, A. Koutchenkov, G. Safronov et al., "*A high pressure xenon self-triggered scintillation drift chamber with 3D sensitivity in the range of 20–140 keV deposited energy*", Nuclear Instruments and Methods in Physics Research Section A: Accelerators, Spectrometers, Detectors and Associated Equipment, vol. 385, no. 2, pp. 225–238, 1997.

[183] A. Bolozdynya, V. V. Egorov, A. V. Koutchenkov, G. Safronov et al., "*High pressure xenon electronically collimated camera for low energy gamma ray imaging*", Nuclear Science, IEEE Transactions on, vol. 44, no. 6, pp. 2408–2414, 1997.

[184] C. E. Ordonez, A. Bolozdynya and W. Chang, "*Doppler broadening of energy spectra in Compton cameras*", In *Nuclear Science Symposium, 1997. IEEE*, 1997.

[185] L. Han, "*Statistical performance evaluation, system modeling, distributed computation and signal pattern matching for a Compton medical imaging system*", The University of Michigan, 2008.

[186] R. Ribberfors and K. F. Berggren, "*Incoherent-x-ray-scattering functions and cross sections ($d\sigma/d\,\Omega)_{incoh}$ by means of a pocket calculator*", Physical Review A, vol. 26, no. 6, pp. 3325, 1982.

[187] F. Biggs, L. Mendelsohn and J. Mann, "*Hartree-Fock Compton profiles for the elements*", Atomic data and nuclear data tables, vol. 16, no. 3, pp. 201–309, 1975.

[188] G. H. Zschornack, "*Handbook of X-ray Data*", Springer Science & Business Media, 2007.

[189] C. H. Hua, N. Clinthorne, S. Wilderman, J. LeBlanc et al., "*Decoding penalty calculation for a ring Compton camera using uniform Cramer-Rao bound*", In *Nuclear Science Symposium, 1998. Conference Record. 1998 IEEE*, 1998.

[190] J. LeBlanc, N. Clinthorne, C. H. Hua, E. Nygård et al., "*C-SPRINT: a prototype Compton camera system for low energy gamma ray imaging*", Nuclear Science, IEEE Transactions on, vol. 45, no. 3, pp. 943–949, 1998.

[191] A. Bolozdynya and V. L. Morgunov, "*Multilayer electroluminescence camera: concept and Monte Carlo study*", Nuclear Science, IEEE Transactions on, vol. 45, no. 3, pp. 1646–1655, 1998.

[192] C. Azevedo, S. Biagi, R. Veenhof, P. Correia et al., "*Position resolution limits in pure noble gaseous detectors for X-ray energies from 1 to 60 keV*", Physics Letters B, vol. 741, pp. 272–275, 2015.

[193] C. Conde and A. Policarpo, "*A gas proportional scintillation counter*", Nuclear Instruments and Methods, vol. 53, pp. 7–12, 1967.

[194] A. J. Policarpo, "*The gas proportional scintillation counter*", Space Science Instrumentation, vol. 3, pp. 77–107, 1977.

[195] G. Charpak, H. Ngoc and A. Policarpo, "*Neutral radiation detection and localization*", US Patent 4,286,158, 1981.

[196] T. Lopes, A. Silva, C. Azevedo, L. Carramate et al., "*Position sensitive VUV gaseous photomultiplier based on Thick-multipliers with resistive line readout*", Journal of Instrumentation, vol. 8, no. 09, pp. P09002, 2013.

[197] B. L. Paredes, C. Azevedo, S. Paganis, A. Silva et al., "*Cryogenic Gaseous Photomultiplier for position reconstruction of liquid argon scintillation light*", Journal of Instrumentation, vol. 10, no. 07, pp. P07017, 2015.

[198] H. N. Da Luz, J. Veloso, N. Mendes, J. Dos Santos et al., "*MHSP with position detection capability*", Nuclear Instruments and Methods in Physics Research Section A: Accelerators, Spectrometers, Detectors and Associated Equipment, vol. 573, no. 1, pp. 191–194, 2007.

[199] H. N. Da Luz, J. Veloso, J. Santos and J. Mir, "*A simple X-ray position detection system based on a MHSP*", Nuclear Instruments and Methods in Physics Research Section A: Accelerators, Spectrometers, Detectors and Associated Equipment, vol. 580, no. 2, pp. 1083–1086, 2007.

[200] H. Luz, C. A. Oliveira, C. D. Azevedo, J. Mir et al., "*Single photon counting X-ray imaging system using a micro hole and strip plate*", Nuclear Science, IEEE Transactions on, vol. 55, no. 4, pp. 2341–2345, 2008.

[201] D. Xu, "*Gamma-ray imaging and polarization measurement using 3-D position-sensitive CdZnTe detectors*", The University of Michigan, 2006.

[202] E. Aprile, A. Bolotnikov, D. Chen, R. Mukherjee et al., "*Electron extraction from a CsI photocathode into condensed Xe, Kr, and Ar*", Nuclear Instruments and Methods in Physics Research Section A: Accelerators, Spectrometers, Detectors and Associated Equipment, vol. 343, no. 1, pp. 129–134, 1994.

[203] E. Aprile, "*The XENON1T dark matter search experiment*", Springer, pp. 93–96, 2013.

[204] A. Barabash, "*Double-beta decay: Present status*", Physics of Atomic Nuclei, vol. 73, no. 1, pp. 162–178, 2010.

[205] A. Breskin, "*Liquid Hole-Multipliers: A potential concept for large single-phase noble-liquid TPCs of rare events*", In *Journal of Physics: Conference Series*, 2013.

[206] R. Alon, J. Miyamoto, M. Cortesi, A. Breskin et al., "*Operation of a thick gas electron multiplier (THGEM) in Ar, Xe and Ar-Xe*", Journal of Instrumentation, vol. 3, no. 01, pp. P01005, 2008.

[207] V. Peskov, A. Di Mauro, P. Fonte, P. Martinengo et al., "*Development of a new generation of micropattern gaseous detectors for high energy physics, astrophysics and environmental applications*", Nuclear Instruments and Methods in Physics Research Section A: Accelerators, Spectrometers, Detectors and Associated Equipment, vol. 732, pp. 255–259, 2013.

[208] D. Covita, C. Azevedo, C. Caldas and J. Veloso, "*Photoelectron extraction efficiency from cesium iodide photocathodes in a pressurized atmosphere of argon and xenon up to 10 bar*", Physics Letters B, vol. 701, no. 2, pp. 151–154, 2011.